UNIVERSITÉ CÔTE D'AZUR

UNIVERSITE COTE D'AZUR - UFR Sciences
Ecole Doctorale en Sciences Fondamentales et Appliquées EDSFA

T H E S E

pour obtenir le titre de
Docteur en Sciences
de l'UNIVERSITE COTE D'AZUR

Discipline : Mathématiques

Julian HENNICKER

Discrétisation gradient de modèles d'écoulements à dimensions hybrides dans les milieux poreux fracturés

Thèse dirigée par Roland MASSON
soutenue le 10 juillet 2017

Jury :

M.	BASTIAN Peter	Rapporteur
M.	EYMARD Robert	Rapporteur
M.	ERN Alexandre	Examinateur
M.	SAMIER Pierre	Examinateur
M.	TERPOLILLI Peppino	Examinateur
M.	BRENNER Konstantin	Co-Directeur de thèse
M.	MASSON Roland	Directeur de thèse

Discrétisation gradient de modèles d'écoulements à dimensions hybrides dans les milieux poreux fracturés

Résumé: Cette thèse porte sur la modélisation d'écoulements Darcy dans les milieux poreux fracturés et la discrétisation des modèles sur des maillages généraux. Dans le chapitre 1, nous tournons notre regard vers les écoulements monophasiques et considérons un modèle à dimensions hybrides comportant un réseau complexe de fractures planes. Le modèle prend en compte les interactions hydrodynamiques entre matrice et fractures et traite des fractures agissant comme conduites ou comme barrières, ce que nécessite de prendre en compte les sauts de pression aux interfaces matrice-fracture. L'analyse numérique est menée dans le cadre général de la méthode de discrétisations gradients (MDG), qui est étendue au modèle considéré. Deux familles de schémas numériques, le schéma VAG (Vertex Approximate Gradient) et le schéma HFV (Hybrid Finite Volume) sont adaptées aux modèles à dimensions hybrides. On prouve que les schémas VAG et HFV sont des schémas gradients, pour lesquels la convergence est établie. Des expériences numériques confirment les résultats théoriques. Dans le chapitre 2, nous proposons comme extension du modèle précédent aux écoulement diphasiques deux différents modèles à dimensions hybrides, qui prennent en compte les sauts de pressions aux interfaces matrice-fracture. Les modèles permettent de reconstituer les forces gravitaires, notamment dans les fractures, ainsi que les sauts de saturations aux interfaces entre différents types de roches dû a la capillarité. Nous adaptons le schéma VAG à ce problème et présentons une série de cas tests afin de comparer ces deux modèles à dimensions hybrides au modèle dimensionnel hybride à pression continue (proposé dans [16]) et au modèle équi dimensionnel de référence, dans lequel les fractures ont la même dimension que la matrice. A part quantifier le gain en performance de calcul, ces tests montrent aussi la qualité des différents modèles réduits. Dans le chapitre 3, une couche de roches endommagées est ajoutée au modèle à dimensions hybrides du chapitre 2. Pour ce modèle, l'analyse numérique est conduite dans le cadre MDG. Des techniques de compacité sont employées pour établir des résultats de convergence pour un large nombre de possibles schémas numériques; l'existence d'une solution pour le modèle diphasique est ainsi obtenue en passant. Une série d'expériences numériques conclut le chapitre avec une étude sur l'influence de la couche endommagée sur la solution.

Mots-clés: modèles matrice fractures discrètes (DFM); écoulement Darcy multiphasique; pression capillaire discontinue; Méthode de Discrétisations Gradients; analyse numérique; schémas volumes finis; maillages polyédriques

Hybrid dimensional modeling of multi-phase Darcy flows in fractured porous media

Abstract: This thesis investigates the modelling of Darcy flow through fractured porous media and its discretization on general polyhedral meshes. In chapter 1, we concentrate on single phase flow and consider a hybrid dimensional model, invoking a complex network of planar fractures. The model accounts for matrix-fracture interactions and fractures acting either as drains or as barriers, i.e. we have to deal with pressure discontinuities at matrix-fracture interfaces. The numerical analysis is performed in the general framework of the Gradient Discretisation Method (GDM), which is extended to the model under consideration. Two families of schemes namely the Vertex Approximate Gradient scheme (VAG) and the Hybrid Finite Volume scheme (HFV) are detailed and shown to fit in the gradient scheme framework, which yields, in particular, convergence. Numerical tests confirm the theoretical results. In chapter 2, two different hybrid dimensional models are proposed as an extension of the single phase model of chapter 1 to two phase flow. They both allow for pressure jumps at the matrix-fracture interfaces. The models also permit to treat gravity dominated flow as well as discontinuous capillary pressure at the material interfaces. We adapt the VAG scheme to this problem by using an upwind procedure for the fluxes that respects the different rock properties. We then present several test cases to compare our hybrid-dimensional models to the hybrid-dimensional, continuous pressure model (proposed in [16]) and to the generic equi-dimensional model, in which fractures have the same dimension as the matrix. This does not only provide quantitative evidence about computational gain, but also leads to deep insight about the quality of the proposed reduced models. In chapter 3, a layer of damaged rock at the matrix-fracture interfaces is added to the hybrid dimensional model of chapter 2. For this model, the numerical analysis is carried out in the framework of GDM. Compactness techniques are used to establish convergence results for a wide range of possible numerical schemes including the VAG and HFV schemes; the existence of a solution for the two phase flow model is obtained as a byproduct of the convergence analysis. A series of numerical experiments conclude the chapter, with a study of the influence of the damaged layer on the numerical solution.

Keywords: Discrete Fracure-Matrix (DFM) models; Two Phase Darcy Flow; Discontinuous Capillary Pressure; Gradient Discretization Method; Numerical Analysis; Finite Volume Schemes; Polyhedral Meshes

Remerciements

Tout d'abord, je souhaite exprimer ma reconnaissance à mon directeur de thèse, Roland Masson, qui a initié une collaboration industrialo-scientifique avec Alexandre Lapène de Total S.A., dont le fruit est la présente thèse. Puis je remercie Total S.A. et l'ANRT pour le financement.

Merci à Roland de m'avoir acceuilli au sein de ton équipe à Nice pendant ces trois années passées. Je me sens privilégié d'avoir pu travailler dans une ambiance de générosité, de partage et d'enthousiasme. Merci également pour toutes les possibilités, les nombreuses conférences, l'école d'été et avant tout le séjour de recherche à Melbourne.

Merci à Jérôme Droniou de Monash University d'avoir accepté de m'accueillir à Clayton pendant trois mois pour travailler sur l'analyse numérique présentée dans le chapitre 3. Tes explications instructives sur notre problème complexe m'ont élargies le regard envers l'exploitation des propriétés de compacité pour l'analyse de convergence.

Merci Konstantin Brenner, d'avoir partagé avec moi des idées inédites et des réflexions en direct dans des nombreuses discussions. Et merci pour ton amitié.

Merci également à Pierre Samier de Total S.A. pour le suivi du projet du point de vue ingénierie de réservoir.

Je remercie chaleureusement l'ensemble du jury. Merci à mes rapporteurs, Peter Bastian de l'Université de Heidelberg et Robert Eymard de l'Université Paris-Est pour tout le temps que vous avez consacré à l'évaluation de ma thèse. Merci aux examinateurs, Alexandre Ern de l'Université Paris-Est, Pierre Samier et Peppino Terpolilli de Total S.A. d'avoir accepté de faire partie de ce jury et pour votre interêt à ce projet de recherche.

Merci à l'équipe administrative du Laboratoire Dieudonné ainsi qu'à l'équipe RH du Centre de Recherche J. Féger de m'avoir facilité la vie.

A Enzo.

Contents

Introduction

Contexte de l'étude et état de l'art

Depuis la nuit des temps, l'esprit humain s'occupe d'extraire des lois causales à partir d'observations, afin de comprendre et de décrire le monde. Comme langue commune, les mathématiques se sont établies. Dans l'ère numérique, les ordinateurs sont à disposition, qui nous permettent de simuler des processus à l'aide de leurs descriptions mathématiques. Prenons donc un modèle valable pour une classe de processus, mais sa résolution numérique étant beaucoup trop coûteuse pour les ordinateurs contemporains. Les étapes à suivre seraient

1. développer un nouveau modèle et des méthodes numériques adaptées pour réduire le temps de calcul,
2. vérifier la convergence des algorithmes,
3. valider le nouveau modèle en le comparant avec le modèle de référence.

Ceci est le contexte de la présente thèse.

Les roches fracturées sont omniprésentes dans les milieux géologiques, on estime par exemple que la moitié des réservoirs pétroliers sont fracturés. L'écoulement dans ces milieux est dominé par la connectivité et la conductivité du réseau de fractures en interaction avec le milieu matrice environnant. Leur modélisation numérique est donc cruciale pour une meilleure gestion des ressources du sous sol. Elle représente un défi du fait de la complexité et du caractère multiéchelle du réseau et du fait des très forts contrastes d'échelles et de propriétés pétrophysiques et hydrodynamiques entre la matrice et les fractures.

Le modèle générique pour décrire ces écoulements (appelé équi dimensionnel dans le contexte des modèles à dimensions réduites) traite les fractures comme des couches géologiques hétérogènes de la même dimension que le milieu matrice, correspondant à la géométrie réelle. En conséquence, les fractures doivent être maillées explicitement, dans la résolution numérique du modèle. La présence de très petites mailles étant incompatible avec des larges pas de temps, ce modèle n'est pas praticable à l'échelle d'un champs.

Il existe deux types de modèles pour contourner ce problème. Le premier concerne les réseaux de fractures suffisamment connectés et uniformes pour que les fractures puissent être homogénéisées et représentées par un milieu poreux 3D équivalent couplé au milieu

poreux 3D matriciel environnant. Le modèle d'écoulement couple alors les écoulements 3D de type Darcy dans chacun des milieux matrice et fracture couplés par des termes sources d'échange entre le milieu matrice et le milieu fracture (voir les travaux [9, 53, 55, 60, 70] et la Figure 1 qui illustre schématiquement cet approche).

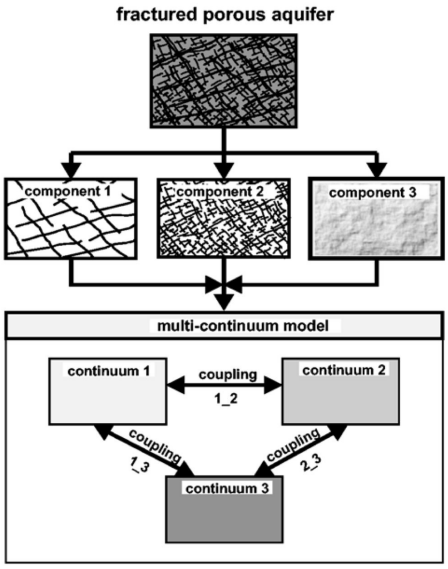

Figure 1: Illustration schématique par D. Jansen du modèle multi milieu.

Le deuxième type de modèles, dits à dimension réduite ou dimensionnels hybrides sur lequel se concentre la thèse, représente les réseaux de fractures explicitement comme des surfaces de codimension 1 immergées dans la matrice (voir Figure 2). L'écoulement couple alors un écoulement de Darcy 3D dans le milieu matriciel avec un écoulement 2D dans le réseau de fractures, le couplage étant obtenu par des conditions de transmission à l'interface matrice fracture. La représentation des fractures comme entités de codimension 1 à été introduite dans [5, 11, 45, 54, 56], afin de faciliter la génération du maillage ainsi que de réduire le nombre de degrés de liberté du modèle discrétisé. La réduction de dimension dans le réseau de fractures est obtenu à partir du modèle équi dimensionnel par intégration dans l'épaisseur de la fracture. Les conditions de transmission dépendent de la nature mathématique du modèle équi dimensionnel et d'hypothèses physiques supplémentaires. Dans le cas du modèle d'écoulement de Darcy monophasique, elles imposent typiquement soit la continuité de la pression, pour des fractures fortement conductibles [5, 15], soit des conditions de type Robin, pour tenir compte de fractures agissant comme des drains ou comme des barrières [6, 45, 56]. Ce dernier cas plus général, dit à pressions discontinues, fait l'objet de cette thèse.

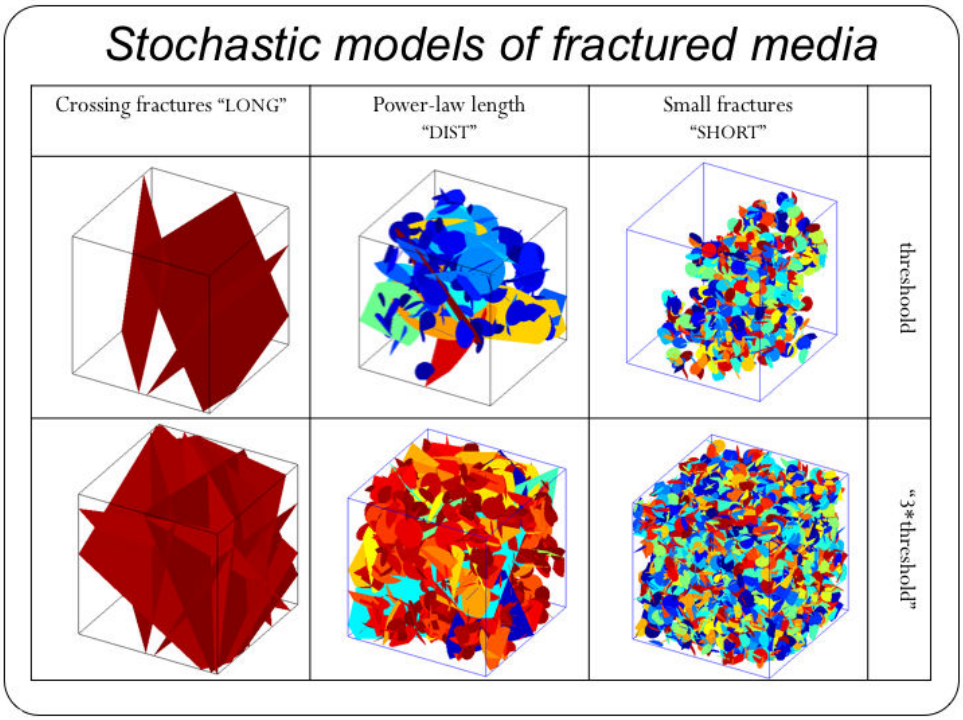

Figure 2: Représentation de milieux poreux fracturés par des réseaux de fractures discrètes avec différentes échelles de longueurs. Figure de J. R. de Dreuzy, Geosciences Rennes et équipe-projet Inria Sage.

La principale difficulté pour l'extension des modèles de Darcy dimensionnels hybrides au cas diphasique repose sur la prise en compte des sauts de saturations aux interfaces matrice fracture liés à la discontinuité des pressions capillaires entre le milieu matrice et le milieu fracture. Le point de départ naturel sera donc les travaux [14, 20, 21, 36] sur la formulation mathématique des écoulements diphasiques traitant les interfaces entre différents types de roches avec pressions capillaires discontinues. Le modèle proposé dans [40] nous servira de point de départ. Il utilise les pressions des deux phases comme variables primaires et exprime les saturations comme fonctions de la pression capillaire de façon à capter les sauts des saturations aux interfaces entre différents types de roches. Le cas de modèles dimensionnels hybrides à pressions continues est traité dans [16]. En sus des sauts de saturations aux interfaces matrice fracture, une autre subtilité est à considérer : contrairement aux modèles dimensionnels hybrides à pressions continues, le modèle dimensionnel hybride à pressions discontinues permet de reproduire des variations de saturation dans l'épaisseur de la fracture. Cette information supplémentaire doit être prise en compte dans la condition de Robin aux interfaces matrice fracture, utilisée dans ce dernier type de modèles, en introduisant un décentrage de la mobilité. On peut aussi mentionner les modèles formulés en pression globale proposés dans [2, 52] dans le cas de modèles dimensionnels hybrides à pressions discontinues. Par contre, ces modèles négli-

gent la gravité dans la direction normale dans la fracture ainsi que la modification de la condition Robin et, en conséquence, donnent une fausse approximation de l'échange de masse entre matrice et fracture.

La discrétisation des modèles de Darcy dimensionnels hybrides avec pressions continues ou discontinues aux interfaces matrice fracture a fait l'objet de nombreux travaux. Pour une présentation plus complète de méthodes existantes, on réfère à [65, 68]. Dans [6, 54], les auteurs proposent un schéma volumes finis centrés avec approximation deux points des flux (Two Point Flux Approximation ou TPFA) qui suppose une condition d'orthogonalité du maillage et l'isotropie des perméabilités. Les schémas volume finis centrés avec approximation multi points des flux (Multi Point Flux Approximation ou MPFA) ont été étendus au cas de maillages généraux et de perméabilités anisotropes dans [3, 66, 69] pour les modèles à pressions discontinues. Néanmoins ces schémas peuvent manquer de robustesse dans le cas de mailles déformées et de fortes anisotropies du fait de leur coercivité dépendante du maillage et de l'anisotropie. Ils sont aussi très coûteux dans le cas de maillages tétraédriques par comparaison à des discrétisations nodales. Plus récemment, le schéma Volumes Finis Hybrides (HFV), introduit dans [37], à été étendu dans [43] à une discrétisation de deux modèles réduits de failles avec maillage matrice et fracture non conforme. Un schéma de différences finies mimétiques (MFD) dans la matrice couplé avec un schéma TPFA dans le réseau de fractures est utilisé dans [7]. Dans [5], une méthode d'Eléments Finis Mixtes (EFM) a été introduite pour le modèle monophasiques à pression continue, présenté dans ladite référence. Dans [62], un schéma de type Control Volume Finite Element (CVFE) est proposé, dans [15] le schéma HFV et dans [15, 16], une extension des discrétisations Vertex Approximate Gradient (VAG), introduites dans [38], sont appliquées au modèle [5]. Pour les modèles monophasiques à pressions discontinues, les EFM sont introduits dans [56] et adaptés aux maillages matrice fracture non conformes dans [23]. Les méthodes mimétiques pour ce type de modèles sont présentées dans [7] et dans [43]. L'extension au cas diphasique est traitée dans [50] dans le cadre d'un schéma ImPES (Implicite en Pression et Explicite en Saturation) en utilisant une méthode d'Eléments Finis Mixtes Hybrides (EFMH) pour l'équation de pression et d'une méthode de Galerkin Discontinue pour l'équation de saturation (cet ouvrage comporte également une introduction, qui résume les approches numériques les plus courants). Ces méthodes sont adaptées aux maillages généraux et aux perméabilités anisotropes mais nécessitent un grand nombre de degrés de liberté de l'ordre du nombre de faces du maillage. Les méthodes de type CVFE, proposées dans [62], [59] dans le cas diphasique, ont l'avantage de n'utiliser que des inconnues nodales, ce qui conduit à un faible nombre de degrés de liberté dans le cas de maillages tétraédriques. Néanmoins, ces méthodes ont l'inconvénient dans le cas diphasique de mélanger les différents types de roches aux noeuds situés à l'interface entre différents types de roches. Il est alors nécessaire de raffiner fortement le maillage à l'interface matrice fracture pour éviter d'élargir artificiellement les drains que constituent les fractures.

En ce qui concerne l'analyse de convergence, le modèle dimensionnel hybride à pressions continues [5] est étudié dans [15] pour des réseaux de fractures généraux, mais l'état de l'art pour les modèles à pressions discontinues est encore resteint à des géométries simples. Rappelons que la famille de modèles introduite dans [56] et [6] dépend d'un paramètre de quadrature $\xi \in [\frac{1}{2}, 1]$ pour l'intégration numérique dans l'épaisseur de la fracture. Pour ces modèles, la convergence de discrétisations EFM est établie dans [23, 56] pour $\xi \in (\frac{1}{2}, 1]$, dans le cas d'une seule fracture séparant le domaine matriciel en deux sous-domaines. Dans [6], le cas d'une fracture non débouchante en dimension 2 est analysé pour une discrétisation TPFA et toute la gamme de paramètres $\xi \in [\frac{1}{2}, 1]$. Pour les modèles diphasiques à dimensions hybrides, la seule analyse de convergence à été faite dans [16] pour le schéma VAG du modèle à pressions continues.

Dans cette thèse, l'analyse numérique sera conduite dans le cadre abstrait de la méthode de discrétisations gradient. Rappelons que la méthode de discrétisations gradient est adéquate pour l'analyse de convergence pour les discrétisations conformes et non conformes de problèmes linéaires et non linéaires, paraboliques et elliptiques d'ordre deux. La classe de discrétisations gradient comprend entre autres les méthodes d'éléments finis conformes, d'EFM et d'EFMH, certains schémas TPFA et MPFA symétriques ainsi que les schémas VAG et les méthodes Hybrid Mimetic Mixed (HMM, qui contient les schémas HFV et MFD [30]), comme discuté dans [32]. L'avantage de la méthode de discrétisations gradient est surtout que l'analyse de convergence est faite dans un cadre abstrait, qui s'applique à toutes les discrétisations, satisfaisant un nombre condensé de conditions typiques comme la coercivité, la consistance, la conformité et la compacité, dans le contexte de cette thèse (cf. aussi [27, 28, 31, 38, 40]). On se réfère à [29] pour une présentation plus détaillée de la méthode de discrétisations gradient.

Dans le cas sans fractures, les premiers résultats de convergence par compacité vers une solution faible d'un écoulement diphasique ont été obtenus dans [58] et [42] dans le cas d'un schéma volumes finis centré avec approximation TPFA des flux sur maillages orthogonaux. Dans [42] la convergence du schéma est obtenue dans le cadre de la formulation de référence dans l'ingénierie pétrolière basée sur les deux inconnues primaires pression et saturation et sur le décentrage par phase des mobilités. Ce résultat très technique repose sur des fonctions tests non linéaires et est restreint aux schémas TPFA sur maillages orthogonaux. Dans [58] la convergence est établie toujours pour les schémas TPFA sur maillages orthogonaux dans le cas plus simple d'une formulation en pression globale introduite dans [22] (voir aussi [8]) en supposant une pression capillaire homogène. Dans le cadre de cette formulation en pression globale pour une pression capillaire homogène, l'extension à des schémas volumes finis sur maillages généraux est étudiée dans [13] dans le cas des schémas HFV, dans [18] dans le cas du schéma VAG et dans [41] dans le cadre général de la méthode de discrétisations gradient.

Dans le cadre de cette thèse, il nous faut prendre en compte deux difficultés essentielles. La première est liée à la discontinuité des pressions capillaires notamment à l'interface matrice fracture. Ce problème est traité dans [14] en utilisant un schéma TPFA sur maillages orthogonaux adapté aux discontinuités de la pression capillaire à l'aide d'inconnues d'interface. Une extension au cas de maillages polyédriques généraux est proposée dans

[40] dans le cadre général des schémas gradients en utilisant une formulation en pressions des phases. Cette formulation a l'avantage d'utiliser uniquement deux inconnues primaires par degré de liberté, à savoir les pressions des deux phases. Contrairement aux résultats obtenus dans [14] pour un schéma TPFA, la preuve de convergence nécessite une hypothèse restrictive sur le plan physique de non dégénérescence des perméabilités relatives. La deuxième difficulté marquante constitue le passage à la limite de la condition de Robin décentrée. La monotonicité de ce terme doit être exploitée afin de démontrer sa convergence.

Plan de la thèse

La thèse comporte trois chapitres. Le premier chapitre se concentre sur la définition du modèle monophasique dimensionnel hybride pour des réseaux complexes de fractures planes, sa discrétisation par les schémas VAG et HFV et sur l'analyse de la convergence des schémas dans le cadre général de la méthode de discrétisations gradient. Le performance des deux schémas est ensuite étudiée dans des cas tests numériques sur maillages cartésiens, cartésiens perturbés et tétraédriques, à l'aide de solutions sur un domaine hétérogène fracturé isotrope et anisotrope.

Le second chapitre porte sur le modèle diphasique en formulation pressions des phases adaptée aux pressions capillaires discontinues et permettant de capter les sauts de saturations aux interfaces entre différents types de roches, notamment à l'interface matrice fracture. En outre, grâce à la discontinuité des pressions entre interface et intérieur de la fracture, ce modèle permet de reconstituer des gradients capillaires ainsi que des effets de ségrégation dans la direction normale à la fracture. Le schéma VAG est étendu à ce modèle dans le cadre d'une formulation fully implicite, en vue des aspects d'anisotropie et d'hétérogénéité et de l'applicabilité aux maillages généraux. Deux versions de modèles discrets sont développées, la première étant conforme au modèle continu et la seconde une «interpolation» entre les conditions aux interfaces matrice fracture des modèles à pressions continues et discontinues. Des cas tests sont présentés en diphasique et pour le problème de transport, afin de comparer les différents modèles dimensionnels hybrides à pressions continues et discontinues à l'aide du modèle de référence, qui représente les fractures dans les mêmes dimensions que la matrice.

Dans le chapitre trois, on propose un modèle diphasique, qui tient compte d'une couche endommagée à l'interface matrice fracture, qui a son propre type de roche. L'analyse numérique est conduite dans le cadre de la méthode de discrétisations gradient. Ainsi, des techniques de compacité sont employées pour établir des résultats de convergence pour une large classe de schémas numériques, entre autre les schémas VAG et HFV. L'existence de la solution du modèle diphasique est obtenue à travers l'analyse de convergence. Une série d'expériences numériques conclut le chapitre avec une étude de l'influence de la zone endommagée sur la solution numérique.

Chapitre 1: modèles monophasiques

Ce chapitre présente le modèle d'écoulement monophasique dit dimensionnel hybride couplant l'écoulement dans la matrice et celui dans le réseau de fractures représentées comme des surfaces de codimension 1. On considère le cas où la pression peut être discontinue aux interfaces matrice fracture, ce qui permet de traiter les fractures jouant soit le rôle d'une barrière, soit celle d'un drain, comme décrit dans [45], [56] et [6]. Dans ce chapitre, on étend la famille de modèles [6, 56] au cas de réseaux complexes de fractures planes comportant des intersections, des fractures débouchantes et des fractures non débouchantes. Rappelons que cette famille de modèles dépend d'un paramètre de quadrature $\xi \in [\frac{1}{2}, 1]$ pour l'intégration approximée dans l'épaisseur de la fracture.

Le principal but de ce chapitre est d'étudier la discrétisation de tels modèles et de présenter la première preuve de convergence pour un réseau général de fractures dans un domaine 3D matriciel environnant comportant des fractures entièrement, partiellement et non débouchantes ainsi que des intersections de fractures. Chaque fracture est supposée plane dans l'analyse, qui couvrira la plage de paramètres $\xi \in (\frac{1}{2}, 1]$. La valeur $\xi = \frac{1}{2}$ est exclue afin de permettre une formulation variationnelle primale du problème. Cet objectif sera atteint par la méthode de discrétisations gradient [31, 38] étendue au cas de modèles dimensionnels hybrides.

Le second objectif de ce chapitre est de développer les schémas VAG et HFV, définis dans [38] et [37], pour la famille de modèles d'écoulements Darcy à dimensions hybrides, et de démontrer que ces schémas satisfont les conditions posées par la méthode de discrétisations gradient, concrètement, la coercivité, la consistance et la conformité à la limite. La preuve de ces propriétés est basée sur un résultat clé prouvé dans l'appendice de ce chapitre, qui établit la densité de sous-espaces lisses des espaces fonctionnels de pression ainsi que de flux. Le maillage est supposé polyédrique avec des faces pouvant être non planes pour le schéma VAG et plane pour HVF. Il est supposé que le maillage est conforme au réseau de fractures, dans le sens que le réseau est constitué d'une collection de faces du maillage. Deux versions de VAG sont considérées. La première version correspond aux éléments finis sur un sous-maillage tétraédrique et la deuxième à un schéma volumes finis avec lumping pour les termes sources et les flux matrice fracture. Il est à noter que le schéma HFV [37] a été généralisé dans [30] à la famille de schémas HMM contenant les schémas MFD [19].

Le troisième objectif est de comparer les discrétisations VAG et HFV numériquement en ce qui concerne l'erreur et le temps de calcul sur des maillages cartésiens, cartésiens perturbés et tétraédriques. Dans ce but, une famille de solutions analytiques est proposée dans le cas d'un domaine matriciel divisé en sous-domaines par quatre fractures s'intersectant. Les solutions dépendent de l'hétérogénéité et de l'anisotropie des domaines matrice et fracture. Le schéma HFV utilise des inconnues aux mailles, faces et arêtes fractures, alors que VAG utilise des inconnues aux mailles, nœuds et faces fractures. Evoquons que les schémas MPFA utilisent des inconnues aux mailles, faces fractures et arêtes aux intersections des fractures (cf. [3, 66, 69]). Exceptés les maillages tétraédriques et parallélépipédiques, les schémas MPFA sont non symétriques et leur coercivité est conditionnée

par le maillage et l'anisotropie des champs de perméabilités. Le schéma VAG a l'avantage, comparé aux schémas HFV ou MPFA, de mener à une discrétisation plus creuse sur les maillages tétraédriques et triangulaires prismatiques, comme ici, le nombre de nœuds est beaucoup moins élevé que le nombre de faces ou mailles. Un autre avantage de VAG est de permettre des faces non planes.

Dans la section 1.2, nous introduisons la géométrie des domaines matrice et fracture et nous présentons le modèle en formulations forte et faible. La section 1.3 est consacrée à la présentation de la méthode de discrétisations gradient ainsi qu'à la dérivation de l'estimation d'erreur. Dans la section 1.4, nous présentons les discrétisations VAG et HFV et nous montrons qu'elles appartiennent à la classe des discrétisations gradient, pour lesquelles l'estimation d'erreur est établie. Dans 1.5, les schémas VAG et HFV sont comparés numériquement. L'appendice contient deux sections. Dans la section 1.A, la densité des sous-espaces lisses dans l'espace de pression et dans l'espace des flux est établie, ce qui est nécessaire pour la preuve de l'estimation d'erreur des schémas gradients. En vue de l'application aux écoulements diphasiques, nous présentons dans la section 1.B une formulation volumes finis unifiée pour les deux schémas VAG et HFV.

Chapitre 2: modèles diphasiques

Le premier objectif de ce chapitre est de développer des modèles dimensionnels hybrides pour les écoulements de Darcy diphasiques, en prenant en compte des sauts de pressions aux interfaces matrice fracture ainsi que des réseaux de fractures complexes. Le second objectif est de valider les modèles à dimensions hybrides en les comparant numériquement au modèle non réduit de référence.

Un modèle dimensionnel hybride diphasique à pressions discontinues en formulation pression globale a été présenté dans [2, 52]. Dans les modèles présentés dans ce chapitre, les pressions de phases sont les inconnues primaires, ce qui permet de traiter plus efficacement des pressions capillaires discontinues aux interfaces entre des différents types de roches. Cette formulation s'appuie sur l'inverse des extensions graphes monotones des pressions capillaires et peut facilement être adaptée aux graphes généraux de pressions capillaires, notamment au cas sans capillarité dans la fracture, en utilisant une formulation avec changement de variable comme décrit dans [17]. En outre, les conditions de transmission aux interfaces matrice fracture du modèle présenté ici diffèrent de ceux du modèle [2, 52], dans le sens où elles sont calculées par décentrage avec soit la mobilité matricielle, soit celle de la fracture, et où elles prennent en compte la gravité dans la direction normale dans la fracture. Le décentrage est prépondérant pour le transport d'un fluide de la matrice vers la fracture et la gravité ne peut pas être négligée pour des écoulements à gravité dominante, indépendamment de l'épaisseur de la fracture. Le modèle dimensionnel hybride à pressions discontinues, présenté dans la section 2.2.1, repose sur la continuité des flux de Darcy aux interfaces matrice fracture. Au niveau discret, nous proposons une modification de ce modèle dans la section 2.3.3, qui linéarise les conditions de transmission aux interfaces matrice fracture tout en y captant les sauts des pressions.

Les modèles hybrides à pressions continues et discontinues sont comparés dans une série de cas tests. Le modèle à pressions continues est discrétisé avec le schéma VAG, comme décrit dans [16]. Pour la discrétisation des modèles à pressions discontinues, nous adaptons le schéma VAG décrit dans chapitre 1 au diphasique, qui utilise des dégrés de liberté supplémentaires aux interfaces matrice fracture, afin de capturer les sauts des pressions. On choisit un schéma centré aux nœuds, car il mène à moins de degrés de liberté, comparé aux schémas centrés aux mailles, sur des maillages symplectiques, qui à leur tour sont adaptés quand on traite des géométries complexes. La version non conforme de VAG permet de respecter les sauts de saturations (causés par la capillarité) aux interfaces des types de roches, comportant les interfaces matrice fracture. Un autre avantage de cette méthode est illustré dans la section des cas tests de ce chapitre : les inconnues discrètes supplémentaires aux interfaces matrice fracture sont nécessaires pour reproduire les effets gravitaires ou capillaires dans la direction normale dans l'épaisseur de la fracture, qui sont mal modélisés par des approches qui éliminent ces inconnues au niveau linéaire, comme c'est le cas des approches centrés classiques (cf. par exemple [54]).

Le plan de ce chapitre est le suivant. Les modèles à dimensions hybrides sont présentés dans la section 2.2. La section 1.4.1 présente les discrétisations VAG et les formulations volumes finis pour les différents modèles. Dans la section 2.4, le modèle non réduit et les modèles dimensionnels hybrides sont comparés sur le problème de transport à l'aide de solutions analytiques. L'effet d'un terme de diffusion normale dans la fracture est également étudié pour le modèle non réduit. Dans la section 2.5, les différents modèles dimensionnels hybrides sont comparés au modèle non réduit sur un problème diphasique avec différentes configurations de perméabilités et pressions capillaires dans les milieux matrice et fractures.

Chapitre 3: analyse diphasique

Dans ce chapitre, on propose un modèle dimensionnel hybride à pressions discontinues pour écoulements de Darcy diphasiques, qui comprend une couche de roche endommagée aux interfaces matrice fracture. Cette couche de roche endommagée a ses propres courbes de mobilités et de pression capillaire. Elle est essentielle à l'analyse numérique ainsi qu'à la convergence des itérations non linéaires de l'algorithme de Newton dans la résolution implicite du problème discret. Le principal propos de ce chapitre est d'étendre la méthode de discrétisations gradient à ce modèle et d'obtenir des résultats de convergence pour cette classe générale de discrétisations. On prouve la convergence de solutions schémas gradients vers une solution faible du modèle, ce qui entraîne l'existence d'une solution au problème diphasique. L'analyse numérique s'appuie partiellement sur le travail fait dans [40], qui s'applique aux discrétisations gradient d'écoulements Darcy diphasiques dans un domaine sans fractures. La difficulté majeure qu'on affronte ici, comparée aux analyses dans [40] et dans [16] pour les milieux fracturés, vient des conditions de transmission aux interfaces matrice fracture, qui implique un décentrage entre les pressions dans la fracture et les traces de pressions dans la matrice pour chaque phase. Comme dans [40] et [16],

l'analyse de convergence suppose la non dégénérescence des mobilités.

Ce chapitre est structuré comme suit. Dans la section 3.2, le modèle est présenté ainsi que les hypothèses sur les données. La méthode de discrétisations gradient est développée dans la section 3.3, ce qui inclut la définition abstraite des opérateurs de reconstruction, la formulation discrète variationnelle du problème et l'énoncé des propriétés essentielles des discrétisations gradient pour des problèmes paraboliques : la coercivité, la consistance, la conformité à la limite et la compacité. La section 3.4 présente la preuve du résultat principal de ce chapitre, la convergence de la solution discrète d'un schéma gradient vers une solution faible du modèle. Cette convergence est établie avec des arguments de compacité et demande des résultats de compacité préliminaires sur les solutions approximées, plus concrètement la convergence moyennée en espace et en temps et la convergence uniforme en temps et faible en espace. Complémentairement, dans [34], la convergence uniforme en temps et forte en espace à été démontré. L'astuce de Minty est invoquée pour identifier la limite des termes non linéaires de la condition de Robin décentrée aux interfaces matrice fracture. Dans la section 3.5, on étudie par un exemple numérique l'influence de la couche endommagée aux interfaces sur la solution du modèle. La discrétisation utilisée dans ce cas test est la discrétisation VAG, pour laquelle on peut montrer qu'elle satisfait les propriétés des discrétisations gradient.

Chapter 1

One phase Darcy flow

1.1 Introduction

This chapter deals with the discretization of Darcy flows in fractured porous media for which the fractures are modelled as interfaces of codimension one. In this framework, the $d-1$ dimensional flow in the fractures is coupled with the d dimensional flow in the matrix leading to the so called, hybrid dimensional Darcy flow model. We consider the case for which the pressure can be discontinuous at the matrix fracture interfaces in order to account for fractures acting either as drains or as barriers as described in [45], [56] and [6]. In this chapter, we will study the family of models described in [56] and [6].

It is also assumed in the following that the pressure is continuous at the fracture intersections. This corresponds to a ratio between the permeability at the fracture intersection and the width of the fracture assumed to be large compared with the ratio between the tangential permeability of each fracture and its length. We refer to [46] for a more general reduced model taking into account discontinuous pressures at fracture intersections in dimension $d = 2$.

The discretization of such hybrid dimensional Darcy flow models has been the object of several works. In [45], [54], [6] a cell-centered Finite Volume scheme using a Two Point Flux Approximation (TPFA) is proposed assuming the orthogonality of the mesh and isotropic permeability fields. Cell-centered Finite Volume schemes using MultiPoint Flux Approximations (MPFA) have been studied in [69], [66], and [3]. In [56], a Mixed Finite Element (MFE) method is proposed and a MFE discretization adapted to non-matching fracture and matrix meshes is studied in [23]. More recently the Hybrid Finite Volume (HFV) scheme, introduced in [37], has been extended in [43] for the non matching discretization of two reduced fault models. Also a Mimetic Finite Difference (MFD) scheme is used in [7] in the matrix domain coupled with a TPFA scheme in the fracture network. Discretizations of the related reduced model [5] assuming a continuous pressure at the matrix fracture interfaces have been proposed in [5] using a MFE method, in [62] using a Control Volume Finite Element method (CVFE), in [15] using the HFV scheme, and in [15, 16] using an extension of the Vertex Approximate Gradient (VAG) scheme

introduced in [38].

In terms of convergence analysis, the model assuming continuous pressure at the matrix fracture interfaces [5] is studied in [15] for a general fracture network but the current state of the art for the discontinuous pressure models is still limited to rather simple geometries. Let us recall that the family of models introduced in [56] and [6] depends on a quadrature parameter denoted by $\xi \in [\frac{1}{2}, 1]$ for the approximate integration in the width of the fractures.

For such models, convergence of MFE discretizations in [56] and non matching MFE discretizations in [23] for the range $\xi \in (\frac{1}{2}, 1]$ has been established in the case of a single fracture separating the matrix domain into two subdomains. In [6], the case of one fully immersed fracture in dimension $d = 2$ using a TPFA discretization is analysed for the full range of parameters $\xi \in [\frac{1}{2}, 1]$.

The main goal of this chapter is to study the discretization of such models and provide the first proof of convergence for a general fracture network in a 3D surrounding matrix domain including fully, partially and non immersed fractures as well as fracture intersections. Each individual fracture will be assumed to be planar and our analysis will cover the range of parameters $\xi \in (\frac{1}{2}, 1]$. The value $\xi = \frac{1}{2}$ is excluded in order to allow for a primal variational formulation. This objective will be achieved by extension to the hybrid dimensional Darcy flow model of the gradient scheme framework introduced in [38], [31]. The gradient scheme framework allows to analyze the convergence of both conforming and non conforming discretizations for linear and nonlinear second order diffusion and parabolic problems. As shown in [31], it accounts for various schemes such as Finite Element methods, Mixed and Mixed Hybrid Finite Element methods, some Finite Volume schemes like symmetric MPFA, the VAG schemes [38], and the HFV schemes [37]. The main advantage of this framework is to provide the convergence proof for all schemes satisfying some abstract conditions, namely coercivity, consistency and limit conformity, at the price of a single convergence analysis for a given model. Let us also refer to [12] for an alternative general framework based on the concept of compatible discrete operator for the discretization of diffusion problems on polyhedral meshes.

The second objective of this chapter is to prove the coercivity, consistency and limit conformity properties for two examples of gradient discretizations, namely the extension of the VAG and HFV schemes defined in [38] and [37] to the family of hybrid dimensional Darcy flow models. The proof of these properties is as usual based on a key result proved in the appendix and stating the density of smooth functions subspaces in both the variational space and in the flux space of the model. The mesh is assumed to be polyhedral with possibly non planar faces for the VAG scheme and planar faces for the HFV scheme. It is assumed that the fracture network is conforming to the mesh in the sense that it is defined as a collection of faces of the mesh. Two versions of the VAG scheme will be studied, the first corresponding to the conforming $\mathbb{P}_1$ finite element on a tetrahedral submesh, and the second to a finite volume scheme using lumping for the source terms as well as for the matrix fracture fluxes. Note that the HFV scheme of [37] has been generalized in [30] as the family of Hybrid Mimetic Mixed methods which which encompasses the family of MFD schemes [19]. In this article, we will focus without restriction on the particular case

presented in [37] for the sake of simplicity.

Our third objective is to compare numerically the VAG and HFV discretizations in terms of accuracy and CPU time on Cartesian, hexahedral and tetrahedral families of meshes. For that, an original family of analytical solutions is built in the case of four intersecting fractures, which takes into account heterogeneity and anisotropy of the medium. The HFV scheme uses cell, face and fracture edge unknowns, while the VAG scheme uses cell, node, and fracture face unknowns. In both cases, the cell unknowns can be eliminated without any fill-in before solving the linear system. As a remainder, MPFA schemes use cell and fracture face unknowns as well as edge unknowns at fracture intersections (see [69], [66], and [3]). Also, except on tetrahedral and parallepipedic meshes, MPFA schemes are non symmetric and their coercivity is conditioned to the mesh and to the anisotropy of the permeability fields. The VAG scheme has the advantage, compared with the HFV or MPFA schemes, to lead to a much sparser discretization on tetrahedral or triangular prismatic meshes, since the number of nodes is much smaller than the number of faces or cells for such meshes. Another advantage of the VAG scheme compared with the HFV scheme is to allow for non planar faces.

In section 1.2 we introduce the geometry of the matrix and fracture domains and present the strong and weak formulations of the model. Section 1.3 is devoted to the introduction of the of gradient discretization framework and the derivation of the error estimate. In section 1.4 we introduce and investigate the families of VAG and HFV discretizations. In section 1.5, the VAG and HFV schemes are compared in terms of accuracy and CPU efficiency for Cartesian, hexahedral and tetrahedral meshes on heterogeneous isotropic and anisotropic media using a family of analytical solutions with 4 intersecting fractures. Accounting for applications to multi-phase flow, we present in the appendix a Finite Volume formulation involving conservative fluxes, which applies for both schemes.

1.2 Hybrid dimensional Darcy Flow Model in Fractured Porous Media

1.2.1 Discrete fracture network

Let Ω denote a bounded domain of $\mathbb{R}^d$ ($d = 2, 3$), polyhedral for $d = 3$ and polygonal for $d = 2$. To fix ideas the dimension will be fixed to $d = 3$ when it needs to be specified, for instance in the naming of the geometrical objects or for the space discretisation in the next section. The adaptations to the case $d = 2$ are straightforward.

Let $\overline{\Gamma} = \bigcup_{i\in I} \overline{\Gamma}_i$ and its interior $\Gamma = \overline{\Gamma} \setminus \partial\overline{\Gamma}$ denote the network of fractures $\Gamma_i \subset \Omega$, $i \in I$. Each Γ_i is a planar polygonal simply connected open domain included in a plane $\mathcal{P}_i$ of $\mathbb{R}^d$. It is assumed that the angles of Γ_i are strictly smaller than 2π, and that $\Gamma_i \cap \overline{\Gamma}_j = \emptyset$ for all $i \neq j$. For all $i \in I$, let us set $\Sigma_i = \partial\Gamma_i$, with $\mathbf{n}_{\Sigma_i}$ as unit vector in $\mathcal{P}_i$, normal to Σ_i and outward to Γ_i. Further $\Sigma_{i,j} = \Sigma_i \cap \Sigma_j$ for $i \neq j$, $\Sigma_{i,0} = \Sigma_i \cap \partial\Omega$, $\Sigma_{i,N} = \Sigma_i \setminus (\bigcup_{j\in I\setminus\{i\}} \Sigma_{i,j} \cup \Sigma_{i,0})$, $\Sigma = \bigcup_{(i,j)\in I\times I, i\neq j}(\Sigma_{i,j} \setminus \Sigma_{i,0})$ and $\Sigma_0 = \bigcup_{i\in I} \Sigma_{i,0}$.

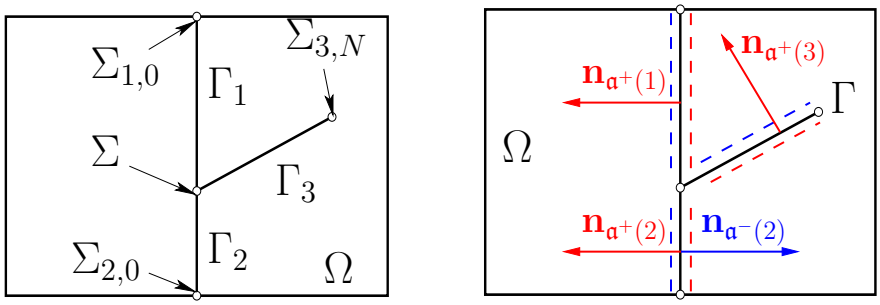

Figure 1.1: Example of a 2D domain Ω and 3 intersecting fractures $\Gamma_i, i = 1, 2, 3$. We define the fracture plane orientations by $\mathfrak{a}^{\pm}(i) \in \chi$ for Γ_i, $i \in I$.

We define the two unit normal vectors $\mathbf{n}_{\mathfrak{a}^{\pm}(i)}$ at each planar fracture Γ_i, such that $\mathbf{n}_{\mathfrak{a}^+(i)} + \mathbf{n}_{\mathfrak{a}^-(i)} = 0$ (cf. figure 1.1). We define the set of indices $\chi = \{\mathfrak{a}^+(i), \mathfrak{a}^-(i) \mid i \in I\}$, such that $\#\chi = 2\#I$. For ease of notation, we use the convention $\Gamma_{\mathfrak{a}^+(i)} = \Gamma_{\mathfrak{a}^-(i)} = \Gamma_i$.

1.2.2 Function spaces

We will denote by $\mathrm{d}\tau(\mathbf{x})$ the $d-1$ dimensional Lebesgue measure on Γ. On the fracture network Γ, we define the function space $L^2(\Gamma) = \{v = (v_i)_{i\in I}, v_i \in L^2(\Gamma_i), i \in I\}$, endowed with the norm $\|v\|_{L^2(\Gamma)} = (\sum_{i\in I} \|v_i\|^2_{L^2(\Gamma_i)})^{\frac{1}{2}}$ and its subspace $H^1(\Gamma)$ consisting of functions $v = (v_i)_{i\in I}$ such that $v_i \in H^1(\Gamma_i)$, $i \in I$ with continuous traces at the fracture intersections $\Sigma_{i,j}$, $j \in I\backslash\{i\}$. The space $H^1(\Gamma)$ is endowed with the norm $\|v\|_{H^1(\Gamma)} = (\sum_{i\in I} \|v_i\|^2_{H^1(\Gamma_i)})^{\frac{1}{2}}$. We also define it's subspace with vanishing traces on Σ_0, which we denote by $H^1_{\Sigma_0}(\Gamma)$.

On $\Omega\backslash\overline{\Gamma}$, the gradient operator from $H^1(\Omega\backslash\overline{\Gamma})$ to $L^2(\Omega)^d$ is denoted by ∇. On the fracture network Γ, the tangential gradient, acting from $H^1(\Gamma)$ to $L^2(\Gamma)^{d-1}$, is denoted by ∇_τ, and such that

$$\nabla_\tau v = (\nabla_{\tau_i} v_i)_{i\in I},$$

where, for each $i \in I$, the tangential gradient ∇_{τ_i} is defined from $H^1(\Gamma_i)$ to $L^2(\Gamma_i)^{d-1}$ by fixing a reference Cartesian coordinate system of the plane $\mathcal{P}_i$ containing Γ_i. We also denote by div_{τ_i} the divergence operator from $H_{\mathrm{div}}(\Gamma_i)$ to $L^2(\Gamma_i)$.

Then, for $\mathfrak{a} = \mathfrak{a}^{\pm}(i) \in \chi$, we can define the trace operator on $\Gamma_{\mathfrak{a}}$:

$$\gamma_{\mathfrak{a}} : H^1(\Omega \setminus \overline{\Gamma}) \to L^2(\Gamma_{\mathfrak{a}}),$$

and the normal trace operator on $\Gamma_{\mathfrak{a}}$ outward to the side $\mathfrak{a}$:

$$\gamma_{\mathbf{n}_{\mathfrak{a}}} : H_{\mathrm{div}}(\Omega \setminus \overline{\Gamma}) \to \mathcal{D}'(\Gamma_{\mathfrak{a}}),$$

that satisfy $\gamma_{\mathfrak{a}}(h) = \gamma_{\mathfrak{a}}(h\restriction_{\omega_{\mathfrak{a}}})$ and $\gamma_{\mathbf{n}_{\mathfrak{a}}}(\mathbf{p}) = \gamma_{\mathbf{n}_{\mathfrak{a}}}(\mathbf{p}\restriction_{\omega_{\mathfrak{a}}})$, where $\omega_{\mathfrak{a}} = \{\mathbf{x} \in \Omega \mid (\mathbf{x} - \mathbf{y}) \cdot \mathbf{n}_{\mathfrak{a}} < 0,\ \forall \mathbf{y} \in \Gamma_i\}$. Subsequently, the (one sided) jump operator on $\Gamma_{\mathfrak{a}}$,

$$[\![\cdot]\!]_{\mathfrak{a}} : H^1(\Omega \setminus \overline{\Gamma}) \times H^1(\Gamma) \to L^2(\Gamma_{\mathfrak{a}})$$

is defined by $[\![(h_m, h_f)]\!]_{\mathfrak{a}} = \gamma_{\mathfrak{a}} h_m - h_f$.

We now define the hybrid dimensional function spaces that will be used as variational spaces for the Darcy flow model in the next subsection, namely

$$V = H^1(\Omega \setminus \overline{\Gamma}) \times H^1(\Gamma)$$

and its subspace

$$V^0 = H^1_{\partial\Omega}(\Omega \setminus \overline{\Gamma}) \times H^1_{\Sigma_0}(\Gamma),$$

where (with $\gamma_{\partial\Omega} \colon H^1(\Omega\setminus\overline{\Gamma}) \to L^2(\partial\Omega)$ denoting the trace operator on $\partial\Omega$)

$$H^1_{\partial\Omega}(\Omega \setminus \overline{\Gamma}) = \{v \in H^1(\Omega\setminus\overline{\Gamma}) \mid \gamma_{\partial\Omega} v = 0 \text{ on } \partial\Omega\},$$

as well as

$$W = W_m \times W_f,$$

where

$$\begin{aligned} W_m &= \left\{\mathbf{q}_m \in H_{\mathrm{div}}(\Omega \setminus \overline{\Gamma}) \mid \gamma_{\mathbf{n}_{\mathfrak{a}}} \mathbf{q}_m \in L^2(\Gamma_{\mathfrak{a}}) \text{ for all } \mathfrak{a} \in \chi\right\} \text{ and} \\ W_f &= \{\mathbf{q}_f = (\mathbf{q}_{f,i})_{i\in I} \mid \mathbf{q}_{f,i} \in H_{\mathrm{div}}(\Gamma_i) \text{ for all } i \in I \\ &\quad \text{and } \sum_{i\in I} \int_{\Gamma_i} \Big(\nabla_\tau v \cdot \mathbf{q}_{f,i} + v \cdot \mathrm{div}_{\tau_i} \mathbf{q}_{f,i}\Big) \mathrm{d}\tau(\mathbf{x}) = 0 \text{ for all } v \in H^1_{\Sigma_0}(\Gamma)\}. \end{aligned}$$

On V, we define the positive semidefinite, symmetric bilinear form

$$((u_m, u_f), (v_m, v_f))_V = \int_\Omega \nabla u_m \cdot \nabla v_m \mathrm{d}\mathbf{x} + \int_\Gamma \nabla_\tau u_f \cdot \nabla_\tau v_f \mathrm{d}\tau(\mathbf{x}) + \sum_{\mathfrak{a}\in\chi} \int_{\Gamma_{\mathfrak{a}}} [\![u]\!]_{\mathfrak{a}} [\![v]\!]_{\mathfrak{a}} \mathrm{d}\tau(\mathbf{x}),$$

for $u = (u_m, u_f), v = (v_m, v_f) \in V$. Note that $(\cdot,\cdot)_V$ is a scalar product on V^0 with induced norm denoted by $\|\cdot\|_{V^0}$ in the following. We define for all $(\mathbf{p}_m, \mathbf{p}_f), (\mathbf{q}_m, \mathbf{q}_f) \in W$ the scalar product

$$\begin{aligned} ((\mathbf{p}_m, \mathbf{p}_f), (\mathbf{q}_m, \mathbf{q}_f))_W = &\int_\Omega \mathbf{p}_m \mathbf{q}_m \mathrm{d}\mathbf{x} + \int_\Omega \mathrm{div}\mathbf{p}_m \cdot \mathrm{div}\mathbf{q}_m \mathrm{d}\mathbf{x} \\ &+ \int_\Gamma \mathbf{p}_f \mathbf{q}_f \mathrm{d}\tau(\mathbf{x}) + \int_\Gamma \mathrm{div}_\tau \mathbf{p}_f \cdot \mathrm{div}_\tau \mathbf{q}_f \mathrm{d}\tau(\mathbf{x}) \\ &+ \sum_{\mathfrak{a}\in\chi} \int_{\Gamma_{\mathfrak{a}}} (\gamma_{\mathbf{n}_{\mathfrak{a}}} \mathbf{p}_m \cdot \gamma_{\mathbf{n}_{\mathfrak{a}}} \mathbf{q}_m) d\tau(\mathbf{x}), \end{aligned}$$

which induces the norm $\|(\mathbf{q}_m, \mathbf{q}_f)\|_W$, and where we have used the notation $\mathrm{div}_\tau \mathbf{p}_f = \mathrm{div}_{\tau_i} \mathbf{p}_{f,i}$ on Γ_i for all $i \in I$ and $\mathbf{p}_f = (\mathbf{p}_{f,i})_{i\in I} \in W_f$.

Using similar arguments as in the proof of [61], example II.3.4, one can prove the following Poincaré type inequality.

Proposition 1.2.1 *The norm $\|\cdot\|_{V^0}$ satisfies the following inequality*

$$\|v_m\|_{H^1(\Omega\setminus\overline{\Gamma})} + \|v_f\|_{H^1(\Gamma)} \leq \mathcal{C}_P \|(v_m, v_f)\|_{V^0},$$

for all $(v_m, v_f) \in V^0$.

Proof We apply the ideas of the proof of [61], example II.3.4 and assume that the statement of the proposition is not true. Then we can define a sequence $(v_l)_{l\in\mathbb{N}}$ in V^0, such that

$$\|v_l\|_{H^1} = 1 \qquad \text{and} \qquad \|v_l\|_{V^0} < \frac{1}{l}, \tag{1.1}$$

where, for this proof, $\|\cdot\|_{H^1} = \|\cdot\|_{H^1(\Omega\setminus\overline{\Gamma})} + \|\cdot\|_{H^1(\Gamma)}$. The imbedding

$$(V^0, \|\cdot\|_{H^1}) \hookrightarrow \Big(L^2(\Omega)\times L^2(\Gamma), \|\cdot\|_{L^2(\Omega)} + \|\cdot\|_{L^2(\Gamma)}\Big)$$

is compact, provided that $\Omega\setminus\overline{\Gamma}$ has the cone property (see [1], theorem 6.2). Thus, there is a subsequence $(v_\mu)_\mu$ of $(v_l)_{l\in\mathbb{N}}$ and $v \in L^2(\Omega)\times L^2(\Gamma)$, such that

$$v_\mu \longrightarrow v \qquad \text{in } L^2(\Omega)\times L^2(\Gamma).$$

On the other hand it follows from (1.1) that

$$\begin{aligned} \nabla v_{m_\mu} &\longrightarrow 0 \qquad \text{in } L^2(\Omega) \\ \nabla_\tau v_{f_\mu} &\longrightarrow 0 \qquad \text{in } L^2(\Gamma). \end{aligned}$$

Since $(V^0, \|\cdot\|_{H^1})$ is complete, we have

$$v_\mu \longrightarrow v \qquad \text{in } V^0,$$

with

$$\|v\|_{V^0} = \lim_{\mu\to\infty} \|v_\mu\|_{V^0} = 0.$$

Since $\|\cdot\|_{V^0}$ is a norm on V^0, we have $v = 0 \in V^0$, but $\|v\| = 1$, which is a contradiction. □

The convergence analysis presented in section 1.4 requires some results on the density of smooth subspaces of V and W, which we state below.

Definition 1.2.1 *1. C^∞_Ω is defined as the subspace of functions in $C^\infty_b(\Omega\setminus\overline{\Gamma})$ vanishing on a neighbourhood of the boundary $\partial\Omega$, where $C^\infty_b(\Omega\setminus\overline{\Gamma}) \subset C^\infty(\Omega\setminus\overline{\Gamma})$ is the set of functions φ, such that for all $\mathbf{x}\in\Omega$ there exists $r > 0$, such that for all connected components ω of $\{\mathbf{x}+\mathbf{y}\in\mathbb{R}^d \mid |\mathbf{y}| < r\} \cap (\Omega\setminus\overline{\Gamma})$ one has $\varphi \in C^\infty(\overline{\omega})$.*

2. $C^\infty_\Gamma = \gamma_\Gamma(C^\infty_0(\Omega))$ is defined as the image of $C^\infty_0(\Omega)$ of the trace operator $\gamma_\Gamma\colon H^1_0(\Omega) \to L^2(\Gamma)$.

3. $\mathbf{C}_\Omega^\infty = C_b^\infty(\Omega \setminus \overline{\Gamma})^d$.

4. $\mathbf{C}_\Gamma^\infty = \{\mathbf{q}_f = (\mathbf{q}_{f,i})_{i\in I} \mid \mathbf{q}_{f,i} \in C^\infty(\overline{\Gamma}_i)^{d-1},\ \sum_{i\in I} \mathbf{q}_{f,i}\cdot\mathbf{n}_{\Sigma_i} = 0 \text{ on } \Sigma,\ \mathbf{q}_{f,i}\cdot\mathbf{n}_{\Sigma_i} = 0 \text{ on } \Sigma_{i,N},\ i \in I\}$.

The proofs of the two following propositions can be found in the appendix.

Proposition 1.2.2 *$C_\Omega^\infty \times C_\Gamma^\infty$ is dense in V^0.*

Proposition 1.2.3 *$\mathbf{C}_\Omega^\infty \times \mathbf{C}_\Gamma^\infty$ is dense in W.*

1.2.3 Hybrid dimensional Darcy flow model

This section is devoted to the presentation of the hybrid dimensional model. We will give a short review of the derivation and refer to [45], [56] for more details.

As a starting point, the so called equi dimensional model consists of the mass conservation equation and Darcy's law on Ω containing a spacially extended fracture network $\Omega_f \subset \Omega$ (a neighbourhood of Γ of width d_f, cf. figure 1.2).

$$\operatorname{div}(\overline{\mathbf{q}}) = \overline{h} \tag{1.2a}$$

$$\overline{\mathbf{q}} = -\Lambda\nabla\overline{u}, \tag{1.2b}$$

with Darcy velocity $\overline{\mathbf{q}} \in H_{\mathrm{div}}(\Omega)$, pressure $\overline{u} \in H^1(\Omega)$, production $\overline{h} \in L^2(\Omega)$ and permeability $\Lambda \in L^\infty(\Omega)$.

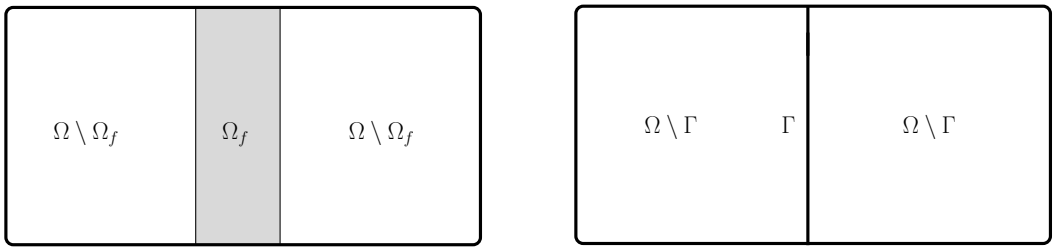

Figure 1.2: Geometries of the equi-dimensional model (left) and the hybrid-dimensional model (right) in the case of a single fracture dividing the matrix domain.

From this, the hybrid dimensional model is derived by integration of the equations on Ω_f over the fracture width. We place us in the case of a single fracture having the representation $\Omega_f = \{\mathbf{x} \in \Omega \mid \mathbf{x} = \mathbf{y} + r\mathbf{n}(\mathbf{y}), \mathbf{y} \in \Gamma, r \in (-\frac{d_f(\mathbf{y})}{2}, \frac{d_f(\mathbf{y})}{2})\}$, where $\mathbf{n}$ is a unit normal vector and d_f is the fracture width. We assume that inside the fractures, the normal direction is a permeability principal direction, such that the permeability tensor decomposes into a tangential part and a normal part as

$$\Lambda = \Lambda_f + \lambda_{f,n}\ \mathbf{n}\otimes\mathbf{n}, \tag{1.3}$$

with $\Lambda_f \mathbf{n} = 0$. Writing

$$\overline{\mathbf{q}} = \sum_{i=1}^{d-1} (\overline{\mathbf{q}} \cdot \boldsymbol{\tau}_i)\boldsymbol{\tau}_i + (\mathbf{q} \cdot \mathbf{n})\mathbf{n},$$

the equi dimensional Darcy equation (1.2b) splits into a tangential and a normal part,

$$\sum_{j=1}^{d-1} (\overline{\mathbf{q}} \cdot \boldsymbol{\tau}_j)\boldsymbol{\tau}_j = -\Lambda_f \nabla_\tau \overline{u} \tag{1.4a}$$

$$\overline{\mathbf{q}} \cdot \mathbf{n} = -\lambda_{f,n} \partial_{\mathbf{n}} \overline{u} \tag{1.4b}$$

The fracture quantities of the hybrid dimensional model are the averaged pressure

$$u_f = \frac{1}{d_f} \int_{-\frac{d_f}{2}}^{\frac{d_f}{2}} \overline{u} \mathrm{d}\mathbf{n},$$

the integrated tangential Darcy velocity

$$\mathbf{q}_f = \sum_{i=1}^{d-1} \int_{-\frac{d_f}{2}}^{\frac{d_f}{2}} (\overline{\mathbf{q}} \cdot \boldsymbol{\tau}_i)\boldsymbol{\tau}_i \mathrm{d}\mathbf{n}.$$

and the integrated source term $h_f = \int_{-\frac{d_f}{2}}^{\frac{d_f}{2}} \overline{h} \mathrm{d}\mathbf{n}$.

Strong formulation

Integration of the conservation equation (1.2a) and the tangential Darcy law (1.4a) over the fracture width yields the fracture equations for the hybrid-dimensional model,

$$\begin{cases} \mathrm{div}_{\tau_i}(\mathbf{q}_f) - \gamma_{\mathbf{n}_{\mathfrak{a}^+(i)}} \mathbf{q}_m - \gamma_{\mathbf{n}_{\mathfrak{a}^-(i)}} \mathbf{q}_m = d_f h_f & \text{on } \Gamma_i, i \in I \\ \mathbf{q}_f = -d_f \, \Lambda_f \nabla_\tau u_f, & \text{on } \Gamma. \end{cases} \tag{1.5a}$$

The matrix equations for the hybrid-dimensional model are

$$\begin{cases} \mathrm{div}(\mathbf{q}_m) = h_m & \text{on } \Omega \setminus \overline{\Gamma}, \\ \mathbf{q}_m = -\Lambda_m \nabla u_m & \text{on } \Omega \setminus \overline{\Gamma}, \end{cases} \tag{1.5b}$$

The remaining equation (1.4b) is then used to provide boundary conditions along $\Gamma_{\mathfrak{a}(i)^\pm}, i \in I$. In [56], a class of coupling conditions between matrix and fracture equations is proposed, depending on the parameter $\xi \in (\frac{1}{2}, 1]$, each of which represents a certain choice of approximating the normal part of the Darcy velocity at the matrix-fracture interfaces. We adopt here this class of coupling conditions and refer to [56] for its derivation. Hence the model is completed by the equation

$$\gamma_{\mathbf{n}_{\mathfrak{a}^\pm(i)}} \mathbf{q}_m = \frac{2\lambda_{f,n}}{d_f} \frac{1}{2\xi - 1} (\xi [\![u]\!]_{\mathfrak{a}^\pm(i)} + (1 - \xi)[\![u]\!]_{\mathfrak{a}^\mp(i)}) \qquad \text{on } \Gamma_i, \ i \in I. \tag{1.5c}$$

The boundary conditions of the model are contained in the definitions of the function spaces V^0, W, which are stated in Subsection 1.2.2.

The extension of model (1.5) to complex, possibly immersed DFN is already contained in the definition of the function spaces as well. In particular, closure conditions at the immersed boundary of the fracture network (fracture tip) and at the intersection between fractures are needed. The definition of W_f imposes homogeneous Neumann boundary conditions at the fracture tips, meaning that the flow at the tip of a fracture can be neglected compared with the flow along the sides of the fracture, and normal flux conservation equations at the fracture intersection, meaning that the volume at the intersection between fractures is neglected. The definition of V_f contains the assumption of pressure continuity at the fracture intersections. This amounts to assume a high ratio between the permeability at the intersection and the fracture width compared with the ratio between the tangential permeability of each fracture and its length.

We now state the assumptions under which the model is considered for the rest of this chapter.

- $\xi \in (\frac{1}{2}, 1]$.
- The permeability tensors $\Lambda_m \in L^\infty(\Omega)^{d\times d}$ and $\Lambda_f \in L^\infty(\Gamma)^{(d-1)\times(d-1)}$ are assumed to be chosen symmetric, and such that there exist $\overline{\lambda}_m \geq \underline{\lambda}_m > 0$ and $\overline{\lambda}_f \geq \underline{\lambda}_f > 0$, with

$$\underline{\lambda}_m|\zeta|^2 \leq (\Lambda_m(\mathbf{x})\zeta,\zeta) \leq \overline{\lambda}_m|\zeta|^2 \text{ for all } \zeta \in \mathbb{R}^d, \mathbf{x} \in \Omega$$
$$\underline{\lambda}_f|\zeta|^2 \leq (\Lambda_f(\mathbf{x})\zeta,\zeta) \leq \overline{\lambda}_f|\zeta|^2 \text{ for all } \zeta \in \mathbb{R}^{d-1}, \mathbf{x} \in \Gamma.$$

  Inside the fractures, the normal direction is assumed to be a permeability principal direction. The normal permeability $\lambda_{f,\mathbf{n}} \in L^\infty(\Gamma)$ is such that $\underline{\lambda}_{f,\mathbf{n}} \leq \lambda_{f,\mathbf{n}}(\mathbf{x}) \leq \overline{\lambda}_{f,\mathbf{n}}$ for a.e. $\mathbf{x} \in \Gamma$ with $0 < \underline{\lambda}_{f,\mathbf{n}} \leq \overline{\lambda}_{f,\mathbf{n}}$.
- The width of the fractures, $d_f \in L^\infty(\Gamma)$, is assumed to be such that there exist $\overline{d}_f \geq \underline{d}_f > 0$ with, for a.e. $\mathbf{x} \in \Gamma$, $\underline{d}_f \leq d_f(\mathbf{x}) \leq \overline{d}_f$.
- $h_m \in L^2(\Omega)$ and $h_f \in L^2(\Gamma)$.

Let us define the weighted Lebesgue $d-1$ dimensional measure on Γ by $d\tau_f(\mathbf{x}) = d_f(\mathbf{x})\mathrm{d}\tau(\mathbf{x})$. in the matrix domain $\Omega \setminus \overline{\Gamma}$ (resp. in the fracture network Γ). The half normal transmissibility in the fracture network is denoted by $T_f = \frac{2\lambda_{f,\mathbf{n}}}{d_f}$.

Weak formulation

The hybrid dimensional weak formulation amounts to find $u = (u_m, u_f) \in V^0$ satisfying the following variational equality for all $v = (v_m, v_f) \in V^0$:

$$\begin{aligned}
&\int_\Omega \Lambda_m \nabla u_m \cdot \nabla v_m \mathrm{d}\mathbf{x} + \int_\Gamma \Lambda_f \nabla_\tau u_f \cdot \nabla_\tau v_f \mathrm{d}\tau_f(\mathbf{x}) \\
&+ \sum_{i\in I} \int_{\Gamma_i} \frac{T_f}{2\xi - 1} \sum_{(\mathfrak{a},\mathfrak{b})\in\{(\mathfrak{a}^\pm(i),\mathfrak{a}^\mp(i))\}} \Big(\xi[\![u]\!]_\mathfrak{a} + (1-\xi)[\![u]\!]_\mathfrak{b}\Big)[\![v]\!]_\mathfrak{a} \mathrm{d}\tau(\mathbf{x}) \\
&- \int_\Omega h_m v_m \mathrm{d}\mathbf{x} - \int_\Gamma h_f v_f \mathrm{d}\tau_f(\mathbf{x}) = 0.
\end{aligned} \tag{1.6}$$

The following proposition states the well posedness of the variational formulation (1.6).

Proposition 1.2.4 *For all $\xi \in (\frac{1}{2}, 1]$, the variational problem* (1.6) *has a unique solution $(u_m, u_f) \in V^0$ which satisfies the a priori estimate*

$$\|(u_m, u_f)\|_{V^0} \le C\Big(\|h_m\|_{L^2(\Omega)} + \|h_f\|_{L^2(\Gamma)}\Big),$$

with C depending only on ξ, $\mathcal{C}_P$, $\underline{\lambda}_m$, $\underline{\lambda}_f$, $\underline{d}_f$, $\overline{d}_f$, and $\underline{\lambda}_{f,n}$. In addition $(\mathbf{q}_m, \mathbf{q}_f) = -(\Lambda_m \nabla u_m, d_f \Lambda_f \nabla_\tau u_f)$ belongs to W.

Proof Using that for all $\xi \in (\frac{1}{2}, 1]$ and for all $(a, b) \in \mathbb{R}^2$ one has

$$a^2 + b^2 \le (\xi a + (1-\xi)b)a + (\xi b + (1-\xi)a)b \le \frac{1}{2\xi - 1}(a^2 + b^2),$$

the Lax-Milgram Theorem applies, which ensures the statement of the proposition. □

1.3 Gradient Discretization of the Hybrid Dimensional Model

1.3.1 Gradient Scheme Framework

A gradient discretization $\mathcal{D}$ of hybrid dimensional Darcy flow models is defined by a vector space of discrete unknowns $X_\mathcal{D}$, its subspace satisfying ad hoc homogeneous boundary conditions $X_\mathcal{D}^0$, and the following gradient and reconstruction operators:

- Gradient operator on the matrix domain: $\nabla_\mathcal{D}^m : X_\mathcal{D} \to L^2(\Omega)^d$
- Gradient operator on the fracture network: $\nabla_\mathcal{D}^f : X_\mathcal{D} \to L^2(\Gamma)^{d-1}$
- A function reconstruction operator on the matrix domain: $\Pi_\mathcal{D}^m : X_\mathcal{D} \to L^2(\Omega)$
- A function reconstruction operator on the fracture network: $\Pi_\mathcal{D}^f : X_\mathcal{D} \to L^2(\Gamma)$

- Reconstruction operators of the jump on $\Gamma_{\mathfrak{a}}$ for $\mathfrak{a} \in \chi$: $[\![\cdot]\!]_{\mathcal{D}}^{\mathfrak{a}} : X_{\mathcal{D}} \to L^2(\Gamma_{\mathfrak{a}})$.

The space $X_{\mathcal{D}}$ is endowed with the seminorm

$$\|v_{\mathcal{D}}\|_{\mathcal{D}} = \Big(\|\nabla_{\mathcal{D}}^m v_{\mathcal{D}}\|_{L^2(\Omega)^d}^2 + \|\nabla_{\mathcal{D}}^f v_{\mathcal{D}}\|_{L^2(\Gamma)^{d-1}}^2 + \sum_{\mathfrak{a} \in \chi} \|[\![v_{\mathcal{D}}]\!]_{\mathcal{D}}^{\mathfrak{a}}\|_{L^2(\Gamma_{\mathfrak{a}})}^2 \Big)^{\frac{1}{2}},$$

which is assumed to define a norm on $X_{\mathcal{D}}^0$.

Discretizing (1.6) in the sense of gradient discretizations yields: find $u_{\mathcal{D}} \in X_{\mathcal{D}}^0$ such that

$$\begin{aligned} &\int_\Omega \Lambda_m \nabla_{\mathcal{D}}^m u_{\mathcal{D}} \cdot \nabla_{\mathcal{D}}^m v_{\mathcal{D}} \mathrm{d}\mathbf{x} + \int_\Gamma \Lambda_f \nabla_{\mathcal{D}}^f u_{\mathcal{D}} \cdot \nabla_{\mathcal{D}}^f v_{\mathcal{D}} \mathrm{d}\tau_f(\mathbf{x}) + \sum_{i \in I} \int_{\Gamma_i} \frac{T_f}{2\xi - 1} \\ &\qquad \sum_{(\mathfrak{a},\mathfrak{b}) \in \{(\mathfrak{a}^\pm(i), \mathfrak{a}^\mp(i))\}} \Big(\xi [\![u_{\mathcal{D}}]\!]_{\mathcal{D}}^{\mathfrak{a}} + (1-\xi) [\![u_{\mathcal{D}}]\!]_{\mathcal{D}}^{\mathfrak{b}} \Big) [\![v_{\mathcal{D}}]\!]_{\mathcal{D}}^{\mathfrak{a}} \mathrm{d}\tau(\mathbf{x}) \\ &- \int_\Omega h_m \Pi_{\mathcal{D}}^m v_{\mathcal{D}} \mathrm{d}\mathbf{x} - \int_\Gamma h_f \Pi_{\mathcal{D}}^f v_{\mathcal{D}} \mathrm{d}\tau_f(\mathbf{x}) = 0, \end{aligned} \tag{1.7}$$

for all $v_{\mathcal{D}} \in X_{\mathcal{D}}^0$.

Of course the above definition of a gradient discretization is at this stage very general. Some stability and consistency conditions must be imposed in order to expect a well posed and convergent discretization. Since the gradient scheme framework accounts for non conforming discretizations (in the sense that $\nabla_{\mathcal{D}}^m \neq \nabla \Pi_{\mathcal{D}}^m$ or or $\nabla_{\mathcal{D}}^f \neq \nabla_\tau \Pi_{\mathcal{D}}^f$ or $[\![\cdot]\!]_{\mathcal{D}}^{\mathfrak{a}} \neq [\![\Pi_{\mathcal{D}}^m, \Pi_{\mathcal{D}}^f]\!]_{\mathfrak{a}}$), a third condition must be assumed, which roughly speaking states that integration by part w.r.t. the discrete operators provides a residual "close" to zero.

Coercivity: Let

$$\mathcal{C}_{\mathcal{D}} = \max_{0 \neq v_{\mathcal{D}} \in X_{\mathcal{D}}^0} \frac{\|\Pi_{\mathcal{D}}^m v_{\mathcal{D}}\|_{L^2(\Omega)} + \|\Pi_{\mathcal{D}}^f v_{\mathcal{D}}\|_{L^2(\Gamma)}}{\|v_{\mathcal{D}}\|_{\mathcal{D}}}.$$

A sequence $(\mathcal{D}_l)_{l \in \mathbb{N}}$ of gradient discretizations is said to be coercive, if there exists $\overline{\mathcal{C}}_P > 0$ such that $\mathcal{C}_{\mathcal{D}_l} \leq \overline{\mathcal{C}}_P$ for all $l \in \mathbb{N}$.

Consistency: For $u = (u_m, u_f) \in V^0$ and $v_{\mathcal{D}} \in X_{\mathcal{D}}^0$ let us define

$$\begin{aligned} s(v_{\mathcal{D}}, u) = &\|\nabla_{\mathcal{D}}^m v_{\mathcal{D}} - \nabla u_m\|_{L^2(\Omega)^d} + \|\nabla_{\mathcal{D}}^f v_{\mathcal{D}} - \nabla_\tau u_f\|_{L^2(\Gamma)^{d-1}} \\ &+ \|\Pi_{\mathcal{D}}^m v_{\mathcal{D}} - u_m\|_{L^2(\Omega)} + \|\Pi_{\mathcal{D}}^f v_{\mathcal{D}} - u_f\|_{L^2(\Gamma)} + \textstyle\sum_{\mathfrak{a} \in \chi} \|[\![v_{\mathcal{D}}]\!]_{\mathcal{D}}^{\mathfrak{a}} - [\![u]\!]_{\mathfrak{a}}\|_{L^2(\Gamma_{\mathfrak{a}})} \end{aligned}$$

and $\mathcal{S}_{\mathcal{D}}(u) = \min_{v_{\mathcal{D}} \in X_{\mathcal{D}}^0} s(v_{\mathcal{D}}, u)$. A sequence $(\mathcal{D}_l)_{l \in \mathbb{N}}$ of gradient discretizations is said to be consistent, if for all $u = (u_m, u_f) \in V^0$ holds

$$\lim_{l \to \infty} \mathcal{S}_{\mathcal{D}_l}(u) = 0.$$

Limit Conformity: For all $\mathbf{q} = (\mathbf{q}_m, \mathbf{q}_f) \in W,\ v_{\mathcal{D}} = v_{\mathcal{D}}$ we define

$$\begin{aligned} w(v_{\mathcal{D}}, \mathbf{q}) = &\int_\Omega \Big(\nabla_{\mathcal{D}}^m v_{\mathcal{D}} \cdot \mathbf{q}_m + (\Pi_{\mathcal{D}}^m v_{\mathcal{D}}) \mathrm{div} \mathbf{q}_m \Big) \mathrm{d}\mathbf{x} \\ &+ \int_\Gamma \Big(\nabla_{\mathcal{D}}^f v_{\mathcal{D}} \cdot \mathbf{q}_f + (\Pi_{\mathcal{D}}^f v_{\mathcal{D}}) \mathrm{div}_\tau \mathbf{q}_f \Big) \mathrm{d}\tau(\mathbf{x}) \\ &- \sum_{\mathfrak{a} \in \chi} \int_{\Gamma_\mathfrak{a}} \gamma_{\mathbf{n}_\mathfrak{a}} \mathbf{q}_m \Big([\![v_{\mathcal{D}}]\!]_{\mathcal{D}}^\mathfrak{a} + \Pi_{\mathcal{D}}^f v_{\mathcal{D}} \Big) \mathrm{d}\tau(\mathbf{x}) \end{aligned}$$

and $\mathcal{W}_{\mathcal{D}}(\mathbf{q}) = \max_{0 \neq v_{\mathcal{D}} \in X_{\mathcal{D}}^0} \frac{1}{\|v_{\mathcal{D}}\|_{\mathcal{D}}} |w(v_{\mathcal{D}}, \mathbf{q})|$. A sequence $(\mathcal{D}_l)_{l \in \mathbb{N}}$ of gradient discretizations is said to be limit conforming, if for all $\mathbf{q} = (\mathbf{q}_m, \mathbf{q}_f) \in W$ holds

$$\lim_{l \to \infty} \mathcal{W}_{\mathcal{D}_l}(\mathbf{q}) = 0.$$

As will be seen in the two examples of gradient schemes in the next section, the practical definition of the operators $\Pi_{\mathcal{D}}^m$ and $\Pi_{\mathcal{D}}^f$ satisfying the above assumptions is very flexible. This flexibility can be exploited in order to adapt the discretization to heterogeneities when coupling the Darcy flow model with a transport equation (see [39] for details). On the other hand, the choice of the operators $[\![\cdot]\!]_{\mathcal{D}}^\mathfrak{a}$ is more constrained by the limit conformity property.

The limit conformity property is enhanced by the following proposition which roughly speaking states that, the limit(s) of bounded sequences in $X_{\mathcal{D}_l}^0$, $l \in \mathbb{N}$, belong to V^0.

Proposition 1.3.1 (Regularity at the Limit) *Let $(\mathcal{D}_l)_{l \in \mathbb{N}}$ be a coercive and limit conforming sequence of gradient discretizations and let $(v_{\mathcal{D}_l})_{l \in \mathbb{N}}$ be a uniformly bounded sequence in $X_{\mathcal{D}_l}^0$. Then, there exist $v = (v_m, v_f) \in V^0$ and a subsequence still denoted by $(v_{\mathcal{D}_l})_{l \in \mathbb{N}}$ such that*

$$\left\{ \begin{array}{ll} \Pi_{\mathcal{D}}^m v_{\mathcal{D}_l} \rightharpoonup v_m & \text{in } L^2(\Omega), \\ \nabla_{\mathcal{D}_l}^m v_{\mathcal{D}_l} \rightharpoonup \nabla v_m & \text{in } L^2(\Omega)^d, \\ \Pi_{\mathcal{D}_l}^f v_{\mathcal{D}_l} \rightharpoonup v_f & \text{in } L^2(\Gamma), \\ \nabla_{\mathcal{D}_l}^f v_{\mathcal{D}_l} \rightharpoonup \nabla_\tau v_f & \text{in } L^2(\Gamma)^{d-1}, \\ [\![v_{\mathcal{D}_l}]\!]_{\mathcal{D}_l}^\mathfrak{a} \rightharpoonup [\![v]\!]_\mathfrak{a} & \text{in } L^2(\Gamma_\mathfrak{a}), \text{ for all } \mathfrak{a} \in \chi. \end{array} \right.$$

Proof By definition of the norm of $X_{\mathcal{D}_l}^0$ and by coercivity, $\Pi_{\mathcal{D}_l}^m v_{\mathcal{D}_l}$, $\Pi_{\mathcal{D}_l}^f v_{\mathcal{D}_l}$, $\nabla_{\mathcal{D}}^m v_{\mathcal{D}_l}$, $\nabla_{\mathcal{D}}^f v_{\mathcal{D}_l}$ and $([\![u_{\mathcal{D}_l}]\!]_{\mathcal{D}_l}^\mathfrak{a})$, $\mathfrak{a} \in \chi$, are uniformly bounded in L^2 (for $l \to \infty$). Therefore there exist $v_m \in L^2(\Omega)$, $v_f \in L^2(\Gamma)$, $G \in L^2(\Omega)^d$, $H \in L^2(\Gamma)^{d-1}$ and $J_\mathfrak{a} \in L^2(\Gamma_\mathfrak{a})$, $\mathfrak{a} \in \chi$, and a subsequence still denoted by $(v_{\mathcal{D}_l})_{l \in \mathbb{N}}$ such that

$$\begin{array}{ll} \Pi_{\mathcal{D}_l}^m v_{\mathcal{D}_l} \rightharpoonup v_m & \text{in } L^2(\Omega), \\ \nabla_{\mathcal{D}}^m v_{\mathcal{D}_l} \rightharpoonup G & \text{in } L^2(\Omega)^d, \\ \Pi_{\mathcal{D}_l}^f v_{\mathcal{D}_l} \rightharpoonup v_f & \text{in } L^2(\Gamma), \\ \nabla_{\mathcal{D}}^f v_{\mathcal{D}_l} \rightharpoonup H & \text{in } L^2(\Gamma)^{d-1}, \\ [\![v_{\mathcal{D}_l}]\!]_{\mathcal{D}_l}^\mathfrak{a} \rightharpoonup J_\mathfrak{a} & \text{in } L^2(\Gamma_\mathfrak{a}), \text{ for } \mathfrak{a} \in \chi. \end{array}$$

Using limit conformity we obtain (by letting $l \to \infty$)

$$\int_\Omega (G \cdot \mathbf{q}_m + v_m \mathrm{div} \mathbf{q}_m) \mathrm{d}\mathbf{x} + \int_\Gamma (H \cdot \mathbf{q}_f + v_f \mathrm{div}_\tau \mathbf{q}_f) \mathrm{d}\tau(\mathbf{x}) - \sum_{\mathfrak{a} \in \chi} \int_{\Gamma_\mathfrak{a}} \gamma_{\mathbf{n}_\mathfrak{a}} \mathbf{q}_m (J_\mathfrak{a} + v_f) \mathrm{d}\tau(\mathbf{x}) = 0$$

for all $(\mathbf{q}_m, \mathbf{q}_f) \in \mathbf{C}^\infty_\Omega \times \mathbf{C}^\infty_\Gamma$. The statement of the proposition follows now from Lemma 1.A.1. □

Corollary 1.3.1 *Let $(\mathcal{D}_l)_{l \in \mathbb{N}}$ be a sequence of gradient discretizations, assumed to be limit conforming against regular test functions $(\mathbf{q}_m, \mathbf{q}_f) \in \mathbf{C}^\infty_\Omega \times \mathbf{C}^\infty_\Gamma$ and let $(v_{\mathcal{D}_l})_{l \in \mathbb{N}}$ be a uniformly bounded sequence in $X^0_{\mathcal{D}_l}$, such that $\Pi^m_{\mathcal{D}_l} v_{\mathcal{D}_l}$ and $\Pi^f_{\mathcal{D}_l} v_{\mathcal{D}_l}$ are uniformly bounded in L^2 (for $l \to \infty$). Then holds the conclusion of Proposition 1.3.1.*

1.3.2 Application to (1.6)

We now want to exploit the previous results for the non conforming discrete variational formulation of the model problem, (1.7).

Proposition 1.3.2 *Let $\xi \in (\frac{1}{2}, 1]$ and $\mathcal{D}$ be a gradient discretization, then (1.7) has a unique solution $u_\mathcal{D} \in X^0_\mathcal{D}$ satisfying the a priori estimate*

$$\|u_\mathcal{D}\|_\mathcal{D} \leq C \Big(\|h_m\|_{L^2(\Omega)} + \|h_f\|_{L^2(\Gamma)} \Big)$$

with C depending only on ξ, $\mathcal{C}_\mathcal{D}$, $\underline{\lambda}_m$, $\underline{\lambda}_f$, $\underline{d}_f$, $\overline{d}_f$, and $\underline{\lambda}_{f,n}$.

Proof The Lax-Milgram Theorem applies, which ensures this result. □

The main theoretical result for gradient schemes is stated by the following proposition:

Proposition 1.3.3 (Error Estimate) *Let $u = (u_m, u_f) \in V^0$, $\mathbf{q} = (\mathbf{q}_m, \mathbf{q}_f) \in W$ be the solution of (1.5). Let $\xi \in (\frac{1}{2}, 1]$, $\mathcal{D}$ be a gradient discretization and $u_\mathcal{D} \in X^0_\mathcal{D}$ be the solution of (1.7). Then, there exists $C_0 > 0$ depending only on ξ, $\mathcal{C}_\mathcal{D}$, $\underline{\lambda}_m$, $\underline{\lambda}_f$,$\overline{\lambda}_m$, $\overline{\lambda}_f$, $\underline{d}_f$, $\overline{d}_f$, $\underline{\lambda}_{f,n}$, and $\overline{\lambda}_{f,n}$ such that one has the following error estimate:*

$$\|\Pi^m_\mathcal{D} u_\mathcal{D} - u_m\|_{L^2(\Omega)} + \|\Pi^f_\mathcal{D} u_\mathcal{D} - u_f\|_{L^2(\Gamma)} + \sum_{\mathfrak{a} \in \chi} \|[\![u_\mathcal{D}]\!]^\mathfrak{a}_\mathcal{D} - [\![u]\!]_\mathfrak{a}\|_{L^2(\Gamma_\mathfrak{a})}$$
$$+ \|\nabla u_m - \nabla^m_\mathcal{D} u_\mathcal{D}\|_{L^2(\Omega)^d} + \|\nabla_\tau u_f - \nabla^f_\mathcal{D} u_\mathcal{D}\|_{L^2(\Gamma)^{d-1}} \leq C_0 (\mathcal{S}_\mathcal{D}(u_m, u_f) + \mathcal{W}_\mathcal{D}(\mathbf{q}_m, \mathbf{q}_f)).$$

Proof From the definition of $\mathcal{W}_\mathcal{D}$, and using the definitions (1.5) of the solution $u, \mathbf{q}$ and (1.7) of the discrete solution $u_\mathcal{D}$, it holds for all $v_\mathcal{D} \in X_\mathcal{D}^0$

$$
\begin{aligned}
&\|v_\mathcal{D}\|_\mathcal{D} \mathcal{W}_\mathcal{D}(\mathbf{q}_m, \mathbf{q}_f) \\
&\geq \left| \int_\Omega \Big(\nabla_\mathcal{D}^m v_\mathcal{D} \cdot \mathbf{q}_m + (\Pi_\mathcal{D}^m v_\mathcal{D}) h_m \Big) \mathrm{d}\mathbf{x} + \int_\Gamma \Big(\nabla_\mathcal{D}^f v_\mathcal{D} \cdot \mathbf{q}_f + (\Pi_\mathcal{D}^f v_\mathcal{D}) d_f h_f \Big) \mathrm{d}\tau(\mathbf{x}) \right. \\
&\left. - \sum_{i \in I} \int_{\Gamma_i} \frac{T_f}{2\xi - 1} \sum_{(\mathfrak{a},\mathfrak{b}) \in \{(\mathfrak{a}^\pm(i), \mathfrak{a}^\mp(i))\}} \Big(\xi [\![u]\!]_\mathfrak{a} + (1-\xi) [\![u]\!]_\mathfrak{b} \Big) [\![v_\mathcal{D}]\!]_\mathcal{D}^\mathfrak{a} \mathrm{d}\tau(\mathbf{x}) \right| \\
&= \left| \int_\Omega \Big(\Lambda_m \nabla_\mathcal{D}^m v_\mathcal{D} \cdot (\nabla_\mathcal{D}^m u_\mathcal{D} - \nabla u_m) \Big) \mathrm{d}\mathbf{x} + \int_\Gamma \Big(\Lambda_f \nabla_\mathcal{D}^f v_\mathcal{D} \cdot (\nabla_\mathcal{D}^f u_\mathcal{D} - \nabla_\tau u_f) \Big) \mathrm{d}\tau_f(\mathbf{x}) \right. \\
&\left. - \sum_{i \in I} \int_{\Gamma_i} \frac{T_f}{2\xi - 1} \sum_{(\mathfrak{a},\mathfrak{b}) \in \{(\mathfrak{a}^\pm(i), \mathfrak{a}^\mp(i))\}} \Big(\xi [\![u]\!]_\mathfrak{a} + (1-\xi) [\![u]\!]_\mathfrak{b} - \xi [\![u_\mathcal{D}]\!]_\mathcal{D}^\mathfrak{a} - (1-\xi) [\![u_\mathcal{D}]\!]_\mathcal{D}^\mathfrak{b} \Big) [\![v_\mathcal{D}]\!]_\mathcal{D}^\mathfrak{a} \mathrm{d}\tau(\mathbf{x}) \right|
\end{aligned}
\tag{1.8}
$$

For the following calculations, to shorten the notation, we introduce the continuous and coercive bilinear form

$$
\begin{aligned}
a_{\mathcal{D},\xi}(v_\mathcal{D}, w_\mathcal{D}) = &\int_\Omega \Lambda_m \nabla_\mathcal{D}^m v_\mathcal{D} \cdot \nabla_\mathcal{D}^m w_\mathcal{D} \mathrm{d}\mathbf{x} + \int_\Gamma \Lambda_f \nabla_\mathcal{D}^f v_\mathcal{D} \cdot \nabla_\mathcal{D}^m w_\mathcal{D} \mathrm{d}\tau_f(\mathbf{x}) \\
&+ \sum_{i \in I} \int_{\Gamma_i} \frac{T_f}{2\xi - 1} \sum_{(\mathfrak{a},\mathfrak{b}) \in \{(\mathfrak{a}^\pm(i), \mathfrak{a}^\mp(i))\}} \Big(\xi [\![w_\mathcal{D}]\!]_\mathcal{D}^\mathfrak{a} + (1-\xi) [\![w_\mathcal{D}]\!]_\mathcal{D}^\mathfrak{b} \Big) [\![v_\mathcal{D}]\!]_\mathcal{D}^\mathfrak{a} \mathrm{d}\tau(\mathbf{x})
\end{aligned}
$$

for all $v_\mathcal{D}, w_\mathcal{D} \in X_\mathcal{D}^0$. Let us choose $w_\mathcal{D} \in X_\mathcal{D}^0$, s.t. $s(w_\mathcal{D}, u) = \mathcal{S}_\mathcal{D}(u)$. Using inequality (1.8), we derive

$$
|a_{\mathcal{D},\xi}(v_\mathcal{D}, u_\mathcal{D} - w_\mathcal{D})| \leq \|v_\mathcal{D}\|_\mathcal{D} (\mathcal{W}_\mathcal{D}(\mathbf{q}_m, \mathbf{q}_f) + cst \cdot \mathcal{S}_\mathcal{D}(u_m, u_f)).
$$

Let us choose now $v_\mathcal{D} = u_\mathcal{D} - w_\mathcal{D}$. Then follows, from the coercivity of $a_{\mathcal{D},\xi}$ and by applying the definition of $\mathcal{S}_\mathcal{D}(u_m, u_f)$ on the left hand side of the inequality, that holds

$$
\begin{aligned}
&\|\nabla u_m - \nabla_\mathcal{D}^m u_\mathcal{D}\|_{L^2(\Omega)^d} + \|\nabla_\tau u_f - \nabla_\mathcal{D}^f u_\mathcal{D}\|_{L^2(\Gamma)^{d-1}} + \sum_{\mathfrak{a} \in \chi} \|[\![u_\mathcal{D}]\!]_\mathcal{D}^\mathfrak{a} - [\![u]\!]_\mathfrak{a}\|_{L^2(\Gamma_\mathfrak{a})} \\
&\leq C \cdot (\mathcal{S}_\mathcal{D}(u_m, u_f) + \mathcal{W}_\mathcal{D}(\mathbf{q}_m, \mathbf{q}_f)),
\end{aligned}
$$

with a constant $C > 0$ depending only on ξ, $\underline{\lambda}_m$, $\underline{\lambda}_f$,$\overline{\lambda}_m$, $\overline{\lambda}_f$, $\underline{d}_f$, $\overline{d}_f$, $\underline{\lambda}_{f,n}$, and $\overline{\lambda}_{f,n}$. Taking into account the definition of the coercivity constant $\mathcal{C}_\mathcal{D}$ leads to the statement of the proposition. □

1.4 Two Examples of Gradient Schemes

Following [38], we consider generalised polyhedral meshes of Ω. Let $\mathcal{M}$ be the set of cells that are disjoint polyhedral open subsets of Ω such that $\bigcup_{K \in \mathcal{M}} \overline{K} = \overline{\Omega}$. For all $K \in \mathcal{M}$,

$\mathbf{x}_K$ denotes the so-called "center" of the cell K under the assumption that K is star-shaped with respect to $\mathbf{x}_K$. Let $\mathcal{F}$ denote the set of faces of the mesh. The faces are not assumed to be planar for the VAG discretization, hence the term "generalised polyhedral cells", but they need to be planar for the HFV discretization. We denote by $\mathcal{V}$ the set of vertices of the mesh. Let $\mathcal{V}_K$, $\mathcal{F}_K$, $\mathcal{V}_\sigma$ respectively denote the set of the vertices of $K \in \mathcal{M}$, faces of K, and vertices of $\sigma \in \mathcal{F}$. For any face $\sigma \in \mathcal{F}_K$, we have $\mathcal{V}_\sigma \subset \mathcal{V}_K$. Let $\mathcal{M}_s$ (resp. $\mathcal{F}_s$) denote the set of the cells (resp. faces) sharing the vertex $s \in \mathcal{V}$. The set of edges of the mesh is denoted by $\mathcal{E}$ and $\mathcal{E}_\sigma$ denotes the set of edges of the face $\sigma \in \mathcal{F}$. Let $\mathcal{F}_e$ denote the set of faces sharing the edge $e \in \mathcal{E}$, and $\mathcal{M}_\sigma$ denote the set of cells sharing the face $\sigma \in \mathcal{F}$. We denote by $\mathcal{F}_{ext}$ the subset of faces $\sigma \in \mathcal{F}$ such that $\mathcal{M}_\sigma$ has only one element, and we set $\mathcal{E}_{ext} = \bigcup_{\sigma \in \mathcal{F}_{ext}} \mathcal{E}_\sigma$, and $\mathcal{V}_{ext} = \bigcup_{\sigma \in \mathcal{F}_{ext}} \mathcal{V}_\sigma$. The mesh is assumed to be conforming in the sense that for all $\sigma \in \mathcal{F} \setminus \mathcal{F}_{ext}$, the set $\mathcal{M}_\sigma$ contains exactly two cells. It is assumed that for each face $\sigma \in \mathcal{F}$, there exists a so-called "center" of the face $\mathbf{x}_\sigma$ such that

$$\mathbf{x}_\sigma = \sum_{s \in \mathcal{V}_\sigma} \beta_{\sigma,s}\, \mathbf{x}_s, \text{ with } \sum_{s \in \mathcal{V}_\sigma} \beta_{\sigma,s} = 1,$$

where $\beta_{\sigma,s} \geq 0$ for all $s \in \mathcal{V}_\sigma$. The face σ is assumed to match with the union of the triangles $T_{\sigma,e}$ defined by the face center $\mathbf{x}_\sigma$ and each of its edge $e \in \mathcal{E}_\sigma$.

The mesh is assumed to be conforming w.r.t. the fracture network Γ in the sense that there exist subsets $\mathcal{F}_{\Gamma_i}$, $i \in I$ of $\mathcal{F}$ such that

$$\overline{\Gamma}_i = \bigcup_{\sigma \in \mathcal{F}_{\Gamma_i}} \bar{\sigma}.$$

We will denote by $\mathcal{F}_\Gamma$ the set of fracture faces $\bigcup_{i \in I} \mathcal{F}_{\Gamma_i}$. Similarly, we will denote by $\mathcal{E}_\Gamma$ the set of fracture edges $\bigcup_{\sigma \in \mathcal{F}_\Gamma} \mathcal{E}_\sigma$ and by $\mathcal{V}_\Gamma$ the set of fracture vertices $\bigcup_{\sigma \in \mathcal{F}_\Gamma} \mathcal{V}_\sigma$.

We also define a submesh $\mathcal{T}$ of tetrahedra, where each tetrahedron $D_{K,\sigma,e}$ is the convex hull of the cell center $\mathbf{x}_K$ of K, the face center $\mathbf{x}_\sigma$ of $\sigma \in \mathcal{F}_K$ and the edge $e \in \mathcal{E}_\sigma$. Similarly we define a triangulation Δ of Γ, such that we have:

$$\mathcal{T} = \bigcup_{K \in \mathcal{F}, \sigma \in \mathcal{F}_K, e \in \mathcal{E}_\sigma} \{D_{K,\sigma,e}\} \quad \text{and} \quad \Delta = \bigcup_{\sigma \in \mathcal{F}_\Gamma, e \in \mathcal{E}_\sigma} \{T_{\sigma,e}\}.$$

We introduce for $D \in \mathcal{T}$ the diameter h_D of D and set $h_\mathcal{T} = \max_{D \in \mathcal{T}} h_D$. The regularity of our polyhedral mesh will be measured by the shape regularity of the tetrahedral submesh defined by $\theta_\mathcal{T} = \max_{D \in \mathcal{T}} \frac{h_D}{\rho_D}$ where ρ_D is the insphere diameter of $D \in \mathcal{T}$.

The set of matrix and fracture degrees of freedom is denoted by $dof_\mathcal{D} = dof_{\mathcal{D}_m} \cup dof_{\mathcal{D}_f}$, with $dof_{\mathcal{D}_m} \cap dof_{\mathcal{D}_f} = \emptyset$. The real vector space $X_\mathcal{D}$ of discrete unknowns is then defined by

$$X_\mathcal{D} = \text{span}\{\mathfrak{e}_\nu \mid \nu \in dof_\mathcal{D}\}$$

where

$$\mathfrak{e}_\nu = (\delta_{\nu\mu})_{\mu \in dof_\mathcal{D}} \qquad \text{for } \nu \in dof_\mathcal{D}.$$

Obviously, we have $\dim X_{\mathcal{D}} = \#dof_{\mathcal{D}_m} + \#dof_{\mathcal{D}_f}$. For $u_{\mathcal{D}} \in X_{\mathcal{D}}$ and $\nu \in dof_{\mathcal{D}}$, we denote by u_ν the νth component of $u_{\mathcal{D}}$. To account for Dirichlet boundary conditions on $\partial\Omega$ and Σ_0 we introduce the subsets $dof_{Dir_m} \subset dof_{\mathcal{D}_m}$, and $dof_{Dir_f} \subset dof_{\mathcal{D}_f}$, and we set $dof_{Dir} = dof_{Dir_m} \cup dof_{Dir_f}$, and

$$X^0_{\mathcal{D}} = \{u_{\mathcal{D}} \in X_{\mathcal{D}} \,|\, u_\nu = 0 \text{ for all } \nu \in dof_{Dir}\}.$$

1.4.1 Vertex Approximate Gradient Discretization

In this subsection, the VAG discretization introduced in [38] for diffusive problems on heterogeneous anisotropic media is extended to the hybrid dimensional model. We consider the $\mathbb{P}_1$ finite element construction as well as a finite volume version using lumping both for the source terms and the matrix fracture fluxes.

We first establish an equivalence relation on each $\mathcal{M}_s,\ s \in \mathcal{V}$, by

$$\begin{aligned} K \equiv_{\mathcal{M}_s} L \quad \Longleftrightarrow \quad & \text{there exists } n \in \mathbb{N} \text{ and a sequence } (\sigma_i)_{i=1,\dots,n} \text{ in } \mathcal{F}_s \backslash \mathcal{F}_\Gamma, \\ & \text{such that } K \in \mathcal{M}_{\sigma_1}, L \in \mathcal{M}_{\sigma_n} \text{ and } \mathcal{M}_{\sigma_{i+1}} \cap \mathcal{M}_{\sigma_i} \neq \emptyset \\ & \text{for } i = 1, \dots, n-1. \end{aligned}$$

Let us then denote by $\overline{\mathcal{M}}_s$ the set of all classes of equivalence of $\mathcal{M}_s$ and by $\overline{K}_s$ the element of $\overline{\mathcal{M}}_s$ containing $K \in \mathcal{M}$. Obviously $\overline{\mathcal{M}}_s$ might have more than one element only if $s \in \mathcal{V}_\Gamma$. Then we define (cf. Figure 1.3)

$$\begin{aligned} dof_{\mathcal{D}_m} &= \mathcal{M} \cup \Big\{K_\sigma \;\Big|\; \sigma \in \mathcal{F}_\Gamma, K \in \mathcal{M}_\sigma\Big\} \cup \Big\{\overline{K}_s \;\Big|\; s \in \mathcal{V}, \overline{K}_s \in \overline{\mathcal{M}}_s\Big\}, \\ dof_{\mathcal{D}_f} &= \mathcal{F}_\Gamma \cup \mathcal{V}_\Gamma, \\ dof_{Dir_m} &:= \Big\{\overline{K}_s \;\Big|\; s \in \mathcal{V}_{ext}, \overline{K}_s \in \overline{\mathcal{M}}_s\Big\}, \\ dof_{Dir_f} &= \mathcal{V}_\Gamma \cap \mathcal{V}_{ext}. \end{aligned}$$

We thus have

$$\begin{aligned} X_{\mathcal{D}} = \ & \Big\{u_K \;\Big|\; K \in \mathcal{M}\Big\} \cup \Big\{u_{K_\sigma} \;\Big|\; \sigma \in \mathcal{F}_\Gamma, K \in \mathcal{M}_\sigma\Big\} \\ & \cup \Big\{u_{\overline{K}_s} \;\Big|\; s \in \mathcal{V}, \overline{K}_s \in \overline{\mathcal{M}}_s\Big\} \\ & \cup \Big\{u_\sigma \;\Big|\; \sigma \in \mathcal{F}_\Gamma\Big\} \cup \Big\{u_s \;\Big|\; s \in \mathcal{V}_\Gamma\Big\}. \end{aligned} \tag{1.9}$$

Now we can introduce the piecewise affin reconstruction operators

$$\Pi_{\mathcal{T}} \colon X_{\mathcal{D}} \longrightarrow H^1(\Omega \backslash \overline{\Gamma}) \qquad \text{and} \qquad \Pi_\Delta \colon X_{\mathcal{D}} \longrightarrow H^1(\Gamma),$$

which act linearly on $X_{\mathcal{D}}$, and are such that $\Pi_{\mathcal{T}} u_{\mathcal{D}}$ is affine on each $D_{K,\sigma,e} \in \mathcal{T}$ and satisfies on each cell $K \in \mathcal{M}$

$$\begin{aligned}
&\Pi_{\mathcal{T}} u_{\mathcal{D}}(\mathbf{x}_K) = u_K, \\
&\Pi_{\mathcal{T}} u_{\mathcal{D}}(\mathbf{x}_s) = u_{\overline{K}_s} && \forall s \in \mathcal{V}_K, \\
&\Pi_{\mathcal{T}} u_{\mathcal{D}}(\mathbf{x}_\sigma) = u_{K_\sigma} && \forall \sigma \in \mathcal{F}_K \cap \mathcal{F}_\Gamma, \\
&\Pi_{\mathcal{T}} u_{\mathcal{D}}(\mathbf{x}_\sigma) = \sum_{s \in \mathcal{V}_\sigma} \beta_{\sigma,s} u_{\overline{K}_s} && \forall \sigma \in \mathcal{F}_K \backslash \mathcal{F}_\Gamma,
\end{aligned}$$

while $\Pi_\Delta u_{\mathcal{D}}$ is affine on each $T_{\sigma,e} \in \Delta$ and satisfies

$$\Pi_\Delta u_{\mathcal{D}}(\mathbf{x}_\nu) = u_\nu \qquad \forall \nu \in dof_{\mathcal{D}_f},$$

where $\mathbf{x}_\nu \in \overline{\Omega}$ is the grid point associated with the degree of freedom $\nu \in dof_{\mathcal{D}}$.

The matrix and fracture discrete gradients on $X_{\mathcal{D}}$ are subsequently defined by

$$\nabla^m_{\mathcal{D}} = \nabla \Pi_{\mathcal{T}} \qquad \text{and} \qquad \nabla^f_{\mathcal{D}} = \nabla_\tau \Pi_\Delta. \tag{1.10}$$

The so defined reconstruction operators and discrete gradients correspond to the V^0 conforming $\mathbb{P}_1$ Finite Element reconstructions on a tetrahedral submesh using barycentric interpolation to eliminate the d.o.f. at faces $\sigma \in \mathcal{F}_K \backslash \mathcal{F}_\Gamma$.

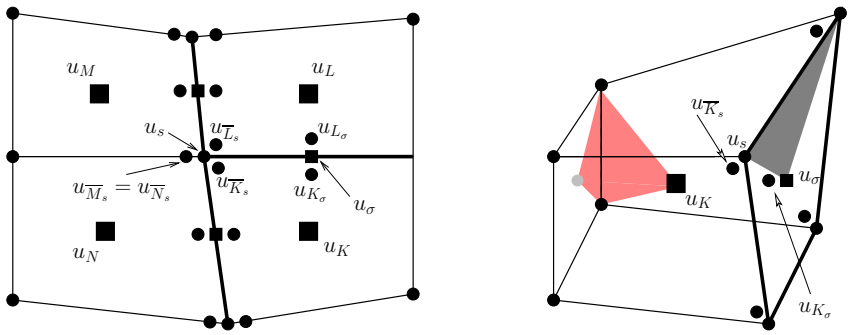

Figure 1.3: Left: Illustration of d.o.f. in 2D for four cells intersected by three fractures (thick lines).
Right: 3D cell K touching a fracture face σ. Illustration of the simplices on which $\nabla^m_{\mathcal{D}}$ is constant (red) and $\nabla^f_{\mathcal{D}}$ is constant (grey).

We define VAG-FE scheme's reconstruction operators by

$$\begin{aligned}
&\bullet\ \Pi^m_{\mathcal{D}} = \Pi_{\mathcal{T}}, \\
&\bullet\ \Pi^f_{\mathcal{D}} = \Pi_\Delta, \\
&\bullet\ [\![\cdot]\!]^{\mathfrak{a}}_{\mathcal{D}} = \gamma_{\mathfrak{a}} \Pi_{\mathcal{T}} - \Pi_\Delta \quad \text{for all } \mathfrak{a} \in \chi.
\end{aligned} \tag{1.11}$$

For the family of VAG-CV schemes, reconstruction operators are piecewise constant. For $K \in \mathcal{M}$ let $dof_K = \{\overline{K}_s, s \in \mathcal{V}_K\} \cup \{K_\sigma, \sigma \in \mathcal{F}_K \cap \mathcal{F}_\Gamma\}$. Analogously, in the

fracture domain, for $\sigma \in \mathcal{F}_\Gamma$ let $dof_\sigma = \mathcal{V}_\sigma$. We introduce, for any given $K \in \mathcal{M}$, a partition $\{\omega_K^\nu\}_{\nu \in \{K\} \cup dof_K \setminus dof_{Dir}}$ of K. Similarly, we define for any given $\sigma \in \mathcal{F}_\Gamma$ a partition $\{\omega_\sigma^\nu\}_{\nu \in \{\sigma\} \cup dof_\sigma \setminus dof_{Dir}}$ of σ. For each $\nu \in dof_{\mathcal{D}_m}$, we define the open set $\omega_\nu = \mathrm{int}\Big(\bigcup_{K \in \mathcal{M}} \overline{\omega}_K^\nu\Big)$, with the convention $\omega_K^\nu = \emptyset$, if $\nu \notin dof_K$. For each $\nu \in dof_{\mathcal{D}_f}$, we define the open set $\omega_\nu = \mathrm{int}\Big(\bigcup_{\sigma \in \mathcal{F}} \overline{\omega}_\sigma^\nu\Big)$, where $\omega_\sigma^\nu = \emptyset$, if $\nu \notin dof_\sigma$. We thus obtain the partitions $\{\omega_\nu\}_{\nu \in dof_{\mathcal{D}_m} \setminus dof_{Dir_m}}$ of Ω and $\{\omega_\nu\}_{\nu \in dof_{\mathcal{D}_f} \setminus dof_{Dir_f}}$ of Γ. We also introduce for each $T = T_{\sigma,s,s'} \in \Delta$ a partition $\{T_i\}_{i=1,\dots,3}$ of T, which we need for the definition of the VAG-CV matrix-fracture interaction operators. We assume that holds $|T_1| = |T_2| = |T_3| = \frac{1}{3}|T|$ in order to preserve the first order accuracy of the scheme. The VAG-CV discretization is particularly adapted for the treatment of multiphase flow processes through heterogeneous media (cf. [39]). Provided the mesh is conforming w.r.t. the heterogeneous layers, we can assume that key geological quantities are constant per cell and per fracture face. Therefore, in the numerical scheme, we do not need to reconstruct the just introduced partitions explicitly, but only have to define their corresponding volumes. Finally, we need a mapping between the degrees of freedom of the matrix domain, which are situated on one side of the fracture network, and the set of indices χ. For $K_\sigma \in dof_{\mathcal{D}_m}$ we have the one-element set $\chi(K_\sigma) = \{\mathfrak{a} \in \chi \mid (\mathbf{x}_K - \mathbf{x}_\sigma) \cdot \mathbf{n}_\mathfrak{a} < 0\}$ and therefore the notation $\mathfrak{a}(K_\sigma) = \mathfrak{a} \in \chi(K_\sigma)$.

The VAG-CV scheme's reconstruction operators are

$$
\begin{aligned}
&\bullet\ \Pi_\mathcal{D}^m u_\mathcal{D} = \sum_{\nu \in dof_{\mathcal{D}_m} \setminus dof_{Dir_m}} u_\nu \mathbb{1}_{\omega_\nu},\\
&\bullet\ \Pi_\mathcal{D}^f u_\mathcal{D} = \sum_{\nu \in dof_{\mathcal{D}_f} \setminus dof_{Dir_f}} u_\nu \mathbb{1}_{\omega_\nu},\\
&\bullet\ [\![u_\mathcal{D}]\!]_\mathcal{D}^\mathfrak{a} = \sum_{T_{\sigma,s,s'} \in \Delta} \sum_{K \in \mathcal{M}_\sigma} ((u_{K_\sigma} - u_\sigma)\mathbb{1}_{T_1} + (u_{\overline{K}_s} - u_s)\mathbb{1}_{T_2} + (u_{\overline{K}_{s'}} - u_{s'})\mathbb{1}_{T_3})\delta_{\mathfrak{a}(K_\sigma)\mathfrak{a}}\mathbb{1}_{\Gamma_\mathfrak{a}}.
\end{aligned}
\tag{1.12}
$$

Remark 1.4.1 *The VAG-CV scheme leads us to recover fluxes for the matrix-fracture interactions involving degrees of freedom located at the same physical point (see appendix section 1.B).*

Proposition 1.4.1 *Let us consider a sequence of meshes $(\mathcal{M}_l)_{l \in \mathbb{N}}$ and let us assume that the sequence $(\mathcal{T}_l)_{l \in \mathbb{N}}$ of tetrahedral submeshes is shape regular, i.e. $\theta_{\mathcal{T}_l}$ is uniformly bounded. We also assume that $\lim_{l \to \infty} h_{\mathcal{T}_l} = 0$. Then, the corresponding sequence of gradient discretizations $(\mathcal{D}_l)_{l \in \mathbb{N}}$, defined by (1.9), (1.10), (1.11), is coercive, consistent and limit conforming.*

Proof The *VAG-FE* scheme's reconstruction operators are conforming in the sense that $\nabla_\mathcal{D}^m = \nabla \Pi_\mathcal{D}^m$, $\nabla_\mathcal{D}^f = \nabla_\tau \Pi_\mathcal{D}^f$, $[\![\cdot]\!]_\mathcal{D}^\mathfrak{a} \neq [\![\Pi_\mathcal{D}^m, \Pi_\mathcal{D}^f]\!]_\mathfrak{a}$. Therefore we deduce coercivity from Proposition 1.2.1. Furthermore, we have by partial integration $\mathcal{W}_\mathcal{D}(\mathbf{q}_m, \mathbf{q}_f) = 0$ for all $(\mathbf{q}_m, \mathbf{q}_f) \in W$. Hence $(\mathcal{D}_l)_{l \in \mathbb{N}}$ is limit conforming.

To prove consistency, we need the following prerequisites. We define the linear mapping $P_{\mathcal{D}}\colon C^\infty_\Omega \times C^\infty_\Gamma \to X^0_{\mathcal{D}}$, by

$$(P_{\mathcal{D}}(\psi_m,\psi_f))_\nu = \begin{cases} \psi_m(\mathbf{x}_\nu) & \text{if } \nu \in dof_{\mathcal{D}_m} \\ \psi_f(\mathbf{x}_\nu) & \text{if } \nu \in dof_{\mathcal{D}_f} \end{cases} \tag{1.13}$$

It follows from the classical Finite Element approximation theory and from the fact that the interpolation $\sum_{s\in\mathcal{V}_\sigma} \beta_{\sigma,s}(P_D(\psi_m,\psi_f))_{\overline{K}_s}$ at the point $\mathbf{x}_\sigma$, $\sigma \in \mathcal{F}_K \setminus \mathcal{F}_\Gamma$ is exact on cellwise affine functions, that for all $\psi = (\psi_m,\psi_f) \in C^\infty_\Omega \times C^\infty_\Gamma$ holds

$$\|\Pi_{\mathcal{T}} P_{\mathcal{D}}\psi - \psi_m\|_{H^1(\Omega\setminus\overline{\Gamma})} + \|\Pi_\Delta P_{\mathcal{D}}\psi - \psi_f\|_{H^1(\Gamma)} \le C(\psi_m,\psi_f,\theta_{\mathcal{T}})h_{\mathcal{T}}. \tag{1.14}$$

The trace inequality implies that for all $v \in H^1_{\partial\Omega}(\Omega\setminus\overline{\Gamma})$ holds

$$\|\gamma_{\mathfrak{a}} v\|_{L^2(\Gamma_{\mathfrak{a}})} \le C(\Omega\setminus\overline{\Gamma})\|v\|_{H^1(\Omega\setminus\overline{\Gamma})} \quad \text{for } \mathfrak{a} \in \chi.$$

We can then calculate for $u = (u_m,u_f) \in C^\infty_\Omega \times C^\infty_\Gamma$:

$$\begin{aligned}\mathcal{S}_{\mathcal{D}}(u_m,u_f) &\le \sqrt{2}\|\Pi_{\mathcal{T}}P_{\mathcal{D}}u - u_m\|_{H^1(\Omega\setminus\overline{\Gamma})} + \sum_{\mathfrak{a}\in\chi}\|\gamma_{\mathfrak{a}}(\Pi_{\mathcal{T}}P_{\mathcal{D}}u - u_m)\|_{L^2(\Gamma_{\mathfrak{a}})} \\ &\quad + \sum_{i\in I}\sqrt{8}\|\Pi_\Delta P_{\mathcal{D}}u - u_f\|_{H^1(\Gamma_i)} \le C(\Omega\setminus\overline{\Gamma},(u_m,u_f),\theta_{\mathcal{T}})\ h_{\mathcal{T}}.\end{aligned}$$

Since $C^\infty_\Omega \times C^\infty_\Gamma$ is dense in V^0, the sequence of *VAG-FE* discretisations $(\mathcal{D}^l)_{l\in\mathbb{N}}$ is consistent if $h_{\mathcal{T}^l} \to 0$ and $\theta_{\mathcal{T}^l}$ is bounded for $l \to \infty$. □

Proposition 1.4.2 *Let us consider a sequence of meshes $(\mathcal{M}^l)_{l\in\mathbb{N}}$ and let us assume that the sequence $(\mathcal{T}^l)_{l\in\mathbb{N}}$ of tetrahedral submeshes is shape regular, i.e. $\theta_{\mathcal{T}^l}$ is uniformly bounded. We also assume that $\lim_{l\to\infty} h_{\mathcal{T}^l} = 0$. Then, any corresponding sequence of gradient discretizations $(\mathcal{D}^l)_{l\in\mathbb{N}}$, defined by* (1.9), (1.10), (1.12), *is coercive, consistent and limit conforming.*

Proof For this proof, let us denote by $(\mathcal{D}^l)_{l\in\mathbb{N}}$ the sequence of *VAG-CV* gradient discretisations and by $(\overline{\mathcal{D}}^l)_{l\in\mathbb{N}} = (X_{\mathcal{D}^l}, \Pi^m_{\overline{\mathcal{D}}_l}, \Pi^f_{\overline{\mathcal{D}}_l}, [\![\cdot]\!]^{\mathfrak{a}}_{\overline{\mathcal{D}}_l}, \nabla^m_{\mathcal{D}_l}, \nabla^f_{\mathcal{D}_l})_{l\in\mathbb{N}}$ the corresponding sequence of *VAG-FE* gradient discretisations. It can be verified that [18], Lemma 3.4 applies to our case, both, in the matrix domain, where face unknowns might occur, as well as in the fracture network, a domain of codimension 1. This means that we can state that there exist constants $C_m(\theta_{\mathcal{T}}), C_f(\theta_{\mathcal{T}}) > 0$, such that

$$\|\Pi^m_{\overline{\mathcal{D}}}u_{\mathcal{D}} - \Pi^m_{\mathcal{D}}u_{\mathcal{D}}\|_{L^2(\Omega)} \le C_m h_{\mathcal{T}}\|\nabla^m_{\mathcal{D}}u_{\mathcal{D}}\|_{L^2(\Omega)^d} \quad \text{and} \tag{1.15}$$

$$\|\Pi^f_{\overline{\mathcal{D}}}u_{\mathcal{D}} - \Pi^f_{\mathcal{D}}u_{\mathcal{D}}\|_{L^2(\Gamma)} \le C_f h_\Delta\|\nabla^f_{\mathcal{D}}u_{\mathcal{D}}\|_{L^2(\Gamma)^{d-1}}. \tag{1.16}$$

Coercivity: It is easy to check that

$$\|[\![u_{\mathcal{D}}]\!]^{\mathfrak{a}}_{\overline{\mathcal{D}}}\|_{L^2(\Gamma_{\mathfrak{a}})} \le \sqrt{3}\|[\![u_{\mathcal{D}}]\!]^{\mathfrak{a}}_{\mathcal{D}}\|_{L^2(\Gamma_{\mathfrak{a}})},$$

and therefore $\|u_{\mathcal{D}}\|_{\overline{\mathcal{D}}} \leq C\|u_{\mathcal{D}}\|_{\mathcal{D}}$, for a $C > 0$. Coercivity for $(\overline{\mathcal{D}}^l)_{l\in\mathbb{N}}$ can then be deduced from coercivity for $(\mathcal{D}^l)_{l\in\mathbb{N}}$ via the inequality

$$\begin{aligned}\|\Pi^m_{\mathcal{D}} u_{\mathcal{D}}\|_{L^2(\Omega)} + \|\Pi^f_{\mathcal{D}} u_{\mathcal{D}}\|_{L^2(\Gamma)} \leq \|\Pi^m_{\overline{\mathcal{D}}} u_{\mathcal{D}}\|_{L^2(\Omega)} + \|\Pi^f_{\overline{\mathcal{D}}} u_{\mathcal{D}}\|_{L^2(\Gamma)} \\ + (\|\nabla^m_{\mathcal{D}} u_{\mathcal{D}}\|_{L^2(\Omega)^d} + \|\nabla^f_{\mathcal{D}} u_{\mathcal{D}}\|_{L^2(\Gamma)^{d-1}}) \cdot \mathcal{O}(h_{\mathcal{T}}),\end{aligned}$$

where we have used (1.15) and (1.16).

Consistency: Classically, for all $\varphi = (\varphi_m, \varphi_f) \in C^\infty_\Omega \times C^\infty_\Gamma$, we have the estimate

$$\begin{aligned}&\|\Pi^m_{\mathcal{D}} P_{\mathcal{D}}\varphi - \varphi_m\|_{L^2(\Omega)} + \|\Pi^f_{\mathcal{D}} P_{\mathcal{D}}\varphi - \varphi_f\|_{L^2(\Gamma)} \\ &+ \sum_{\mathfrak{a}\in\chi} \|[\![P_{\mathcal{D}}\varphi]\!]^{\mathfrak{a}}_{\mathcal{D}} - [\![(\varphi_m, \varphi_f)]\!]_{\mathfrak{a}}\|_{L^2(\Gamma_{\mathfrak{a}})} \leq cst(\varphi_m, \varphi_f) \cdot h_{\mathcal{T}},\end{aligned}$$

while (1.14) grants that holds

$$\|\nabla^m_{\mathcal{D}} P_{\mathcal{D}}\varphi - \nabla\varphi\|_{L^2(\Omega)} + \|\nabla^f_{\mathcal{D}} P_{\mathcal{D}}\varphi - \nabla\varphi\|_{L^2(\Gamma)} \leq cst(\varphi_m, \varphi_f, \theta_{\mathcal{T}}) h_{\mathcal{T}}.$$

Taking into account that $C^\infty_\Omega \times C^\infty_\Gamma$ is dense in V, we see that the treated discretisation is consistent with $\mathcal{S}_{\mathcal{D}}(\varphi_m, \varphi_f) = \mathcal{O}(h_{\mathcal{T}})$ for $(\varphi_m, \varphi_f) \in C^\infty_\Omega \times C^\infty_\Gamma$.

Limit Conformity: For all $T \in \Delta$ and for all $u_{\mathcal{D}} \in X_{\mathcal{D}}$ we have

$$\int_T ([\![u_{\mathcal{D}}]\!]^{\mathfrak{a}}_{\overline{\mathcal{D}}} - [\![u_{\mathcal{D}}]\!]^{\mathfrak{a}}_{\mathcal{D}}) \mathrm{d}\tau(\mathbf{x}) = 0.$$

Introducing the linear operator $P : L^2(\Gamma_{\mathfrak{a}}) \to L^2(\Gamma_{\mathfrak{a}})$ such that $P(\varphi) = \frac{1}{|T|}\int_T \varphi \mathrm{d}\tau(\mathbf{x})$ on T for all $T \in \Delta$, we first calculate for any $\mathbf{q}_m \in \mathbf{C}^\infty_\Omega$

$$\|\gamma_{\mathbf{n}_{\mathfrak{a}}}\mathbf{q}_m - P(\gamma_{\mathbf{n}_{\mathfrak{a}}}\mathbf{q}_m)\|^2_{L^2(\Gamma_{\mathfrak{a}})} = \sum_{\sigma\in\mathcal{F}_{\mathfrak{a}}} \sum_{\substack{T\in\Delta \\ \text{s.t. } T\subset\sigma}} \|\gamma_{\mathbf{n}_{\mathfrak{a}}}\mathbf{q}_m - P(\gamma_{\mathbf{n}_{\mathfrak{a}}}\mathbf{q}_m)\|^2_{L^2(T)} \leq C(\mathbf{q}_m, \theta_{\mathcal{T}}) \cdot h^2_{\mathcal{T}}.$$

For the discrete part, we are able to derive (taking into account [18], Lemma 3.4)

$$\|[\![u_{\mathcal{D}}]\!]^{\mathfrak{a}}_{\overline{\mathcal{D}}} - [\![u_{\mathcal{D}}]\!]^{\mathfrak{a}}_{\mathcal{D}}\|^2_{L^2(\Gamma_{\mathfrak{a}})} \leq C h_\Delta \Big(\|\nabla^m_{\mathcal{D}} u_{\mathcal{D}}\|^2_{L^2(\Omega)^d} + \|\nabla^f_{\mathcal{D}} u_{\mathcal{D}}\|^2_{L^2(\Gamma)^{d-1}} \Big).$$

with a constant C depending only on $\theta_{\mathcal{T}}$. We can thus proceed

$$\begin{aligned}|\int_{\Gamma_{\mathfrak{a}}} \gamma_{\mathbf{n}_{\mathfrak{a}}}\mathbf{q}_m([\![u_{\mathcal{D}}]\!]^{\mathfrak{a}}_{\overline{\mathcal{D}}} - [\![u_{\mathcal{D}}]\!]^{\mathfrak{a}}_{\mathcal{D}})\mathrm{d}\tau(\mathbf{x})| &= |\int_{\Gamma_{\mathfrak{a}}} (\gamma_{\mathbf{n}_{\mathfrak{a}}}\mathbf{q}_m - P(\gamma_{\mathbf{n}_{\mathfrak{a}}}\mathbf{q}_m))([\![u_{\mathcal{D}}]\!]^{\mathfrak{a}}_{\overline{\mathcal{D}}} - [\![u_{\mathcal{D}}]\!]^{\mathfrak{a}}_{\mathcal{D}})\mathrm{d}\tau(\mathbf{x})| \\ &\leq \|\gamma_{\mathbf{n}_{\mathfrak{a}}}\mathbf{q}_m - P(\gamma_{\mathbf{n}_{\mathfrak{a}}}\mathbf{q}_m)\|_{L^2(\Gamma_{\mathfrak{a}})} \|[\![u_{\mathcal{D}}]\!]^{\mathfrak{a}}_{\overline{\mathcal{D}}} - [\![u_{\mathcal{D}}]\!]^{\mathfrak{a}}_{\mathcal{D}}\|_{L^2(\Gamma_{\mathfrak{a}})} \\ &\leq C(\mathbf{q}_m, \theta_{\mathcal{T}}) h^{\frac{3}{2}}_{\mathcal{T}} \Big(\|\nabla^m_{\mathcal{D}} u_{\mathcal{D}}\|^2_{L^2(\Omega)^d} + \|\nabla^f_{\mathcal{D}} u_{\mathcal{D}}\|^2_{L^2(\Gamma)^{d-1}} \Big)^{\frac{1}{2}}.\end{aligned}$$

for all $\mathbf{q}_m \in \mathbf{C}^\infty_\Omega$. Taking into account (1.14), (1.16) and the conformity of $\overline{\mathcal{D}}$, we can now conclude by calculating for all $\mathbf{q} = (\mathbf{q}_m, \mathbf{q}_f) \in \mathbf{C}^\infty_\Omega \times \mathbf{C}^\infty_\Gamma$

$$
\begin{aligned}
|w_{\overline{\mathcal{D}}}(u_\mathcal{D}, \mathbf{q})| &= |(w_{\overline{\mathcal{D}}} - w_\mathcal{D})(u_\mathcal{D}, \mathbf{q})| \\
&= \Big| \int_\Omega \mathrm{div}\mathbf{q}_m(\Pi^m_\mathcal{D} - \Pi^m_{\overline{\mathcal{D}}})u_\mathcal{D} \mathrm{d}\mathbf{x} + \int_\Gamma \mathrm{div}_\tau \mathbf{q}_f(\Pi^f_\mathcal{D} - \Pi^f_{\overline{\mathcal{D}}})u_\mathcal{D} \mathrm{d}\tau(\mathbf{x}) \\
&\quad + \sum_{\mathfrak{a}\in\chi} \int_{\Gamma_\mathfrak{a}} \gamma_{\mathbf{n}_\mathfrak{a}} \mathbf{q}_m \Big((\llbracket u_\mathcal{D} \rrbracket^\mathfrak{a}_{\overline{\mathcal{D}}} - \llbracket u_\mathcal{D} \rrbracket^\mathfrak{a}_\mathcal{D}) + (\Pi^f_{\overline{\mathcal{D}}} - \Pi^f_\mathcal{D})u_\mathcal{D} \Big) \mathrm{d}\tau(\mathbf{x}) \Big| \\
&\quad \le \|\Pi^m_{\overline{\mathcal{D}}} u_\mathcal{D} - \Pi^m_\mathcal{D} u_\mathcal{D}\|_{L^2(\Omega)} \cdot \|\mathrm{div}\mathbf{q}_m\|_{L^2(\Omega)} + \|\Pi^f_{\overline{\mathcal{D}}} u_\mathcal{D} - \Pi^f_\mathcal{D} u_\mathcal{D}\|_{L^2(\Gamma)} \cdot \|\mathrm{div}_\tau \mathbf{q}_f\|_{L^2(\Gamma)} \\
&\quad + \sum_{\mathfrak{a}\in\chi} \Big(\|\Pi^f_{\overline{\mathcal{D}}} u_\mathcal{D} - \Pi^f_\mathcal{D} u_\mathcal{D}\|_{L^2(\Gamma_\mathfrak{a})} \|\gamma_{\mathbf{n}_\mathfrak{a}} \mathbf{q}_m\|_{L^2(\Gamma_\mathfrak{a})} + \Big| \int_{\Gamma_\mathfrak{a}} \gamma_{\mathbf{n}_\mathfrak{a}} \mathbf{q}_m (\llbracket u_\mathcal{D} \rrbracket^\mathfrak{a}_{\overline{\mathcal{D}}} - \llbracket u_\mathcal{D} \rrbracket^\mathfrak{a}_\mathcal{D}) \Big| \Big) \\
&\quad \le C(\theta_\mathcal{T}, \mathbf{q}) \cdot h_\mathcal{T} \cdot \|u_\mathcal{D}\|_\mathcal{D}.
\end{aligned}
$$

Taking into account the density of $\mathbf{C}^\infty_\Omega \times \mathbf{C}^\infty_\Gamma$ in W, the proof is complete. □

Remark 1.4.2 *The proofs of Propositions 1.4.1 and 1.4.2 show that for solutions $(u_m, u_f) \in V^0$ and $(\mathbf{q}_m, \mathbf{q}_f) \in W$ of (1.5) such that $u_m \in C^2(\overline{K})$, $u_f \in C^2(\overline{\sigma})$, $\mathbf{q}_m \in (C^1(\overline{K}))^d$, $\mathbf{q}_f \in (C^1(\overline{\sigma}))^{d-1}$ for all $K \in \mathcal{M}$ and all $\sigma \in \Gamma_f$, the VAG schemes are consistent and limit conforming of order 1, and therefore convergent of order 1.*

1.4.2 Hybrid Finite Volume Discretization

In this subsection, the HFV scheme introduced in [37] is extended to the hybrid dimensional Darcy flow model. We assume here that the faces are planar and that $\mathbf{x}_\sigma$ is the barycenter of σ for all $\sigma \in \mathcal{F}$.

The set of degrees of freedom $dof_{\mathcal{D}_m} \times dof_{\mathcal{D}_f}$ (cf. Figure 1.4) is defined by

$$
\begin{aligned}
dof_{\mathcal{D}_m} &= \mathcal{M} \cup \Big(\bigcup_{\sigma\in\mathcal{F}} \overline{\mathcal{M}}_\sigma \Big) \\
dof_{\mathcal{D}_f} &= \mathcal{F}_\Gamma \cup \mathcal{E}_\Gamma, \\
dof_{Dir_m} &= \mathcal{F}_{ext}, \\
dof_{Dir_f} &= \mathcal{E}_\Gamma \cap \mathcal{E}_{ext},
\end{aligned}
$$

where for $\sigma \in \mathcal{F}$ and $K \in \mathcal{M}_\sigma$

$$
\overline{K}_\sigma = \begin{cases} \sigma & \text{if } \sigma \in \mathcal{F} \setminus \mathcal{F}_\Gamma \\ K_\sigma & \text{if } \sigma \in \mathcal{F}_\Gamma \end{cases}
$$

and $\overline{\mathcal{M}}_\sigma = \{\overline{K}_\sigma \mid K \in \mathcal{M}_\sigma\}$. We thus have

$$
\begin{aligned}
X_\mathcal{D} &= \Big\{ u_K \mid K \in \mathcal{M} \Big\} \cup \Big\{ u_{\overline{K}_\sigma} \mid \sigma \in \mathcal{F}, \overline{K}_\sigma \in \overline{\mathcal{M}}_\sigma \Big\}, \\
X_\mathcal{D} &= \Big\{ u_\sigma \mid \sigma \in \mathcal{F}_\Gamma \Big\} \cup \Big\{ u_e \mid e \in \mathcal{E}_\Gamma \Big\}.
\end{aligned}
\tag{1.17}
$$

The discrete gradients in the matrix (respectively in the fracture domain) are piecewise constant in each 3D (respectively 2D) half diamond as shown at Figure 1.4. Following [37] we first define a cellwise constant discrete gradient

$$\nabla_K u_{\mathcal{D}} = \frac{1}{|K|} \sum_{\sigma \in \mathcal{F}_K} |\sigma| (u_{\overline{K}_\sigma} - u_K) \mathbf{n}_{K,\sigma},$$

which is exact on affine functions, but does not lead to a definite bilinear form (see [37], p. 8) and therefore has to be stabilized. Let

$$\nabla_{K,\sigma} u_{\mathcal{D}} = \nabla_K u_{\mathcal{D}} + R_{K,\sigma}(u_{\mathcal{D}}) \mathbf{n}_{K,\sigma},\ \sigma \in \mathcal{F}_K,$$

where $\mathbf{n}_{K,\sigma}$ is the unit normal vector of the face $\sigma \in \mathcal{F}_K$ outward to the cell K and

$$R_{K,\sigma}(u_{\mathcal{D}}) = \frac{\sqrt{d}}{d_{K,\sigma}} \Big(u_{\overline{K}_\sigma} - u_K - \nabla_K u_{\mathcal{D}} \cdot (\mathbf{x}_\sigma - \mathbf{x}_K) \Big),$$

with $d_{K,\sigma} = \mathbf{n}_{K,\sigma} \cdot (\mathbf{x}_\sigma - \mathbf{x}_K)$. This leads to the definition of the matrix discrete gradient

$$\nabla^m_{\mathcal{D}} u_{\mathcal{D}}(\mathbf{x}) = \nabla_{K,\sigma} u_{\mathcal{D}} \text{ on } D_{K,\sigma} \text{ for all } K \in \mathcal{M}, \sigma \in \mathcal{F}_K, \tag{1.18}$$

where $D_{K,\sigma} = \bigcup_{e \in \mathcal{E}_\sigma} D_{K,\sigma,e}$ is the cone joining the face σ to the cell center $\mathbf{x}_K$.

The fracture discrete gradient is defined analogously by

$$\nabla^f_{\mathcal{D}} u_{\mathcal{D}}(\mathbf{x}) = \nabla_{\sigma,e} u_{\mathcal{D}} \text{ on } T_{\sigma,e} \text{ for all } \sigma \in \mathcal{F}_\Gamma, e \in \mathcal{E}_\sigma, \tag{1.19}$$

with

$$\nabla_{\sigma,e} u_{\mathcal{D}} = \nabla_\sigma u_{\mathcal{D}} + R_{\sigma,e}(u_{\mathcal{D}}) \mathbf{n}_{\sigma,e},$$

and

$$\nabla_\sigma u_{\mathcal{D}} = \frac{1}{|\sigma|} \sum_{e \in \mathcal{E}_\sigma} |e| (u_e - u_\sigma) \mathbf{n}_{\sigma,e}, \qquad R_{\sigma,e}(u_{\mathcal{D}}) = \frac{\sqrt{d-1}}{d_{\sigma,e}} \Big(u_e - u_\sigma - \nabla_\sigma u \cdot (\mathbf{x}_e - \mathbf{x}_\sigma) \Big),$$

where $\mathbf{n}_{\sigma,e}$ is the unit normal vector to the edge e in the tangent plane of the face σ and outward to the face σ, $d_{\sigma,e} = \mathbf{n}_{\sigma,e} \cdot (\mathbf{x}_e - \mathbf{x}_\sigma)$, and $T_{\sigma,e}$ is the triangle of base e and vertex $\mathbf{x}_\sigma$.

The function reconstruction operators are piecewise constant on a partition of the cells and of the fracture faces. For $K \in \mathcal{M}$ let $dof_K = \{\overline{K}_\sigma, \sigma \in \mathcal{F}_K\}$. Analogously, in the fracture domain, for $\sigma \in \mathcal{F}_\Gamma$ let $dof_\sigma = \mathcal{E}_\sigma$. We introduce, for any given $K \in \mathcal{M}$, a partition $\{\omega^\nu_K\}_{\nu \in \{K\} \cup dof_K \setminus dof_{Dir}}$ of K. Similarly, we define for any given $\sigma \in \mathcal{F}_\Gamma$ a partition $\{\omega^\nu_\sigma\}_{\nu \in \{\sigma\} \cup dof_\sigma \setminus dof_{Dir}}$ of σ. For each $\nu \in dof_{\mathcal{D}_m}$, we define the open set $\omega_\nu = \text{int}\Big(\bigcup_{K \in \mathcal{M}} \overline{\omega}^\nu_K\Big)$, with the convention $\omega^\nu_K = \emptyset$, if $\nu \notin dof_K$. For each $\nu \in dof_{\mathcal{D}_f}$, we define the open set $\omega_\nu = \text{int}\Big(\bigcup_{\sigma \in \mathcal{F}} \overline{\omega}^\nu_\sigma\Big)$, where $\omega^\nu_\sigma = \emptyset$, if $\nu \notin dof_\sigma$. We thus obtain the partitions $\{\omega_\nu\}_{\nu \in dof_{\mathcal{D}_m} \setminus dof_{Dir_m}}$ of Ω and $\{\omega_\nu\}_{\nu \in dof_{\mathcal{D}_f} \setminus dof_{Dir_f}}$ of Γ. Like the VAG-CV

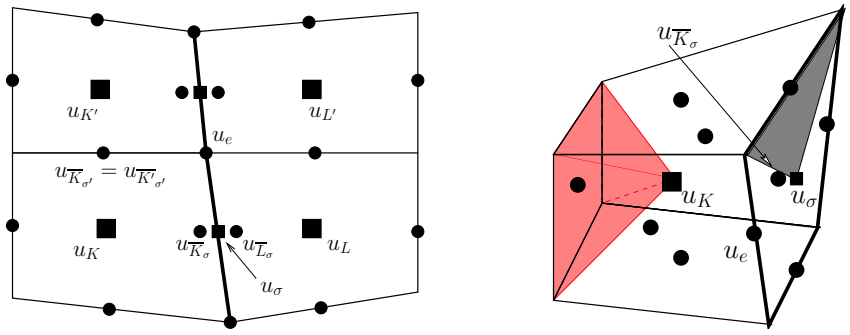

Figure 1.4: Left: Illustration of d.o.f. in 2D for four cells intersected by a vertical fracture (thick line).
Right: 3D cell K touching a fracture face σ. Illustration of the polyhedron and polygone on which $\nabla_{\mathcal{D}}^m$ is constant (red) and $\nabla_{\mathcal{D}}^f$ is constant (grey).

discretization, the HFV discretization is particularly adapted for the treatment of multiphase flow processes through heterogeneous media (cf. [39]). Provided the mesh is comform w.r.t. the heterogeneous layers, we can assume that key geological quantities are constant per cell and per fracture face. Therefore, in the numerical scheme, we do not need to reconstruct the just introduced partitions explicitly, but only have to define their corresponding volumes. Finally, we need a mapping between the degrees of freedom of the matrix domain, which are situated on one side of the fracture network, and the set of indices χ. For $\sigma \in \mathcal{F}_\Gamma$ and $\overline{K}_\sigma \in \overline{\mathcal{M}}_\sigma$ holds by definition $\overline{K}_\sigma = \{K\}$ for a $K \in \mathcal{M}_\sigma$ and hence $\mathbf{n}_{\overline{K}_\sigma} = \mathbf{n}_{K,\sigma}$ is well defined. We obtain the one-element set $\chi(\overline{K}_\sigma) = \{\mathfrak{a} \in \chi \mid \mathbf{n}_{\overline{K}_\sigma} = \mathbf{n}_{\mathfrak{a}} \text{ on } \sigma\}$ and therefore the notation $\mathfrak{a}(\overline{K}_\sigma) = \mathfrak{a} \in \chi(\overline{K}_\sigma)$.

We define the HFV scheme's reconstruction operators by

$$\begin{aligned}
&\bullet\ \Pi_{\mathcal{D}}^m u_{\mathcal{D}} = \sum_{\nu \in dof_{\mathcal{D}_m} \setminus dof_{Dir_m}} u_\nu \mathbb{1}_{\omega_\nu},\\
&\bullet\ \Pi_{\mathcal{D}}^f u_{\mathcal{D}} = \sum_{\nu \in dof_{\mathcal{D}_f} \setminus dof_{Dir_f}} u_\nu \mathbb{1}_{\omega_\nu},\\
&\bullet\ [\![u_{\mathcal{D}}]\!]_{\mathcal{D}}^{\mathfrak{a}} = \sum_{\sigma \in \mathcal{F}_\Gamma} \sum_{\overline{K}_\sigma \in \overline{\mathcal{M}}_\sigma} (u_{\overline{K}_\sigma} - u_\sigma)\delta_{\mathfrak{a}(\overline{K}_\sigma)\mathfrak{a}} \mathbb{1}_\sigma \quad \text{for all } \mathfrak{a} \in \chi.
\end{aligned} \tag{1.20}$$

Proposition 1.4.3 *Let us consider a sequence of meshes $(\mathcal{M}^l)_{l\in\mathbb{N}}$ and let us assume that the sequence $(\mathcal{T}^l)_{l\in\mathbb{N}}$ of tetrahedral submeshes is shape regular, i.e. $\theta_{\mathcal{T}^l}$ is uniformly bounded. We also assume that $\lim_{l\to\infty} h_{\mathcal{T}^l} = 0$. Then, any corresponding sequence of gradient discretizations $(\mathcal{D}^l)_{l\in\mathbb{N}}$, defined by (1.17), (1.18), (1.19) and definition (1.20), is coercive, consistent and limit conforming.*

Proof Let us first give the proof of the proposition in the special case $\omega_{\overline{K}_\sigma} = \omega_e = \emptyset$ for all $\overline{K}_\sigma \in \bigcup_{\sigma\in\mathcal{F}} \overline{\mathcal{M}}_\sigma$ and $e \in \mathcal{E}_\Gamma$. We denoting in that case by $\Pi_{\mathcal{M}}$ and $\Pi_{\mathcal{F}}$ the HFV matrix

and fracture function reconstruction operators.

Coercivity: We first prove that limit conformity against regular test functions, as proved below, implies coercivity.

Assume that the sequence of discretizations $(\mathcal{D}^l)_{l\in\mathbb{N}}$ is not coercive. Then we can find a sequence $(u_{\mathcal{D}^l})_{l\in\mathbb{N}}$ with $u_{\mathcal{D}^l} \in X^0_{\mathcal{D}^l}$, such that

$$\|\Pi^m_{\mathcal{D}_l} u_{\mathcal{D}^l}\|_{L^2(\Omega)} + \|\Pi^f_{\mathcal{D}_l} u_{\mathcal{D}^l}\|_{L^2(\Gamma)} = 1 \qquad \text{and} \qquad \|u_{\mathcal{D}^l}\|_{\mathcal{D}^l} < \frac{1}{l}.$$

Then, it follows from a compactness result of [29] that there exists a $u = (u_m, u_f) \in L^2(\Omega) \times L^2(\Gamma)$, s.t. up to a subsequence

$$(\Pi^m_{\mathcal{D}_l} u_{\mathcal{D}^l}, \Pi^f_{\mathcal{D}_l} u_{\mathcal{D}^l}) \longrightarrow (u_m, u_f) \qquad \text{in } L^2(\Omega) \times L^2(\Gamma) \qquad (\text{ for } l \to \infty)$$

and therefore $\|u_m\|_{L^2(\Omega)} + \|u_f\|_{L^2(\Gamma)} = 1$. On the other hand it follows from the discretization's limit conformity against regular test functions stated in Corollary 1.3.1 that $(u_m, u_f) \in V^0$ and that up to a subsequence

$$\begin{cases} \nabla^m_{\mathcal{D}} u_{\mathcal{D}^l} \rightharpoonup \nabla u_m & \text{in } L^2(\Omega)^d, \\ \nabla^f_{\mathcal{D}} u_{\mathcal{D}^l} \rightharpoonup \nabla_\tau u_f & \text{in } L^2(\Gamma)^{d-1}, \\ [\![u_{\mathcal{D}}]\!]^{\mathfrak{a}}_{\mathcal{D}} \rightharpoonup [\![v]\!]_{\mathfrak{a}} & \text{in } L^2(\Gamma_{\mathfrak{a}}), \text{ for } \mathfrak{a} \in \chi. \end{cases}$$

Since by construction $\|u_{\mathcal{D}^l}\|_{\mathcal{D}^l} \to 0$ holds, we obtain $\|(u_m, u_f)\|_{V^0} = 0$. But $\|\cdot\|_{V^0}$ is a norm on V^0, which contradicts the fact that $\|u_m\|_{L^2(\Omega)} + \|u_f\|_{L^2(\Gamma)} = 1$.

Consistency: Recall the definition (1.13) of the projection $P_{\mathcal{D}} \colon C^\infty_\Omega \times C^\infty_\Gamma \to X^0_{\mathcal{D}}$. It is easily seen that for $u_{\mathcal{D}} = P_{\mathcal{D}}(\varphi_m, \varphi_f)$ holds

$$\begin{aligned} &\|\Pi_{\mathcal{M}} u_{\mathcal{D}} - \varphi_m\|_{L^2(\Omega)} + \|\Pi_{\mathcal{F}} u_{\mathcal{D}} - \varphi_f\|_{L^2(\Gamma)} \\ &+ \sum_{\mathfrak{a}\in\chi} \|[\![u_{\mathcal{D}}]\!]^{\mathfrak{a}}_{\mathcal{D}} - [\![u]\!]_{\mathfrak{a}}\|_{L^2(\Gamma_{\mathfrak{a}})} \le cst \cdot h_{\mathcal{T}} \cdot (|\Gamma|^{\frac{1}{2}} + |\Omega|^{\frac{1}{2}}), \end{aligned}$$

with a constant depending only on φ. Furthermore, it follows from Lemma 4.3 of [37] that there exists $C > 0$ depending only on $\theta_{\mathcal{T}}$ and φ such that

$$\|\nabla^m_{\mathcal{D}} u_{\mathcal{D}} - \nabla\varphi\|_{L^2(\Omega)} + \|\nabla^f_{\mathcal{D}} u_{\mathcal{D}} - \nabla\varphi\|_{L^2(\Gamma)} \le C h_{\mathcal{T}}$$

Taking into account that $C^\infty_\Omega \times C^\infty_\Gamma$ is dense in V^0, we see that the treated discretisation is consistent.

Limit Conformity: In [15], proof of Proposition 10, the limit conformity of HFV scheme is shown in the case of continuous pressure at the matrix-fracture interfaces. This proof adapts straightforward to our case, so that we obtain

$$w_{\mathcal{D}}(u_{\mathcal{D}}, \mathbf{q}) \le C \cdot h_{\mathcal{T}} \cdot \|u_{\mathcal{D}}\|_{\mathcal{D}} \qquad \text{for all } \mathbf{q} \in \mathbf{C}^\infty_\Omega \times \mathbf{C}^\infty_\Gamma.$$

This result is shown above to imply coercivity. From the coercivity and the density of $\mathbf{C}^\infty_\Omega \times \mathbf{C}^\infty_\Gamma$ in W, we derive limit conformity on the whole space of test functions.

Generalization to arbitrary HFV discretizations: Let us notice, that from [37] Lemma 4.1 follows that there are positive constants C_m and C_f only depending on $\theta_\mathcal{T}$, such that for all $u_\mathcal{D} \in X_\mathcal{D}$ holds

$$\|\Pi_\mathcal{M} u_\mathcal{D} - \Pi^m_\mathcal{D} u_\mathcal{D}\|^2_{L^2(\Omega)} = \sum_{K\in\mathcal{M}} \sum_{\sigma\in\mathcal{F}_K} |\omega_K^{\overline{K}_\sigma}|(u_K - u_{\overline{K}_\sigma})^2 \leq C_m \cdot h^2_\mathcal{T} \cdot \|\nabla^m_\mathcal{D} u_\mathcal{D}\|^2_{L^2(\Omega)^d}$$
$$\|\Pi_\mathcal{F} u_\mathcal{D} - \Pi^f_\mathcal{D} u_\mathcal{D}\|^2_{L^2(\Gamma)} = \sum_{\sigma\in\mathcal{F}_\Gamma} \sum_{e\in\mathcal{E}_\sigma} |\omega^e_\sigma|(u_\sigma - u_e)^2 \leq C_f \cdot h^2_\Delta \cdot \|\nabla^f_\mathcal{D} u_\mathcal{D}\|^2_{L^2(\Gamma)^{d-1}}.$$

It follows that coercivity, consistency and limit conformity can immediately be shown. □

Remark 1.4.3 *The precedent proof shows that for solutions $(u_m, u_f) \in V^0$ and $(\mathbf{q}_m, \mathbf{q}_f) \in W$ of (1.5) such that $u_m \in C^2(\overline{K})$, $u_f \in C^2(\overline{\sigma})$, $\mathbf{q}_m \in (C^1(\overline{K}))^d$, $\mathbf{q}_f \in (C^1(\overline{\sigma}))^{d-1}$ for all $K \in \mathcal{M}$ and all $\sigma \in \Gamma_f$, the HFV schemes are consistent and limit conforming of order 1, and therefore convergent of order 1.*

1.5 Numerical Results

The objective of this section is to compare the VAG-FE, VAG-CV, and the HFV schemes in terms of accuracy and CPU efficiency for both hexahedral and tetrahedral meshes on heterogeneous isotropic and anisotropic media. For that purpose an original family of analytical solutions is built for the fixed value of the parameter $\xi = 1$. We refer to [56], [6], [3] for a comparison of the solutions obtained with different values of the parameter $\xi \in [\frac{1}{2}, 1]$ with the solution obtained with a 3D representation of the fractures.

Table 1.1 exhibits for the hexahedral and tetrahedral meshes, as well as for both the VAG and HFV schemes, the number of degrees of freedom (Nb dof), the number of d.o.f. after elimination of the cell and Dirichlet unknowns (nb dof el.), and the number of nonzero element in the linear system after elimination without any fill-in of the cell unknowns (Nb Jac).

The hexahedral meshes used here are divided into two families. The first family consists of Cartesian meshes and hence satisfies the well known ortogonality property. The second family of meshes is obtained from the previous one by a perturbation of its nodes. The perturbation is chosen randomly inside the ball around each node of radius one third the distance to it's closest neighbour, of course in respect of the domain's boundaries. The perturbation of a fracture node is done in the fracture plane. Note that this leads to hexahedral cells with non planar faces and therefore the HFV scheme is no longer consistent on this family of meshes.

In all test cases, the linear system obtained after elimination of the cell unknowns is solved using GMRes iterative solver with the stopping criteria 10^{-10}. The GMRes solver

is preconditioned by ILUT [63], [64] using the thresholding parameter 10^{-4} chosen small enough in such a way that all the linear systems can be solved for both schemes and for all meshes. In tables 1.2 and 1.3, we report the number of GMRes iterations $Iter$ and the CPU time taking into account the elimination of the cell unknowns, the ILUT factorization, the GMRes iterations, and the computation of the cell values. Regarding the choice of the preconditioner, we also mention that the resolution of the anisotropic problem with an AMG preconditioner revealed less efficiency compared to ILUT on tetrahedral meshes (particularly for the HFV scheme).

We ran the program on a 2,6 GHz Intel Core i5 processor with 8 GB 1600 MHz DDR3 memory.

1.5.1 A class of analytical solutions

We consider a 3-dimensional domain $\Omega = (-0.5, 0.5)^3$ with four intersecting fractures $\Gamma_{12} = \{(x,y,z) \in \Omega \mid x = 0, y > 0\}$, $\Gamma_{23} = \{(x,y,z) \in \Omega \mid y = 0, x > 0\}$, $\Gamma_{34} = \{(x,y,z) \in \Omega \mid x = 0, y < 0\}$ and $\Gamma_{14} = \{(x,y,z) \in \Omega \mid y = 0, x < 0\}$. We also introduce four disjoint subsets of Ω, $\Omega_1 = \{(x,y,z) \in \Omega \mid y > 0, x < 0\}$, $\Omega_2 = \{(x,y,z) \in \Omega \mid y > 0, x > 0\}$, $\Omega_3 = \{(x,y,z) \in \Omega \mid y < 0, x > 0\}$ and $\Omega_4 = \{(x,y,z) \in \Omega \mid y < 0, x < 0\}$.

Derivation: For $(u_m, u_f) \in V$, we denote $u_m(x,y,z) = u_i(x,y,z)$ on Ω_i, $i = 1, \ldots, 4$ and $u_f(x,y,z) = u_{ij}(y,z)$ on Γ_{ij}, $ij \in J$, where we have introduced $J = \{12, 23, 34, 14\}$. We assume that a solution of the discontinuous pressure model writes in the fracture network as $u_{ij}(y,z) = \alpha_f(z) + \beta_{ij}(z)\gamma_{ij}(y)$, $ij \in J$ and in the matrix domain as

$$\begin{cases} u_1(x,y,z) = \alpha_1(z)u_{12}(y,z)u_{14}(x,z) \\ u_2(x,y,z) = \alpha_2(z)u_{12}(y,z)u_{23}(x,z) \\ u_3(x,y,z) = \alpha_3(z)u_{34}(y,z)u_{23}(x,z) \\ u_4(x,y,z) = \alpha_4(z)u_{34}(y,z)u_{14}(x,z). \end{cases}$$

We assume $\gamma_{ij}(0) = 0, ij \in J$ so that the continuity of u_f at the fracture-fracture intersection is satisfied and we set $\gamma'_{ij}(0) = 1$, to ease the following calculations. For $i = 1, \ldots, 4$ let $K_i = \Lambda_m|_{\Omega_i}$ and for $ij \in J$ let $T_{ij} = T_f|_{\Gamma_{ij}}$. From the conditions $\gamma_{\mathbf{n}_\mathfrak{a}}\mathbf{q}_m = T_f[\![u]\!]_\mathfrak{a}$ on $\Gamma_\mathfrak{a}$, $\mathfrak{a} \in \chi$, we then get, after some effort in computation,

$$\begin{aligned}
\alpha_1(z) &= \Big(\alpha_f(z) - \frac{K_{1y}}{T_{14}}\beta_{12}(z)\Big)^{-1}, & \beta_{14}(z) &= -\frac{K_{1y}T_{12}}{K_{1x}T_{14}}\beta_{12}(z), \\
\alpha_2(z) &= \Big(\alpha_f(z) - \frac{K_{1y}K_{2x}K_{3y}K_{4x}}{K_{1x}K_{3x}K_{4y}T_{23}}\beta_{12}(z)\Big)^{-1}, & \beta_{23}(z) &= \frac{K_{1y}K_{3y}K_{4x}T_{12}}{K_{1x}K_{3x}K_{4y}T_{23}}\beta_{12}(z), \\
\alpha_3(z) &= \Big(\alpha_f(z) - \frac{K_{1y}K_{3y}K_{4x}T_{12}}{K_{1x}K_{4y}T_{23}T_{34}}\beta_{12}(z)\Big)^{-1}, & \beta_{34}(z) &= -\frac{K_{1y}K_{4x}T_{12}}{K_{1x}K_{4y}T_{34}}\beta_{12}(z) \\
\alpha_4(z) &= \Big(\alpha_f(z) - \frac{K_{1y}K_{4x}T_{12}}{K_{1x}T_{14}T_{34}}\beta_{12}(z)\Big)^{-1}, & \frac{K_{1y}K_{2x}K_{3y}K_{4x}}{K_{1x}K_{2y}K_{3x}K_{4y}} &= 1.
\end{aligned} \tag{1.21}$$

Obviously, we have taken α_f and β_{12} as degrees of freedom, here. However, these functions must be chosen in such a way that $\frac{1}{\alpha_i(z)} \neq 0$ for $i = 1, \ldots, 4$.

Remark 1.5.1 *We would like to explicitly calculate the jump at the matrix-fracture interfaces for this class of solutions. At Γ_{ij} we have*

$$u_i(0, y, z) - u_j(0, y, z) = (\alpha_i(z) - \alpha_j(z)) \cdot \alpha_f(z) \cdot u_{ij}(y, z), \qquad \text{for } ij \in \{12, 34\}$$
$$u_i(x, 0, z) - u_j(x, 0, z) = (\alpha_i(z) - \alpha_j(z)) \cdot \alpha_f(z) \cdot u_{ij}(x, z), \qquad \text{for } ij \in \{23, 14\}.$$

From (1.21), we observe, that the pressure becomes continuous at the matrix-fracture interfaces, as the T_{ij} tend to ∞ uniformly.

Remark 1.5.2 *In order to obtain solutions with discontinuities at the matrix-fracture interfaces, we had to omit the constraint of flux conservation at fracture-fracture intersections. Numerically this is treated by adding an additional source term for the corresponding fracture unknowns.*

1.5.2 Test Case

We define a solution by setting $\alpha_f(z) = e^{sin(\pi z)}$, $\beta_{12}(z) = -1$, $\gamma_{12}(y) = cos(2\pi y) + y - 1$, $\gamma_{23}(x) = x$, $\gamma_{34}(y) = -e^{cos(\pi y)} + y + e$, $\gamma_{14}(x) = \frac{sin(\pi x)}{\pi}$. The parameters we used for the different test cases are

- Isotropic Heterogeneous Permeability:

$$\begin{aligned} &K_{1x} = K_{1y} = K_{1z} = 1,\ K_{2x} = K_{2y} = K_{2z} = 100,\\ &K_{3x} = K_{3y} = K_{3z} = 3,\ K_{4x} = K_{4y} = K_{4z} = 40,\\ &T_{12} = 1,\ T_{23} = 0.2,\ T_{34} = 100,\ T_{14} = 10,\\ &K_{12} = 1,\ K_{23} = 2,\ K_{34} = 3,\ K_{14} = 10. \end{aligned}$$

- Anisotropic Heterogeneous Permeability:

$$\begin{aligned} &K_{1x} = K_{1z} = 1,\ K_{1y} = 50,\ K_{2x} = K_{2z} = 2,\ K_{2y} = 100,\\ &K_{3y} = K_{3z} = 3,\ K_{3x} = 30,\ K_{4z} = 4,\ K_{4x} = K_{4y} = 40,\\ &T_{12} = T_{23} = T_{34} = T_{14} = 1,\\ &K_{12} = K_{23} = K_{34} = K_{14} = 1. \end{aligned}$$

In Figures 1.5 we represent the normalized L^2 norms of the errors, which are calculated as follows:

- normalized error of the solution: $err_{sol} = \frac{\|\Pi_{\mathcal{D}}^m u_{\mathcal{D}} - u_m\|_{L^2(\Omega)} + \|\Pi_{\mathcal{D}}^f u_{\mathcal{D}} - u_f\|_{L^2(\Gamma)}}{\|u_m\|_{L^2(\Omega)} + \|u_f\|_{L^2(\Gamma)}}$
- normalized error of the gradient: $err_{grad} = \frac{\|\nabla_{\mathcal{D}}^m u_{\mathcal{D}} - \nabla u_m\|_{L^2(\Omega)^d} + \|\nabla_{\mathcal{D}}^f u_{\mathcal{D}} - \nabla_\tau u_f\|_{L^2(\Gamma)^{d-1}}}{\|\nabla u_m\|_{L^2(\Omega)^d} + \|\nabla_\tau u_f\|_{L^2(\Gamma)^{d-1}}}$

In the following tables is additionally found the normalized error of the jump: $err_{jump} = \frac{\sum_{\mathfrak{a}\in\chi} \|[\![u_{\mathcal{D}}]\!]_{\mathcal{D}}^{\mathfrak{a}} - [\![u]\!]_{\mathfrak{a}}\|_{L^2(\Gamma_{\mathfrak{a}})}}{\sum_{\mathfrak{a}\in\chi} \|[\![u]\!]_{\mathfrak{a}}\|_{L^2(\Gamma_{\mathfrak{a}})}}$.

		VAG			***HFV***		
Key	**Nb Cells**	**Nb dof**	**Nb dof el.**	**Nb Jac**	**Nb dof**	**Nb dof el.**	**Nb Jac**
Hexahedral Meshes							
1	512	1949	1437	31253	2776	2264	20696
2	4096	11701	7605	178845	19248	15152	150320
3	32768	79205	46437	1154861	142432	109664	1141856
4	262144	578245	316101	8152653	1093824	831680	8892608
5	2097152	4408709	2311557	60910733	8569216	6472064	70173056
Tetrahedral Meshes							
6	1337	2514	1177	18729	4943	3606	22642
7	10706	15765	5059	81741	35520	24814	164246
8	100782	131204	30422	492158	317367	216585	1474817
9	220106	279281	59175	956659	685718	465612	3190244
10	428538	533442	104904	1694008	1324614	896076	6167300
11	2027449	2452416	424967	6818299	6193783	4166334	28862986

Table 1.1: **Key** defines the mesh reference; **Nb Cells** is the number of cells of the mesh; **Nb dof** is the number of discrete unknowns; **Nb dof el.** is the number of discrete unknowns after elimination of cell unknowns; **Nb Jac** refers to the number of non-zero Jacobian entries after elimination of the cell unknowns and equations.

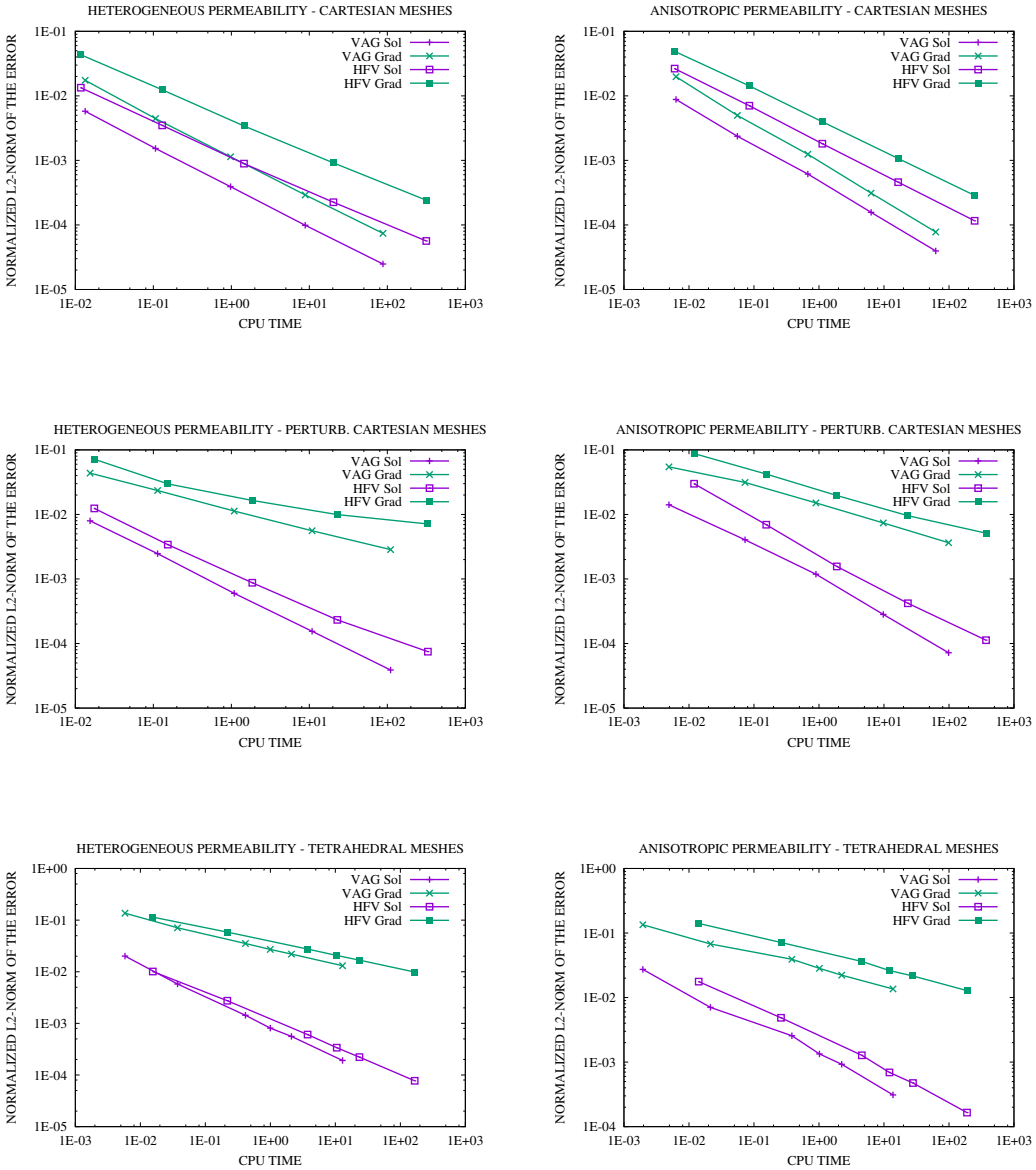

Figure 1.5: Comparison of VAG-FE and HFV on Cartesian (upper line), perturbated Cartesian (mid line) and tetrahedral (lower line) meshes. Left column: heterogeneous permeability. Right column: heterogeneous and anisotropic permeability.

	Heterogeneous Permeability: ***VAG***							
Key	**Iter**	**CPU**	err_{sol}	err_{grad}	err_{jump}	α_{sol}	α_{grad}	α_{jump}
Hexahedral Meshes (Cartesian)								
1	8	1.34E-2	5.78E-3	1.74E-2	8.99E-3	-	-	-
2	12	0.11	1.53E-3	4.44E-3	2.53E-3	1.92	1.97	1.83
3	22	0.98	3.92E-4	1.14E-3	6.72E-4	1.97	1.96	1.91
4	41	8.86	9.89E-5	2.91E-4	1.73E-4	1.99	1.97	1.96
5	79	87.91	2.48E-5	7.40E-5	4.40E-5	1.99	1.98	1.98
Hexahedral Meshes (perturbated Cartesian)								
1	8	1.54E-2	7.96E-3	4.36E-2	1.14E-2	-	-	-
2	12	0.11	2.46E-3	2.34E-2	3.62E-3	1.69	0.89	1.65
3	21	1.09	5.99E-4	1.12E-2	8.92E-4	2.04	1.05	2.02
4	41	10.84	1.55E-4	5.58E-3	2.32E-4	1.95	1.01	1.94
5	77	110.13	3.89E-5	2.85E-3	5.872E-5	1.99	0.96	1.98
Tetrahedral Meshes								
6	7	5.82E-3	2.01E-2	0.14	2.25E-2	-	-	-
7	10	3.73E-2	5.78E-3	7.09E-2	7.03E-3	1.80	0.94	1.68
8	20	0.41	1.44E-3	3.52E-2	1.81E-3	1.86	0.94	1.82
9	26	1.00	8.11E-4	2.71E-2	1.06E-3	2.20	1.01	2.06
10	32	2.11	5.60E-4	2.19E-2	7.36E-4	1.67	0.95	1.62
11	53	12.92	1.92E-4	1.31E-2	2.58E-4	2.07	1.00	2.03

	Heterogeneous Permeability: ***HFV***							
Key	**Iter**	**CPU**	err_{sol}	err_{grad}	err_{jump}	α_{sol}	α_{grad}	α_{jump}
Hexahedral Meshes (Cartesian)								
1	11	1.18E-2	1.34E-2	4.3E-2	2.15E-2	-	-	-
2	19	0.13	3.49E-3	1.24E-2	5.44E-3	1.94	1.80	1.98
3	35	1.45	8.91E-4	3.41E-3	1.38E-3	1.97	1.86	1.98
4	73	20.36	2.25E-4	9.15E-4	3.47E-4	1.99	1.90	1.99
5	141	315.38	5.65E-5	2.42E-4	8.69E-5	1.99	1.92	2.00
Hexahedral Meshes (perturbated Cartesian)								
1	10	1.74E-2	1.23E-2	7.17E-2	2.19E-2	-	-	-
2	18	0.15	3.40E-3	2.97E-2	5.74E-3	1.86	1.27	1.93
3	33	1.85	8.73E-4	1.64E-2	1.67E-3	1.96	0.85	1.77
4	69	22.83	2.32E-4	9.94E-3	5.44E-4	1.90	0.72	1.62
5	128	330.77	7.48E-5	7.12E-3	2.36E-4	1.63	0.48	1.19
Tetrahedral Meshes								
6	12	1.56E-2	1.01E-2	0.11	1.74E-2	-	-	-
7	21	0.22	2.74E-3	5.87E-2	5.24E-3	1.88	0.96	1.73
8	43	3.75	6.07E-4	2.75E-2	1.17E-3	2.02	1.02	2.00
9	60	10.51	3.38E-4	2.07E-2	6.62E-4	2.25	1.08	2.20
10	73	23.52	2.22E-4	1.68E-2	4.37E-4	1.90	0.94	1.87
11	119	166.46	7.73E-5	9.87E-3	1.58E-4	2.03	1.02	1.96

Table 1.2: Isotropic test case. **Key** refers to the mesh defined in table 1.1; **Iter** is the number of solver iterations; **CPU** refers to the solver CPU time in seconds; $err_{sol}, err_{grad}, err_{jump}$ are the respective L^2-errors as defined above; $\alpha_{sol}, \alpha_{grad}, \alpha_{jump}$ are the orders of convergence of the solution, of the gradient and of the jump, respectively.

	Anisotropic Permeability: ***VAG***							
Key	**Iter**	**CPU**	err_{sol}	err_{grad}	err_{jump}	α_{sol}	α_{grad}	α_{jump}
Hexahedral Meshes (Cartesian)								
1	7	6.32E-3	8.78E-3	1.98E-2	8.69E-3	-	-	-
2	9	5.56E-2	2.37E-3	4.97E-3	2.34E-3	1.89	1.99	1.89
3	14	0.67	6.15E-4	1.24E-3	6.06E-4	1.95	2.00	1.95
4	26	6.35	2.28E-4	1.57E-4	3.11E-4	1.97	2.00	1.97
5	47	62.65	3.95E-5	7.78E-5	3.89E-5	1.99	2.00	1.99
Hexahedral Meshes (perturbated Cartesian)								
1	7	4.92E-3	1.40E-2	5.45E-2	1.39E-2	-	-	-
2	8	7.28E-2	4.04E-3	3.13E-2	4.01E-3	1.80	0.80	1.79
3	14	0.89	1.18E-3	1.50E-2	1.17E-3	1.77	1.05	1.77
4	25	9.75	2.82E-4	7.37E-3	2.80E-4	2.06	1.03	2.06
5	45	98.75	7.20E-5	3.64E-3	7.14E-5	1.97	1.01	1.97
Tetrahedral Meshes								
6	7	1.95E-3	2.73E-2	0.13	2.70E-2	-	-	-
7	8	2.14E-2	7.05E-3	6.76E-2	6.98E-3	1.95	0.99	1.95
8	15	0.38	2.56E-3	3.92E-2	2.53E-3	1.35	0.73	1.36
9	21	1.02	1.34E-3	2.84E-2	1.32E-3	2.49	1.24	2.49
10	25	2.24	9.26E-4	2.22E-2	9.14E-4	1.66	1.10	1.67
11	41	13.78	3.10E-4	1.36E-2	3.07E-4	2.11	0.95	2.11

	Anisotropic Permeability: ***HFV***							
Key	**Iter**	**CPU**	err_{sol}	err_{grad}	err_{jump}	α_{sol}	α_{grad}	α_{jump}
Hexahedral Meshes (Cartesian)								
1	9	6.02E-3	2.64E-2	4.89E-2	3.35E-2	-	-	-
2	16	8.48E-2	7.02E-3	1.43E-2	8.30E-3	1.91	1.78	2.01
3	29	1.13	1.81E-3	3.96E-3	2.07E-3	1.95	1.85	2.00
4	55	16.55	4.60E-4	1.07E-3	5.19E-4	1.98	1.89	2.00
5	108	248.20	1.16E-4	2.86E-4	1.30E-4	1.99	1.91	2.00
Hexahedral Meshes (perturbated Cartesian)								
1	8	1.20E-2	2.99E-2	8.77E-2	3.94E-2	-	-	-
2	15	0.15	6.92E-3	4.22E-2	8.30E-3	2.11	1.05	2.24
3	28	1.87	1.56E-3	1.96E-2	1.74E-3	2.14	1.10	2.24
4	55	23.34	4.20E-4	9.57E-3	4.58E-4	1.89	1.03	1.92
5	102	371.45	1.12E-4	5.13E-3	1.20E-4	1.89	0.89	1.93
Tetrahedral Meshes								
6	10	1.41E-2	1.77E-2	0.14	1.79E-2	-	-	-
7	19	0.26	4.86E-3	7.13E-2	4.75E-3	1.86	0.98	1.91
8	37	4.56	1.28E-3	3.63E-2	1.21E-3	1.79	0.90	1.83
9	47	12.16	6.92E-4	2.62E-2	6.66E-4	2.35	1.25	2.28
10	63	27.96	4.75E-4	2.16E-2	4.68E-4	1.69	0.88	1.59
11	105	189.66	1.65E-4	1.28E-2	1.58E-4	2.04	1.00	2.09

Table 1.3: Anisotropic test case. **Key** refers to the mesh defined in table 1.1; **Iter** is the number of solver iterations; **CPU** refers to the solver CPU time in seconds; $err_{sol}, err_{grad}, err_{jump}$ are the respective L^2-errors as defined above; $\alpha_{sol}, \alpha_{grad}, \alpha_{jump}$ are the orders of convergence w.r.t. $\#\mathcal{M}^{-\frac{1}{3}}$ of the solution, of the gradient and of the jump, respectively.

The test case shows that, on Cartesian grids, we obtain, as expected, convergence of order 2 for both, the solution and it's gradient. For tetrahedral grids, we obtain convergence of order 2 for the solution and convergence of order 1 for it's gradient. We observe that the VAG scheme is more efficient than the HFV scheme and this observation gets more obvious with increasing anisotropy. Comparing the precision of the discrete solution (and it's gradient) for VAG and HFV on a given mesh, we see that on hexahedral meshes, the advantage is on the side of VAG, whereas on tetrahedral meshes HFV is more precise (but much more expensive). On a given mesh, HFV is usually (see [15]) more accurate than VAG both for tetrahedral and Cartesian meshes. This is not true in the test cases using Cartesian meshes maybe due to the higher number for VAG than for HFV of d.o.f. at the interfaces $\Gamma_{\mathfrak{a}}$ on the matrix side. For perturbated Cartesian grids, we obtain convergence of order 2 for the solution and convergence of order 1 for it's gradient for the VAG scheme, which is able to deal with non-planar faces. However, the HFV scheme reveals a slight deterioration of the convergence rate, for the solution and in particular for it's gradient, which is not surprising, since HFV is not consistent on this family of meshes.

It is also worth mentioning that we have conducted this test for VAG with lumped mf-fluxes, and observed that that there is literally no difference compared to VAG-FE in the ordinary version, concerning accuracy and convergence rate.

1.6 Conclusion

In this chapter, we extended the framework of gradient schemes (see [38]) to the model problem (1.5) of stationary Darcy flow through fractured porous media and gave numerical analysis results for this general framework.

The model problem (an extension to a network of fractures of a PDE model presented in [45], [56] and [6]) takes heterogeneities and anisotropy of the porous medium into account and involves a complex network of planar fractures, which might act either as barriers or as drains.

We also extended the VAG and HFV schemes to our model, where fractures acting as barriers force us to allow for pressure jumps across the fracture network. We developed two versions of VAG schemes, the conforming finite element version and the non-conforming control volume version, the latter particularly adapted for the treatment of material interfaces (cf. [39]). We showed, furthermore, that both versions of VAG schemes, as well as the proposed non-conforming HFV schemes, are incorporated by the gradient scheme's framework. Then, we applied the results for gradient schemes on VAG and HFV to obtain convergence, and, in particular, convergence of order 1 for "piecewise regular" solutions.

For implementation purposes and in view of the application to multi-phase flow, we also propose a uniform Finite Volume formulation for VAG and HFV schemes in the appendix. The numerical experiments on a family of analytical solutions show that the VAG scheme offers a better compromise between accuracy and CPU time than the HFV scheme especially for anisotropic problems.

1.A Density Results for V^0 and W

Let us first state the following Lemma that will be used to prove the density of $\mathbf{C}^\infty_\Omega \times \mathbf{C}^\infty_\Gamma$ in W.

Lemma 1.A.1 *Let $v_m \in L^2(\Omega)$, $v_f \in L^2(\Gamma)$, $G \in L^2(\Omega)^d$, $H \in L^2(\Gamma)^{d-1}$ and $J_\mathfrak{a} \in L^2(\Gamma_\mathfrak{a})$, $\mathfrak{a} \in \chi$ such that*

$$\int_\Omega (G \cdot \mathbf{q}_m + v_m \mathrm{div} \mathbf{q}_m) \mathrm{d}\mathbf{x} + \int_\Gamma (H \cdot \mathbf{q}_f + v_f \mathrm{div}_\tau \mathbf{q}_f) \mathrm{d}\tau(\mathbf{x}) + \sum_{\mathfrak{a} \in \chi} \int_{\Gamma_\mathfrak{a}} \gamma_{\mathbf{n}_\mathfrak{a}} \mathbf{q}_m \mathrm{d}\tau(\mathbf{x})(J_\mathfrak{a} - v_f) = 0 \tag{1.22}$$

for all $(\mathbf{q}_m, \mathbf{q}_f) \in \mathbf{C}^\infty_\Omega \times \mathbf{C}^\infty_\Gamma$. Then holds $(v_m, v_f) \in V^0$, $(G, H) = (\nabla v_m, \nabla_\tau v_f)$ and $J_\mathfrak{a} = v_f - \gamma_\mathfrak{a} v_m$ for $\mathfrak{a} \in \chi$.

Proof Firstly, for all $\mathbf{q}_m \in C^\infty_0(\Omega \backslash \overline{\Gamma})^d$, we have

$$\int_\Omega (G \cdot \mathbf{q}_m + v_m \mathrm{div} \mathbf{q}_m) \mathrm{d}\mathbf{x} = 0$$

and therefore $v_m \in H^1(\Omega \backslash \overline{\Gamma})$ and $\nabla v_m = G$.

For a.e. $\mathbf{x} \in \partial\Omega$, there exists an open planar domain $\omega \subset\subset \partial\Omega \backslash \partial\Gamma$ containing $\mathbf{x}$ such that for all $f \in C^\infty_0(\omega)$ there exists $\mathbf{q}_m \in \mathbf{C}^\infty_\Omega$ with

$$\gamma_{\mathbf{n}_{\partial\Omega}} \mathbf{q}_m = \begin{cases} f & \text{on } \omega, \\ 0 & \text{on } \partial\Omega \backslash \omega, \end{cases}$$
$$\gamma_{\mathbf{n}_\mathfrak{a}} \mathbf{q}_m = 0 \quad \text{on } \Gamma_\mathfrak{a}, \ \mathfrak{a} \in \chi,$$

where $\gamma_{\mathbf{n}_{\partial\Omega}}$ denotes the normal trace operator on the boundary of Ω. From (1.22), taking $\mathbf{q}_f = 0$, we obtain

$$0 = \int_\Omega (\nabla v_m \cdot \mathbf{q}_m + v_m \mathrm{div} \mathbf{q}_m) \mathrm{d}\mathbf{x} = \int_{\partial\Omega} \gamma_{\partial\Omega} v_m \gamma_{\mathbf{n}_{\partial\Omega}} \mathbf{q}_m \mathrm{d}\tau(\mathbf{x}) = \int_\omega \gamma_{\partial\Omega} v_m f \mathrm{d}\tau(\mathbf{x}).$$

where $\gamma_{\partial\Omega}$ denotes the trace operator on the boundary of Ω. We deduce $\gamma_{\partial\Omega} v_m = 0$ a.e. on $\partial\Omega \backslash \partial\Gamma$. Hence $v_m \in H^1_{\partial\Omega}(\Omega \backslash \overline{\Gamma})$.

Further, for a.e. $\mathbf{x} \in \Gamma_\mathfrak{a}$ there exists an open planar domain $\omega_\mathfrak{a} \subset\subset \Gamma_\mathfrak{a}$ containing $\mathbf{x}$ such that for all $g \in C^\infty_0(\omega_\mathfrak{a})$ there exists $\mathbf{q}_m \in \mathbf{C}^\infty_\Omega$ with

$$\gamma_{\mathbf{n}_\mathfrak{a}} \mathbf{q}_m = \begin{cases} g & \text{on } \omega_\mathfrak{a}, \\ 0 & \text{on } \Gamma_\mathfrak{a} \backslash \omega_\mathfrak{a}, \end{cases}$$
$$\gamma_{\mathbf{n}_\mathfrak{b}} \mathbf{q}_m = 0 \quad \text{on } \Gamma_\mathfrak{b}, \text{ for } \mathfrak{b} \neq \mathfrak{a},$$
$$\gamma_{\mathbf{n}_{\partial\Omega}} \mathbf{q}_m = 0 \quad \text{on } \partial\Omega.$$

From (1.22) we obtain

$$0 = \int_\Omega (\nabla v_m \cdot \mathbf{q}_m + v_m \mathrm{div}\mathbf{q}_m)\mathrm{d}\mathbf{x} + \sum_{\mathfrak{a}\in\chi} \int_{\Gamma_\mathfrak{a}} \gamma_{\mathbf{n}_\mathfrak{a}} \mathbf{q}_m (J_\mathfrak{a} - v_f)\mathrm{d}\tau(\mathbf{x})$$
$$= \int_{\Gamma_\mathfrak{a}} \gamma_{\mathbf{n}_\mathfrak{a}} \mathbf{q}_m (J_\mathfrak{a} - v_f + \gamma_\mathfrak{a} v_m)\mathrm{d}\tau(\mathbf{x}) = \int_{\omega_\mathfrak{a}} g(J_\mathfrak{a} - v_f + \gamma_\mathfrak{a} v_m)\mathrm{d}\tau(\mathbf{x}).$$

We deduce $J_\mathfrak{a} = v_f - \gamma_\mathfrak{a} v_m$ a.e. on $\Gamma_\mathfrak{a},\ \mathfrak{a} \in \chi$.

Next, for all $\mathbf{q}_f \in C_0^\infty(\Gamma_i)^{d-1},\ i \in I$, we have from (1.22)

$$\int_{\Gamma_i} (H \cdot \mathbf{q}_f + v_f \mathrm{div}\mathbf{q}_f)\mathrm{d}\tau(\mathbf{x}) = 0$$

and therefore $v_f\restriction_{\Gamma_i} \in H^1(\Gamma_i)$ for $i \in I$ and $\nabla_{\tau_i} v_f\restriction_{\Gamma_i} = H\restriction_{\Gamma_i}$.

Let $i, j \in I$, $i \neq j$. For a.e. $\mathbf{x} \in \Sigma_{i,j} \setminus \Sigma_{i,0}$ there exists an open interval $c_{ij} \subset\subset \Sigma_{i,j} \setminus \Sigma_{i,0}$ containing $\mathbf{x}$ such that for all $h \in C_0^\infty(c_{ij})$ there exists $s \in \mathbf{C}_\Gamma^\infty$ with

$$\gamma_{\mathbf{n}_{\Sigma_i}} s = h = -\gamma_{\mathbf{n}_{\Sigma_j}} s \quad \text{on } c_{ij},$$
$$\gamma_{\mathbf{n}_{\Sigma_k}} s = 0 \quad \text{on } \Sigma_k \backslash c_{ij},\ k \in I.$$

From (1.22) we obtain

$$0 = \int_\Gamma (\nabla_\tau v_f \cdot s + v_f \mathrm{div}_\tau s)\mathrm{d}\tau(\mathbf{x}) = \int_{c_{ij}} (\gamma_{\Sigma_i} v_f - \gamma_{\Sigma_j} v_f)\gamma_{\mathbf{n}_{\Sigma_i}} s \mathrm{d}\sigma(\mathbf{x}),$$

$\mathrm{d}\sigma(\mathbf{x})$ denoting the $d-2$ dimensional Lebesgue measure on Σ. We deduce $\gamma_{\Sigma_i} v_f = \gamma_{\Sigma_j} v_f$ a.e. on $\Sigma_{i,j} \setminus \Sigma_{i,0},\ i, j \in I, i \neq j$. The proof of $\gamma_{\Sigma_0} v_f = 0$ a.e. on Σ_0 goes analogously. Hence $v_f \in H^1_{\Sigma_0}(\Gamma)$. □

Proof of Proposition 1.2.2 Firstly from Proposition 1.2.1, note that on V^0, the norm $\|\cdot\|_{V^0}$ is equivalent to the standart norm $\|\cdot\|_{H^1(\Omega)} + \|\cdot\|_{H^1(\Gamma)}$. The density of C_Ω^∞ in $H^1_{\partial\Omega}(\Omega\setminus\overline{\Gamma})$ being a classical result, we are concerned to prove the density of C_Γ^∞ in $H^1_{\Sigma_0}(\Gamma)$ in the following. Since $H^1_{\Sigma_0}(\Gamma) \subset \gamma_\Gamma(H_0^1(\Omega))$, we can define $\tilde{V}^0 = \gamma_\Gamma^{-1}(H^1_{\Sigma_0}(\Gamma)) \subset H_0^1(\Omega)$. In Proposition 2 of [15] it is shown that $C_0^\infty(\Omega)$ is dense in $(\tilde{V}^0, \|\cdot\|_{H^1(\Omega)} + \|\gamma_\Gamma \cdot\|_{H^1(\Gamma)})$. Hence C_Γ^∞ is dense in $(H^1_{\Sigma_0}(\Gamma), \|\cdot\|_{H^1(\Gamma)})$. □

Proof of Proposition 1.2.3 Since W_f is a closed subspace of the Hilbert space $\prod_{i\in I} H_{\mathrm{div}}(\Gamma_i)$, any linear form $l \in W_f'$ is the restriction to W_f of a linear form still denoted by l in $\prod_{i\in I} H_{\mathrm{div}}(\Gamma_i)'$. Then, for some $f \in L^2(\Gamma)$ and $\boldsymbol{g} \in L^2(\Gamma)^{d-1}$ holds

$$< l, \mathbf{q}_f >= \sum_{i\in I} \int_{\Gamma_i} \Big(\boldsymbol{g} \cdot \mathbf{q}_f + f \cdot \mathrm{div}_\tau \mathbf{q}_f\Big)\mathrm{d}\tau(\mathbf{x}),$$

for all $\mathbf{q}_f \in W_f$. Let us assume now that $< l, \boldsymbol{\varphi} >= 0$ for all $\boldsymbol{\varphi} \in \mathbf{C}_\Gamma^\infty$. Corresponding to Lemma 1.A.1 holds $f \in H^1_{\Sigma_0}(\Gamma)$ and $\boldsymbol{g} = \nabla_\tau f$. From the definition of W_f we conclude that $< l, \mathbf{q}_f >= 0$ for all $\mathbf{q}_f \in W_f$.

Let now $l \in W_m'$. Then there exist $f \in L^2(\Omega)$, $\boldsymbol{g} \in L^2(\Omega)^d$ and $h_\mathfrak{a} \in L^2(\Gamma_\mathfrak{a})$ $(\mathfrak{a} \in \chi)$, such that

$$< l, \mathbf{q}_m >= \int_\Omega \Big(\boldsymbol{g} \cdot \mathbf{q}_m + f \cdot \mathrm{div} \mathbf{q}_m \Big) \mathrm{d}\mathbf{x} + \sum_{\mathfrak{a} \in \chi} \int_{\Gamma_\mathfrak{a}} h_\mathfrak{a} \gamma_{\mathbf{n}_\mathfrak{a}} \mathbf{q}_m \mathrm{d}\tau(\mathbf{x}),$$

for all $\mathbf{q}_m \in W_m$. Furthermore, let us assume that $< l, \boldsymbol{\varphi} >= 0$ for all $\boldsymbol{\varphi} \in \mathbf{C}_\Omega^\infty$. From Lemma 1.A.1 we deduce that $f \in H^1_{\partial\Omega}(\Omega \setminus \overline{\Gamma})$, that $\boldsymbol{g} = \nabla f$ and that $h_\mathfrak{a} = \gamma_\mathfrak{a} f$ $(\mathfrak{a} \in \chi)$. Using this, we conclude, again by the rule of partial integration, that $< l, \mathbf{q}_m >= 0$ for all $\mathbf{q}_m \in W_m$. □

1.B Finite Volume Formulation for VAG and HFV Schemes

The VAG and HFV schemes can be written in a flux conservative formulation, both with matrix-matrix fluxes local to each cell, fracture-fracture fluxes local to each fracture face and two point matrix-fracture fluxes (for HFV and VAG-CV). These fluxes are particularly useful for the discetization of the monophasic model coupled with a transport equation. Such systems typically arise in models for diphasic flow through porous media. In this section, we present a unified Finite Volume Formulation for both schemes.

For $\nu \in dof_\mathcal{D}$, let us denote by $dof_\nu \subset dof_\mathcal{D}$ the set consisting of all ν', such that there is a discrete flux connection between ν and ν' as illustrated in figure 1.6. More concretely, for the the discontinuous hybrid-dimensional model 1, these sets are defined as follows.

- For $K \in \mathcal{M}$:

$$dof_K = \begin{cases} \{\overline{K}_s, s \in \mathcal{V}_K\} \cup \{K_\sigma, \sigma \in \mathcal{F}_K \cap \mathcal{F}_\Gamma\} \text{ for } VAG, \\ \{\overline{K}_\sigma, \sigma \in \mathcal{F}_K\} \text{ for } HFV. \end{cases}$$

- For $\sigma \in \mathcal{F}_\Gamma$:

$$dof_\sigma = \begin{cases} \mathcal{V}_\sigma \cup \{K_\sigma, K \in \mathcal{M}_\sigma\} \text{ for } VAG, \\ \mathcal{E}_\sigma \cup \overline{\mathcal{M}}_\sigma \text{ for } HFV. \end{cases}$$

- For $\nu_m \in dof^\Gamma_{\mathcal{D}_m}$: $dof_{\nu_m} = \{K \in \mathcal{M} \mid \nu_m \in dof_K\} \cup \{\nu_f \in dof_{\mathcal{D}_f} \mid \mathbf{x}_{\nu_f} = \mathbf{x}_{\nu_m}\}$
- For $\nu_f \in dof_{\mathcal{D}_f}$: $dof_{\nu_f} = \{\sigma \in \mathcal{F}_\Gamma \mid \nu_f \in dof_\sigma\} \cup \{\nu_m \in dof^\Gamma_{\mathcal{D}_m} \mid \mathbf{x}_{\nu_f} = \mathbf{x}_{\nu_m}\}$

Since the fluxes connect exactly two unknowns, the definition of the sets dof_ν is complemented by

$$\nu' \in dof_\nu \Longleftrightarrow \nu \in dof_{\nu'}.$$

Then, for any $\nu \in dof_K$ the discrete *matrix-matrix*-fluxes are defined as

$$F_{K\nu}(u_\mathcal{D}) = \sum_{\nu' \in dof_K} \Big(\int_K \Lambda_m \nabla^m_\mathcal{D} \mathfrak{e}_\nu \nabla^m_\mathcal{D} \mathfrak{e}_{\nu'} \mathrm{d}\mathbf{x} \Big) (u_K - u_{\nu'}).$$

such that $\int_\Omega \Lambda_m \nabla_{\mathcal{D}}^m u_{\mathcal{D}} \nabla_{\mathcal{D}}^m v_{\mathcal{D}} \mathrm{d}\mathbf{x} = \sum_{K\in\mathcal{M}} \sum_{\nu\in dof_K} F_{K\nu}(u_{\mathcal{D}})(v_K - v_\nu)$. For all $\nu \in dof_\sigma \cap dof_{\mathcal{D}_f}$ the discrete *fracture-fracture*-fluxes are defined as

$$F_{\sigma\nu}(u_{\mathcal{D}}) = \sum_{\nu'\in dof_\sigma \cap dof_{\mathcal{D}_f}} \Big(\int_\sigma \Lambda_f \nabla_{\mathcal{D}}^f \mathfrak{e}_\nu \nabla_{\mathcal{D}}^f \mathfrak{e}_{\nu'} \mathrm{d}\tau_f(\mathbf{x})\Big)(u_\sigma - u_{\nu'}),$$

such that $\int_\Gamma \Lambda_f \nabla_{\mathcal{D}}^f u_{\mathcal{D}} \nabla_{\mathcal{D}}^f v_{\mathcal{D}} \mathrm{d}\tau_f(\mathbf{x}) = \sum_{\sigma\in\mathcal{F}_\Gamma} \sum_{\nu\in dof_\sigma\cap dof_{\mathcal{D}_f}} F_{\sigma\nu}(u_{\mathcal{D}})(v_\sigma - v_\nu)$. To take interactions of the matrix and the fracture domain into account we introduce the set of *matrix-fracture* (mf) connectivities

$$\mathcal{C} = \{(\nu_m, \nu_f) \,|\, \nu_m \in dof_{\mathcal{D}_m}^\Gamma, \nu_f \in dof_{\mathcal{D}_f} \text{ s.t. } \mathbf{x}_{\nu_m} = \mathbf{x}_{\nu_f}\}$$

with $dof_{\mathcal{D}_m}^\Gamma = \{\nu \in dof_{\mathcal{D}_m} \,|\, \mathbf{x}_\nu \in \overline{\Gamma}\}$. The mf-fluxes are built such that

$$\begin{aligned} a_{\mathcal{D}_{mf}}(u_{\mathcal{D}}, v_{\mathcal{D}}) &= \sum_{(\nu_m,\nu_f)\in\mathcal{C}} F_{\nu_m\nu_f}(u_{\mathcal{D}})(v_{\nu_m} - v_{\nu_f}) \\ &= \sum_{i\in I} \int_{\Gamma_i} \frac{T_f}{2\xi - 1} \sum_{(\mathfrak{a},\mathfrak{b})\in\{(\mathfrak{a}^\pm(i),\mathfrak{a}^\mp(i))\}} \Big(\xi[\![u_{\mathcal{D}}]\!]_{\mathcal{D}}^{\mathfrak{a}} + (1-\xi)[\![u_{\mathcal{D}}]\!]_{\mathcal{D}}^{\mathfrak{b}}\Big)[\![v_{\mathcal{D}}]\!]_{\mathcal{D}}^{\mathfrak{a}} \mathrm{d}\tau(\mathbf{x}), \end{aligned}$$

for all $v_{\mathcal{D}} \in X_{\mathcal{D}}$. For all $\sigma \in \mathcal{F}_\Gamma$ and $K \in \mathcal{M}_\sigma$, let us denote by $\mathfrak{a}(K,\sigma)$ the unique $\mathfrak{a} \in \chi$ such that $\sigma \in \mathcal{F}_{\mathfrak{a}}$ and $\mathbf{n}_{\mathfrak{a}} = \mathbf{n}_{K,\sigma}$. Let us also set for all $\sigma \in \mathcal{F}_\Gamma$, $(\chi\times\chi)_\sigma = \{(\mathfrak{a}(K,\sigma), \mathfrak{a}(L,\sigma)), (\mathfrak{a}(L,\sigma), \mathfrak{a}(K,\sigma))\}$ with $\mathcal{M}_\sigma = \{K, L\}$. Then, holds

$$a_{\mathcal{D}_{mf}}(u_{\mathcal{D}}, v_{\mathcal{D}}) = \sum_{\sigma\in\mathcal{F}_\Gamma} \sum_{(\mathfrak{a},\mathfrak{b})\in(\chi\times\chi)_\sigma} \int_\sigma \frac{T_f}{2\xi-1}\Big(\xi[\![u_{\mathcal{D}}]\!]_{\mathcal{D}}^{\mathfrak{a}} + (1-\xi)[\![u_{\mathcal{D}}]\!]_{\mathcal{D}}^{\mathfrak{b}}\Big)[\![v_{\mathcal{D}}]\!]_{\mathcal{D}}^{\mathfrak{a}} \mathrm{d}\tau(\mathbf{x}).$$

For all $\sigma \in \mathcal{F}_\Gamma$, $K \in \mathcal{M}_\sigma$ and $\mathbf{x} \in \sigma$, let us notice that, for the VAG scheme, one has $[\![\mathfrak{e}_{K_\sigma} + \mathfrak{e}_\sigma]\!]_{\mathcal{D}}^{\mathfrak{a}(K,\sigma)}(\mathbf{x}) = 0$, and $[\![\mathfrak{e}_{\overline{K}_s} + \mathfrak{e}_s]\!]_{\mathcal{D}}^{\mathfrak{a}(K,\sigma)}(\mathbf{x}) = 0$ for all $s \in \mathcal{V}_\sigma$, and for the HFV scheme, one has $[\![\mathfrak{e}_{\overline{K}_\sigma} + \mathfrak{e}_\sigma]\!]_{\mathcal{D}}^{\mathfrak{a}(K,\sigma)}(\mathbf{x}) = 0$. It result after some computations that the VAG matrix fracture fluxes are defined by

$$\begin{aligned} F_{K_\sigma\sigma}(u_{\mathcal{D}}) = &\sum_{s\in\mathcal{V}_\sigma} \Big(\int_\sigma \frac{T_f}{2\xi-1}([\![\mathfrak{e}_\sigma]\!]_{\mathcal{D}}^{\mathfrak{a}(K,\sigma)})([\![\mathfrak{e}_s]\!]_{\mathcal{D}}^{\mathfrak{a}(K,\sigma)})\mathrm{d}\tau(\mathbf{x})\Big)\Big(\xi u_{\overline{K}_s} + (1-\xi)u_{\overline{L}_s} - u_s\Big) \\ &+ \Big(\int_\sigma \frac{T_f}{2\xi-1}([\![\mathfrak{e}_\sigma]\!]_{\mathcal{D}}^{\mathfrak{a}(K,\sigma)})^2\mathrm{d}\tau(\mathbf{x})\Big)\Big(\xi u_{K_\sigma} + (1-\xi)u_{L_\sigma} - u_\sigma\Big), \end{aligned}$$

for all $\sigma \in \mathcal{F}_\Gamma$, $\mathcal{M}_\sigma = \{K, L\}$, and by

$$\begin{aligned} F_{\overline{Q}_s s}(u_{\mathcal{D}}) = &\sum_{\sigma\in(\bigcup_{Q\in\overline{Q}_s}\mathcal{F}_Q)\cap\mathcal{F}_s\cap\mathcal{F}_\Gamma} \quad \sum_{K\in\mathcal{M}_\sigma\cap\overline{Q}_s,\, L\in\mathcal{M}_\sigma\setminus\{K\}} \Big\{ \\ &\Big(\int_\sigma \frac{T_f}{2\xi-1}([\![\mathfrak{e}_s]\!]_{\mathcal{D}}^{\mathfrak{a}(K,\sigma)})^2\mathrm{d}\tau(\mathbf{x})\Big)\Big(\xi u_{\overline{K}_s} + (1-\xi)u_{\overline{L}_s} - u_s\Big) \\ &+ \sum_{s'\in\mathcal{V}_\sigma \,|\, ss'\in\mathcal{E}_\sigma} \Big(\int_\sigma \frac{T_f}{2\xi-1}([\![\mathfrak{e}_{s'}]\!]_{\mathcal{D}}^{\mathfrak{a}(K,\sigma)})([\![\mathfrak{e}_s]\!]_{\mathcal{D}}^{\mathfrak{a}(K,\sigma)})\mathrm{d}\tau(\mathbf{x})\Big)\Big(\xi u_{\overline{K}_{s'}} + (1-\xi)u_{\overline{L}_{s'}} - u_{s'}\Big) \\ &+ \Big(\int_\sigma \frac{T_f}{2\xi-1}([\![\mathfrak{e}_\sigma]\!]_{\mathcal{D}}^{\mathfrak{a}(K,\sigma)})([\![\mathfrak{e}_s]\!]_{\mathcal{D}}^{\mathfrak{a}(K,\sigma)})\mathrm{d}\tau(\mathbf{x})\Big)\Big(\xi u_{K_\sigma} + (1-\xi)u_{L_\sigma} - u_\sigma\Big) \qquad \Big\}, \end{aligned}$$

for all $s \in \mathcal{V}_\Gamma$, $\overline{Q}_s \in \overline{\mathcal{M}}_s$. Similarly the HFV matrix fracture fluxes are defined by

$$F_{\overline{K}_\sigma\sigma}(u_\mathcal{D}) = \frac{1}{2\xi - 1}\Big(\int_\sigma T_f(\mathbf{x})\mathrm{d}\tau(\mathbf{x})\Big)\Big(\xi u_{K_\sigma} + (1-\xi)u_{L_\sigma} - u_\sigma\Big),$$

for all $\sigma \in \mathcal{F}_\Gamma$, $\mathcal{M}_\sigma = \{K, L\}$.

We observe that for the HFV scheme as well as for the VAG-CV scheme, the fluxes $F_{\nu_m\nu_f}$ are two point flux approximations (since for all $\mathfrak{a} \in \chi$: $\int_\sigma T_f([\![\mathfrak{e}_{s'}]\!]^\mathfrak{a}_\mathcal{D})([\![\mathfrak{e}_s]\!]^\mathfrak{a}_\mathcal{D})\mathrm{d}\tau(\mathbf{x}) = 0$ for $s \neq s'$ and $\int_\sigma T_f([\![\mathfrak{e}_\sigma]\!]^\mathfrak{a}_\mathcal{D})([\![\mathfrak{e}_s]\!]^\mathfrak{a}_\mathcal{D})\mathrm{d}\tau(\mathbf{x}) = 0$).

The discrete source terms are defined by

$$H_\nu = \begin{cases} \displaystyle\int_\Omega h_m \Pi^m_\mathcal{D}\mathfrak{e}_\nu \mathrm{d}\mathbf{x} & \text{for } \nu \in dof_{\mathcal{D}_m}, \\ \displaystyle\int_\Gamma h_f \Pi^f_\mathcal{D}\mathfrak{e}_\nu \mathrm{d}\tau_f(\mathbf{x}) & \text{for } \nu \in dof_{\mathcal{D}_f}. \end{cases}$$

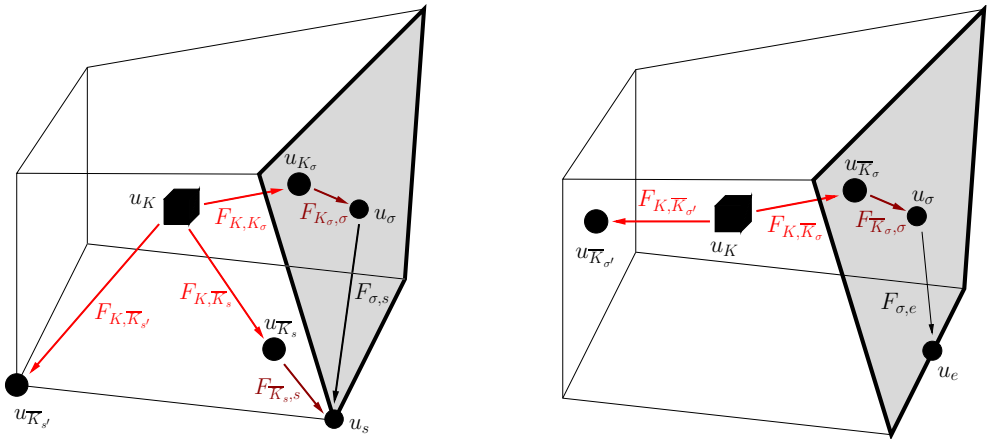

Figure 1.6: *mm*-fluxes (red), *mf*-fluxes (dark red) and *ff*-fluxes (black) for VAG (left) and HFV (right) on a 3D cell touching a fracture

The following Finite Volume formulation of (1.6) is equivalent to the discrete variational formulation (1.7): find $u_\mathcal{D} \in X^0_\mathcal{D}$ such that

$$\sum_{\nu' \in dof_\nu} F_{\nu\nu'}(u_\mathcal{D}) = H_\nu \qquad \text{for all } \nu \in dof_\mathcal{D}.$$

It is important to note that, using the equation in each cell, the cell unknowns u_K, $K \in \mathcal{M}$, can be eliminated without fill-in.

Chapter 2

Two phase Darcy flow

2.1 Introduction

This chapter has two aims: providing reduced models for two phase flows in porous media with complex Discrete Fracture Networks (DFN) and validating the reduced models by comparing them to the full (non reduced) model. More precisely, we are concerned with the modelling and the discretization of two phase Darcy flows in fractured porous media, for which the fractures are represented as interfaces of codimension one. In this framework, the $(d-1)$-dimensional flow in the fractures is coupled with the d-dimensional flow in the matrix leading to the so called, hybrid-dimensional Darcy flow models. These models are derived from the so called equi-dimensional model, where fractures are represented as geological structures of equal dimension as the matrix, by averaging fracture quantities over the fracture width. We consider the case for which the pressure can be discontinuous at the matrix-fracture (mf) interfaces in order to account for fractures acting either as drains or as barriers as described in [6, 45, 56] and chapter 1, contrary to the continuous pressure model described in [5, 15] developed for conductive fractures. A hybrid-dimensional discontinuous pressure model for two phase flow in global pressure formulation has been derived in [2, 52]. In order to account more efficiently for discontinuous capillary pressures, our models use the phase pressures as primary unknowns. This formulation is based on the inverse of the monotone graph extension of the capillary pressure curves and can be easily extended to general capillary pressure curves including vanishing capillary pressures in the fracture using a switch of variable formulation as described in [17]. Our coupling conditions at the mf interfaces also differ from the ones presented in [2, 52] in the sense that they incorporate an upwinding between the matrix and fracture mobilities and do not neglect the gravitational force. This upwinding is crucial in order to transport fluid from the matrix to the fractures and the gravitational force in the width of the fracture cannot be neglected for gravity dominant flows independently on the fracture width. The discontinuous hybrid-dimensional model, presented in section 2.2.1 is based on the two phase Darcy flux continuity at the mf interfaces. At the discrete level, we propose a modification of this model in section 2.3.3, which still accounts for pressure discontinuities at the mf interfaces, but provides linear matrix-

fracture transmission conditions. Subsequently, in a series of test cases, we compare the discontinuous hybrid-dimensional models with the equi-dimensional model and with the hybrid-dimensional model presented in [16] and which assumes pressure continuity across the fractures accounting only for conductive fractures.

The discretization of hybrid-dimensional Darcy flow models has been the object of several works. For an exhaustive review of existing methods, we refer to [65, 68]. For two-phase Darcy flow, a cell-centred Finite Volume scheme using a Two Point Flux Approximation (TPFA) is proposed in [54], assuming the orthogonality of the mesh and isotropic permeability fields. Cell-centred Finite Volume schemes can be extended to general meshes and anisotropic permeability fields using MultiPoint Flux Approximations (MPFA) following the ideas introduced in [69] for discontinuous pressure models. Nevertheless, MPFA schemes can lack robustness on distorted meshes and large anisotropies due to the non symmetry of the discretization. They are also very expensive compared to nodal discretizations on tetrahedral meshes. In [50], the two-phase flow equations are solved in an IMPES framework, using a Mixed Hybrid Finite Element (MHFE) discretization for the pressure equation and a Discontinuous Galerkin discretization of the saturation equation. The paper also contains a review on the most common numerical approaches, when dealing with discrete fractures. The Hybrid Finite Volume discretization (HFV, see [37]) is extended to two phase Darcy flow in fractured media in [48]. These approaches are adapted to general meshes and anisotropy but require as many degrees of freedom as faces. An early paper to use a Control Volume Finite Element method (CVFE) for the discretization of hybrid-dimensional two-phase flow is [11]. In [62], a CVFE scheme is proposed that use reconstruction operators for the saturations that depend on the rock characteristic capillary pressure curves. In this way, the saturation jumps (due to discontinuous capillary pressure) at the material interfaces are respected. A similar approach can be found in [59] in phase pressure formulation. However, the rigid choice of the control volumes (that are the dual cells) leads to the need of small matrix cells at the DFN neighbourhood, in order not to enlarge the drain artificially. In [16], the VAG scheme is used, which is very flexible in the distribution of control volumes and hence circumvents this problem. To the author's knowledge, there has not yet appeared a comparison of different hybrid-dimensional models with the generic equi-dimensional model for two phase flow. This is one of the achievements of the present chapter.

In this chapter, we present an adaptation of the VAG scheme to the hybrid-dimensional discontinuous pressure model using supplementary unknowns at the mf interfaces to capture the pressure jumps as initially proposed in chapter 1. We choose a vertex based scheme, because it leads, compared to the cell-centered and face-centered approaches, to a smaller number of degrees of freedom when dealing with symplectic meshes, which in turn often arise when complex geometries have to be taken into account. Furthermore, the control volume version of the VAG scheme, presented here, allows to take into account saturation jumps (due to capillary pressure) at rock type interfaces including the mf interfaces. An important novelty of the proposed scheme is that the saturations at the interfacial unknowns are explicitly calculated, in addition to the saturations inside the fractures. All of the aforementioned schemes lack in this supplementary information.

They either have just one unknown at the fractures, which is the case for the hybrid dimensional continuous pressure models, or they eliminate the interfacial unknowns at the linear level. The importance of preserving the information on interfacial and interior saturations at the fractures becomes obvious in the test case section of this chapter: the influence on the solution of capillary or gravitational forces in normal direction within the fractures is far from being negligible, in general. The supplementary unknowns at the mf interfaces enable the method presented in this chapter to capture these effects.

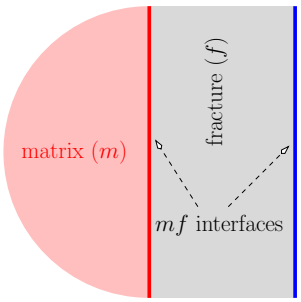

Figure 2.1: Nomenclature.

The outline of this chapter is as follows. The hybrid-dimensional two phase flow models are provided in section 2.2. Section 2.3 is devoted to the VAG discretization and provides a finite volume formulation of the models. In section 2.4, the hybrid and equi-dimensional models are compared on a tracer problem with analytical solutions. The effect of a normal diffusion term in the fracture for the equi-dimensional model is also investigated. The last section 2.5 compares the three hybrid-dimensional models with the equi-dimensional model on a two phase flow problem with different matrix and fracture permeabilities and capillary pressures.

2.2 Hybrid-dimensional Modelling of Flow in Fractured Porous Media

Fractures and faults are geological structures with highly contrasted petro- and hydrological properties and a small thickness compared to the surrounding matrix. To derive the hybrid-dimensional model, we average the continuity and Darcy equations over the fracture width. The main objectives are to facilitate mesh generation and to decrease the number of degrees of freedom involved in the numerical resolution of the corresponding discrete problem. For the following, the definitions of sections 1.2.1 and 1.2.2 will be of avail.

2.2.1 Two phase Darcy flow models

Equi-dimensional model. We consider the flow equations for incompressible, immiscible two phase flow on a d-dimensional porous domain Ω containing a fracture Ω_f as illustrated in figure 2.2. To simplify, we consider no sources or sinks.

$$\phi \partial_t S^\alpha(\mathbf{x}, p) + \operatorname{div}(\mathbf{q}^\alpha) = 0, \tag{2.1a}$$

$$\mathbf{q}^\alpha = -k^\alpha(\mathbf{x}, S^\alpha(\mathbf{x}, p))\ \Lambda(\nabla u^\alpha - \rho^\alpha \mathbf{g}), \tag{2.1b}$$

with phase parameter $\alpha \in \{1, 2\}$ (1 for a non wetting phase and 2 for a wetting phase), phase pressures u^α, phase Darcy velocities $\mathbf{q}^\alpha$, capillary pressure p, phase saturations

S^α, permeability tensor Λ (positive definite), porosity ϕ, phase mobility k^α phase mass densities ρ^α gravitational vector field $\mathbf{g}$ and space coordinate $\mathbf{x} \in \Omega$. The system is closed by the equations

$$p = u^1 - u^2, \qquad S^1(\mathbf{x}, p) + S^2(\mathbf{x}, p) = 1. \tag{2.1c}$$

Model (2.1) will be referred to as the equi-dimensional model, in the following.

Derivation of the hybrid-dimensional models. We suppose that the matrix and the fracture network consist of a finite number of geological formations, that define finite partitions of $\Omega \setminus \Omega_f$ and Ω_f. To identify those geological formations mathematically, we attribute a proper rock type rt to each open set ω_{rt} of these partitions. Then, we assume that on each ω_{rt}, k^α and S^α are not explicitly space dependent. Moreover, on ω_{rt}, $S^1(q) \in [0, 1]$ for all $q \in \mathbb{R}$ and S^1 is a non decreasing continuous function on $\mathbb{R}$, and k^α is a continuous, non-negative valued function on $[0, 1]$, for $\alpha = 1, 2$.

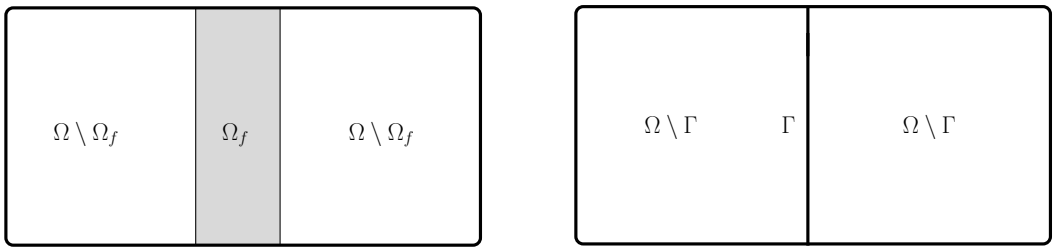

Figure 2.2: Geometries of the equi-dimensional model (left) and the hybrid-dimensional model (right) in the case of a single fracture dividing the matrix domain.

The fracture has the representation $\Omega_f = \{\mathbf{x} \in \Omega \mid \mathbf{x} = \mathbf{y} + r\mathbf{n}(\mathbf{y}), \mathbf{y} \in \Gamma, r \in (-\frac{d_f(\mathbf{y})}{2}, \frac{d_f(\mathbf{y})}{2})\}$, where $\mathbf{n}$ is a unit normal vector and d_f is the fracture width. Let us further introduce the orthonormal system of tangential vectors $(\boldsymbol{\tau}_1, \ldots, \boldsymbol{\tau}_{d-1})$ on Γ and the corresponding tangential divergence div_τ and gradient ∇_τ. We assume that inside the fractures, the normal direction is a permeability principal direction, such that the permeability tensor decomposes in a tangential part and a normal part as

$$\Lambda = \Lambda_f + \lambda_{f,n}\ \mathbf{n} \otimes \mathbf{n}, \tag{2.2}$$

with $\Lambda_f \mathbf{n} = 0$. On Ω_f, we also assume that the permeability and porosity, as well as the constitutive relations for the phase saturations and mobilities do not explicitly depend on the normal component of the spacial coordinate (we will use the index f to denote their projections on Γ).

To start, we write

$$\mathbf{q}^\alpha = \sum_{i=1}^{d-1} (\mathbf{q}^\alpha \cdot \boldsymbol{\tau}_i)\boldsymbol{\tau}_i + (\mathbf{q}^\alpha \cdot \mathbf{n})\mathbf{n}. \tag{2.3}$$

Let $\mathbf{g}_\tau = \mathbf{g} - (\mathbf{g}\cdot\mathbf{n})\mathbf{n}$. With (2.2) and (2.3), (2.1b) is equivalent to

$$\sum_{i=1}^{d-1}(\mathbf{q}^\alpha\cdot\boldsymbol{\tau}_i)\boldsymbol{\tau}_i = -k_f^\alpha(\mathbf{x},S_f^\alpha(\mathbf{x},p))\ \Lambda_f(\nabla_\tau u^\alpha - \rho^\alpha\mathbf{g}_\tau) \tag{2.4a}$$

$$\mathbf{q}^\alpha\cdot\mathbf{n} = -k_f^\alpha(\mathbf{x},S_f^\alpha(\mathbf{x},p))\ \lambda_{f,n}(\partial_{\mathbf{n}}u^\alpha - \rho^\alpha\mathbf{g}\cdot\mathbf{n}). \tag{2.4b}$$

Respectively, the averaged pressure and the integrated tangential Darcy velocity across the fracture are defined by

$$u_f^\alpha = \frac{1}{d_f}\int_{-\frac{d_f}{2}}^{\frac{d_f}{2}} u^\alpha \mathrm{d}\mathbf{n} \qquad \text{and} \qquad \mathbf{q}_f^\alpha = \sum_{i=1}^{d-1}\int_{-\frac{d_f}{2}}^{\frac{d_f}{2}}(\mathbf{q}^\alpha\cdot\boldsymbol{\tau}_i)\boldsymbol{\tau}_i\mathrm{d}\mathbf{n}.$$

Furthermore, let us use the approximations

$$k_f^\alpha(\mathbf{x},S_f^\alpha(\mathbf{x},p)) \approx k_f^\alpha(\mathbf{x},S_f^\alpha(\mathbf{x},p_f)) \qquad \text{and} \qquad S_f^\alpha(\mathbf{x},p_f) \approx \frac{1}{d_f}\int_{-\frac{d_f}{2}}^{\frac{d_f}{2}} S_f^\alpha(\mathbf{x},p)\mathrm{d}\mathbf{n}.$$

Integration of the conservation equation (2.1a) and the tangential Darcy law (2.4a) over the fracture width yields the fracture equations for the hybrid-dimensional model,

$$\begin{cases} \phi_f d_f \partial_t S_f^\alpha(\mathbf{x},p_f) + \mathrm{div}_\tau(\mathbf{q}_f^\alpha) = \sum_{\mathfrak{a}\in\chi}\gamma_{\mathbf{n}_\mathfrak{a}}\mathbf{q}_m^\alpha & \text{on } \Gamma \\ \mathbf{q}_f^\alpha = -d_f k_f^\alpha(\mathbf{x},S_f^\alpha(\mathbf{x},p_f))\ \Lambda_f(\nabla_\tau u_f - \rho^\alpha\mathbf{g}_\tau) & \text{on } \Gamma \end{cases} \tag{2.5a}$$

The matrix equations for the hybrid-dimensional model are

$$\begin{cases} \phi_m\partial_t S_m^\alpha(\mathbf{x},p_m) + \mathrm{div}(\mathbf{q}_m^\alpha) = 0 & \text{on } \Omega\setminus\overline{\Gamma} \\ \mathbf{q}_m^\alpha = -k_m^\alpha(\mathbf{x},S_m^\alpha(\mathbf{x},p_m))\ \Lambda_m(\nabla u_m^\alpha - \rho^\alpha\mathbf{g}) & \text{on } \Omega\setminus\overline{\Gamma} \end{cases} \tag{2.5b}$$

Moreover, both phases are coupled by the equations

$$(p_m,p_f) = (u_m^1 - u_m^2, u_f^1 - u_f^2), \qquad (S_m^2,S_f^2) = 1 - (S_m^1,S_f^1). \tag{2.5c}$$

Discontinuous hybrid-dimensional model. The matrix and the fracture equations are coupled by Robin boundary conditions imposed at each $\Gamma_\mathfrak{a}$, $\mathfrak{a}\in\chi$. For this, we use a two point approximation of the normal derivative of the pressure in the linear part of (2.4b), which leads to the definition of the velocity

$$V_{f,n}^{\alpha,\mathfrak{a}} = \lambda_{f,n}\Big(\frac{\gamma_\mathfrak{a}u_m^\alpha - u_f^\alpha}{d_f/2} - \rho^\alpha\gamma_{\mathbf{n}_\mathfrak{a}}\mathbf{g}\Big). \tag{2.6}$$

In order to transport the saturations between the matrix and the fractures, the mobility has to be upwinded in the definition of the normal flux $\gamma_{\mathbf{n}_\mathfrak{a}}\mathbf{q}_m^\alpha$. For any $a\in\mathbb{R}$, let us set $a^+ = \max\{0,a\}$ and $a^- = (-a)^+$. The resulting equation on $\Gamma_\mathfrak{a}$, $\mathfrak{a}\in\chi$ is

$$\begin{aligned} \gamma_{\mathbf{n}_\mathfrak{a}}\mathbf{q}_m^\alpha &= \mathbf{q}_{f,\mathbf{n}_\mathfrak{a}}^\alpha \\ \mathbf{q}_{f,\mathbf{n}_\mathfrak{a}}^\alpha &= k_f^\alpha(\mathbf{x},S_f^\alpha(\mathbf{x},\gamma_\mathfrak{a}p_m))(V_{f,n}^{\alpha,\mathfrak{a}})^+ - k_f^\alpha(\mathbf{x},S_f^\alpha(\mathbf{x},p_f))(V_{f,n}^{\alpha,\mathfrak{a}})^-. \end{aligned} \tag{2.7}$$

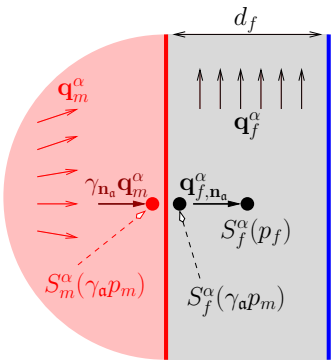

Figure 2.3: Illustration of the coupling condition $\mathbf{q}_{f,\mathbf{n}_\mathfrak{a}}^\alpha = \gamma_{\mathbf{n}_\mathfrak{a}}\mathbf{q}_m^\alpha$ for the discontinuous hybrid-dimensional model.

As illustrated in figure 2.3, the upwinding of the mobilities in the definition of the flux $\mathbf{q}_{f,\mathbf{n}_\mathfrak{a}}^\alpha$ takes into account the saturation jump due to discontinuous capillary pressure curves at the matrix-fracture interface.

Model (2.5),(2.7) will be referred to as the type hybrid-dimensional model accounting for pressure discontinuities at the matrix-fracture interfaces, or shortly, the discontinuous hybrid-dimensional model.

Continuous hybrid-dimensional model. When $\frac{\lambda_{f,n}}{d_f} \gg \frac{|\Lambda_m|}{\mathrm{diam}(\Omega)}$, condition (2.6) can be further approximated by the pressure continuity condition at the matrix fracture interface Γ

$$\gamma_{\mathfrak{a}(i)^+} u_m^\alpha = \gamma_{\mathfrak{a}(i)^-} u_m^\alpha = u_f, \tag{2.8}$$

recovering the condition introduced in [5] for single phase Darcy flows and in [11, 16, 62] for two phase flows. The model defined by (2.5),(2.8) will be referred to as the continuous hybrid-dimensional model, in the rest of this chapter.

DFN closure conditions. Finally, closure conditions are set at the immersed boundary of the fracture network (fracture tips) as well as at the intersection between fractures. For $i \in I$, let γ_{Σ_i} (resp. $\gamma_{\mathbf{n}_{\Sigma_i}}$) denote the trace (resp. normal trace) operator at the fracture Γ_i boundary oriented outward to Γ_i, and let $\gamma_{\mathbf{n}_{\partial\Gamma}}$ denote the normal trace operator at the fracture network boundary oriented outward to Γ. At fracture tips $\partial\Gamma \setminus \partial\Omega$, it is classical to assume homogeneous Neumann boundary conditions in the sense that

$$\gamma_{\mathbf{n}_{\partial\Gamma}} \mathbf{q}_f^\alpha = 0 \quad \text{on } \partial\Gamma \setminus \partial\Omega,\ \alpha = 1, 2,$$

meaning that the flow at the tip of a fracture can be neglected compared with the flow along the sides of the fracture. At the fracture intersection $\Sigma_{i,j} \setminus \Sigma_{i,0}$, $i, j \in I, i \neq j$, we impose the normal flux conservation equations

$$\sum_{k \in I} \gamma_{\mathbf{n}_{\Sigma_k}} \mathbf{q}_f^\alpha = 0 \quad \text{on } \Sigma_{i,j} \setminus \Sigma_{i,0},\ \alpha = 1, 2,$$

meaning that the volume at the intersection between fractures is neglected. In addition, we impose continuity of the phase pressures at $\Sigma_{i,j}$

$$\gamma_{\Sigma_i} u_f^\alpha = \gamma_{\Sigma_j} u_f^\alpha \quad \text{on } \Sigma_{i,j},\ \alpha = 1, 2.$$

This amounts to assume a high ratio between the permeability at the intersection and the fracture width compared with the ratio between the tangential permeability of each fracture and its length.

Up to now, the only existing, comparable hybrid-dimensional two-phase flow model to the discontinuous hybrid-dimensional model presented above is the model described in [2, 52], which is presented in global pressure formulation. We adapted here a formulation using the phase pressures as primary unknowns, accounting for complex fracture networks and general invertible capillary pressure functions. As illustrated in the numerical section it can be easily extended to general capillary pressure curves including vanishing capillary pressure in the fractures using a switch of variable formulation as described in [17].

Another difference is, that the discontinuous hybrid-dimensional model uses an upwind coupling condition for the matrix-fracture normal fluxes (see (2.7)). This upwinding is necessary to transport the saturations from the matrix to the fractures. The coupling condition (2.7) also takes into account gravitational force inside the fractures for the matrix-fracture mass exchange. In the test cases below, we see that this is an important feature for the simulation of gravity dominant flow.

2.3 Vertex Approximate Gradient Scheme

In this section, the VAG scheme, introduced in [38] for diffusive problems on heterogeneous anisotropic media and extended to discrete fractures in [15] for the continuous and in chapter 1 for the discontinuous hybrid dimensional models, is adapted to the hybrid-dimensional two phase flow models. We consider a finite volume version using lumping both for the accumulation terms and the matrix fracture fluxes.

2.3.1 VAG Discretization

Polyhedral meshes

The meshes underlying the discretization are considered to be of generalized polyhedral type, as defined in section 1.4. Let us just recall that $\mathcal{M}$ and $\mathcal{F}_\Gamma$ denote the set of cells and fracture faces, respectively, and that the mesh is assumed to be conforming w.r.t. the fracture network, i.e. $\overline{\Gamma}_i = \bigcup_{\sigma \in \mathcal{F}_{\Gamma_i}} \overline{\sigma}$, for some $\mathcal{F}_{\Gamma_i} \subset \mathcal{F}_\Gamma$, $i \in I$. Also, the mesh admits to define a tetrahedral submesh $\mathcal{T}$ and a subtriangulation Δ of Γ, in the sense of 1.4. The mesh is also assumed to be conforming w.r.t. the rock types, in the sense that we have a well defined rock type for each cell and fracture face, denoted by rt_K and rt_σ, for $K \in \mathcal{M}$ and $\sigma \in \mathcal{F}_\Gamma$.

Degrees of freedom

We summarize some notation of section 1.4. The set of matrix and fracture degrees of freedom is denoted by $dof_{\mathcal{D}} = dof_{\mathcal{D}_m} \cup dof_{\mathcal{D}_f}$, with $dof_{\mathcal{D}_m} \cap dof_{\mathcal{D}_f} = \emptyset$. The real vector

space of discrete unknowns is denoted by $X_{\mathcal{D}} = \mathbb{R}^{\#dof_{\mathcal{D}}}$. For $u_{\mathcal{D}} \in X_{\mathcal{D}}$ and $\nu \in dof_{\mathcal{D}}$, we denote by u_ν the νth component of $u_{\mathcal{D}}$. To account for Dirichlet boundary conditions on $\partial\Omega$ and Σ_0 we introduce the subsets $dof_{Dir_m} \subset dof_{\mathcal{D}_m}$, and $dof_{Dir_f} \subset dof_{\mathcal{D}_f}$, and we set $dof_{Dir} = dof_{Dir_m} \cup dof_{Dir_f}$, and $X^0_{\mathcal{D}} = \{u_{\mathcal{D}} \in X_{\mathcal{D}} \,|\, u_\nu = 0 \text{ for all } \nu \in dof_{Dir}\}$. Concretely, we consider the set of d.o.f. as illustrated in figure 2.4, for the different models.

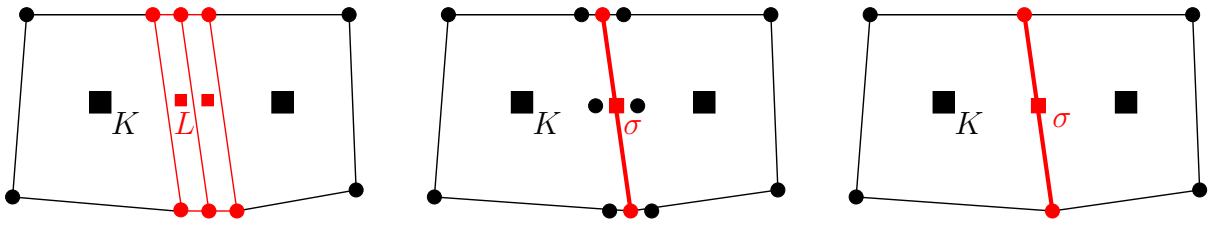

Figure 2.4: Illustration of d.o.f. in 2D for a matrix domain (in black) intersected by a fracture (in red) for the equi-dimensional and discontinuous and continuous hybrid-dimensional models (from left to right).

Equi-dimensional model. Since the equi-dimensional approach does not reduce the fracture dimension, we have to deal with small fracture cells. The standard VAG scheme, as introduced in [38] for single phase flow and in [39] for multiphase flows, which is based on cell and node unknowns, is used for this model.

Discontinuous hybrid-dimensional model. The set $dof_{\mathcal{D}_f}$ of fracture d.o.f. relate to face unknowns and node unknowns. This corresponds to the d.o.f. of the standard VAG scheme in dimension $d-1$ on the fracture network. Let us split $dof_{\mathcal{D}_m}$ in the interfacial d.o.f. $dof^{\Gamma}_{\mathcal{D}_m}$, located at the fracture network, and the bulk d.o.f. $dof_{\mathcal{D}_m} \setminus dof^{\Gamma}_{\mathcal{D}_m}$. The unknowns at the interfaces are necessary in order to capture the pressure discontinuities between the matrix and fractures. Since we have to take into account these pressure jumps for all fracture unknowns and all mf interfaces, $dof^{\Gamma}_{\mathcal{D}_m}$ refers to node unknowns plus face unknowns, which are related to the fracture d.o.f. one-to-one for each side of the DFN. Most often, the fractures cut the matrix domain in two. For immersed fracture tips or multiple fracture intersections, however, we have up to as many unknowns as fractures connected to the spot (cf. figure 2.5). The set $dof_{\mathcal{D}_m} \setminus dof^{\Gamma}_{\mathcal{D}_m}$ corresponds to cell unknowns and node unknowns, which are the classical unknowns for the VAG scheme in d dimensions. We refer to section 1.4., for a more detailed presentation.

Continuous hybrid-dimensional model. The set $dof_{\mathcal{D}}$ consisting of the model degrees of freedom, corresponds to cell, node and fracture face unknowns as illustrated in figure 2.4. These are the unknowns of the hybrid-dimensional models above, with the exception that $dof^{\Gamma}_{\mathcal{D}_m} = \emptyset$. For more details, we refer to [15].

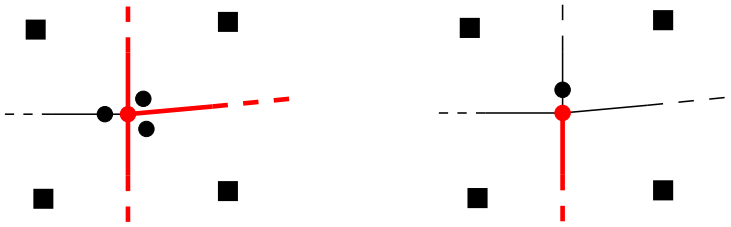

Figure 2.5: Zoom on the fracture intersection for three fractures (left) and on the fracture tip for one immersed fracture (right). Illustrated are four cells (indicated as boxes) and the d.o.f. at the singular point for the discontinuous hybrid-dimensional models (interfacial d.o.f. in black and fracture d.o.f. in red).

$\mathbb{P}_1$ Finite Element basis functions

The basis functions we use to discretize the diffusion terms, denoted by η_ν, $\nu \in dof_{\mathcal{D}}$, in the following, are the $\mathbb{P}_1$ Finite Element basis functions on the tetrahedral submesh $\mathcal{T}$, for $\nu \in dof_{\mathcal{D}_m}$ and on the triangulation Δ of the DFN, for $\nu \in dof_{\mathcal{D}_f}$. The discrete gradients are then defined as the $\mathbb{P}_1$ Finite Element gradients on each of the connected matrix subdomains and on the DFN, respectively. For the treatment of the jump terms at the matrix-fracture interfaces, the basis functions are lumped onto a dual mesh of the triangulation Δ. For a more detailed presentation of the construction of the basis functions and discrete gradients, we refer to 1.4, for the discontinuous and to [16] for the continuous hybrid-dimensional models. To respect the heterogeneities of the media, the *VAG* reconstructions of the accumulation terms are piecewise constant, as described below.

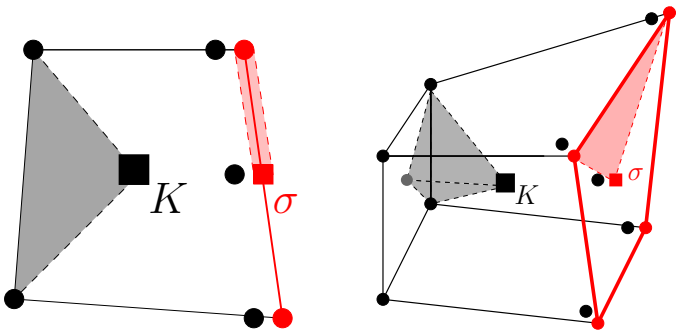

Figure 2.6: 2D (left) resp. 3D (right) cell K touching a fracture face σ. Illustration of the simplices on which the matrix (grey) and fracture (red) discrete gradients are constant. The facial unknown located at the coordinate in light grey is eliminated by barycentric interpolation.

Control volumes

As mentioned above, the mesh is conforming with the partition in rock types. So, we introduce, for any given $K \in \mathcal{M}$, a partition of K, which takes the general form $\{\omega_K^\nu\}_{\nu \in \{K\} \cup (dof_K \cap dof_{\mathcal{D}_m}) \setminus dof_{Dir}}$ and for any given $\sigma \in \mathcal{F}_\Gamma$ a partition

$\{\omega_\sigma^\nu\}_{\nu\in\{\sigma\}\cup(dof_\sigma\cap dof_{\mathcal{D}_f})\setminus dof_{Dir}}$ of σ. Here, dof_K and dof_σ stand for the d.o.f. connected to K and σ, respectively, as explained below. The *VAG* reconstructions of the accumulation terms are piecewise constant on these distributions, and therefore respect the heterogeneities of the media (see chapter 3). Integrating the reconstructed accumulations shows that, in the numerical scheme, we do not need to provide these partitions explicitly, but only have to define their corresponding volumes.

2.3.2 Finite Volume Formulation of the discontinuous hybrid-dimensional model

For $\nu \in dof_{\mathcal{D}}$, let us denote by $dof_\nu \subset dof_{\mathcal{D}}$ the set consisting of all ν', such that there is a discrete flux connection between ν and ν' as illustrated in figure 2.7. More concretely, for the the discontinuous hybrid-dimensional model, these sets are defined as follows (cf. also section 1.B). The denomination of the different types of d.o.f. (i.e. $K, \sigma, \nu_m, \nu'_m, \nu_f$) here is consistent with the notations in figure 2.7.

- For $K \in \mathcal{M}$: $dof_K = \{\nu_m \in dof_{\mathcal{D}_m} \setminus dof^\Gamma_{\mathcal{D}_m} \mid \mathbf{x}_{\nu_m} \in \partial K\} \cup \{\nu_m \in dof^\Gamma_{\mathcal{D}_m} \mid \mathbf{x}_{\nu_m} \in \partial K$ and ν_m refers to an interfacial unknown located on the same side of Γ as $K\}$
- For $\sigma \in \mathcal{F}_\Gamma$: $dof_\sigma = \{\nu_f \in dof_{\mathcal{D}_f} \mid \mathbf{x}_{\nu_f} \in \partial\sigma\} \cup \{\nu_m \in dof^\Gamma_{\mathcal{D}_m} \mid \mathbf{x}_{\nu_m} \in \partial\sigma\}$
- For $\nu_m \in dof^\Gamma_{\mathcal{D}_m}$: $dof_{\nu_m} = \mathcal{M}_{\nu_m} \cup \{\nu_f \in dof_{\mathcal{D}_f} \mid \mathbf{x}_{\nu_f} = \mathbf{x}_{\nu_m}\}$

Since the fluxes connect exactly two unknowns, the definition of the sets dof_ν is complemented by

$$\nu' \in dof_\nu \Longleftrightarrow \nu \in dof_{\nu'}. \tag{2.9}$$

The well defined constitutive relations for the mobilities and saturations for each of these rock types are then denoted by $k^\alpha(rt_\nu, \cdot)$ and $S^\alpha(rt_\nu, \cdot)$, $\nu \in \mathcal{M} \cup \mathcal{F}_\Gamma$, respectively. In order to calculate the fracture mobility for the non linear matrix-fracture two point fluxes of the discontinuous hybrid-dimensional model, for nodal unknowns, we have to define fracture node rock types, in addition to cell and fracture face rock types. The fracture node rock types serve exclusively for this purpose and its introduction is consistent with our pressure continuity assumption at fracture intersections which assumes that the properties of intersecting fractures are not too contrasted.

For any $\nu \in dof_K$ the discrete *matrix-matrix*-fluxes are defined as

$$F^\alpha_{K\nu}(u^1_{\mathcal{D}}, u^2_{\mathcal{D}}) = k^\alpha(rt_K, S^\alpha(rt_K, p_K))f^\alpha_{K\nu}(u^\alpha_{\mathcal{D}})^+ - k^\alpha(rt_K, S^\alpha(rt_K, p_\nu))f^\alpha_{K\nu}(u^\alpha_{\mathcal{D}})^-, \tag{2.10}$$

and $F^\alpha_{\nu K}(u^1_{\mathcal{D}}, u^2_{\mathcal{D}}) = -F^\alpha_{K\nu}(u^1_{\mathcal{D}}, u^2_{\mathcal{D}})$, where

$$-f^\alpha_{\nu K}(u^\alpha_{\mathcal{D}}) = f^\alpha_{K\nu}(u^\alpha_{\mathcal{D}}) = \sum_{\nu'\in dof_K} T_K^{\nu\nu'}(u^\alpha_K - u^\alpha_{\nu'} - \rho^\alpha(\mathbf{x}_K - \mathbf{x}_{\nu'}) \cdot \mathbf{g}),$$

with transmissivities

$$T_K^{\nu\nu'} = \int_K \Lambda_m \nabla\eta_\nu \nabla\eta_{\nu'} \mathrm{d}\mathbf{x}.$$

For all $\nu \in dof_\sigma$ the discrete *fracture-fracture*-fluxes are defined as

$$F^\alpha_{\sigma\nu}(u^1_{\mathcal{D}}, u^2_{\mathcal{D}}) = k^\alpha(rt_\sigma, S^\alpha(rt_\sigma, p_\sigma)) f^\alpha_{\sigma\nu}(u^\alpha_{\mathcal{D}})^+ - k^\alpha(rt_\sigma, S^\alpha(rt_\sigma, p_\nu)) f^\alpha_{\sigma\nu}(u^\alpha_{\mathcal{D}})^-,$$

and $F^\alpha_{\nu\sigma}(u^1_{\mathcal{D}}, u^2_{\mathcal{D}}) = -F^\alpha_{\sigma\nu}(u^1_{\mathcal{D}}, u^2_{\mathcal{D}})$, where

$$-f^\alpha_{\nu\sigma}(u^\alpha_{\mathcal{D}}) = f^\alpha_{\sigma\nu}(u^\alpha_{\mathcal{D}}) = \sum_{\nu' \in dof_\sigma} T^{\nu\nu'}_\sigma (u^\alpha_\sigma - u^\alpha_{\nu'} - \rho^\alpha(\mathbf{x}_\sigma - \mathbf{x}_{\nu'}) \cdot \mathbf{g}),$$

with transmissivities

$$T^{\nu\nu'}_\sigma = \int_\sigma d_f \Lambda_f \nabla_\tau \eta_\nu \nabla_\tau \eta_{\nu'} \mathrm{d}\tau(\mathbf{x}).$$

Let us further introduce the set of *matrix-fracture* (mf) connectivities

$$\mathcal{C} = \{(\nu_m, \nu_f) \,|\, \nu_m \in dof^\Gamma_{\mathcal{D}_m}, \nu_f \in dof_{\mathcal{D}_f} \text{ s.t. } \mathbf{x}_{\nu_m} = \mathbf{x}_{\nu_f}\}.$$

The mf-fluxes are defined as

$$F^\alpha_{\nu_m\nu_f}(u^1_{\mathcal{D}}, u^2_{\mathcal{D}}) = k^\alpha(rt_{\nu_f}, S^\alpha(rt_{\nu_f}, p_{\nu_m})) f^\alpha_{\nu_m\nu_f}(u^\alpha_{\mathcal{D}})^+ - k^\alpha(rt_{\nu_f}, S^\alpha(rt_{\nu_f}, p_{\nu_f})) f^\alpha_{\nu_m\nu_f}(u^\alpha_{\mathcal{D}})^-, \tag{2.11}$$

and $F^\alpha_{\nu_f\nu_m}(u^1_{\mathcal{D}}, u^2_{\mathcal{D}}) = -F^\alpha_{\nu_m\nu_f}(u^1_{\mathcal{D}}, u^2_{\mathcal{D}})$, where

$$-f^\alpha_{\nu_f\nu_m}(u^\alpha_{\mathcal{D}}) = f^\alpha_{\nu_m\nu_f}(u^\alpha_{\mathcal{D}}) = T_{\nu_m\nu_f}(u^\alpha_{\nu_m} - u^\alpha_{\nu_f} - \frac{\rho^\alpha d_f}{2} \gamma_{\mathbf{n}_\mathfrak{a}} \mathbf{g}),$$

with transmissivities

$$T_{\nu_m\nu_f} = \sum_{\substack{T \in \Delta \\ \text{s.t. } \mathbf{x}_{\nu_f} \in \overline{T}}} \frac{1}{3} \int_T \frac{2\lambda_{f,n}}{d_f} \mathrm{d}\tau(\mathbf{x}).$$

We observe that the fluxes $F^\alpha_{\nu_m\nu_f}$ are two point flux approximations.

Let $0 = t^0 < t^1 < \cdots < t^N = T$, with $\Delta t^n = t^n - t^{n-1}$ be a time discretization. Given $p^0_{\mathcal{D}} \in X_{\mathcal{D}}$, and using an implicit Euler time integration, the Finite Volume formulation of

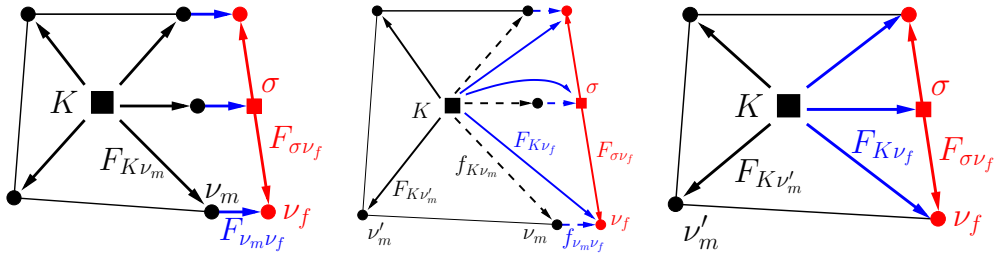

Figure 2.7: VAG *mm*-fluxes (black), *mf*-fluxes (blue) and *ff*-fluxes (red) on a 2D cell touching a fracture. Discontinuous hybrid-dimensional models 1 and 2 and continuous hybrid-dimensional model (from left to right). The fluxes indicated by solid lines and capital F correspond to non linear fluxes incorporating the mobility and appear in the flux conservation equations of each of the two control volumes they connect. The dashed fluxes f for the model 2, are linearly depending on the pressure. Consequently, the equations for interfacial $\nu_m \in dof^{\Gamma}_{\mathcal{D}_m}$ are the linear flux conservation equations (2.14), for this model.

(2.5),(2.7) reads as follows: Find $\{u^{\alpha}_{\mathcal{D}}\}_{\alpha=1,2} \in (X^0_{\mathcal{D}})^{2N}$ such that for all $n \in \{1,\dots,N\}$

$$
\begin{cases}
\text{for all } K \in \mathcal{M}: \\
\qquad |\omega^K_K|\phi_K \frac{S^{\alpha}(rt_K,p^n_K)-S^{\alpha}(rt_K,p^{n-1}_K)}{\Delta t^n} + \sum_{\nu\in dof_K} F^{\alpha}_{K\nu}(u^{1,n}_{\mathcal{D}},u^{2,n}_{\mathcal{D}}) = 0 \\
\text{for all } \nu_m \in dof_{\mathcal{D}_m} \setminus (\mathcal{M} \cup dof_{Dir_m}): \\
\qquad \sum_{K\in\mathcal{M}_{\nu_m}} |\omega^{\nu_m}_K|\phi_K \frac{S^{\alpha}(rt_K,p^n_{\nu_m})-S^{\alpha}(rt_K,p^{n-1}_{\nu_m})}{\Delta t^n} + \sum_{\nu\in dof_{\nu_m}} F^{\alpha}_{\nu_m\nu}(u^{1,n}_{\mathcal{D}},u^{2,n}_{\mathcal{D}}) = 0 \\
\text{for all } \sigma \in \mathcal{F}_{\Gamma}: \\
\qquad |\omega^{\sigma}_{\sigma}|\phi_{\sigma} \frac{S^{\alpha}(rt_{\sigma},p^n_{\sigma})-S^{\alpha}(rt_{\sigma},p^{n-1}_{\sigma})}{\Delta t^n} + \sum_{\nu\in dof_{\sigma}} F^{\alpha}_{\sigma\nu}(u^{1,n}_{\mathcal{D}},u^{2,n}_{\mathcal{D}}) = 0 \\
\text{for all } \nu_f \in dof_{\mathcal{D}_f} \setminus (\mathcal{F}_{\Gamma} \cup dof_{Dir_f}): \\
\qquad \sum_{\sigma\in\mathcal{F}_{\Gamma,\nu_f}} |\omega^{\nu_f}_{\sigma}|\phi_{\sigma} \frac{S^{\alpha}(rt_{\sigma},p^n_{\nu_f})-S^{\alpha}(rt_{\sigma},p^{n-1}_{\nu_f})}{\Delta t^n} + \sum_{\nu\in dof_{\nu_f}} F^{\alpha}_{\nu_f\nu}(u^{1,n}_{\mathcal{D}},u^{2,n}_{\mathcal{D}}) = 0.
\end{cases}
\tag{2.12}
$$

In (2.12), the set $\mathcal{M}_{\nu_m}$ stands for the set of indices $\{K \in \mathcal{M} \mid \nu_m \in dof_K\}$, and $\mathcal{F}_{\Gamma,\nu_f}$ stands for the set $\{\sigma \in \mathcal{F}_{\Gamma} \mid \nu_f \in dof_{\sigma}\}$. The model of this subsection will be referred to as the discontinuous hybrid-dimensional model 1, in the following.

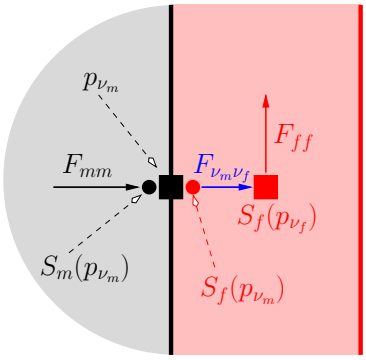

Figure 2.8: Model 1. Sketch of how VAG accounts for saturation jumps at the mf interfaces. The interfacial unknown is indicated by the black box and the fracture unknown by the red box. The capillary pressure p_{ν_m} for the interfacial unknown is well defined, which allows to calculate the matrix and fracture saturations at the interface, $S_m(p_{\nu_m})$ and $S_f(p_{\nu_m})$, respectively, as the inverse of the matrix and fracture capillary pressure curves. F_{mm} is calculated with $S_m(p_{\nu_m})$ and $F_{\nu_m\nu_f}$ is calculated with $S_f(p_{\nu_m})$.

2.3.3 mf-Linearization of the discontinuous hybrid-dimensional model

For practical considerations, the equations for the interfacial unknowns $\nu_m \in dof^{\Gamma}_{\mathcal{D}_m}$ are quite costly to solve, since the interfacial accumulation volumes $\bigcup_{K\in\mathcal{M}_{\nu_m}} \omega_{K,\nu_m}$ generally have to be chosen significantly smaller than the accumulation volumes at unknowns located inside the fractures. In this section, we propose a model that uses linear equations for $\nu_m \in dof^{\Gamma}_{\mathcal{D}_m}$ to calculate the phase pressures at the matrix-fracture interfaces. On the other hand, interfacial saturations are not calculated, but matrix-fracture mass transfer uses the saturations inside the fractures, instead.

As illustrated in figure 2.7 for the mf-linearized discontinuous hybrid-dimensional model, the non linear flux connections defined by the sets dof_ν are modified for $\nu \in dof_{\mathcal{D}} \setminus dof^{\Gamma}_{\mathcal{D}_m}$ as follows:

- For $K \in \mathcal{M}$: $dof_K = \{\nu \in dof_{\mathcal{D}} \setminus dof^{\Gamma}_{\mathcal{D}_m} \mid \mathbf{x}_\nu \in \partial K\}$
- For $\sigma \in \mathcal{F}_\Gamma$: $dof_\sigma = \{\nu_f \in dof_{\mathcal{D}_f} \mid \mathbf{x}_{\nu_f} \in \partial\sigma\} \cup \mathcal{M}_\sigma$

together with the relation (2.9) for $\nu \in dof_{\mathcal{D}} \setminus dof^{\Gamma}_{\mathcal{D}_m}$.

Let us denote by $\nu_f(\nu_m) \in dof_{\mathcal{D}_f}$ for each $\nu_m \in dof^{\Gamma}_{\mathcal{D}_m}$, the unique d.o.f. $\nu_f \in dof_{\mathcal{D}_f}$ such that $\mathbf{x}_{\nu_m} = \mathbf{x}_{\nu_f}$. Unlike for the discontinuous hybrid-dimensional model 1, the d.o.f. $\nu_m \in dof^{\Gamma}_{\mathcal{D}_m}$ are not linked to their neighbours via non linear fluxes. Also, in the above definition (see also figure 2.7), for $K \in \mathcal{M}_{\nu_m}$, ν_m is replaced by $\nu_f(\nu_m)$ in dof_K (and K is added to $dof_{\nu_f(\nu_m)}$). The mass exchange between matrix and DFN is accounted for by the non linear fluxes

$$F^{\alpha}_{K\nu_f}(u^1_{\mathcal{D}}, u^2_{\mathcal{D}}) = k^{\alpha}(rt_K, S^{\alpha}(rt_K, p_K)) \cdot f^{\alpha}_{K\nu_m}(u^{\alpha}_{\mathcal{D}})^+ - k^{\alpha}(rt_K, S^{\alpha}(rt_K, p_{\nu_f})) \cdot f^{\alpha}_{K\nu_m}(u^{\alpha}_{\mathcal{D}})^-, \tag{2.13}$$

with $\nu_f = \nu_f(\nu_m)$ and $K \in \mathcal{M}_{\nu_m}$. Note that the definition (2.13) uses the linear fluxes $f^{\alpha}_{K\nu_m}$ to construct the non linear flux $F^{\alpha}_{K\nu_f}$. This is the key difference between this model and the continuous pressure model, which means that pressure discontinuities are accounted for in the matrix-fracture mass exchange fluxes. For the mf-linearized model,

the interfacial control volumes are set to zero, i.e. $\omega_{\nu_m} = \emptyset$ for $\nu_m \in dof^{\Gamma}_{\mathcal{D}_m}$. Equation (2.12) becomes (for all $n \in \{1, \dots, N\}$)

$$\sum_{K \in \mathcal{M}_{\nu_m}} f^{\alpha}_{K\nu_m}(u^{\alpha,n}_{\mathcal{D}}) = f^{\alpha}_{\nu_m\nu_f}(u^{\alpha,n}_{\mathcal{D}}) \qquad \text{for all } \nu_m \in dof^{\Gamma}_{\mathcal{D}_m}, \tag{2.14}$$

again with $\nu_f = \nu_f(\nu_m)$. We see that the non linear equations have been replaced by linear equations for the interfacial unknowns, which constitutes the main advantage of this model compared with the non-linearized discontinuous hybrid-dimensional model. This is equivalent to the procedure of eliminating interfacial unknowns by harmonic averaging of the half transmissibilities for cell centered schemes, as described in [54], for example. This model will be referred to as the discontinuous hybrid-dimensional model 2, in the following.

2.3.4 Finite Volume Formulation of the continuous hybrid-dimensional model

Recall that for this model, $dof^{\Gamma}_{\mathcal{D}_m} = \emptyset$. For $K \in \mathcal{M}$ and $\nu \in dof_K \cap dof_{\mathcal{D}_f}$, we define $F_{K\nu}$ similarly to (2.13), but without taking into account the interfacial pressures:

$$F^{\alpha}_{K\nu}(u^1_{\mathcal{D}}, u^2_{\mathcal{D}}) = k^{\alpha}(rt_K, S^{\alpha}(rt_K, p_K)) \cdot f^{\alpha}_{K\nu}(u^{\alpha}_{\mathcal{D}})^{+} - k^{\alpha}(rt_K, S^{\alpha}(rt_K, p_\nu)) \cdot f^{\alpha}_{K\nu}(u^{\alpha}_{\mathcal{D}})^{-}.$$

Note that this model can also be obtained from the mf-linearized discontinuous hybrid-dimensional model by replacing the interfacial equations (2.14) by the continuity of the phase pressures

$$u^{\alpha}_{\nu_m} = u^{\alpha}_{\nu_f(\nu_m)} \text{ for all } \nu_m \in dof^{\Gamma}_{\mathcal{D}_m}.$$

2.4 Tracer test case

The models in this section describe the transport of a tracer in a solvant through fractured porous media. It can be seen as a special case of the two phase flow models presented above assuming that the phase mobilities satisfy $k^{\alpha}(S^{\alpha}) = S^{\alpha}$, that the capillarity vanishes and that the gravity field is set to zero. In the following, the primary unknowns are denoted by u for the pressure and c for the tracer concentration.

2.4.1 Analytical solution for the hybrid-dimensional model

Let us denote by (x, y) the Cartesian coordinates of $\mathbf{x}$ and let us set $\Omega = (0, 1)^2$, $\mathbf{x}_1 = (0, \frac{1}{4})$, $\theta \in (0, \arctan(\frac{3}{4}))$, $\mathbf{x}_2 = (1, \frac{1}{4} + \tan(\theta))$. Let $\Omega_1 = \{(x, y) \in \Omega \,|\, y > \frac{1}{4} + x\tan(\theta)\}$, and $\Omega_2 = \Omega \setminus \overline{\Omega}_1$. We consider a single fracture defined by $\Gamma = (\mathbf{x}_1, \mathbf{x}_2) = \partial\Omega_1 \cap \partial\Omega_2$ with tangential permeability $\lambda_f > 0$, normal permeability $\lambda_{f,n}$ and width $d_f > 0$. The matrix

permeability is isotropic and set to $\lambda_m = 1$. The matrix and fracture porosities are set to $\phi_m = 1$ and $\phi_f = 1$. Let us denote the tangential and normal vectors to Γ by

$$\mathbf{t} = \begin{pmatrix} \cos(\theta) \\ \sin(\theta) \end{pmatrix}, \quad \mathbf{n} = \begin{pmatrix} -\sin(\theta) \\ \cos(\theta). \end{pmatrix}$$

Looking for a pressure solution equal to $u_{m,k}(x,y) = -x + \gamma_k$ in the matrix domains Ω_k, $k = 1, 2$, and to $u_f = 1 - x$ in the fracture leads to

$$\gamma_1 = 1 + \frac{\sin(\theta)}{2} d_f \frac{\lambda_m}{\lambda_{f,\mathbf{n}}}, \quad \gamma_2 = 1 - \frac{\sin(\theta)}{2} d_f \frac{\lambda_m}{\lambda_{f,\mathbf{n}}}.$$

for the discontinuous hybrid-dimensional models and to

$$\gamma_1 = \gamma_2 = 1$$

for the continuous hybrid-dimensional model $(u_{m,1}, u_{m,2}, u_f)$ are solutions of the corresponding stationary pressure models, see chapter 1 and [17], respectively). We deduce that the matrix velocity is equal to

$$\mathbf{q}_m = \lambda_m \begin{pmatrix} 1 \\ 0 \end{pmatrix},$$

and the tangential velocity in the fracture to

$$\mathbf{q}_f = d_f \lambda_f \cos(\theta) \mathbf{t}.$$

Note that the velocity fields are the same for the discontinuous and continuous hybrid-dimensional models. The transport model reduces, for the three hybrid-dimensional models presented in section 2.2, to the same following system of equations which specifies our choice of the boundary and initial conditions:

$$\begin{cases} \partial_t c_{m,k}(x,y,t) + \partial_x c_{m,k}(x,y,t) = 0 & \text{on } \Omega_k \times (0,T),\ k = 1,2, \\ c_{m,k}(x,y,0) = 0 & \text{on } \Omega_k,\ k = 1,2, \\ c_{m,1}(0,y,t) = 1 & \text{on } (\frac{1}{4},1) \times (0,T), \\ c_{m,2}(0,y,t) = 1 & \text{on } (0,\frac{1}{4}) \times (0,T), \\ c_{m,2}(x, \frac{1}{4} + x\tan(\theta), t) = c_f(x,t) & \text{on } (0,1) \times (0,T), \\ \partial_t c_f(x,t) + k\partial_x c_f(x,t) + \beta c_f(x,t) & \\ \quad = \beta c_{m,1}(x, \frac{1}{4} + x\tan(\theta), t) & \text{on } (0,1) \times (0,T), \\ c_f(0,t) = 1 & \text{on } (0,T), \\ c_f(x,0) = 0 & \text{on } (0,1), \end{cases} \tag{2.15}$$

where we have set $\lambda_m = 1$ and with $\beta = \frac{\sin(\theta)}{d_f}$ and $k = \lambda_f \cos^2(\theta)$. It is assumed that $k > 1$. This system can be integrated along the characteristics of the matrix and fracture velocity fields leading to the following analytical solution:

$$c_{m,1}(x,y,t) = \begin{cases} 0 \text{ if } & t < x, \\ 1 \text{ if } & t > x, \end{cases}$$

$$c_f(x,t) = \begin{cases} 0 & \text{if } t < \frac{x}{k}, \\ e^{-\frac{\beta}{k-1}(x-t)} & \text{if } \frac{x}{k} < t < x, \\ 1 & \text{if } t > x, \end{cases}$$

$$c_{m,2}(x,y,t) = \begin{cases} \text{if } y \in (0, \frac{1}{4}) \begin{cases} 0 \text{ if } t < x, \\ 1 \text{ if } t > x, \end{cases} \\ \text{if } y \in (\frac{1}{4}, \frac{1}{4} + \tan(\theta)) \begin{cases} 0 & \text{if } t < x - \frac{4y-1}{4\tan(\theta)}, \\ c_f(\frac{4y-1}{4\tan(\theta)}, t + \frac{4y-1}{4\tan(\theta)} - x) & \text{if } t > x - \frac{4y-1}{4\tan(\theta)}. \end{cases} \end{cases}$$

2.4.2 Analytical solution for the equi-dimensional model

Let us set $d = \frac{d_f}{\cos(\theta)}$ and denote by

$$\widetilde{\Omega}_f = \{(x,y) \in \Omega \,|\, y - x\tan(\theta) - \frac{1}{4} \in (-\frac{d}{2}, \frac{d}{2})\},$$

the fracture domain, and by $\widetilde{\Omega}_1 = \{(x,y) \in \Omega \,|\, y > \frac{d}{2} + \frac{1}{4} + x\tan(\theta)\}$, and $\widetilde{\Omega}_2 = \{(x,y) \in \Omega \,|\, y < -\frac{d}{2} + \frac{1}{4} + x\tan(\theta)\}$ the matrix domains. We look for a pressure solution $u_{m,k} = -x + \bar{\gamma}_k$ in the matrix domains $\widetilde{\Omega}_k$, $k = 1, 2$ and

$$u_f = 1 - \alpha_f(\mathbf{x}\cdot\mathbf{t} - \frac{\sin(\theta)}{4})\mathbf{t} + \beta_f(\mathbf{x}\cdot\mathbf{n} - \frac{\cos(\theta)}{4})\mathbf{n},$$

in the fracture domain. It results that $\alpha_f = \cos(\theta)$ and

$$\beta_f = \sin(\theta)\frac{\lambda_m}{\lambda_{f,\mathbf{n}}},$$

and

$$\bar{\gamma}_1 = 1 - (1 - \frac{\lambda_m}{\lambda_{f,\mathbf{n}}})\frac{d_f\sin(\theta)}{2} = \gamma_1 - \frac{d_f\sin(\theta)}{2},$$
$$\bar{\gamma}_2 = 1 + (1 - \frac{\lambda_m}{\lambda_{f,\mathbf{n}}})\frac{d_f\sin(\theta)}{2} = \gamma_2 + \frac{d_f\sin(\theta)}{2}.$$

We deduce that the pressure in the fracture domain is

$$u_f(\mathbf{x}) = 1 - x - \sin(\theta)(1 - \frac{\lambda_m}{\lambda_{f,\mathbf{n}}})d_\Gamma(\mathbf{x})$$

where $d_\Gamma(\mathbf{x}) = \mathbf{x}\cdot\mathbf{n} - \frac{\cos(\theta)}{4}$ is the distance between $\mathbf{x}$ and Γ, and that the velocity field in the matrix is

$$\mathbf{q}_m = \lambda_m \begin{pmatrix} 1 \\ 0 \end{pmatrix},$$

and in the fracture

$$\mathbf{v}_f = -\Lambda_f \nabla u_f = \lambda_f \cos(\theta)\mathbf{t} - \lambda_m \sin(\theta)\mathbf{n}.$$

Note that $\mathbf{v}_f$ is exactly equal to the tangential velocity $\frac{\mathbf{q}_f}{d_f}$ of the hybrid model plus the normal velocity $\mathbf{q}_m \cdot \mathbf{n} = -\lambda_m \sin(\theta)\mathbf{n}$ of the hybrid model. In that sense, the velocity fields are the same both in the matrix and in the fracture for the equi and hybrid-dimensional models for this test case. Also remark that the mean pressure in the width of the fracture is exactly equal to $1 - x$ (except at both ends of the fracture).

Let $\mathbf{v}(\mathbf{x})$ denote the velocity field equal to $\mathbf{q}_m$ in the matrix domains and to $\mathbf{v}_f$ in the fracture domain. The equi-dimensional tracer c is solution of the advection equation

$$\partial_t c + \operatorname{div}(c\mathbf{v}) = 0,$$

with initial condition $c = 0$ on Ω and input condition $c = 1$ on the left boundary $x = 0$. It can be easily computed analytically using the method of characteristics.

2.4.3 Comparisons between the equi and hybrid tracer solutions

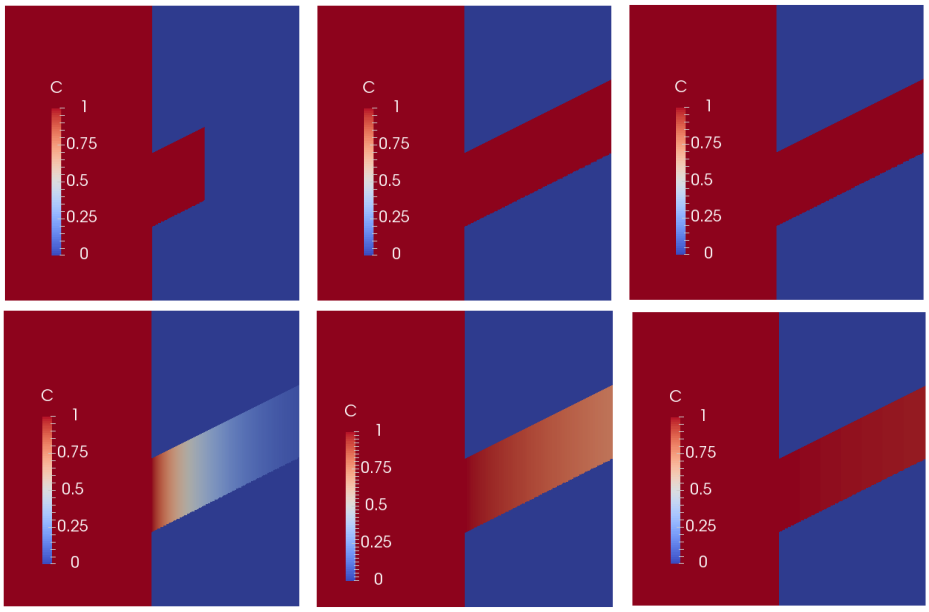

Figure 2.9: Comparisons of the equi-dimensional (above) and hybrid-dimensional (below) tracer analytical solutions at time $t = 0.5$ for $d_f = 0.001$, $\lambda_m = 1$, and λ_f taking the values from left to right 100, 1000 and 10000.

It is clear from Figures (2.9) and (2.11) that the hybrid-dimensional tracer model is accurate as long as the ratio of the fracture and matrix conductivities defined by $\frac{d_f}{L}\frac{\lambda_f}{\lambda_m}$ is large enough where $L = 1$ denotes the characteristic length of the matrix domain. In this test case, the hybrid-dimensional tracer model provides a very accurate solution

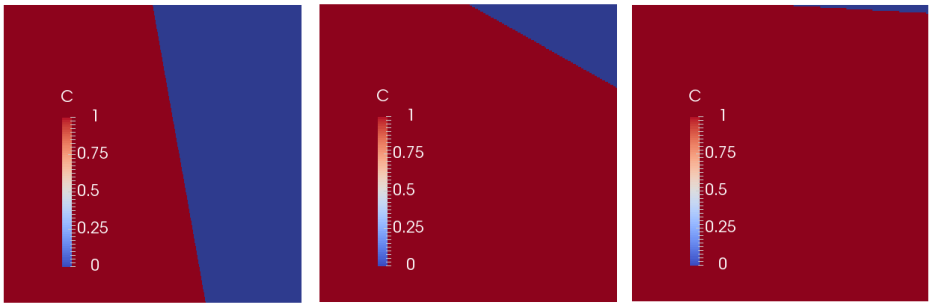

Figure 2.10: Tracer analytical solution in the fracture for the equi-dimensional model at time $t = 0.5$ for $d_f = 0.001$, $\lambda_m = 1$, and λ_f taking the values from left to right 100, 1000 and 10000.

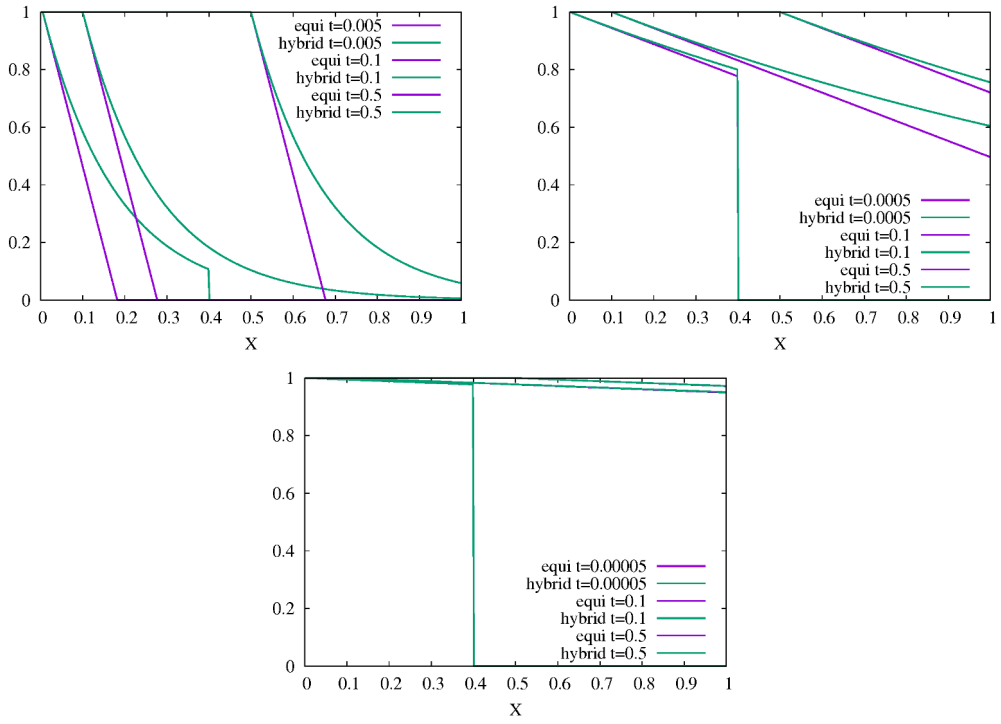

Figure 2.11: Comparisons of the equi and hybrid-dimensional tracer analytical solutions in the fracture at different times as a function of x. The value is averaged in the width of the fracture for the equi-dimensional model. The parameters are set to $d_f = 0.001$, $\lambda_m = 1$, and $\lambda_f = 100, 1000, 10000$ from left to right.

for $\frac{d_f}{L}\frac{\lambda_f}{\lambda_m} = 10$, a rather good one for $\frac{d_f}{L}\frac{\lambda_f}{\lambda_m} = 1$ and shows rather large differences for $\frac{d_f}{L}\frac{\lambda_f}{\lambda_m} = 0.1$.

Geometrically, the condition of a large fracture matrix conductivity ratio $\frac{d_f}{L}\frac{\lambda_f}{\lambda_m}$ means

that the velocity in the fracture $\mathbf{v}_f$ is almost parallel to the fracture Γ. More precisely, it prescribes that the angle between $\mathbf{v}_f$ and $\mathbf{t}$ is small compared with the angle between $\mathbf{t}$ and the ligne joining the bottom left point of the fracture $(0, \frac{1}{4} - \frac{d}{2})$ to the upper right point of the fracture $(1, \frac{1}{4} + \tan(\theta) + \frac{d}{2})$.

2.4.4 Comparisons between the hybrid tracer solution and the equi-dimensional tracer solution with normal diffusion in the fracture

In this test case, a normal diffusion term is added for the equi-dimensional tracer model in the fracture only. The objective is to investigate the amount of normal diffusion needed in the equi-dimensional tracer model to obtain a solution close to the hybrid-dimensional tracer model without diffusion. Since in that case the analytical solution is not known, the solution of the equi-dimensional model is computed numerically using the VAG discretization and an implicit Euler time integration. We consider the above test case with $d_f = 1$ and $\lambda_f = 100$ which exhibits rather large differences between the hybrid and the equi-dimensional tracer models without the additional diffusion term. Let $\mathbf{n}_\Gamma$ denote the unit vector normal to the fracture. A diffusion term $-\mathrm{div}(D_{f,n}\mathbf{n}_\Gamma \otimes \mathbf{n}_\Gamma \nabla c)$ is added in the equi-dimensional tracer model.

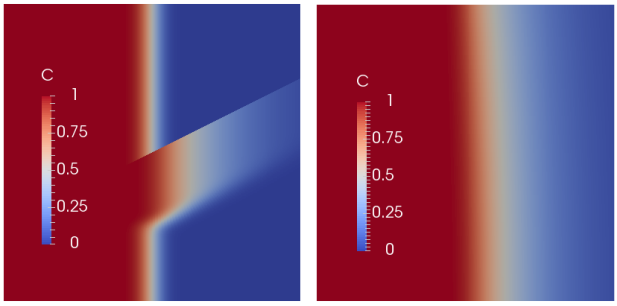

Figure 2.12: Tracer numerical solution at time $t = 0.5$ in the matrix (left) and in the fracture (right) for the equi-dimensional model with normal diffusion in the fracture $D_{f,n} = 0.001$ and for $d_f = 0.001$, $\lambda_m = 1$, and $\lambda_f = 100$.

It is clear from Figures 2.12 and 2.13 and the comparison with the figures of the previous subsection that the normal diffusion in the fracture provides an equi-dimensional solution much closer to the hybrid-dimensional tracer model for the parameters $\lambda_f = 100$, $d_f = 0.001$. This is expected since the hybrid-dimensional tracer model is derived assuming that the tracer concentration is constant in the width of the fractures corresponding to a high normal diffusion $D_{f,n}$ scaled by the fracture width d_f times the normal velocity $|q_m \cdot \mathbf{n}_\Gamma|$. In our test case, this adimensionalized normal diffusion $\frac{D_{f,n}}{d_f |q_m \cdot \mathbf{n}_\Gamma|}$ takes the value $\sqrt{5}$ which suffices to recover a very good match between the equi and hybrid-dimensional models even for a rather small fracture matrix conductivity ratio $\frac{d_f}{L}\frac{\lambda_f}{\lambda_m} = 0.1$.

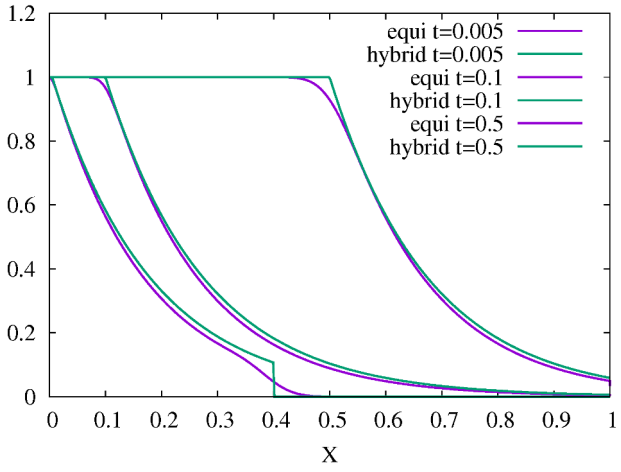

Figure 2.13: For $d_f = 0.001$, $\lambda_m = 1$, and $\lambda_f = 100$, comparison of the mean tracer solution in the fracture for the equi-dimensional model (numerical) with normal diffusion in the fracture $D_{f,n} = 0.001$ and the hybrid-dimensional mode (analytical).

2.5 Two Phase Flow Test Cases

We present in this section a series of test cases for diphasic flow through a fractured 2 dimensional reservoir of geometry as shown in figure 2.14. The domain Ω is of extension $(0, 400)m \times (0, 800)m$ and the fracture width is assumed to be constantly $d_f = 4m$. This corresponds to the width of a fault, although we will keep the terminology fracture in the following. We consider isotropic permeability in the matrix and in the fractures. All tests have in common that initially, the reservoir is saturated with water (density $1000\frac{kg}{m^3}$, viscosity $0.001Pa.s$) and oil (density $700\frac{kg}{m^3}$, viscosity $0.005Pa.s$) is injected in the bottom fracture, which is managed by imposing non-homogeneous Neumann conditions at the injection location. The oil then rises by gravity, thanks to its lower density compared to water and by the overpressure induced by the imposed injection rate. Also, Dirichlet boundary conditions are imposed at the upper boundary of the domain. Elsewhere, we have homogeneous Neumann conditions. The following test cases present a variety of geological and physical configurations in regard to matrix and fracture permeabilities and capillary pressure curves.

We use the VAG discretization to obtain solutions for four different models for this two phase flow test case. In the first model, fractures are represented as geological structures of equal dimension as the matrix and therefore, we refer to this model as the equi-dimensional model. The second and third models are the models that we presented in the first part of this chapter, referred to as discontinuous hybrid-dimensional models 1 and 2, since pressure jumps at the matrix-fracture interfaces are allowed. The fourth model is the continuous hybrid-dimensional model, presented in [16] and recalled in this chapter, which assumes pressure continuity across the fractures.

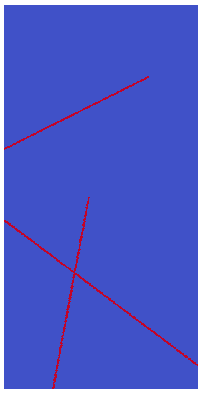

Figure 2.14: Geometry of the reservoir under consideration. DFN in red and matrix domain in blue. $\Omega = (0, 400)\text{m} \times (0, 800)\text{m}$ and $d_f = 4\text{m}$.

The tests are driven on triangular meshes, extended to 3D prismatic meshes by adding a second layer of nodes as a translation of the original nodes in normal direction to the plane of the original 2D domain. Hence, we double the number of nodal unknowns, while keeping the number of cell and face unknowns constant (cf. table 2.1). In order to account for the stratification of saturation in normal direction inside the fractures, which can play a major role in the flow process (see below), we need at least two layers of cells in the fractures for the equi-dimensional model, to obtain valid reference solutions. Obviously, the larger number of cells for the equi-dimensional mesh is due to the need of tiny cells inside the DFN. In this regard, it is worth to mention that, with the hybrid-dimensional models, the size of fracture faces is not restricted by the fracture width, while with the equi-dimensional model, the fracture width imposes an upper bound for the size of faces between the matrix and the fracture, due to mesh regularity. However, the mesh size of all meshes is of the order of the fracture width, here. The mesh for the hybrid-dimensional models is the same, but the number of degrees of freedom differs. The supplementary degrees of freedom for the discontinuous models are located at the matrix-fracture intersections and capture the pressure discontinuities, as described in the previous section.

The discrete problem is solved implicitly, where the non-linear system of equations occurring at each time step is solved via the Newton algorithm with relaxation. The stopping criterion is $crit^{rel}_{Newton}$ on the (L^1) relative residual. The resolution of the linear systems is performed by the GMRes solver (with stopping criterion $crit^{rel}_{GMRes}$ on the relative residual), preconditioned by CPR-AMG. The time loop uses adaptive time stepping, i.e. the objective for the (max per d.o.f.) change in saturation per time step, ΔS_{obj}, is given and from this the time step is deduced under the condition that it does neither exceed a given maximal time step Δt_{max} nor 1.2 times the time step of the previous iteration. Also, if at a given time iteration the Newton algorithm does not converge after 35 iterations, then the actual time step is divided by 2 and the time iteration is repeated. The number of time step failures at the end of a simulation is indicated by $\mathbf{N}_{Chop}$.

Model	Nb Cells	Nb dof	Nb dof el.
equi dim.	22477	45315	22838
disc. hybrid	16889	35355	18466
cont. hybrid	16889	34291	17402

Table 2.1: **Nb Cells** is the number of cells of the mesh; **Nb dof** is the number of d.o.f. (with two physical primary unknowns per d.o.f.); **Nb dof el.** is the number of d.o.f. after elimination of cell unknowns without fill-in.

The numerical parameters are chosen as follows:

Model	$crit^{rel}_{Newton}$	$crit^{rel}_{GMRes}$	ΔS_{obj}	Δt_{max}
equi dim.	$1.E{-}5$	$1.E{-}6$	0.5	$10d$
disc. hybrid 1	$1.E{-}6$	$1.E{-}6$	0.5	$10d$
disc. 2 / cont. hybrid	$1.E{-}6$	$1.E{-}6$	0.5	$60d$

Table 2.2: Numerical parameters.

2.5.1 Comparisons between the equi and hybrid-dimensional solutions for gravity dominated flow with zero capillary pressure

In this test case, we neglect capillary effects by setting the capillary pressure to zero. To solve this problem, we use the matrix and fracture pressure and saturation (for, say, the non-wetting phase) as primary unknowns. The following geological configuration is considered. In the matrix domain, permeability is isotropic of 0.1 Darcy and porosity is 0.2. In the DFN, permeability is isotropic of 100.0 Darcy and porosity is 0.4.

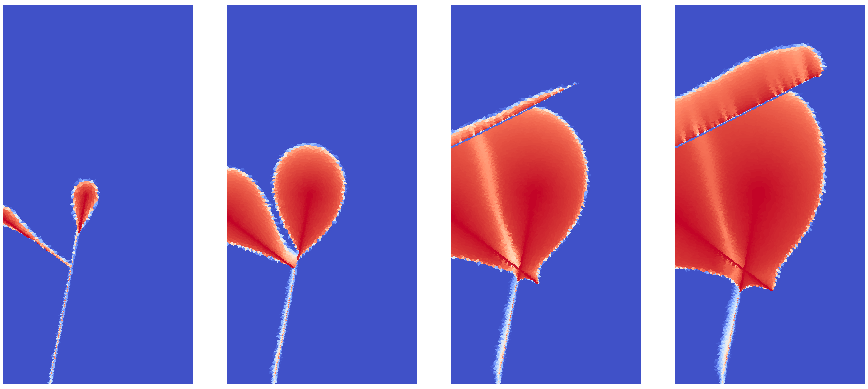

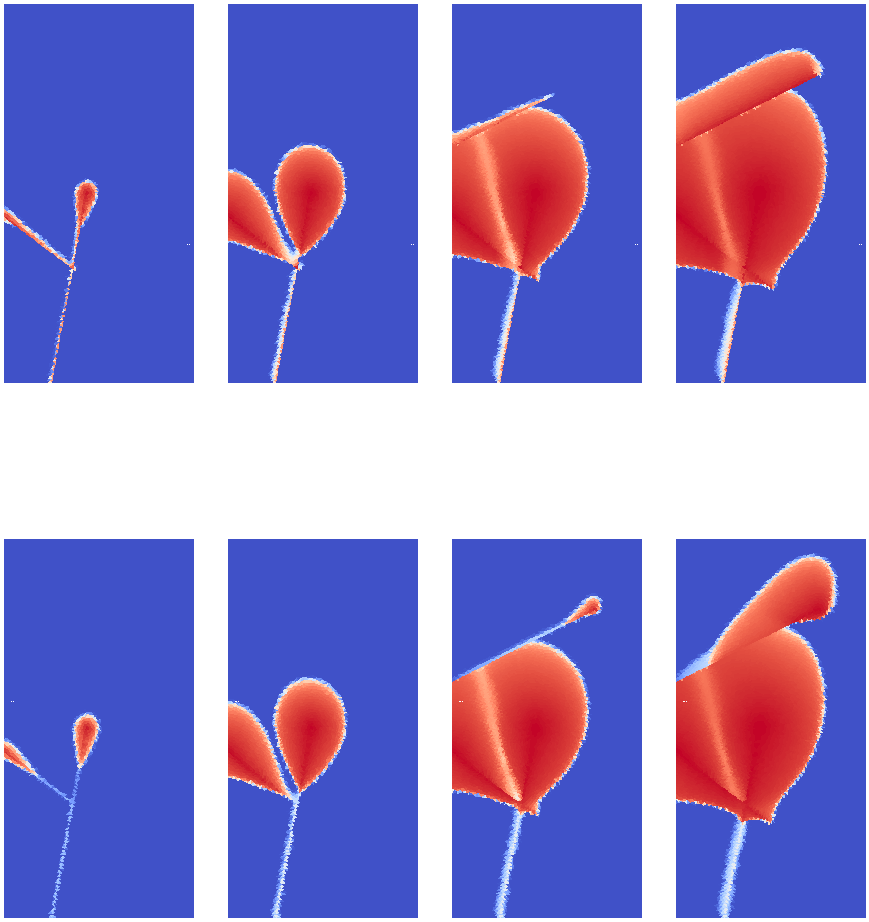

Figure 2.15: Comparison of the equi-dimensional (first line), discontinuous hybrid-dimensional 1 (mid line) and discontinuous 2 / continuous hybrid-dimensional (last line) numerical solutions for oil saturation at times $t = 360, 1800, 3600, 5400$ days (from left to right). Zero matrix and fracture capillary pressures and mf permeability ratio $\lambda_f/\lambda_m = 1000$.

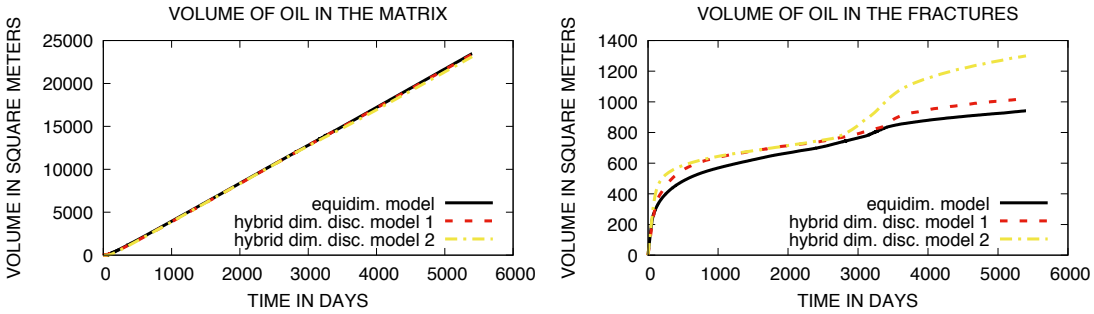

Figure 2.16: Comparison of the equi-dimensional and hybrid-dimensional matrix and fracture volumes occupied by oil as a function of time. Zero matrix and fracture capillary pressures and mf permeability ratio $\lambda_f/\lambda_m = 1000$.

Model	$\mathbf{N}_{\Delta t}$	$\mathbf{N}_{Newton}$	$\mathbf{N}_{Chop}$
equi dim.	1270	8927	71
disc. hybrid 1	907	5023	48
disc. hybrid 2	182	1593	0
cont. hybrid	149	1356	0

Table 2.3: $\mathbf{N}_{\Delta t}$ is the number of successful time steps; $\mathbf{N}_{Newton}$ is the total number of Newton iterations (for successful time steps); $\mathbf{N}_{Chop}$ is the number of time step chops. Zero matrix and fracture capillary pressures and mf permeability ratio $\lambda_f/\lambda_m = 1000$.

This test case shows impressively, how the incorporation of non linear normal fluxes at the mf intersections of the discontinuous hybrid-dimensional model 1 allows to get much closer to the equi-dimensional reference solution than the discontinuous 2 and continuous hybrid-dimensional models. Only one solution is presented for the discontinuous 2 and continuous hybrid-dimensional, since both models produce almost indistinguishable results. The supplementary unknowns at the mf interfaces enable us to capture the segregation of saturation inside the DFN (due to gravity, here). In this view, the supplementary d.o.f. appear as a mesh refinement at the mf interfaces, that allows to reproduce the transport in normal direction to the DFN, which is not the case for the discontinuous 2 and continuous hybrid-dimensional models, since there, saturations at the interfaces are not calculated, but fracture saturations are used for the upwinding in the non linear mf fluxes. In the gravity dominated test case shown in figure 2.15, this becomes particularly important, when gravitational acceleration is in a steep angle to the fracture network, which can be observed at the upper fracture. The drawback of this feature is that we have to deal with small accumulation volumes at the mf intersections, which is reflected in terms of robustness, but the hybrid-dimensional model is still much more robust than the full equi-dimensional model. The absence of capillarity, of course, emphasizes this difference between the hybrid-dimensional models, since at the mf interfaces, the matrix

does not behave as a capillary barrier (saturation does not jump) and nothing holds back the oil from leaving the DFN. Also no capillary diffusion inside the fracture prevents the gravity segregation effect in the normal direction of the fracture.

2.5.2 Comparisons between the equi and hybrid-dimensional solutions for gravity dominated flow with discontinuous capillary pressure

The tests presented here account for capillarity. Inside the matrix domain the capillary pressure function is given by Corey's law $p_m = -a_m \log(1 - S_m^1)$. Inside the fracture network, we suppose $p_f = -a_f \log(1 - S_f^1)$. The hybrid-dimensional models presented in the previous part of this chapter are built to account for saturation jumps at the matrix-fracture interfaces (cf. figure 2.3). To treat the degenerated case of $a_f = 0$, we adopt a novel variable switch technique presented in [17]. This consists of introducing generalized variables as primary unknowns, that are used to parametrize the saturation and capillary pressure curves in order to avoid singularities at the heterogeneities. As a counterpart, for the discontinuous hybrid-dimensional model 1, the derivatives w.r.t. the generalized variables of the saturation at the matrix side of the mf interfaces is zero, for certain values of these generalized variables. To ensure a non singular Jacobian, we replace the accumulation terms occurring in the equations (2.12) for $\nu_m \in dof_{\mathcal{D}_m}^{\Gamma}$ by

$$\frac{1}{2} \sum_{K \in \mathcal{M}_{\nu_m}} |\omega_{K,\nu_m}| \phi_K \Big(\frac{S^\alpha(rt_K, p_{\nu_m}^n) - S^\alpha(rt_K, p_{\nu_m}^{n-1})}{\Delta t^n} + \frac{S^\alpha(rt_{\nu_f}, p_{\nu_m}^n) - S^\alpha(rt_{\nu_f}, p_{\nu_m}^{n-1})}{\Delta t^n} \Big)$$

with $\nu_f = \nu_f(\nu_m)$. This formula is volume conservative. It is important to note that the interfacial volumes $\omega_K^{\nu_m}$, $\nu_m \in dof_{\mathcal{D}_m}^{\Gamma}$, have to be chosen small in comparison with the fracture volumes. Otherwise, the discretization would artificially widen the drain, as discussed in [17] for the continuous hybrid-dimensional model.

drain-matrix permeability ratio of 1000

The geological setting is as follows. In the matrix domain, permeability is isotropic of 0.1 Darcy and porosity is 0.2. In the DFN, permeability is isotropic of 100.0 Darcy and porosity is 0.4. The Corey parameters are $a_m = 10^5$ and $a_f = 0$.

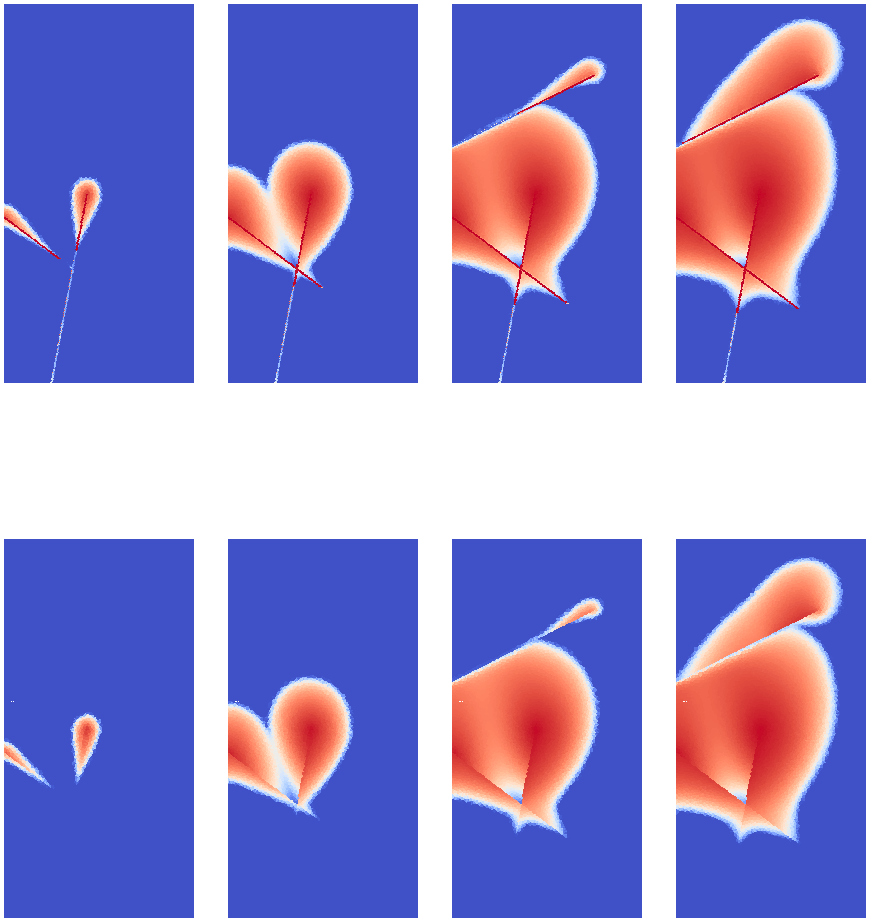

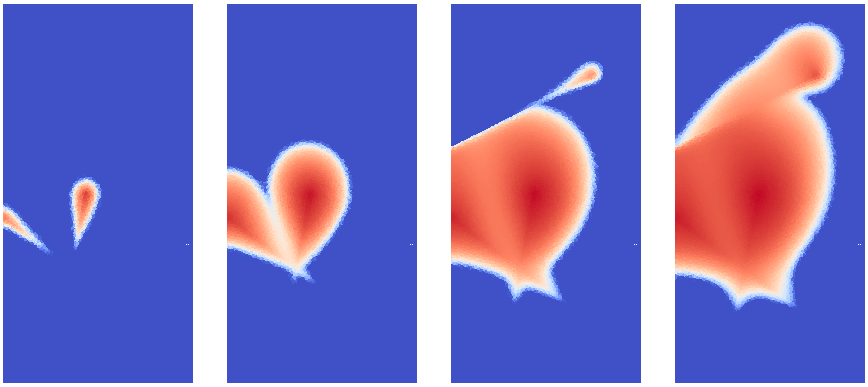

Figure 2.17: Comparison of the equi-dimensional (first line), discontinuous hybrid-dimensional 1 (mid line) and discontinuous 2 / continuous hybrid-dimensional (last line) numerical solutions for oil saturation at times $t = 360, 1800, 3600, 5400$ days (from left to right). Corey parameters are $a_m = 10^5$, $a_f = 0$ and mf permeability ratio $\lambda_f/\lambda_m = 1000$.

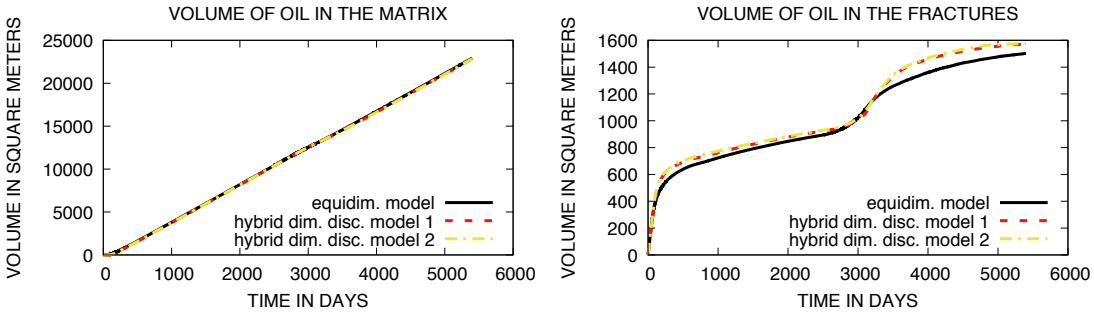

Figure 2.18: Comparison of the equi-dimensional and hybrid-dimensional matrix and fracture volumes occupied by oil as a function of time. Corey parameters are $a_m = 10^5$, $a_f = 0$ and mf permeability ratio $\lambda_f/\lambda_m = 1000$.

Model	$\mathbf{N}_{\Delta t}$	$\mathbf{N}_{Newton}$	$\mathbf{N}_{Chop}$
equi dim.	3054	18993	406
disc. hybrid 1	1530	7839	20
disc. hybrid 2	271	2010	1
cont. hybrid	149	1477	0

Table 2.4: $\mathbf{N}_{\Delta t}$ is the number of successful time steps; $\mathbf{N}_{Newton}$ is the total number of Newton iterations (for successful time steps); $\mathbf{N}_{Chop}$ is the number of time step chops. Corey parameters are $a_m = 10^5$, $a_f = 0$ and mf permeability ratio $\lambda_f/\lambda_m = 1000$.

drain-matrix permeability ratio of 100

The geological setting is as follows. In the matrix domain, permeability is isotropic of 0.1 Darcy and porosity is 0.2. In the DFN, permeability is isotropic of 10.0 Darcy and porosity is 0.4.

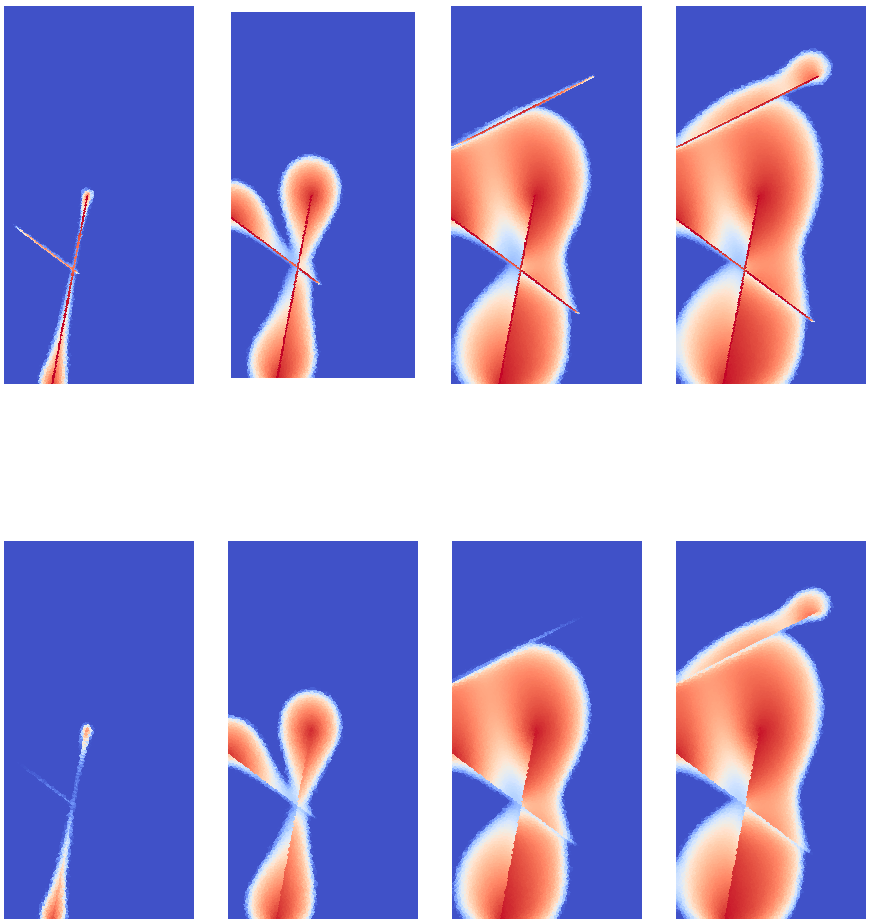

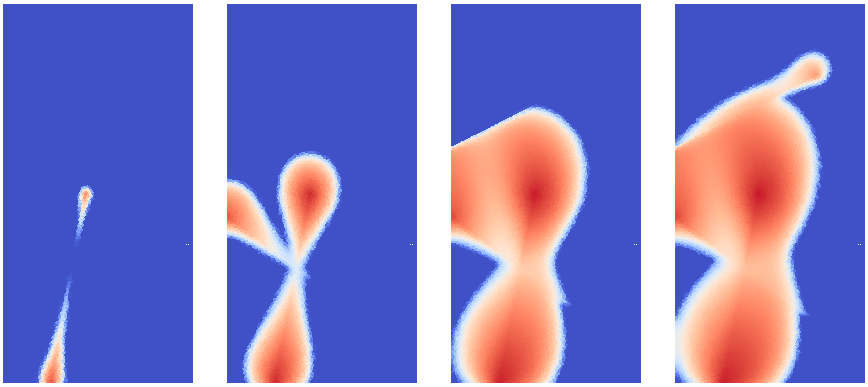

Figure 2.19: Comparison of the equi-dimensional (first line), discontinuous hybrid-dimensional 1 (mid line) and discontinuous 2 / continuous hybrid-dimensional (last line) numerical solutions for oil saturation at times $t = 360, 1800, 4320, 5400$ days (from left to right). Corey parameters are $a_m = 10^5$, $a_f = 10^4$ and mf permeability ratio $\lambda_f/\lambda_m = 100$.

zero capillary pressure in the DFN: The Corey parameters are $a_m = 10^5$ and $a_f = 0$.

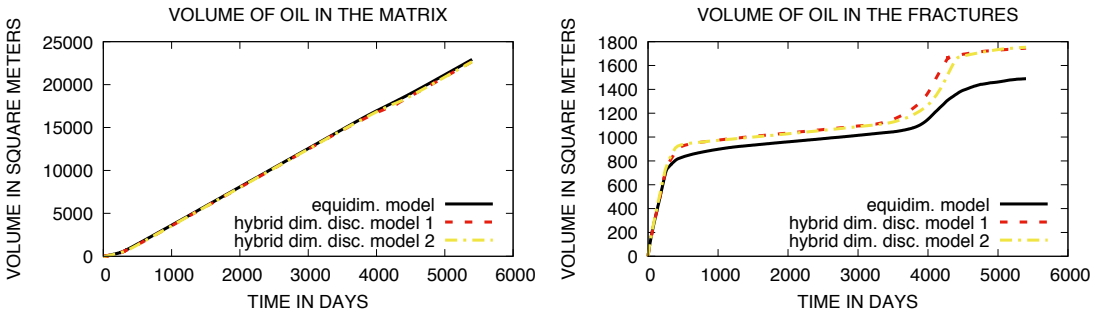

Figure 2.20: Comparison of the equi-dimensional and hybrid-dimensional matrix and fracture volumes occupied by oil as a function of time. Corey parameters are $a_m = 10^5$, $a_f = 0$ and mf permeability ratio $\lambda_f/\lambda_m = 100$.

Model	$\mathbf{N}_{\Delta t}$	$\mathbf{N}_{Newton}$	$\mathbf{N}_{Chop}$
equi dim.	933	6552	30
disc. hybrid 1	1182	5619	19
disc. hybrid 2	185	1196	0
cont. hybrid	149	1082	0

Table 2.5: $\mathbf{N}_{\Delta t}$ is the number of successful time steps; $\mathbf{N}_{Newton}$ is the total number of Newton iterations (for successful time steps); $\mathbf{N}_{Chop}$ is the number of time step chops. Corey parameters are $a_m = 10^5$, $a_f = 0$ and mf permeability ratio $\lambda_f/\lambda_m = 100$.

non-zero capillary pressure in the DFN: The Corey parameters are $a_m = 10^5$ and $a_f = 10^4$.

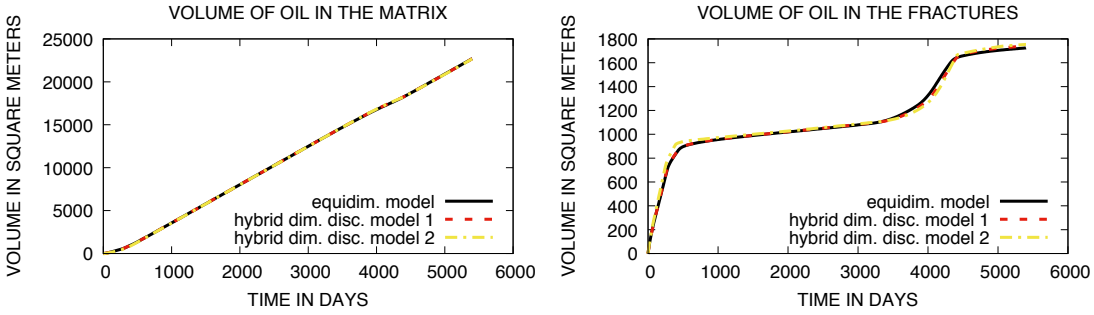

Figure 2.21: Comparison of the equi-dimensional and hybrid-dimensional matrix and fracture volumes occupied by oil as a function of time. Corey parameters are $a_m = 10^5$, $a_f = 10^4$ and mf permeability ratio $\lambda_f/\lambda_m = 100$.

Model	$\mathbf{N}_{\Delta t}$	$\mathbf{N}_{Newton}$	$\mathbf{N}_{Chop}$
equi dim.	610	2697	6
disc. hybrid 1	188	1243	5
disc. hybrid 2	154	801	0
cont. hybrid	192	1222	0

Table 2.6: $\mathbf{N}_{\Delta t}$ is the number of successful time steps; $\mathbf{N}_{Newton}$ is the total number of Newton iterations (for successful time steps); $\mathbf{N}_{Chop}$ is the number of time step chops. Corey parameters are $a_m = 10^5$, $a_f = 10^4$ and mf permeability ratio $\lambda_f/\lambda_m = 100$.

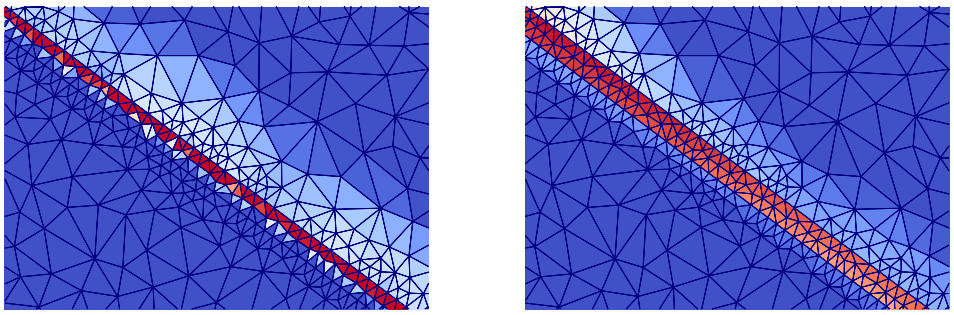

Figure 2.22: Zoom on bottom DFN. Comparison of the equi-dimensional oil saturation stratification in the fractures for Corey parameters $a_f = 0$ (left) and $a_f = 1.E4$ (right) at time $t = 360$ days.

We observe a degradation of the hybrid-dimensional solutions w.r.t. the equi-dimensional solution, when the mf permeability ratio decreases. This is due to the decrease

of the mf conductivity ratio as already observed for the tracer test case in subsection 2.4.3. Figures 2.20 and 2.21 reveal that the matching of equi- and hybrid-dimensional solutions can be enhanced by adding capillarity in the DFN. More precisely, we note that the hybrid-dimensional solutions change insignificantly, but the equi-dimensional solution changes towards the hybrid-dimensional solutions. Capillarity has a diffusive effect and smoothens out the stratification in the DFN, as shown in figure 2.22, which agrees better with the hybrid-dimensional approach of averaging physical quantities over the fracture width. This effect is in analogy to the transport problem with normal diffusion in the fracture, as given in section 2.4.4. We also observe that the discontinuous 2 and continuous hybrid-dimensional models simulate the global behaviour of the flow process quite well and are very competitive in view of robustness. However, compared to the discontinuous hybrid-dimensional model 1, the resolution at the DFN neighbourhood is much lower and local patterns can not be reproduced. It has been checked, that this is not an issue of mesh refinement. Rather, the construction of the mf mass exchange fluxes makes the difference, since, for model 1, the normal derivatives of the capillary pressure inside the fractures are reconstructed, whereas the capillary pressure is assumed to be constant across the fractures for the discontinuous 2 and continuous hybrid-dimensional models. As for the previous test case, only one solution is presented for the discontinuous 2 and continuous hybrid-dimensional, since both models produce almost indistinguishable results.

2.5.3 Comparisons between the equi and hybrid-dimensional solutions for gravity dominated flow with discontinuous capillary pressure at the matrix-drain interfaces and an upper barrier of matrix rock type

In the matrix domain, permeability is isotropic of 0.1 Darcy and porosity is 0.2. The two lower fractures are drains of isotropic permeability 100.0 Darcy and porosity 0.4. In the upper fracture, permeability is isotropic of 0.001 Darcy and porosity is 0.2. Note that the continuous hybrid-dimensional model does not incorporate a normal permeability in the DFN. We conducted the test case also for this model and observed, as expected, the unability to reproduce the barrier behaviour of the upper fracture. The Corey parameters are $a_m = a_{barrier} = 10^5$ and $a_{drain} = 0$.

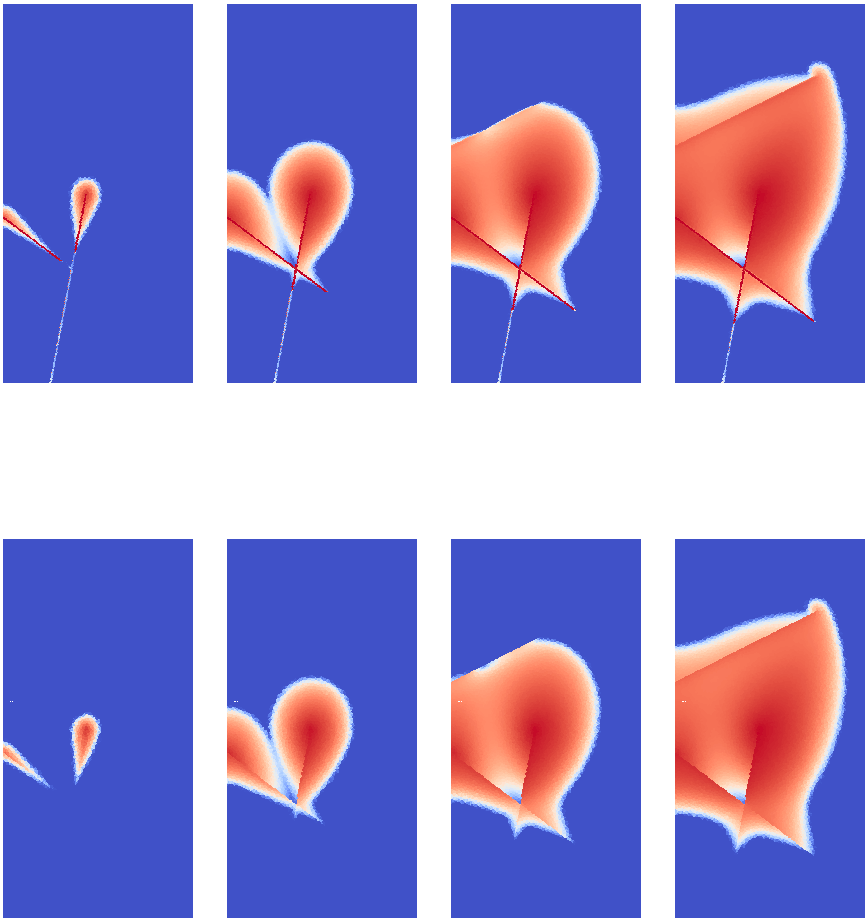

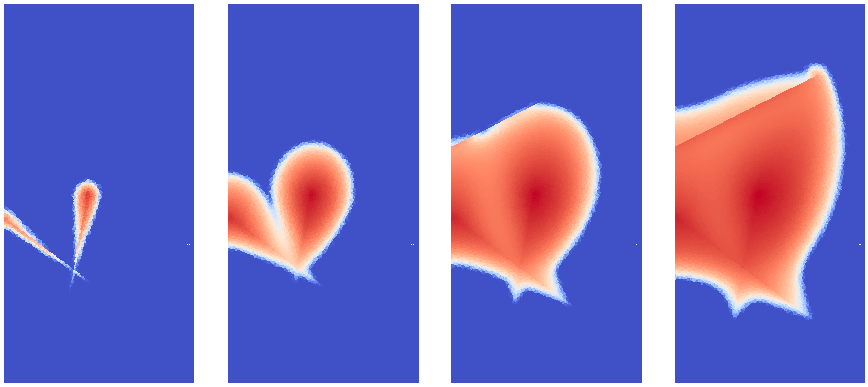

Figure 2.23: Comparison of the equi-dimensional (first line), discontinuous hybrid-dimensional 1 (second line) and discontinuous hybrid-dimensional 2 (last line) numerical solutions for oil saturation at times $t = 360, 1800, 3600, 5400$ days (from left to right). Corey parameters are $a_m = a_{barrier} = 10^5$, $a_{drain} = 0$ and mf permeability ratios $\lambda_{barrier}/\lambda_m = 0.01$ and $\lambda_{drain}/\lambda_m = 1000$.

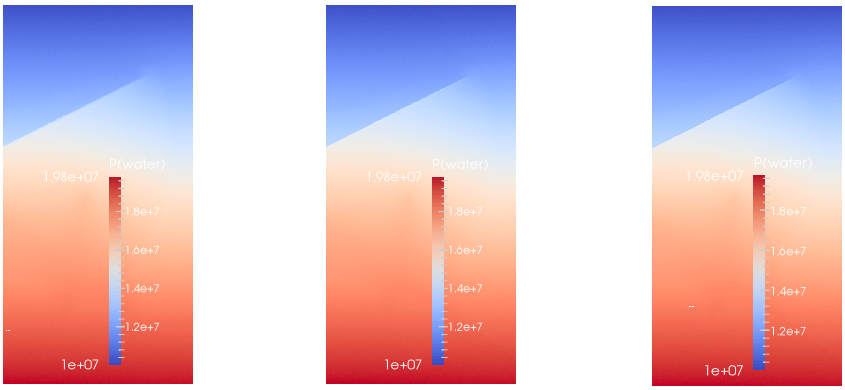

Figure 2.24: Comparison of the equi-dimensional, discontinuous hybrid-dimensional 1 and discontinuous hybrid-dimensional 2 numerical liquid pressure at time $t = 5400$ days (from left to right). Corey parameters are $a_m = a_{barrier} = 10^5$, $a_{drain} = 0$ and mf permeability ratios $\lambda_{barrier}/\lambda_m = 0.01$ and $\lambda_{drain}/\lambda_m = 1000$.

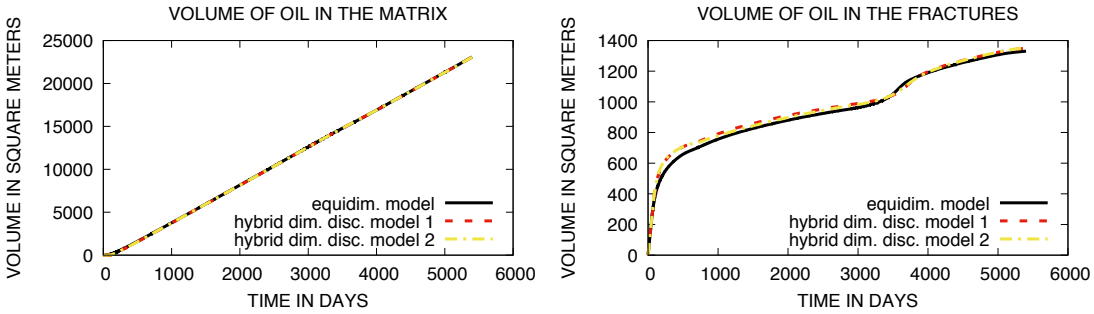

Figure 2.25: Comparison of the equi-dimensional and hybrid-dimensional matrix and fracture volumes occupied by oil as a function of time. Corey parameters are $a_m = a_{barrier} = 10^5$, $a_{drain} = 0$ and mf permeability ratios $\lambda_{barrier}/\lambda_m = 0.01$ and $\lambda_{drain}/\lambda_m = 1000$.

Model	$\mathbf{N}_{\Delta t}$	$\mathbf{N}_{Newton}$	$\mathbf{N}_{Chop}$
equi dim.	2777	15518	376
disc. hybrid 1	1305	6444	9
disc. hybrid 2	241	1676	1

Table 2.7: $\mathbf{N}_{\Delta t}$ is the number of successful time steps; $\mathbf{N}_{Newton}$ is the total number of Newton iterations (for successful time steps); $\mathbf{N}_{Chop}$ is the number of time step chops. Corey parameters are $a_m = a_{barrier} = 10^5$, $a_{drain} = 0$ and mf permeability ratios $\lambda_{barrier}/\lambda_m = 0.01$ and $\lambda_{drain}/\lambda_m = 1000$.

2.6 Conclusion

The discontinuous hybrid-dimensional models 1 and 2 for two-phase flow through fractured porous media with pressure discontinuities at the matrix-fracture (mf) interfaces introduced here account for network of fractures acting both as drains or barrier, general and discontinuous capillary pressures, and gravity forces. It is compared with the equi-dimensional model on various tracer and two-phase flow test cases. For the tracer problem with a fracture dividing the matrix domain, analytical solutions for different model parameters have been derived, both, for the hybrid- and equi-dimensional models. It turned out that the hybrid-dimensional models lose in precision with decreasing conductivity ratios $\frac{d_f \lambda_f}{L \lambda_m}$, which corresponds to steepening the angle between the equi-dimensional velocity inside the fracture and the fracture tangential directions. Then, it has been shown that adding a small normal diffusion, of the order of the normal convective flux divided by the fracture width or larger, in the fracture drives the equi-dimensional solution very close to the hybrid-dimensional solution. It was expected since the averaging procedure in the derivation of the reduced models corresponds to add a diffusion in the normal direction

inside the fracture network. This translates to the two phase flow tests, as described below. The Vertex Aproximate Gradient (VAG) scheme, as introduced in chapter 1 for the monophasic stationary hybrid-dimensional model, has been presented in a finite volume formulation for the two phase flow models. The VAG scheme is used to compare the numerically derived solutions of four different models for a 2D flow process through a faulted reservoir. More precisely, the discontinuous hybrid-dimensional solutions (models 1 and 2 derived in this chapter) have been compared to the continuous hybrid-dimensional solution (cf. [16]) w.r.t. a reference solution given by the equi-dimensional model (full model with fractures represented as heterogeneous layers), for a variety of geological and physical configurations in regard to matrix and fracture permeabilities and capillary pressure curves. Since the stratification in normal direction inside the fractures can play a major role, it is worth to mention that more than one layer of fracture cells is necessary in order to get valid reference solutions. We observed, that the discontinuous 2 and continuous hybrid-dimensional models produce solutions, which are almost indistinguishable. In terms of robustness, the test cases show that these models have a clear advantage. Yet, the discontinuous hybrid-dimensional model 1 still is much more robust than the equi-dimensional model. Moreover, for large ratios $\frac{d_f}{L}$ or $\frac{\lambda_f}{\lambda_m}$, the equi-dimensional model is unpracticable. As for the transport problem, we observed that for high fracture matrix conductivity ratios, the equi- and hybrid-dimensional solutions match well and that for lower conductivity ratios, they differ more. On the other hand, by adding capillarity in the DFN, the hybrid-dimensional solutions fit much more to the equi-dimensional solution. In fact, the equi-dimensional solution moves towards the hybrid-dimensional solutions. In the first test case, gravitational segregation has a major influence on the global flow behaviour. This effect cannot be reproduced by the discontinuous 2 and continuous hybrid-dimensional models, with single unknowns for the saturation at the DFN and instantaneous normal transport between the interior of the fractures and the mf interfaces. This remark applies to any cell centered scheme. The supplementary information on the saturations at the mf interfaces used in the mf mass exchange fluxes of the discontinuous hybrid-dimensional model 1 enables us to capture gravitational segregation inside the DFN. This advantage becomes most striking, when acceleration acts in normal direction to fractures. Furthermore, in the examples given with capillary pressure in the matrix domain, it appears that model 1 restores the forces due to the capillary pressure difference between the mf interfaces and the interior of the fractures, whereas for the discontinuous 2 and continuous hybrid-dimensional models, the capillary pressure is taken constant across the fractures, for the construction of the mf mass exchange fluxes. These features make model 1 much more precise on the transport across the DFN. Due to the assumption of pressure continuity at the mf interfaces (and the induced absence of $\lambda_{f,\mathbf{n}}$ as a model parameter), the continuous hybrid-dimensional model is unusable, when it comes to the simulation of barriers. In the barrier test case presented here, we see that the discontinuous hybrid-dimensional models 1 and 2 perform well, both, in terms of accuracy and robustness. In any case, we observed a significant gain in precision for the discontinuous 1 hybrid-dimensional solution w.r.t. the equi-dimensional reference solution, compared to the discontinuous 2 and continuous hybrid-dimensional solutions.

Chapter 3

Two phase flow analysis

3.1 Introduction

Flow and transport in fractured porous media are of paramount importance for many applications such as petroleum exploration and production, geological storage of carbon dioxide, hydrogeology, or geothermal energy. Two classes of models, dual continuum and discrete fracture models, are typically employed and possibly coupled to simulate flow and transport in fractured porous media. Dual continuum models assume that the fracture network is well connected and can be homogenised as a continuum coupled to the matrix continuum using transfer functions. On the other hand, discrete fracture models (DFM), on which this chapter focuses, represent explicitly the fractures as co-dimension one surfaces immersed in the surrounding matrix domain. The use of lower dimensional rather than equi-dimensional entities to represent the fractures has been introduced in [5, 11, 45, 54, 56] to facilitate the grid generation and to reduce the number of degrees of freedom of the discretised model. The reduction of dimension in the fracture network is obtained from the equi-dimensional model by integration and averaging along the width of each fracture. The resulting so called hybrid-dimensional model couple the 3D model in the matrix with a 2D model in the fracture network taking into account the jump of the normal fluxes as well as additional transmission conditions at the matrix-fracture interfaces. These transmission conditions depend on the mathematical nature of the equi-dimensional model and on additional physical assumptions. They are typically derived for a single phase Darcy flow for which they specify either the continuity of the pressure in the case of fractures acting as drains [5, 15] or Robin type conditions in order to take into account the discontinuity of the pressure for fractures acting either as drains or barriers [6, 45, 56].

Fewer works deal with the extension of hybrid-dimensional models to two-phase Darcy flows. Most of them build directly the model at the discrete level as in [11, 50, 62] or are limited to the case of continuous pressures at the matrix-fracture interfaces as in [11, 16, 62]. In [51], an hybrid-dimensional two-phase flow model with discontinuous pressures at the matrix-fracture interfaces is proposed using a global pressure formulation. However, the transmission conditions at the interface do not take into account correctly

the transport from the matrix to the fracture.

In chapter 2 a hybrid-dimensional two-phase Darcy flow model has been proposed, which accounts for complex networks of fractures acting either as drains or barriers and furthermore integrates discontinuous capillary pressure curves at the matrix-fracture interfaces. The model is extended in this chapter by adding a layer of damaged rock at the matrix-fracture interface with its own mobility and capillary pressure functions. This additional layer is not only a modelling tool, it also plays a major role in the numerical analysis of the model and in the convergence of the non-linear Newton iterations required to solve the discrete equations.

The discretisation of hybrid-dimensional Darcy flow models has been the object of many works using cell-centred Finite Volume schemes with either Two Point or Multi Point Flux Approximations (TPFA and MPFA) [3, 4, 6, 49, 54, 66, 69], Mixed or Mixed Hybrid Finite Element methods (MFE and MHFE) [5, 50, 56], Hybrid Mimetic Mixed Methods (HMM, which contains mixed-hybrid finite volume and mimetic finite difference schemes [30]) [7, 15, 44] and chapter 1, Control Volume Finite Element Methods (CVFE) [11, 49, 57, 59, 62] or also the Vertex Approximate Gradient (VAG) scheme [15, 16, 71] and chapter 1. Let us also mention that non-matching discretisations of the fracture and matrix meshes are studied for single phase Darcy flows in [10, 23, 47, 67]. The convergence analysis for single-phase flow models with a single fracture is established in [5, 56] for MFE methods, in [23] for non matching MFE discretisations, and in [6] for TPFA discretisations. The case of single-phase flows with complex fracture networks is studied in the general framework of gradient discretisations in [15] for continuous pressure models and in chapter 1 for discontinuous pressure models. For hybrid-dimensional two-phase flow models, the only convergence analysis is to our knowledge done in [16] for the VAG discretisation of the continuous pressure model with fractures acting only as drains. Let us recall that the gradient discretisation method (GDM) enables convergence analysis of both conforming and non conforming discretisations for linear and non-linear second order diffusion and parabolic problems. It accounts for various discretisations such as conforming Finite Element methods, MFE and MHFE methods, some TPFA and symmetric MPFA schemes, and the VAG and HMM schemes [32]. The main advantage of this framework is to provide the convergence proof for all schemes satisfying some abstract conditions at the price of a single convergence analysis for a given model, see e.g. [27, 28, 31, 38, 40]. We refer to the monograph [29] for a detailed presentation of the GDM.

The main purpose of this chapter is to propose an extension of the gradient discretisation method to our hybrid-dimensional two-phase Darcy flow model. This provides, in an abstract framework, the convergence of the solution of the gradient scheme to a weak solution of the model; as a by-product, this proves the existence of such a solution. The numerical analysis is partially based on the previous work [40] dealing with the gradient discretisation of single medium two-phase Darcy flows. The main new difficulty addressed in this chapter compared with the analysis of [40] and [16] comes from the transmission conditions at the matrix-fracture interfaces which involve an upwinding between the fracture phase pressures and the traces of the matrix phase pressures. Note that, as in [40] and [16], the convergence analysis assumes that the phase mobilities do not vanish.

The outline of this chapter is as follows. Section 3.2 introduces the strong and weak formulations of the model and the assumptions on the data. We refer to 1.2 for a detailed presentation of the geometry of the fracture network and for the definition of the function spaces. Section 3.3 details the gradient scheme framework including the definition of the abstract reconstruction operators, of the discrete variational formulation, and of the coercivity, consistency, limit conformity and compactness properties. Section 3.4 proves the main result of this chapter which is the convergence of the gradient scheme solution to a weak solution of the model. This convergence is established through compactness arguments, and requires to establish various compactness results on the approximation solutions: averaged in time and space, uniform-in-time and weak-in-space, etc. The Minty monotonicity trick is used to identify the limit of the non-linear term resulting from the the upwinding between the fracture and matrix phase pressures. Section 3.5 studies on a 2D numerical example the influence of the additional layer of damaged rock at the matrix-fracture interface on the solution of the model. The discretisation used in this test case is based on the VAG scheme which can be shown from chapter 1 to satisfy the assumptions of our gradient discretisation method. Note that numerical comparisons of our model with the equi-dimensional model as well as with the continuous pressure model of [16] can be found in chapter 2 without the damaged rock interfacial layer, which plays a minor role in the numerical tests when this layer is thin with respect to the fracture (see Section 3.5). It is shown that the discontinuous pressure model analysed in this chapter is more accurate than the continuous pressure model of [16] even in the case of fracture acting only as drains; this improved accuracy is due to more accurate transmission conditions at the matrix-fracture interfaces, in particular in the case of gravity dominant flows.

3.2 Continuous model

In this section, we present the hybrid-dimensional two-phase Darcy flow model, for which the convergence analysis is done thereafter in the rest of this chapter. The model extends the model proposed in chapter 2 by adding a layer of damaged rock at the matrix-fracture interface with its own mobility and capillary pressure functions. This additional layer is not only a modelling tool, but it is needed for the numerical analysis. Furthermore, it plays a major role in the convergence of the non-linear Newton iterations required to solve the discrete equations. Indeed, for practical simulations in the case of highly contrasted matrix and fracture capillary pressure curves, its necessity has already been stated in subsection 2.5.2 and is regarded in the test case section of this chapter in more detail. There, we also study the impact of the damaged layer on the solution.

First let us describe the continuous model and the assumptions that are implicitly made throughout the chapter. In the matrix domain $\Omega\backslash\overline{\Gamma}$, let us denote by $\Lambda_m \in L^\infty(\Omega)^{d\times d}$ the symmetric permeability tensor, chosen such that there exist $\overline{\lambda}_m \geq \underline{\lambda}_m > 0$ with

$$\underline{\lambda}_m|\zeta|^2 \leq \Lambda_m(\mathbf{x})\zeta\cdot\zeta \leq \overline{\lambda}_m|\zeta|^2 \text{ for all } \zeta\in\mathbb{R}^d, \mathbf{x}\in\Omega.$$

Analogously, in the fracture network Γ, we denote by $\Lambda_f \in L^\infty(\Gamma)^{(d-1)\times(d-1)}$ the symmetric

tangential permeability tensor, and assume that there exist $\overline{\lambda}_f \geq \underline{\lambda}_f > 0$, such that

$$\underline{\lambda}_f |\zeta|^2 \leq \Lambda_f(\mathbf{x})\zeta \cdot \zeta \leq \overline{\lambda}_f |\zeta|^2 \text{ for all } \zeta \in \mathbb{R}^{d-1}, \mathbf{x} \in \Gamma.$$

On the fracture network Γ, we introduce an orthonormal system $(\boldsymbol{\tau}_1(\mathbf{x}), \boldsymbol{\tau}_2(\mathbf{x}), \mathbf{n}(\mathbf{x}))$, defined a.e. on Γ. Inside the fractures, the normal direction is assumed to be a permeability principal direction. The normal permeability $\lambda_{f,\mathbf{n}} \in L^\infty(\Gamma)$ is such that $\underline{\lambda}_{f,\mathbf{n}} \leq \lambda_{f,\mathbf{n}}(\mathbf{x}) \leq \overline{\lambda}_{f,\mathbf{n}}$ for a.e. $\mathbf{x} \in \Gamma$ with $0 < \underline{\lambda}_{f,\mathbf{n}} \leq \overline{\lambda}_{f,\mathbf{n}}$. We also denote by $d_f \in L^\infty(\Gamma)$ the width of the fractures, assumed to be such that there exist $\overline{d}_f \geq \underline{d}_f > 0$ with $\underline{d}_f \leq d_f(\mathbf{x}) \leq \overline{d}_f$ for a.e. $\mathbf{x} \in \Gamma$. The half normal transmissibility in the fracture network is denoted by

$$T_f = \frac{2\lambda_{f,\mathbf{n}}}{d_f}.$$

Furthermore, ϕ_m and ϕ_f are the matrix and fracture porosities, respectively, $\rho^\alpha \in \mathbb{R}^+$ denotes the density of phase α (with $\alpha = 1$ the non-wetting and $\alpha = 2$ the wetting phase) and $\mathbf{g} \in \mathbb{R}^d$ is the gravitational vector field. We assume that $\underline{\phi}_{m,f} \leq \phi_{m,f} \leq \overline{\phi}_{m,f}$, for some $\underline{\phi}_{m,f}, \overline{\phi}_{m,f} > 0$. (k_m^α, k_f^α) and (S_m^α, S_f^α) are the matrix and fracture phase mobilities and saturations, respectively. Hypothesis on these functions are stated below.

3.2.1 Strong formulation

The PDEs model writes: find phase pressures $(\overline{u}_m^\alpha, \overline{u}_f^\alpha)$ and velocities $(\mathbf{q}_m^\alpha, \mathbf{q}_f^\alpha)$ $(\alpha = 1, 2)$, such that

$$\begin{cases} \phi_m \partial_t S_m^\alpha(\overline{p}_m) + \operatorname{div}(\mathbf{q}_m^\alpha) = h_m^\alpha & \text{on } (0,T) \times \Omega \setminus \overline{\Gamma} \\ \mathbf{q}_m^\alpha = -[kS]_m^\alpha(\overline{p}_m)\ \Lambda_m \nabla \overline{u}_m^\alpha & \text{on } (0,T) \times \Omega \setminus \overline{\Gamma} \\ \phi_f d_f \partial_t S_f^\alpha(\overline{p}_f) + \operatorname{div}_\tau(\mathbf{q}_f^\alpha) + \sum_{\mathfrak{a} \in \chi} Q_{f,\mathfrak{a}}^\alpha = d_f h_f^\alpha & \text{on } (0,T) \times \Gamma \\ \mathbf{q}_f^\alpha = -d_f [kS]_f^\alpha(\overline{p}_f)\ \Lambda_f \nabla_\tau \overline{u}_f & \text{on } (0,T) \times \Gamma \\ (\overline{p}_m, \overline{p}_f)|_{t=0} = (\overline{p}_{m,0}, \overline{p}_{f,0}) & \text{on } (\Omega \setminus \overline{\Gamma}) \times \Gamma. \end{cases} \tag{3.1a}$$

The matrix-fracture coupling condition on $(0,T) \times \Gamma_\mathfrak{a}$ (for all $\mathfrak{a} \in \chi$) are

$$\begin{cases} \gamma_{\mathbf{n}_\mathfrak{a}} \mathbf{q}_m^\alpha - Q_{f,\mathfrak{a}}^\alpha = \eta \partial_t S_\mathfrak{a}^\alpha(\gamma_\mathfrak{a} \overline{p}_m) \\ Q_{f,\mathfrak{a}}^\alpha = [kS]_\mathfrak{a}^\alpha(\gamma_\mathfrak{a} \overline{p}_m) T_f [\![\overline{u}^\alpha]\!]_\mathfrak{a}^+ - [kS]_f^\alpha(\overline{p}_f) T_f [\![\overline{u}^\alpha]\!]_\mathfrak{a}^-, \end{cases} \tag{3.1b}$$

where $\eta = d_\mathfrak{a}\phi_\mathfrak{a}$ with given parameters $d_\mathfrak{a} \in (0, \frac{d_f}{2})$ and $\phi_\mathfrak{a} \in (0,1]$. The difference to the model of chapter 2 is that a proper rock type of the matrix fracture interface $\Gamma_\mathfrak{a}$ is accounted for by the upwinded fluxes $Q_{f,\mathfrak{a}}^\alpha$ and by the interfacial accumulation. The saturations and pressures should satisfy

$$S_\mu^2 = 1 - S_\mu^1 \text{ for } \mu \in \{m, f\} \cup \chi, \text{ and } (\overline{p}_m, \overline{p}_f) = (\overline{u}_m^1 - \overline{u}_m^2, \overline{u}_f^1 - \overline{u}_f^2). \tag{3.1c}$$

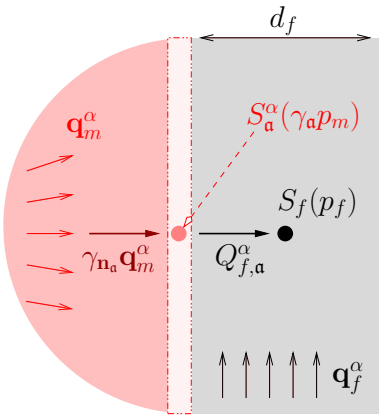

Figure 3.1: Illustration of the coupling condition. It can be seen as an upwind two point approximation of $Q_{f,\mathfrak{a}}^\alpha$. The upwinding takes into account the damaged rock type at the matrix-fracture interfaces. The arrows show the positive orientation of the normal fluxes $\gamma_{\mathbf{n}_\mathfrak{a}}\mathbf{q}_m^\alpha$ and $Q_{f,\mathfrak{a}}^\alpha$.

In the above, we used the short hand notations

$$[\![\overline{u}^\alpha]\!]_\mathfrak{a} = \gamma_\mathfrak{a}\overline{u}_m^\alpha - \overline{u}_f^\alpha\,, \quad [\![\overline{u}^\alpha]\!]_\mathfrak{a}^+ = \max(0, [\![\overline{u}^\alpha]\!]_\mathfrak{a}) \quad \text{and} \quad [\![\overline{u}^\alpha]\!]_\mathfrak{a}^- = [\![-\overline{u}^\alpha]\!]_\mathfrak{a}^+$$

as well as, for $\mu \in \{m, f\} \cup \chi$, $\varphi_\mu \in L^2((0,T) \times M_\mu)$ and a.e. $(t, \mathbf{x}) \in (0,T) \times M_\mu$,

$$S_\mu^\alpha(\varphi_\mu)(t,\mathbf{x}) = S_\mu^\alpha(\mathbf{x}, \varphi_\mu(t,\mathbf{x})) \quad \text{and} \quad [kS]_\mu^\alpha(\varphi_\mu)(t,\mathbf{x}) = k_\mu^\alpha(\mathbf{x}, S_\mu^\alpha(\mathbf{x}, \varphi_\mu(t,\mathbf{x}))).$$

Here and in the following, M_μ is defined by

$$M_\mu = \begin{cases} \Omega & \text{if } \mu = m \\ \Gamma & \text{if } \mu = f \\ \Gamma_\mathfrak{a} & \text{if } \mu = \mathfrak{a} \in \chi. \end{cases}$$

The various boundary conditions imposed on the domain are: homogeneous Dirichlet conditions at the boundary of the domain, pressure continuity and flux conservation at the fracture-fracture intersections, and zero normal flux at the immersed fracture tips. In other words,

$$\gamma_{\partial\Omega\setminus\partial\Gamma}\overline{u}_m = 0 \text{ on } \partial\Omega \setminus \partial\Gamma, \qquad \gamma_{\partial\Omega\cap\partial\Gamma}\overline{u}_f = 0 \text{ on } \partial\Omega \cap \partial\Gamma$$
$$\sum_{i\in I} \gamma_{\mathbf{n}_{\Sigma_i}}\mathbf{q}_{f,i} = 0 \text{ on } \Sigma, \qquad \gamma_{\mathbf{n}_{\Sigma_i}}\mathbf{q}_{f,i} = 0 \text{ on } \Sigma_{i,N},\ i \in I$$

Let us define $L^2(\Gamma) = \{v = (v_i)_{i\in I}, v_i \in L^2(\Gamma_i), i \in I\}$. The assumptions under which the model is considered are:

- $\overline{p}_{m,0} \in H^1(\Omega \setminus \overline{\Gamma})$ and $\overline{p}_{f,0} \in L^2(\Gamma)$,
- For $\mu \in \{m, f\}$ and $\alpha = 1, 2$, $h_\mu^\alpha \in L^2((0,T) \times M_\mu)$,
- For $\mu \in \{m, f\} \cup \chi$: $S_\mu^1 : M_\mu \times \mathbb{R} \to [0,1]$ is a Caratheodory function; for a.e. $\mathbf{x} \in M_\mu$, $S_\mu^1(\mathbf{x}, \cdot)$ is a non-decreasing Lipschitz continuous function on $\mathbb{R}$; $S_\mu^1(\cdot, q)$ is piecewise constant on a finite partition $(M_\mu^j)_{j\in J_\mu}$ of polytopal subsets of M_μ for all $q \in \mathbb{R}$.

- For $\alpha = 1, 2$ and $\mu \in \{m, f\} \cup \chi$: there exist constants $k_{\mu,\min}, k_{\mu,\max} > 0$, such that $k_\mu^\alpha \colon M_\mu \times [0,1] \to [k_{\mu,\min}, k_{\mu,\max}]$ is a Caratheodory function.

Recall that a Caratheodory function is measurable w.r.t. its first argument and continuous w.r.t. its second argument.

3.2.2 Weak formulation

The weak formulation of (3.1) amounts to finding phase pressures $(\overline{u}_m^\alpha, \overline{u}_f^\alpha)_{\alpha=1,2} \in [L^2(0,T;V_m^0) \times L^2(0,T;V_f^0)]^2$ satisfying the following variational equalities, for any $\alpha = 1, 2$ and any $(\overline{\varphi}_m^\alpha, \overline{\varphi}_f^\alpha) \in C_0^\infty([0,T) \times \Omega) \times C_0^\infty([0,T) \times \Gamma)$:

$$\begin{aligned}
&\sum_{\mu\in\{m,f\}} \Big(-\int_0^T \int_{M_\mu} \phi_\mu S_\mu^\alpha(\overline{p}_\mu) \partial_t \overline{\varphi}_\mu^\alpha \mathrm{d}\tau_\mu \mathrm{d}t + \int_0^T \int_{M_\mu} [kS]_\mu^\alpha(\overline{p}_\mu)\ \Lambda_\mu \nabla \overline{u}_\mu^\alpha \cdot \nabla \overline{\varphi}_\mu^\alpha \mathrm{d}\tau_\mu \mathrm{d}t \\
&\qquad - \int_{M_\mu} \phi_\mu S_\mu^\alpha(\overline{p}_{\mu,0}) \overline{\varphi}_\mu^\alpha(0,\cdot) \mathrm{d}\tau_\mu \Big) \\
&+ \sum_{\mathfrak{a}\in\chi} \Big(\int_0^T \int_{\Gamma_\mathfrak{a}} T_f \Big([kS]_\mathfrak{a}^\alpha(\gamma_\mathfrak{a}\overline{p}_m) [\![\overline{u}^\alpha]\!]_\mathfrak{a}^+ - [kS]_f^\alpha(\overline{p}_f) [\![\overline{u}^\alpha]\!]_\mathfrak{a}^- \Big) [\![\overline{\varphi}^\alpha]\!]_\mathfrak{a} \mathrm{d}\tau \mathrm{d}t \\
&\qquad - \int_0^T \int_{\Gamma_\mathfrak{a}} \eta S_\mathfrak{a}^\alpha(\gamma_\mathfrak{a}\overline{p}_m) \partial_t \gamma_\mathfrak{a} \overline{\varphi}_m^\alpha \mathrm{d}\tau \mathrm{d}t - \int_{\Gamma_\mathfrak{a}} \eta S_\mathfrak{a}^\alpha(\gamma_\mathfrak{a}\overline{p}_{m,0}) \gamma_\mathfrak{a} \overline{\varphi}_m^\alpha(0,\cdot) \mathrm{d}\tau \Big) \\
&= \sum_{\mu\in\{m,f\}} \int_0^T \int_{M_\mu} h_\mu^\alpha \overline{\varphi}_\mu^\alpha \mathrm{d}\tau_\mu.
\end{aligned} \tag{3.2}$$

Here,

$$\mathrm{d}\tau_\mu(\mathbf{x}) = \begin{cases} \mathrm{d}\mathbf{x} & \text{if } \mu = m \\ \mathrm{d}\tau_f(\mathbf{x}) = d_f(\mathbf{x}) \mathrm{d}\tau(\mathbf{x}) & \text{if } \mu = f \end{cases}$$

with $\mathrm{d}\tau(\mathbf{x})$ the $d-1$ dimensional Lebesgue measure on Γ.

3.3 The gradient discretisation method for parabolic problems

The gradient discretisation method consists in selecting a set (gradient discretisation) of a finite-dimensional space and reconstruction operators on this space, and in substituting them for their continuous counterpart in the weak formulation of the model. The scheme thus obtained is called a gradient scheme. Besides the additional time dependency of the two phase flow model, the trace operators are only needed for the definition of the jump operators, in the single phase flow model of chapter 1. In addition to the discrete operators of chapter 1, we therefore need to introduce a discrete trace operator, in order to write the gradient scheme for model 3.2. Furthermore, the reconstruction operators

need to be extended in time. Let us now define the set of discrete elements that make up a gradient discretisation.

Definition 3.3.1 (Gradient discretisation (GD)) *A spatial gradient discretisation for a discrete fracture model is* $\mathcal{D}_S = (X^0_{\mathcal{D}_S}, (\Pi^\mu_{\mathcal{D}_S}, \nabla^\mu_{\mathcal{D}_S})_{\mu\in\{m,f\}}, (\llbracket\cdot\rrbracket^\mathfrak{a}_{\mathcal{D}_S})_{\mathfrak{a}\in\chi}, (\mathbb{T}^\mathfrak{a}_{\mathcal{D}_S})_{\mathfrak{a}\in\chi})$*, where*

- $X^0_{\mathcal{D}_S}$ *is a finite dimensional space of degrees of freedom,*
- *For* $\mu \in \{m, f\}$, $\Pi^\mu_{\mathcal{D}_S} : X^0_{\mathcal{D}_S} \to L^2(M_\mu)$ *reconstructs a function on* M_μ *from the DOFs,*
- *For* $\mu \in \{m, f\}$, $\nabla^\mu_{\mathcal{D}_S} : X^0_{\mathcal{D}_S} \to L^2(M_\mu)^{\dim M_\mu}$ *reconstructs a gradient on* M_μ *from the DOFs,*
- *For* $\mathfrak{a} \in \chi$, $\llbracket\cdot\rrbracket^\mathfrak{a}_{\mathcal{D}_S} : X^0_{\mathcal{D}_S} \to L^2(\Gamma_\mathfrak{a})$ *reconstructs, from the DOFs, a jump on* $\Gamma_\mathfrak{a}$ *between the matrix and fracture,*
- *For* $\mathfrak{a} \in \chi$, $\mathbb{T}^\mathfrak{a}_{\mathcal{D}_S} : X^0_{\mathcal{D}_S} \to L^2(\Gamma_\mathfrak{a})$ *reconstructs, from the DOFs, a trace on* $\Gamma_\mathfrak{a}$ *from the matrix.*

These operators must be chosen such that the following defines a norm on $X^0_{\mathcal{D}_S}$*:*

$$\|w_{\mathcal{D}_S}\|_{\mathcal{D}_S} = \left(\|\nabla^m_{\mathcal{D}_S} w_{\mathcal{D}_S}\|^2_{L^2(\Omega)^d} + \|\nabla^f_{\mathcal{D}_S} w_{\mathcal{D}_S}\|^2_{L^2(\Gamma)^{d-1}} + \sum_{\mathfrak{a}\in\chi} \|\llbracket w_{\mathcal{D}_S}\rrbracket^\mathfrak{a}_{\mathcal{D}_S}\|^2_{L^2(\Gamma_\mathfrak{a})}\right)^{1/2}.$$

The gradient discretisation $\mathcal{D}_S$ *is extended to a space-time gradient discretisation by setting* $\mathcal{D} = (\mathcal{D}_S, (\mathrm{I}^\mu_\mathcal{D})_{\mu\in\{m,f\}}, (t^n)_{n=0,\dots,N})$ *with*

- $0 = t^0 < t^1 < \cdots < t^N = T$ *is a discretisation of the time interval* $[0, T]$*,*
- $\mathrm{I}^m_\mathcal{D}\colon H^1(\Omega \setminus \overline{\Gamma}) \to X^0_{\mathcal{D}_S}$ *and* $\mathrm{I}^f_\mathcal{D}\colon L^2(\Gamma) \to X^0_{\mathcal{D}_S}$ *are operators designed to interpolate initial conditions.*

The space-time operators act on a family $u_\mathcal{D} = (u^n_\mathcal{D})_{n=0,\dots,N} \in (X^0_{\mathcal{D}_S})^{N+1}$ *the following way: for all* $n = 0, \dots, N-1$ *and all* $t \in (t^n, t^{n+1}]$*,*

$$\begin{aligned}
\Pi^\mu_\mathcal{D} u_\mathcal{D}(t,\cdot) &= \Pi^\mu_{\mathcal{D}_S} u^{n+1}_\mathcal{D}, \qquad & \nabla^\mu_\mathcal{D} u_\mathcal{D}(t,\cdot) &= \nabla^\mu_{\mathcal{D}_S} u^{n+1}_\mathcal{D},\\
\mathbb{T}^\mathfrak{a}_\mathcal{D} u_\mathcal{D}(t,\cdot) &= \mathbb{T}^\mathfrak{a}_{\mathcal{D}_S} u^{n+1}_\mathcal{D}, \qquad & \llbracket u_\mathcal{D}\rrbracket^\mathfrak{a}_\mathcal{D}(t,\cdot) &= \llbracket u^{n+1}_\mathcal{D}\rrbracket^\mathfrak{a}_{\mathcal{D}_S}.
\end{aligned}$$

We extend these functions at $t = 0$*, by considering the corresponding spatial operators on* $u^0_\mathcal{D}$*.*

If $w = (w^n_\mathcal{D})_{n=0,\dots,N}$ is a family in $X^0_{\mathcal{D}_S}$, the discrete time derivatives $\delta_t w : (0, T] \to X^0_{\mathcal{D}_S}$ are defined such that, for all $n = 0, \dots, N-1$ and all $t \in (t^n, t^{n+1}]$, with $\Delta t^{n+\frac{1}{2}} = t^{n+1} - t^n$,

$$\delta_t w(t) = \frac{w^{n+1}_\mathcal{D} - w^n_\mathcal{D}}{\Delta t^{n+\frac{1}{2}}} \in X^0_{\mathcal{D}_S}.$$

Let $(e_\nu)_{\nu\in dof_\mathcal{D}}$ be a basis of $X^0_{\mathcal{D}_S}$. If $w_{\mathcal{D}_S} \in X^0_{\mathcal{D}_S}$, we write $w_{\mathcal{D}_S} = \sum_{\nu\in dof_\mathcal{D}} w_\nu e_\nu$. Then, for $g \in C(\mathbb{R})$, we define $g(w_{\mathcal{D}_S}) \in X^0_{\mathcal{D}_S}$ by $g(w_{\mathcal{D}_S}) = \sum_{\nu\in dof_\mathcal{D}} g(w_\nu)e_\nu$. In other words, $g(w_{\mathcal{D}_S})$ is defined by applying g to each degree of freedom of $w_{\mathcal{D}_S}$. Although this definition depends on the choice of basis $(e_\nu)_{\nu\in dof_\mathcal{D}}$, we do not indicate that explicitly. This definition of $g(w_{\mathcal{D}_S})$ is particularly meaningful in the context of piecewise constant reconstructions, see Remark 3.3.1 below.

The gradient scheme for (3.1) consists in writing the weak formulation (3.2) with continuous spaces and operators substituted by their discrete counterparts, after a formal integration-by-parts in time. In other words, the gradient scheme is: find $(u^\alpha_\mathcal{D})_{\alpha=1,2} \in [(X^0_{\mathcal{D}_S})^{N+1}]^2$ such that, with $p_\mathcal{D} = u^1_\mathcal{D} - u^2_\mathcal{D}$,

$$p^0_\mathcal{D} = (\mathrm{I}^m_\mathcal{D}\overline{p}_{m,0}, \mathrm{I}^f_\mathcal{D}\overline{p}_{f,0}) \tag{3.3}$$

and, for any $\alpha = 1, 2$ and $v^\alpha_\mathcal{D} \in (X^0_{\mathcal{D}_S})^{N+1}$,

$$\begin{aligned}
&\sum_{\mu\in\{m,f\}} \Big(\int_0^T \int_{M_\mu} \phi_\mu \Pi^\mu_\mathcal{D} \Big[\delta_t S^\alpha_\mu(p_\mathcal{D})\Big] \Pi^\mu_\mathcal{D} v^\alpha_\mathcal{D} \mathrm{d}\tau_\mu \mathrm{d}t \\
&\qquad + \int_0^T \int_{M_\mu} [kS]^\alpha_\mu(\Pi^\mu_\mathcal{D} p_\mathcal{D})\ \Lambda_\mu \nabla^\mu_\mathcal{D} u^\alpha_\mathcal{D} \cdot \nabla^\mu_\mathcal{D} v^\alpha_\mathcal{D} \mathrm{d}\tau_\mu \mathrm{d}t \Big) \\
&+ \sum_{\mathfrak{a}\in\chi} \Big(\int_0^T \int_{\Gamma_\mathfrak{a}} \Big([kS]^\alpha_\mathfrak{a}(\mathbb{T}^\mathfrak{a}_\mathcal{D} p_\mathcal{D}) T_f(\llbracket u^\alpha_\mathcal{D} \rrbracket^\mathfrak{a}_\mathcal{D})^+ - [kS]^\alpha_f(\Pi^f_\mathcal{D} p_\mathcal{D}) T_f(\llbracket u^\alpha_\mathcal{D} \rrbracket^\mathfrak{a}_\mathcal{D})^- \Big) \llbracket v^\alpha_\mathcal{D} \rrbracket^\mathfrak{a}_\mathcal{D} \mathrm{d}\tau \mathrm{d}t \\
&\qquad + \int_0^T \int_{\Gamma_\mathfrak{a}} \eta \mathbb{T}^\mathfrak{a}_\mathcal{D} \Big[\delta_t S^\alpha_\mathfrak{a}(p_\mathcal{D})\Big] \mathbb{T}^\mathfrak{a}_\mathcal{D} v^\alpha_\mathcal{D} \mathrm{d}\tau \mathrm{d}t \Big) = \sum_{\mu\in\{m,f\}} \int_0^T \int_{M_\mu} h^\alpha_\mu \Pi^\mu_\mathcal{D} v^\alpha_\mathcal{D} \mathrm{d}\tau_\mu \mathrm{d}t.
\end{aligned} \tag{3.4}$$

3.3.1 Properties of gradient discretisations

The convergence analysis of the GDM is based a few properties that sequences of GDs must satisfy.

Definition 3.3.2 (Piecewise constant reconstruction operator) *Let $(e_\nu)_{\nu\in dof_\mathcal{D}}$ be the basis of $X^0_{\mathcal{D}_S}$ chosen in Section 3.3. For $\mu \in \{m, f\} \cup \chi$, an operator $\Pi : X^0_{\mathcal{D}_S} \to L^2(M_\mu)$ is called piecewise constant if it has the representation*

$$\Pi u_{\mathcal{D}_S} = \sum_{\nu\in dof_\mathcal{D}} u_\nu \mathbb{1}_{\omega^\mu_\nu} \qquad \text{for all } u_{\mathcal{D}_S} = \sum_{\nu\in dof_\mathcal{D}} u_\nu e_\nu \in X^0_{\mathcal{D}_S},$$

where $(\omega^\mu_\nu)_{\nu\in dof_\mathcal{D}}$ is a partition of M_μ up to a set of zero measure, and $\mathbb{1}_{\omega^\mu_\nu}$ is the characteristic function of ω^μ_ν.

In the following, all considered function reconstruction operators are assumed to be of piecewise constant type.

Remark 3.3.1 *Recall that, if $g \in C^0(\mathbb{R})$ and $u_{\mathcal{D}_S} \in X^0_{\mathcal{D}_S}$, then $g(u_{\mathcal{D}_S}) \in X^0_{\mathcal{D}_S}$ is defined by the degrees of freedom $(g(u_\nu))_{\nu \in dof_{\mathcal{D}}}$. Then, any piecewise constant reconstruction operator Π commutes with g in the sense that $g(\Pi u_{\mathcal{D}_S}) = \Pi g(u_{\mathcal{D}_S})$.*

Other than for the analysis of chapter 1, we have to consider trace reconstructions, here. The coercivity property enables us to control the functions and trace reconstructions by the norm on $X^0_{\mathcal{D}_S}$. This is a combination of a discrete Poincaré and a discrete trace inequality.

Definition 3.3.3 (Coercivity of spatial GD) *Let*

$$\mathcal{C}_{\mathcal{D}_S} = \max_{0 \neq v_{\mathcal{D}_S} \in X^0_{\mathcal{D}_S}} \frac{\|\Pi^m_{\mathcal{D}_S} v_{\mathcal{D}_S}\|_{L^2(\Omega)} + \|\Pi^f_{\mathcal{D}_S} v_{\mathcal{D}_S}\|_{L^2(\Gamma)} + \sum_{\mathfrak{a} \in \chi} \|\mathbb{T}^{\mathfrak{a}}_{\mathcal{D}_S} v_{\mathcal{D}_S}\|_{L^2(\Gamma_{\mathfrak{a}})}}{\|v_{\mathcal{D}_S}\|_{\mathcal{D}_S}}.$$

A sequence $(\mathcal{D}^l_S)_{l \in \mathbb{N}}$ of gradient discretisations is coercive if there exists $\mathcal{C}_P > 0$ such that $\mathcal{C}_{\mathcal{D}^l_S} \leq \mathcal{C}_P$ for all $l \in \mathbb{N}$.

The consistency ensures that a certain interpolation error goes to zero along sequences of GDs.

Definition 3.3.4 (Consistency of spatial GD) *For $\overline{u} = (\overline{u}_m, \overline{u}_f) \in V^0$ and $v_{\mathcal{D}_S} \in X^0_{\mathcal{D}_S}$, define*

$$\begin{aligned} s_{\mathcal{D}_S}(v_{\mathcal{D}_S}, \overline{u}) = {} & \|\nabla^m_{\mathcal{D}_S} v_{\mathcal{D}_S} - \nabla \overline{u}_m\|_{L^2(\Omega)^d} + \|\nabla^f_{\mathcal{D}_S} v_{\mathcal{D}_S} - \nabla_\tau \overline{u}_f\|_{L^2(\Gamma)^{d-1}} \\ & + \|\Pi^m_{\mathcal{D}_S} v_{\mathcal{D}_S} - \overline{u}_m\|_{L^2(\Omega)} + \|\Pi^f_{\mathcal{D}_S} v_{\mathcal{D}_S} - \overline{u}_f\|_{L^2(\Gamma)} \\ & + \sum_{\mathfrak{a} \in \chi} \Big(\|[\![v_{\mathcal{D}_S}]\!]^{\mathfrak{a}}_{\mathcal{D}_S} - [\![\overline{u}]\!]_{\mathfrak{a}}\|_{L^2(\Gamma_a)} + \|\mathbb{T}^{\mathfrak{a}}_{\mathcal{D}_S} v_{\mathcal{D}_S} - \gamma_{\mathfrak{a}} \overline{u}_m\|_{L^2(\Gamma_a)} \Big), \end{aligned}$$

and $\mathcal{S}_{\mathcal{D}_S}(\overline{u}) = \min_{v_{\mathcal{D}_S} \in X^0_{\mathcal{D}_S}} s_{\mathcal{D}_S}(v_{\mathcal{D}_S}, \overline{u})$. A sequence $(\mathcal{D}^l_S)_{l \in \mathbb{N}}$ of gradient discretisations is GD-consistent (or consistent for short) if, for all $\overline{u} = (\overline{u}_m, \overline{u}_f) \in V^0$,

$$\lim_{l \to \infty} \mathcal{S}_{\mathcal{D}^l_S}(\overline{u}) = 0.$$

The limit-conformity imposes that, in the limit, the discrete gradient and function reconstructions satisfy a natural integration-by-part formula (Stokes' theorem). Formally, we slightly modify the limit conformity condition of chapter 1, in order to account for the trace reconstruction operators and still ensure the identification at the limit of the jump operators (see Theorem 3.A.1).

Definition 3.3.5 (Limit-conformity of spatial GD) *For all* $\mathbf{q} = (\mathbf{q}_m, \mathbf{q}_f) \in \mathbf{C}^\infty_\Omega \times \mathbf{C}^\infty_\Gamma$, $\varphi_\mathfrak{a} \in C^\infty_0(\Gamma_\mathfrak{a})$ *and* $v_{\mathcal{D}_S} \in X^0_{\mathcal{D}_S}$, *define*

$$\begin{aligned} w_{\mathcal{D}_S}(v_{\mathcal{D}_S}, \mathbf{q}, \varphi_\mathfrak{a}) = &\int_\Omega \Big(\nabla^m_{\mathcal{D}_S} v_{\mathcal{D}_S} \cdot \mathbf{q}_m + (\Pi^m_{\mathcal{D}_S} v_{\mathcal{D}_S}) \mathrm{div} \mathbf{q}_m \Big) \mathrm{d}\mathbf{x} \\ &+ \int_\Gamma \Big(\nabla^f_{\mathcal{D}_S} v_{\mathcal{D}_S} \cdot \mathbf{q}_f + (\Pi^f_{\mathcal{D}_S} v_{\mathcal{D}_S}) \mathrm{div}_\tau \mathbf{q}_f \Big) \mathrm{d}\tau(\mathbf{x}) \\ &- \sum_{\mathfrak{a} \in \chi} \int_{\Gamma_\mathfrak{a}} \gamma_{\mathbf{n}_\mathfrak{a}} \mathbf{q}_m \mathbb{T}^\mathfrak{a}_{\mathcal{D}_S} v_{\mathcal{D}_S} \mathrm{d}\tau(\mathbf{x}) \\ &+ \sum_{\mathfrak{a} \in \chi} \int_{\Gamma_\mathfrak{a}} \varphi_\mathfrak{a} \Big(\mathbb{T}^\mathfrak{a}_{\mathcal{D}_S} v_{\mathcal{D}_S} - \Pi^f_{\mathcal{D}_S} v_{\mathcal{D}_S} - [\![v_{\mathcal{D}_S}]\!]^\mathfrak{a}_{\mathcal{D}_S} \Big) \mathrm{d}\tau(\mathbf{x}) \end{aligned}$$

and $\mathcal{W}_{\mathcal{D}_S}(\mathbf{q}, \varphi_\mathfrak{a}) = \max_{0 \neq v_{\mathcal{D}_S} \in X^0_{\mathcal{D}_S}} \frac{1}{\|v_{\mathcal{D}_S}\|_{\mathcal{D}_S}} |w_{\mathcal{D}_S}(v_{\mathcal{D}_S}, \mathbf{q}, \varphi_\mathfrak{a})|$. *A sequence* $(\mathcal{D}^l_S)_{l \in \mathbb{N}}$ *of gradient discretisations is limit-conforming if, for all* $\mathbf{q} = (\mathbf{q}_m, \mathbf{q}_f) \in \mathbf{C}^\infty_\Omega \times \mathbf{C}^\infty_\Gamma$ *and all* $\varphi_\mathfrak{a} \in C^\infty_0(\Gamma_\mathfrak{a})$,

$$\lim_{l \to \infty} \mathcal{W}_{\mathcal{D}^l_S}(\mathbf{q}, \varphi_\mathfrak{a}) = 0.$$

Remark 3.3.2 (Domain of $\mathcal{W}_{\mathcal{D}_S}$) *Usually, the measure* $\mathcal{W}_{\mathcal{D}_S}$ *of limit-conformity is defined on spaces in which the Darcy velocities of solutions to the model are expected to be, not smooth spaces as* $\mathbf{C}^\infty_\Omega \times \mathbf{C}^\infty_\Gamma$ *[29, Definition 2.6]. However, if we do not aim at obtaining error estimates (which is the case here, given that such estimates would require unrealistic regular assumptions on the data and the solution),* $\mathcal{W}_{\mathcal{D}_S}$ *only needs to be defined and to converge to* 0 *on spaces of smooth functions – see Lemma 3.A.1.*

For any space dependent function f, define $\mathrm{T}_{\boldsymbol{\xi}} f(\mathbf{x}) = f(\mathbf{x} + \boldsymbol{\xi})$. Likewise, for any time dependent function g, let $\mathrm{T}_h g(t) = g(t + h)$. The compactness property ensures a sort of discrete Rellich theorem (compact embedding of H^1_0 into L^2). By the Kolmogorov theorem, this compactness is equivalent to a uniform control of the translates of the functions.

Definition 3.3.6 (Compactness of spatial GD) *For all* $v_{\mathcal{D}_S} \in X^0_{\mathcal{D}_S}$ *and* $\boldsymbol{\xi} = (\boldsymbol{\xi}_m, \boldsymbol{\xi}_f)$, *with* $\boldsymbol{\xi}_m \in \mathbb{R}^d$ *and* $\boldsymbol{\xi}_f = (\boldsymbol{\xi}_{f,i})_{i \in I} \in \bigoplus_{i \in I} \tau(\mathcal{P}_i)$, *where* $\tau(\mathcal{P}_i)$ *is the (constant) tangent space of* $\mathcal{P}_i$, *define*

$$\begin{aligned} \tau_{\mathcal{D}_S}(v_{\mathcal{D}_S}, \boldsymbol{\xi}) = &\|\mathrm{T}_{\boldsymbol{\xi}_m} \Pi^m_{\mathcal{D}_S} v_{\mathcal{D}_S} - \Pi^m_{\mathcal{D}_S} v_{\mathcal{D}_S}\|_{L^2(\mathbb{R}^d)} \\ &+ \sum_{i \in I} \Big(\|\mathrm{T}_{\boldsymbol{\xi}_{f,i}} \Pi^f_{\mathcal{D}_S} v_{\mathcal{D}_S} - \Pi^f_{\mathcal{D}_S} v_{\mathcal{D}_S}\|_{L^2(\mathcal{P}_i)} + \sum_{\mathfrak{a} = \mathfrak{a}^\pm(i)} \|\mathrm{T}_{\boldsymbol{\xi}_{f,i}} \mathbb{T}^\mathfrak{a}_{\mathcal{D}_S} v_{\mathcal{D}_S} - \mathbb{T}^\mathfrak{a}_{\mathcal{D}_S} v_{\mathcal{D}_S}\|_{L^2(\mathcal{P}_i)} \Big), \end{aligned}$$

where all the functions on Ω *(resp.* Γ_i*) have been extended to* $\mathbb{R}^d$ *(resp.* $\mathcal{P}_i$*) by* 0 *outside their initial domain. Let* $\mathcal{T}_{\mathcal{D}_S}(\boldsymbol{\xi}) = \max_{0 \neq v_{\mathcal{D}_S} \in X^0_{\mathcal{D}_S}} \frac{1}{\|v_{\mathcal{D}_S}\|_{\mathcal{D}_S}} \tau_{\mathcal{D}_S}(v_{\mathcal{D}_S}, \boldsymbol{\xi})$. *A sequence* $(\mathcal{D}^l_S)_{l \in \mathbb{N}}$ *of gradient discretisations is compact if*

$$\lim_{|\boldsymbol{\xi}| \to 0} \sup_{l \in \mathbb{N}} \mathcal{T}_{\mathcal{D}^l_S}(\boldsymbol{\xi}) = 0.$$

All these properties for spatial GDs naturally extend to space–time GDs with, for the consistency, additional requirements on the time steps and on the interpolants of the initial conditions.

Definition 3.3.7 (Properties of space-time gradient discretisations) *A sequence of space-time gradient discretisations $(\mathcal{D}_l)_{l\in\mathbb{N}}$ is*

1. *Coercive if $(\mathcal{D}_S^l)_{l\in\mathbb{N}}$ is coercive.*
2. *Consistent if*
   (i) $(\mathcal{D}_S^l)_{l\in\mathbb{N}}$ is consistent,
   (ii) $\Delta t_l = \max_{n=0,\dots,N_l-1} \Delta t_l^{n+\frac{1}{2}} \to 0$ as $l\to\infty$, and
   (iii) For all $\overline{\varphi}_m \in H^1(\Omega\setminus\overline{\Gamma})$,

$$\|\overline{\varphi}_m - \Pi^m_{\mathcal{D}_S^l} \mathrm{I}^m_{\mathcal{D}_l}\overline{\varphi}_m\|_{L^2(\Omega)} + \sum_{\mathfrak{a}\in\chi} \|\gamma_{\mathfrak{a}}\overline{\varphi}_m - \mathbb{T}^{\mathfrak{a}}_{\mathcal{D}_S^l}\mathrm{I}^m_{\mathcal{D}_l}\overline{\varphi}_m\|_{L^2(\Gamma_{\mathfrak{a}})} \longrightarrow 0 \quad \text{as } l\to\infty$$

   and, for all $\overline{\varphi}_f \in L^2(\Gamma)$, $\|\overline{\varphi}_f - \Pi^f_{\mathcal{D}_S^l}\mathrm{I}^f_{\mathcal{D}_l}\overline{\varphi}_f\|_{L^2(\Gamma)} \longrightarrow 0$ as $l\to\infty$.
3. *Limit-conforming if $(\mathcal{D}_S^l)_{l\in\mathbb{N}}$ is limit-conforming.*
4. *Compact if $(\mathcal{D}_S^l)_{l\in\mathbb{N}}$ is compact.*

Elements of $(X^0_{\mathcal{D}_S})^{N+1}$ are identified with functions $(0,T]\to X^0_{\mathcal{D}_S}$ by setting, for $u_{\mathcal{D}}\in(X^0_{\mathcal{D}_S})^{N+1}$ with $u_{\mathcal{D}} = (u^n_{\mathcal{D}})_{n=0,\dots,N}$,

$$\forall n = 0,\dots,N-1\,,\ \forall t\in(t^n,t^{n+1}]\,,\ u_{\mathcal{D}}(t) = u^{n+1}_{\mathcal{D}}. \tag{3.5}$$

This definition is compatible with the choices of space-time operators made in Definition 3.3.1, in the sense that, for any $t\in(0,T]$, $\Pi^\mu_{\mathcal{D}} u_{\mathcal{D}}(t,\mathbf{x}) = \Pi^\mu_{\mathcal{D}_S}(u_{\mathcal{D}}(t))(\mathbf{x})$ (and similarly for the other reconstruction operators). With the identification (3.5), the norm on $(X^0_{\mathcal{D}_S})^{N+1}$ is

$$\|u_{\mathcal{D}}\|^2_{\mathcal{D}} = \int_0^T \|u_{\mathcal{D}}(t)\|^2_{\mathcal{D}_S}\mathrm{d}t.$$

3.4 Convergence analysis

In the rest of this chapter, when the phase parameter α is absent it implicitly mean that it is equal to 1 so, e.g., we write S_μ for S^1_μ. The main convergence result is the following.

Theorem 3.4.1 (Convergence Theorem) *Let $(\mathcal{D}_l)_{l\in\mathbb{N}}$ be a coercive, consistent, limit-conforming and compact sequence of space-time gradient discretisations, with piecewise constant reconstructions. Then for any $l\in\mathbb{N}$ there is a solution $(u^\alpha_{\mathcal{D}_l})_{\alpha=1,2}$ of (3.4) with $\mathcal{D}=\mathcal{D}_l$.*

Moreover, there exists $(\overline{u}^\alpha)_{\alpha=1,2} = (\overline{u}^\alpha_m,\overline{u}^\alpha_f)_{\alpha=1,2}\in[L^2(0,T;V^0_m)\times L^2(0,T;V^0_f)]^2$ solution of (3.2), such that, up to a subsequence as $l\to\infty$,

1. *The following weak convergences hold, for* $\alpha = 1, 2$,

$$\left\{\begin{array}{ll} \Pi^{\mu}_{\mathcal{D}_l} u^{\alpha}_{\mathcal{D}_l} \rightharpoonup \overline{u}^{\alpha}_{\mu} & \text{in } L^2((0,T)\times M_\mu)\,, \text{ for } \mu \in \{m, f\}, \\ \nabla^{\mu}_{\mathcal{D}_l} u^{\alpha}_{\mathcal{D}_l} \rightharpoonup \nabla \overline{u}^{\alpha}_{\mu} & \text{in } L^2((0,T)\times M_\mu)^{\dim_{M_\mu}}\,, \text{ for } \mu \in \{m, f\}, \\ \mathbb{T}^{\mathfrak{a}}_{\mathcal{D}_l} u^{\alpha}_{\mathcal{D}_l} \rightharpoonup \gamma_{\mathfrak{a}} \overline{u}^{\alpha}_{m} & \text{in } L^2((0,T)\times \Gamma_{\mathfrak{a}})\,, \text{ for all } \mathfrak{a} \in \chi, \\ [\![u^{\alpha}_{\mathcal{D}_l}]\!]^{\mathfrak{a}}_{\mathcal{D}_l} \rightharpoonup [\![\overline{u}^{\alpha}]\!]_{\mathfrak{a}} & \text{in } L^2((0,T)\times \Gamma_{\mathfrak{a}})\,, \text{ for all } \mathfrak{a} \in \chi. \end{array}\right. \tag{3.6}$$

2. *The following strong convergences hold, with* $p = u^1_{\mathcal{D}} - u^2_{\mathcal{D}}$ *and* $\overline{p}_\mu = \overline{u}^1_\mu - \overline{u}^2_\mu$*:*

$$\left\{\begin{array}{ll} \Pi^{\mu}_{\mathcal{D}_l} S_\mu(p_{\mathcal{D}_l}) \to S_\mu(\overline{p}_\mu) & \text{in } L^2((0,T)\times M_\mu)\,, \text{ for } \mu \in \{m, f\}, \\ \mathbb{T}^{\mathfrak{a}}_{\mathcal{D}_l} S_{\mathfrak{a}}(p_{\mathcal{D}_l}) \to S_{\mathfrak{a}}(\gamma_{\mathfrak{a}} \overline{p}_m) & \text{in } L^2((0,T)\times \Gamma_{\mathfrak{a}})\,, \text{ for all } \mathfrak{a} \in \chi. \end{array}\right. \tag{3.7}$$

Remark 3.4.1 *It is additionally proved in [34] that the saturations converge uniformly-in-time strongly in* L^2 *(that is, in* $L^\infty(0,T;L^2)$*).*

3.4.1 Preliminary estimates

Let us introduce some useful auxiliary functions. These functions are the same as in [27, 33], with basic adjustment to account for the fact that the saturation might not vanish at $p = 0$. For $\mu \in \{m, f\} \cup \chi$, let $R_{S_\mu(\mathbf{x},\cdot)}$ be the range of $S_\mu(\mathbf{x},\cdot)$. The pseudo-inverse of $S_\mu(\mathbf{x},\cdot)$ is the mapping $[S_\mu(\mathbf{x},\cdot)]^i : R_{S_\mu(\mathbf{x},\cdot)} \to \mathbb{R}$ defined by

$$[S_\mu(\mathbf{x},\cdot)]^i(q) = \left\{\begin{array}{ll} \inf\{z \in \mathbb{R} \,|\, S_\mu(\mathbf{x},z) = q\} & \text{if } q > S_\mu(\mathbf{x},0)\,, \\ 0 & \text{if } q = S_\mu(\mathbf{x},0)\,, \\ \sup\{z \in \mathbb{R} \,|\, S_\mu(\mathbf{x},z) = q\} & \text{if } q < S_\mu(\mathbf{x},0). \end{array}\right.$$

That is, $[S_\mu(\mathbf{x},\cdot)]^i(q)$ is the point z in $R_{S_\mu(\mathbf{x},\cdot)}$ that is the closest to $S_\mu(\mathbf{x},0)$ and such that $S_\mu(\mathbf{x},z) = q$. The extended function $B_\mu(\mathbf{x},\cdot) : \mathbb{R} \to [0,\infty]$ is given by

$$B_\mu(\mathbf{x},q) = \left\{\begin{array}{ll} \displaystyle\int_{S_\mu(\mathbf{x},0)}^{q} [S_\mu(\mathbf{x},\cdot)]^i(\tau)\mathrm{d}\tau & \text{if } q \in R_{S_\mu(\mathbf{x},\cdot)}\,, \\ \infty & \text{else.} \end{array}\right.$$

$B_\mu(\mathbf{x},\cdot)$ is convex lower semi-continuous (l.s.c.) and satisfies the following properties [33]

$$B_\mu(\mathbf{x}, S_\mu(\mathbf{x},r)) = \int_0^r \tau \frac{\partial S_\mu}{\partial q}(\mathbf{x},\tau)\mathrm{d}\tau, \tag{3.8}$$

$$\forall a, b \in \mathbb{R}\,,\ a(S_\mu(\mathbf{x},b) - S_\mu(\mathbf{x},a)) \le B_\mu(\mathbf{x}, S_\mu(\mathbf{x},b)) - B_\mu(\mathbf{x}, S_\mu(\mathbf{x},a)) \tag{3.9}$$

and, for some K_0, K_1 and K_2 not depending on $\mathbf{x}$ or r,

$$K_0 S_\mu(\mathbf{x},r)^2 - K_1 \le B_\mu(\mathbf{x}, S_\mu(\mathbf{x},r)) \le K_2 r^2. \tag{3.10}$$

In the following, we write $A \lesssim B$ for "$A \le MB$ for a constant M depending only on an upper bound of $C_{\mathcal{D}}$ and on the data in the assumptions of Section 3.2".

Lemma 3.4.1 (Energy estimates) *Under the assumptions of Section 3.2, let $\mathcal{D}$ be a gradient discretisation with piecewise constant reconstructions $\Pi_{\mathcal{D}}^{\mu}$, $\mathbb{T}_{\mathcal{D}}^{\mathfrak{a}}$. Let $(u_{\mathcal{D}}^{\alpha})_{\alpha=1,2} \in [(X_{\mathcal{D}_S}^0)^{N+1}]^2$ be a solution of the gradient scheme of* (3.4)*. Take $T_0 \in (0,T]$ and $k \in \{0,\dots,N-1\}$ such that $T_0 \in (t_k, t_{k+1}]$. Then*

$$\begin{aligned}
&\sum_{\mu\in\{m,f\}} \int_{M_\mu} \phi_\mu \left[B_\mu(S_\mu(\Pi_{\mathcal{D}_S}^{\mu} p_{\mathcal{D}}(T_0))) - B_\mu(S_\mu(\Pi_{\mathcal{D}_S}^{\mu} p_{\mathcal{D}}^0))\right] \mathrm{d}\tau_\mu \\
&\quad + \sum_{\alpha=1}^{2} \sum_{\mu\in\{m,f\}} \int_0^{T_0} \int_{M_\mu} [kS]_\mu^\alpha(\Pi_{\mathcal{D}}^{\mu} p_{\mathcal{D}}) \Lambda_\mu \nabla_{\mathcal{D}}^{\mu} u_{\mathcal{D}}^{\alpha} \cdot \nabla_{\mathcal{D}}^{\mu} u_{\mathcal{D}}^{\alpha} \mathrm{d}\tau_\mu \mathrm{d}t \\
&\quad + \sum_{\mathfrak{a}\in\chi} \int_{\Gamma_{\mathfrak{a}}} \eta \left[B_{\mathfrak{a}}(S_{\mathfrak{a}}(\mathbb{T}_{\mathcal{D}_S}^{\mathfrak{a}} p_{\mathcal{D}}(T_0))) - B_{\mathfrak{a}}(S_{\mathfrak{a}}(\mathbb{T}_{\mathcal{D}_S}^{\mathfrak{a}} p_{\mathcal{D}}^0))\right] \mathrm{d}\tau \\
&\quad + \sum_{\alpha=1}^{2} \sum_{\mathfrak{a}\in\chi} \int_0^{T_0} \int_{\Gamma_{\mathfrak{a}}} \Big([kS]_{\mathfrak{a}}^\alpha(\mathbb{T}_{\mathcal{D}}^{\mathfrak{a}} p_{\mathcal{D}}) T_f([\![u_{\mathcal{D}}^{\alpha}]\!]_{\mathcal{D}}^{\mathfrak{a}})^+ - [kS]_f^\alpha(\Pi_{\mathcal{D}}^{f} p_{\mathcal{D}}) T_f([\![u_{\mathcal{D}}^{\alpha}]\!]_{\mathcal{D}}^{\mathfrak{a}})^- \Big) [\![u_{\mathcal{D}}^{\alpha}]\!]_{\mathcal{D}}^{\mathfrak{a}} \mathrm{d}\tau \mathrm{d}t \\
&\qquad \le \sum_{\alpha=1}^{2} \sum_{\mu\in\{m,f\}} \int_0^{t_{k+1}} \int_{M_\mu} h_\mu^\alpha \Pi_{\mathcal{D}}^{\mu} u_{\mathcal{D}}^{\alpha} \mathrm{d}\tau_\mu \mathrm{d}t.
\end{aligned} \tag{3.11}$$

As a consequence,

$$\sum_{\alpha=1,2} \|u_{\mathcal{D}}^{\alpha}\|_{\mathcal{D}}^2 \lesssim 1 + \sum_{\mu\in\{m,f\}} \|\Pi_{\mathcal{D}}^{\mu} p_{\mathcal{D}}^0\|_{L^2(M_\mu)}^2 + \sum_{\mathfrak{a}\in\chi} \|\mathbb{T}_{\mathcal{D}_S}^{\mathfrak{a}} p_{\mathcal{D}}^0\|_{L^2(\Gamma_{\mathfrak{a}})}^2. \tag{3.12}$$

Proof We remove the spatial coordinate $\mathbf{x}$ in the arguments, when not needed. Reasoning as in [27, Lemma 4.1], Property (3.9) gives

$$\begin{aligned}
&\sum_{\mu\in\{m,f\}} \int_0^{t_{k+1}} \int_{M_\mu} \phi_\mu \Pi_{\mathcal{D}}^{\mu} \Big[\delta_t S_\mu(p_{\mathcal{D}})\Big] \Pi_{\mathcal{D}}^{\mu} p_{\mathcal{D}} \mathrm{d}\tau_\mu \mathrm{d}t \\
&\qquad = \sum_{\mu\in\{m,f\}} \sum_{n=0}^{k} \int_{M_\mu} \phi_\mu \left[S_\mu(\Pi_{\mathcal{D}_S}^{\mu} p_{\mathcal{D}}^{n+1}) - S_\mu(\Pi_{\mathcal{D}_S}^{\mu} p_{\mathcal{D}}^{n})\right] \Pi_{\mathcal{D}_S}^{\mu} p_{\mathcal{D}}^{n+1} \mathrm{d}\tau_\mu \\
&\qquad \ge \sum_{\mu\in\{m,f\}} \sum_{n=0}^{k} \int_{M_\mu} \phi_\mu \left[B_\mu(S_\mu(\Pi_{\mathcal{D}_S}^{\mu} p_{\mathcal{D}}^{n+1})) - B_\mu(S_\mu(\Pi_{\mathcal{D}_S}^{\mu} p_{\mathcal{D}}^{n}))\right] \mathrm{d}\tau_\mu \\
&\qquad = \sum_{\mu\in\{m,f\}} \int_{M_\mu} \phi_\mu \left[B_\mu(S_\mu(\Pi_{\mathcal{D}_S}^{\mu} p_{\mathcal{D}}(T_0))) - B_\mu(S_\mu(\Pi_{\mathcal{D}_S}^{\mu} p_{\mathcal{D}}^0))\right] \mathrm{d}\tau_\mu
\end{aligned} \tag{3.13}$$

where we used, by definition, $\Pi_{\mathcal{D}_S}^{\mu} p_{\mathcal{D}}(T_0) = \Pi_{\mathcal{D}_S}^{\mu} p_{\mathcal{D}}^{k+1}$. Similarly,

$$\int_0^{t_{k+1}} \int_{\Gamma_{\mathfrak{a}}} \eta \mathbb{T}_{\mathcal{D}}^{\mathfrak{a}} \Big[\delta_t S_{\mathfrak{a}}(p_{\mathcal{D}})\Big] \mathbb{T}_{\mathcal{D}}^{\mathfrak{a}} p_{\mathcal{D}} \mathrm{d}\tau \mathrm{d}t \ge \int_{\Gamma_{\mathfrak{a}}} \eta \left[B_{\mathfrak{a}}(S_{\mathfrak{a}}(\mathbb{T}_{\mathcal{D}_S}^{\mathfrak{a}} p_{\mathcal{D}}(T_0))) - B_{\mathfrak{a}}(S_{\mathfrak{a}}(\mathbb{T}_{\mathcal{D}_S}^{\mathfrak{a}} p_{\mathcal{D}}^0))\right] \mathrm{d}\tau. \tag{3.14}$$

Equation (3.11) is then obtained by taking $v_{\mathcal{D}}^\alpha = (u_0^\alpha, \dots, u_{k+1}^\alpha, 0, \dots, 0)$ (for $\alpha = 1, 2$) in the gradient scheme (3.4), by summing the resulting equations over $\alpha = 1, 2$, by using (3.13) and (3.14), and by reducing the time integrals in the left-hand side from $[0, t_{k+1}]$ to $[0, T_0]$, due to the non-negativity of the integrands.

The inequality (3.12) is the consequence of a few simple estimates on the terms of (3.11) with $T_0 = T$. For the symmetric diffusion terms (for $\alpha = 1, 2$ and $\mu \in \{m, f\}$), we write

$$\int_0^T \int_{M_\mu} [kS]_\mu^\alpha(\Pi_{\mathcal{D}}^\mu p_{\mathcal{D}}) \nabla_{\mathcal{D}}^\mu u_{\mathcal{D}}^\alpha \cdot \nabla_{\mathcal{D}}^\mu u_{\mathcal{D}}^\alpha \mathrm{d}\tau_\mu \mathrm{d}t \geq d_{\mu,\min} k_{\mu,\min} \|\nabla_{\mathcal{D}}^\mu u_{\mathcal{D}}^\alpha\|_{L^2((0,T)\times M_\mu)}^2. \tag{3.15}$$

The matrix–fracture coupling terms are handled by noticing that, for any $s \in \mathbb{R}$, $s^+ s = (s^+)^2$ and $s^- s = -(s^-)^2$, so that for $\alpha = 1, 2$ and $\mathfrak{a} \in \chi$,

$$\begin{aligned}
&\int_0^T \int_{\Gamma_\mathfrak{a}} \Big([kS]_\mathfrak{a}^\alpha(\mathbb{T}_{\mathcal{D}}^\mathfrak{a} p_{\mathcal{D}}) T_f([\![u_{\mathcal{D}}^\alpha]\!]_{\mathcal{D}}^\mathfrak{a})^+ - [kS]_f^\alpha(\Pi_{\mathcal{D}}^f p_{\mathcal{D}}) T_f([\![u_{\mathcal{D}}^\alpha]\!]_{\mathcal{D}}^\mathfrak{a})^- \Big) [\![u_{\mathcal{D}}^\alpha]\!]_{\mathcal{D}}^\mathfrak{a} \mathrm{d}\tau \mathrm{d}t \\
&\quad = \int_0^T \int_{\Gamma_\mathfrak{a}} \Big([kS]_\mathfrak{a}^\alpha(\mathbb{T}_{\mathcal{D}}^\mathfrak{a} p_{\mathcal{D}}) T_f(([\![u_{\mathcal{D}}^\alpha]\!]_{\mathcal{D}}^\mathfrak{a})^+)^2 + [kS]_f^\alpha(\Pi_{\mathcal{D}}^f p_{\mathcal{D}}) T_f((([\![u_{\mathcal{D}}^\alpha]\!]_{\mathcal{D}}^\mathfrak{a})^-)^2 \mathrm{d}\tau \mathrm{d}t \Big) \\
&\quad \gtrsim \|[\![u_{\mathcal{D}}^\alpha]\!]_{\mathcal{D}}^\mathfrak{a}\|_{L^2((0,T)\times\Gamma_\mathfrak{a})}^2.
\end{aligned} \tag{3.16}$$

Here, we used $[kS]_\mathfrak{a}^\alpha(\mathbb{T}_{\mathcal{D}}^\mathfrak{a} p_{\mathcal{D}}) \geq k_{\mathfrak{a},\min}$, $[kS]_f^\alpha(\Pi_{\mathcal{D}}^f p_{\mathcal{D}}) \geq k_{f,\min}$ and $|s|^2 = (s^+)^2 + (s^-)^2$. Using (3.10), (3.15) and (3.16) in (3.11) (with $T_0 = T$), Cauchy–Schwarz inequalities lead to

$$\begin{aligned}
&\sum_{\alpha=1}^2 \Big[\|\nabla_{\mathcal{D}}^m u_{\mathcal{D}}^\alpha\|_{L^2((0,T)\times\Omega)^d}^2 + \|\nabla_{\mathcal{D}}^f u_{\mathcal{D}}^\alpha\|_{L^2((0,T)\times\Gamma)^{d-1}}^2 + \sum_{\mathfrak{a}\in\chi} \|[\![u_{\mathcal{D}}^\alpha]\!]_{\mathcal{D}}^\mathfrak{a}\|_{L^2((0,T)\times\Gamma)}^2 \Big] \\
&\lesssim \sum_{\mu\in\{m,f\}} \Big[\sum_{\alpha=1}^2 \|h_\mu^\alpha\|_{L^2((0,T)\times M_\mu)} \|\Pi_{\mathcal{D}}^\mu u_{\mathcal{D}}^\alpha\|_{L^2((0,T)\times M_\mu)} + \|\Pi_{\mathcal{D}}^\mu p_{\mathcal{D}}^0\|_{L^2(M_\mu)}^2 \Big] + \|\mathbb{T}_{\mathcal{D}_S}^\mathfrak{a} p_{\mathcal{D}}^0\|_{L^2(M_\mu)}^2.
\end{aligned}$$

The proof of (3.12) is complete by noticing that the left-hand side is equal to $\sum_{\alpha=1}^2 \|u_{\mathcal{D}}^\alpha\|_{\mathcal{D}}^2$, and by using Young's inequality and the definition of $C_{\mathcal{D}}$ in the right-hand side. □

The existence of a solution to the gradient scheme follows by a standard fixed point argument based on the Leray–Schauder topological degree, see e.g. [16, proof of Lemma 3.2] or [31, Step 1 in the proof of Theorem 3.1].

Corollary 3.4.1 *Under the assumptions of Lemma 3.4.1, there exists a solution to the gradient scheme* (3.4).

We now want to obtain estimates on the discrete time derivatives. Let the dual norm

of $W = [w^m_{\mathcal{D}_S}, w^f_{\mathcal{D}_S}, (w^{\mathfrak{a}}_{\mathcal{D}_S})_{\mathfrak{a}\in\chi}] \in (X^0_{\mathcal{D}_S})^{2+\sharp\chi}$ be defined by

$$|W|_{\mathcal{D}_S,*} = \sup\left\{ \sum_{\mu\in\{m,f\}} \int_{M_\mu} \phi_\mu \Pi^\mu_{\mathcal{D}_S} w^\mu_{\mathcal{D}_S} \Pi^\mu_{\mathcal{D}_S} v_{\mathcal{D}_S} \mathrm{d}\tau_\mu + \sum_{\mathfrak{a}\in\chi} \int_{\Gamma_\mathfrak{a}} \eta \mathbb{T}^{\mathfrak{a}}_{\mathcal{D}_S} w^{\mathfrak{a}}_{\mathcal{D}_S} \mathbb{T}^{\mathfrak{a}}_{\mathcal{D}_S} v_{\mathcal{D}_S} \mathrm{d}\tau \ : \right.$$
$$\left. v_{\mathcal{D}_S} \in X^0_{\mathcal{D}_S}\ ,\ \|v_{\mathcal{D}_S}\|_{\mathcal{D}_S} \le 1 \right\} \tag{3.17}$$

Lemma 3.4.2 (Weak estimate on time derivatives) *Under the assumptions of Section 3.2, let $\mathcal{D}$ be a gradient discretisation with piecewise constant reconstructions $\Pi^\mu_{\mathcal{D}}$, $\mathbb{T}^{\mathfrak{a}}_{\mathcal{D}}$. Let $(u^\alpha_{\mathcal{D}})_{\alpha=1,2} \in [(X^0_{\mathcal{D}_S})^{N+1}]^2$ be a solution of the gradient scheme of* (3.4)*. Then,*

$$\int_0^T \left| \left[\delta_t S_m(p_{\mathcal{D}})(t), \delta_t S_f(p_{\mathcal{D}})(t), (\delta_t S_{\mathfrak{a}}(p_{\mathcal{D}})(t))_{\mathfrak{a}\in\chi} \right] \right|^2_{\mathcal{D}_S,*} \mathrm{d}t \lesssim 1 + \sum_{\alpha=1,2} \|u^\alpha_{\mathcal{D}}\|^2_{\mathcal{D}}$$

Proof Take $v_{\mathcal{D}_S} \in X^0_{\mathcal{D}_S}$ and apply (3.4) with $\alpha = 1$ to the test function $v_{\mathcal{D}} = (0, \dots, 0, v_{\mathcal{D}_S}, 0, \dots, 0)$, where $v_{\mathcal{D}_S}$ is at an arbitrary position n. This shows that, for all $n = 0, \dots, N$ and $t \in (t^n, t^{n+1}]$

$$\begin{aligned}
&\sum_{\mu\in\{m,f\}} \int_{M_\mu} \phi_\mu \Pi^\mu_{\mathcal{D}} \Big[\delta_t S_\mu(p_{\mathcal{D}}) \Big](t) \Pi^\mu_{\mathcal{D}} v_{\mathcal{D}} \mathrm{d}\tau_\mu + \sum_{\mathfrak{a}\in\chi} \int_{\Gamma_\mathfrak{a}} \eta \mathbb{T}^{\mathfrak{a}}_{\mathcal{D}} \Big[\delta_t S_{\mathfrak{a}}(p_{\mathcal{D}}) \Big](t) \mathbb{T}^{\mathfrak{a}}_{\mathcal{D}} v_{\mathcal{D}} \mathrm{d}\tau \\
&= \sum_{\mu\in\{m,f\}} \Big(\int_{M_\mu} \Big[\frac{1}{\Delta t^{n+\frac12}} \int_{t^n}^{t^{n+1}} h_\mu(s) \mathrm{d}s \Big] \Pi^\mu_{\mathcal{D}} v_{\mathcal{D}} \mathrm{d}\tau_\mu \\
&\qquad - \int_{M_\mu} [kS]_\mu(\Pi^\mu_{\mathcal{D}} p_{\mathcal{D}})(t)\ \Lambda_\mu \nabla^\mu_{\mathcal{D}} u_{\mathcal{D}}(t) \cdot \nabla^\mu_{\mathcal{D}} v_{\mathcal{D}} \mathrm{d}\tau_\mu \Big) \\
&\quad - \sum_{\mathfrak{a}\in\chi} \int_{\Gamma_\mathfrak{a}} \Big([kS]_{\mathfrak{a}}(\mathbb{T}^{\mathfrak{a}}_{\mathcal{D}} p_{\mathcal{D}})(t) T_f([\![u_{\mathcal{D}}(t)]\!]^{\mathfrak{a}}_{\mathcal{D}})^+ - [kS]_f(\Pi^f_{\mathcal{D}} p_{\mathcal{D}})(t) T_f([\![u_{\mathcal{D}}(t)]\!]^{\mathfrak{a}}_{\mathcal{D}})^- \Big) [\![v_{\mathcal{D}}]\!]^{\mathfrak{a}}_{\mathcal{D}} \mathrm{d}\tau \\
&\lesssim \left\| \frac{1}{\Delta t^{n+\frac12}} \int_{t^n}^{t^{n+1}} h_\mu(s) \mathrm{d}s \right\|_{L^2(M_\mu)} \|v_{\mathcal{D}_S}\|_{\mathcal{D}_S} + \|u_{\mathcal{D}}(t)\|_{\mathcal{D}_S} \|v_{\mathcal{D}_S}\|_{\mathcal{D}_S},
\end{aligned}$$

where we have used the definition of $C_{\mathcal{D}}$ in the last step. Taking the supremum over all $v_{\mathcal{D}_S}$ such that $\|v_{\mathcal{D}_S}\|_{\mathcal{D}_S} = 1$ shows that

$$\begin{aligned}
&\left| \left[\delta_t S_m(p_{\mathcal{D}})(t), \delta_t S_f(p_{\mathcal{D}})(t), (\delta_t S_{\mathfrak{a}}(p_{\mathcal{D}})(t))_{\mathfrak{a}\in\chi} \right] \right|_{\mathcal{D}_S,*} \\
&\qquad \lesssim \frac{1}{\Delta t^{n+\frac12}} \int_{t^n}^{t^{n+1}_{\mathcal{D}}} \|h_\mu(s)\|_{L^2(M_\mu)} \mathrm{d}s + \|u_{\mathcal{D}}(t)\|_{\mathcal{D}_S}.
\end{aligned} \tag{3.18}$$

Take the square of this relation, use $(a+b)^2 \le 2a^2 + 2b^2$, and apply Jensen's inequality to introduce the square inside the time integral. Multiply then by $\Delta t^{n+\frac12}$ and sum over n to conclude. □

Lemma 3.4.3 (Estimate on time translates) *Under the assumptions of Section 3.2, let $\mathcal{D}$ be a gradient discretisation with piecewise constant reconstructions $\Pi_{\mathcal{D}}^{\mu}$, $\mathbb{T}_{\mathcal{D}}^{\mathfrak{a}}$. For any $h>0$ and any solution $(u_{\mathcal{D}}^{\alpha})_{\alpha=1,2}\in[(X_{\mathcal{D}_S}^0)^{N+1}]^2$ of (3.4),*

$$\sum_{\mu\in\{m,f\}}\|S_\mu(\mathrm{T}_h\Pi_{\mathcal{D}}^{\mu}p_{\mathcal{D}})-S_\mu(\Pi_{\mathcal{D}}^{\mu}p_{\mathcal{D}})\|_{L^2((0,T)\times M_\mu)}^2 + \sum_{\mathfrak{a}\in\chi}\|S_{\mathfrak{a}}(\mathrm{T}_h\mathbb{T}_{\mathcal{D}}^{\mathfrak{a}}p_{\mathcal{D}})-S_{\mathfrak{a}}(\mathbb{T}_{\mathcal{D}}^{\mathfrak{a}}p_{\mathcal{D}})\|_{L^2((0,T)\times\Gamma_{\mathfrak{a}})}^2 \lesssim (h+\Delta t)\Big(\quad 1+\sum_{\alpha=1}^{2}\|u_{\mathcal{D}}^{\alpha}\|_{\mathcal{D}}^2\Big), \tag{3.19}$$

where we recall that $\mathrm{T}_h g(s)=g(s+h)$ and $\Delta t=\max\{\Delta t^{n+\frac12}\,:\,n=0,\dots,N-1\}$, and where all functions of time have been extended by 0 outside $(0,T)$.

Proof Let us start by assuming that $h\in(0,T)$, and let us consider integrals over $(0,T-h)$ (we therefore do not use extensions outside $(0,T)$ yet). By the Lipschitz continuity and monotonicity of the saturations $S_\mu=S_\mu^1$ we have $|S_\mu(b)-S_\mu(a)|^2\lesssim(S_\mu(b)-S_\mu(a))(b-a))$. Thus, setting $n(s)=\min\{k=1,\dots,N\mid t^k\ge s\}$ for all $s\in\mathbb{R}$,

$$\begin{aligned}
&\sum_{\mu\in\{m,f\}}\int_0^{T-h}\int_{M_\mu}|S_\mu(\mathrm{T}_h\Pi_{\mathcal{D}}^{\mu}p_{\mathcal{D}})-S_\mu(\Pi_{\mathcal{D}}^{\mu}p_{\mathcal{D}})|^2\mathrm{d}\tau_\mu\mathrm{d}s \qquad (3.20)\\
&\qquad+\sum_{\mathfrak{a}\in\chi}\int_0^{T-h}\int_{\Gamma_{\mathfrak{a}}}|S_{\mathfrak{a}}(\mathrm{T}_h\mathbb{T}_{\mathcal{D}}^{\mathfrak{a}}p_{\mathcal{D}})-S_{\mathfrak{a}}(\mathbb{T}_{\mathcal{D}}^{\mathfrak{a}}p_{\mathcal{D}})|^2\mathrm{d}\tau\mathrm{d}s\\
&\lesssim\sum_{\mu\in\{m,f\}}\int_0^{T-h}\int_{M_\mu}\phi_\mu\Big(S_\mu(\mathrm{T}_h\Pi_{\mathcal{D}}^{\mu}p_{\mathcal{D}})-S_\mu(\Pi_{\mathcal{D}}^{\mu}p_{\mathcal{D}})\Big)(s)(\mathrm{T}_h\Pi_{\mathcal{D}}^{\mu}p_{\mathcal{D}}-\Pi_{\mathcal{D}}^{\mu}p_{\mathcal{D}})(s)\mathrm{d}\tau_\mu\mathrm{d}s\\
&\qquad+\sum_{\mathfrak{a}\in\chi}\int_0^{T-h}\int_{\Gamma_{\mathfrak{a}}}\eta\Big(S_{\mathfrak{a}}(\mathrm{T}_h\mathbb{T}_{\mathcal{D}}^{\mathfrak{a}}p_{\mathcal{D}})-S_{\mathfrak{a}}(\mathbb{T}_{\mathcal{D}}^{\mathfrak{a}}p_{\mathcal{D}})\Big)(s)(\mathrm{T}_h\mathbb{T}_{\mathcal{D}}^{\mathfrak{a}}p_{\mathcal{D}}-\mathbb{T}_{\mathcal{D}}^{\mathfrak{a}}p_{\mathcal{D}})(s)\mathrm{d}\tau\mathrm{d}s\\
&\lesssim\int_0^{T-h}\Big[\sum_{\mu\in\{m,f\}}\int_{M_\mu}\int_{t^{n(s)}}^{t^{n(s+h)}}\phi_\mu\Pi_{\mathcal{D}}^{\mu}\Big[\delta_t S_\mu(p_{\mathcal{D}})\Big](t)(\mathrm{T}_h\Pi_{\mathcal{D}}^{\mu}p_{\mathcal{D}}-\Pi_{\mathcal{D}}^{\mu}p_{\mathcal{D}})(s)\mathrm{d}t\mathrm{d}\tau_\mu\\
&\qquad+\sum_{\mathfrak{a}\in\chi}\int_{\Gamma_{\mathfrak{a}}}\int_{t^{n(s)}}^{t^{n(s+h)}}\eta\mathbb{T}_{\mathcal{D}}^{\mathfrak{a}}\Big[\delta_t S_{\mathfrak{a}}(p_{\mathcal{D}})\Big](t)(\mathrm{T}_h\mathbb{T}_{\mathcal{D}}^{\mathfrak{a}}p_{\mathcal{D}}-\mathbb{T}_{\mathcal{D}}^{\mathfrak{a}}p_{\mathcal{D}})(s)\mathrm{d}t\mathrm{d}\tau\Big]\mathrm{d}s. \qquad (3.21)
\end{aligned}$$

In the last line, we simply wrote $S_\mu(\mathrm{T}_h\Pi_{\mathcal{D}}^{\mu}p_{\mathcal{D}})(s)-S_\mu(\Pi_{\mathcal{D}}^{\mu}p_{\mathcal{D}})(s)=S_\mu(\Pi_{\mathcal{D}}^{\mu}p_{\mathcal{D}})(s+h)-S_\mu(\Pi_{\mathcal{D}}^{\mu}p_{\mathcal{D}})(s)$ as the sum of the jumps if $S_\mu(\Pi_{\mathcal{D}}^{\mu}p_{\mathcal{D}})$ between s and $s+h$ (likewise for $S_{\mathfrak{a}}(\mathbb{T}_{\mathcal{D}}^{\mathfrak{a}}p_{\mathcal{D}})$).

For a fixed s, define $v_{\mathcal{D}}\in(X_{\mathcal{D}_S}^0)^{N+1}$ by

$$v_{\mathcal{D}}^k=\begin{cases}p_{\mathcal{D}}^{n(s+h)}-p_{\mathcal{D}}^{n(s)} & \text{if } n(s)+1\le k\le n(s+h)\\ 0 & \text{else.}\end{cases}$$

With this choice,

$$\begin{aligned}
\Pi_{\mathcal{D}}^{\mu} v_{\mathcal{D}}(t,\mathbf{x}) &= \mathbb{1}_{[t^{n(s)},t^{n(s+h)}]}(t)\ (\mathrm{T}_h \Pi_{\mathcal{D}}^{\mu} p_{\mathcal{D}} - \Pi_{\mathcal{D}}^{\mu} p_{\mathcal{D}})(s,\mathbf{x}),\\
\mathbb{T}_{\mathcal{D}}^{\mathfrak{a}} v_{\mathcal{D}}(t,\mathbf{x}) &= \mathbb{1}_{[t^{n(s)},t^{n(s+h)}]}(t)\ (\mathrm{T}_h \mathbb{T}_{\mathcal{D}}^{\mathfrak{a}} p_{\mathcal{D}} - \mathbb{T}_{\mathcal{D}}^{\mathfrak{a}} p_{\mathcal{D}})(s,\mathbf{x}),\\
\nabla_{\mathcal{D}}^{\mu} v_{\mathcal{D}}(t,\mathbf{x}) &= \mathbb{1}_{[t^{n(s)},t^{n(s+h)}]}(t)\ (\mathrm{T}_h \nabla_{\mathcal{D}}^{\mu} p_{\mathcal{D}} - \nabla_{\mathcal{D}}^{\mu} p_{\mathcal{D}})(s,\mathbf{x}),\ \text{and}\\
[\![v_{\mathcal{D}}]\!]_{\mathcal{D}}^{\mathfrak{a}}(t,\mathbf{x}) &= \mathbb{1}_{[t^{n(s)},t^{n(s+h)}]}(t)\ (\mathrm{T}_h [\![p_{\mathcal{D}}]\!]_{\mathcal{D}}^{\mathfrak{a}} - [\![p_{\mathcal{D}}]\!]_{\mathcal{D}}^{\mathfrak{a}})(s,\mathbf{x}).
\end{aligned} \tag{3.22}$$

We keep s fixed and concentrate on the integrand of the outer integral in the right-hand side of (3.21). Estimate (3.18), the definition (3.17) of $|\cdot|_{\mathcal{D}_S,*}$, and Young's inequality yield

$$\begin{aligned}
&\sum_{\mu\in\{m,f\}} \int_0^T \int_{M_\mu} \phi_\mu \Pi_{\mathcal{D}}^{\mu} \Big[\delta_t S_\mu(p_{\mathcal{D}})\Big] \Pi_{\mathcal{D}}^{\mu} v_{\mathcal{D}} \mathrm{d}\tau_\mu \mathrm{d}t + \sum_{\mathfrak{a}\in\chi} \int_0^T \int_{\Gamma_{\mathfrak{a}}} \eta \mathbb{T}_{\mathcal{D}}^{\mathfrak{a}} \Big[\delta_t S_{\mathfrak{a}}(p_{\mathcal{D}})\Big] \mathbb{T}_{\mathcal{D}}^{\mathfrak{a}} v_{\mathcal{D}} \mathrm{d}\tau \mathrm{d}t\\
&\quad\lesssim \int_0^T (\|h_\mu(t)\|_{L^2(M_\mu)} + \|u_{\mathcal{D}}(t)\|_{\mathcal{D}_S}) \|v_{\mathcal{D}}(t)\|_{\mathcal{D}_S} \mathbb{1}_{[t^{n(s)},t^{n(s+h)}]}(t) \mathrm{d}t\\
&\quad\lesssim \int_0^T (\|h_\mu(t)\|_{L^2(M_\mu)} + \|u_{\mathcal{D}}(t)\|_{\mathcal{D}_S})^2 \mathbb{1}_{[t^{n(s)},t^{n(s+h)}]}(t) \mathrm{d}t\\
&\qquad + (t^{n(s+h)} - t^{n(s)}) \|p_{\mathcal{D}}^{n(s+h)} - p_{\mathcal{D}}^{n(s)}\|_{\mathcal{D}_S}^2.
\end{aligned}$$

Returning to (3.21), integrate the previous estimate over $s \in (0, T-h)$. In this step, it is crucial to realise that

$$t^{n(s+h)} - t^{n(s)} \le h + \Delta t \quad \text{and} \quad \int_0^{T-h} \mathbb{1}_{[t^{n(s)},t^{n(s+h)}]}(t) \mathrm{d}s \le \int_0^T \mathbb{1}_{[t-h-\Delta t,t]}(s) \mathrm{d}s \le h + \Delta t.$$

Hence, recalling the definition of v,

$$\begin{aligned}
\mathrm{RHS}(3.21) &\lesssim (h+\Delta t) \Bigg[\int_0^T (\|h_\mu(t)\|_{L^2(M_\mu)} + \|u_{\mathcal{D}}(t)\|_{\mathcal{D}_S})^2 \mathrm{d}t\\
&\qquad + \int_0^{T-h} \|p_{\mathcal{D}}^{n(s+h)}\|_{\mathcal{D}_S}^2 \mathrm{d}s + \int_0^{T-h} \|p_{\mathcal{D}}^{n(s)}\|_{\mathcal{D}_S}^2 \mathrm{d}s \Bigg]\\
&\lesssim (h+\Delta t) \Big(1 + \|u_{\mathcal{D}}\|_{\mathcal{D}}^2 + \|p\|_{\mathcal{D}}^2 \Big).
\end{aligned}$$

Since $p = u^1 - u^2$, this proves (3.19) with $L^2(0,T-h)$ norms in the left-hand side, instead of $L^2(0,T)$ norms. The complete form of (3.19) follows by recalling that $0 \le S_\mu \le 1$, so that $\|S_\mu(\Pi_{\mathcal{D}}^{\mu} p_{\mathcal{D}})\|_{L^2((T-h,T)\times M_\mu)}^2 \le h$ (and similarly for other saturation terms). □

Lemma 3.4.4 (Estimate on space translates) *Under the assumptions of Section 3.2, let $\mathcal{D}$ be a gradient discretisation with piecewise constant reconstructions $\Pi_{\mathcal{D}}^{\mu}$, $\mathbb{T}_{\mathcal{D}}^{\mathfrak{a}}$. Let $(u_{\mathcal{D}}^{\alpha})_{\alpha=1,2} \in [(X_{\mathcal{D}_S}^0)^{N+1}]^2$ be a solution of (3.4), and let $\boldsymbol{\xi} = (\boldsymbol{\xi}_m, \boldsymbol{\xi}_f)$, with $\boldsymbol{\xi}_m \in \mathbb{R}^d$ and*

$\boldsymbol{\xi}_f = (\boldsymbol{\xi}_{f,i})_{i\in I} \in \bigoplus_{i\in I}\tau(\mathcal{P}_i)$, *where* $\tau(\mathcal{P}_i)$ *is the (const.) tangent space of* $\mathcal{P}_i$. *Then, extending the functions* $\Pi^\mu_{\mathcal{D}}p_{\mathcal{D}}$ *and* S_μ *by* 0 *outside* M_μ,

$$\|\mathrm{T}_{\boldsymbol{\xi}_m}S_m(\Pi^m_{\mathcal{D}}p_{\mathcal{D}}) - S_m(\Pi^m_{\mathcal{D}}p_{\mathcal{D}})\|^2_{L^2((0,T)\times\mathbb{R}^d)} + \sum_{i\in I}\Big(\|\mathrm{T}_{\boldsymbol{\xi}_{f,i}}S_f(\Pi^f_{\mathcal{D}}p_{\mathcal{D}}) - S_f(\Pi^f_{\mathcal{D}}p_{\mathcal{D}})\|^2_{L^2((0,T)\times\mathcal{P}_i)}$$
$$+ \sum_{\mathfrak{a}=\mathfrak{a}^\pm(i)}\|\mathrm{T}_{\boldsymbol{\xi}_{f,i}}S_{\mathfrak{a}}(\mathbb{T}^{\mathfrak{a}}_{\mathcal{D}}p_{\mathcal{D}}) - S_{\mathfrak{a}}(\mathbb{T}^{\mathfrak{a}}_{\mathcal{D}}p_{\mathcal{D}})\|^2_{L^2((0,T)\times\mathcal{P}_i)}\Big) \lesssim \mathcal{T}_{\mathcal{D}_S}(\boldsymbol{\xi})\sum_{\alpha=1}^{2}\|u^\alpha_{\mathcal{D}}\|^2_{\mathcal{D}} + |\boldsymbol{\xi}|,$$

where we recall that $\mathrm{T}_{\boldsymbol{\zeta}}f(\mathbf{x}) = f(\mathbf{x}+\boldsymbol{\zeta})$, *and* $\mathcal{T}_{\mathcal{D}_S}$ *is given in Definition 3.3.6.*

Proof Let us focus on the matrix Ω, and remember that, as a function of $\mathbf{x}$, S_m is piecewise constant on a polytopal partition $(\Omega_j)_{j\in J_m}$. Write

$$\begin{aligned}\mathrm{T}_{\boldsymbol{\xi}_m}S_m(\Pi^m_{\mathcal{D}}p_{\mathcal{D}}) - S_m(\Pi^m_{\mathcal{D}}p_{\mathcal{D}}) &= S_m(\mathbf{x}+\boldsymbol{\xi}_m, \Pi^m_{\mathcal{D}}p_{\mathcal{D}}(\mathbf{x}+\boldsymbol{\xi}_m,t)) - S_m(\mathbf{x}+\boldsymbol{\xi}_m, \Pi^m_{\mathcal{D}}p_{\mathcal{D}}(\mathbf{x},t))\\ &\quad + S_m(\mathbf{x}+\boldsymbol{\xi}_m, \Pi^m_{\mathcal{D}}p_{\mathcal{D}}(\mathbf{x},t)) - S_m(\mathbf{x}, \Pi^m_{\mathcal{D}}p_{\mathcal{D}}(\mathbf{x},t)). \quad (3.23)\end{aligned}$$

Let $\Omega_{\boldsymbol{\xi}_m} = \bigcup_j\{\mathbf{x}\in\Omega_j \mid \mathbf{x}+\boldsymbol{\xi}_m\notin\Omega_j\}\cup\{\mathbf{x}\in\mathbb{R}^d\setminus\Omega \mid \mathbf{x}+\boldsymbol{\xi}_m\in\Omega\}$ be the set of points $\mathbf{x}$ that do not belong to the same element Ω_j as their translate $\mathbf{x}+\boldsymbol{\xi}_m$. By assumption on S_m,

$$\sup_{q\in\mathbb{R}}|S_m(\mathbf{x}+\boldsymbol{\xi}_m,q) - S_m(\mathbf{x},q)| \le \begin{cases} 0 & \text{on } \mathbb{R}^d\setminus\Omega_{\boldsymbol{\xi}_m},\\ 1 & \text{on } \Omega_{\boldsymbol{\xi}_m}.\end{cases}$$

Moreover, since each Ω_j is polytopal, $|\Omega_{\boldsymbol{\xi}_m}| \lesssim |\boldsymbol{\xi}_m|$. Hence,

$$\int_0^T\int_{\mathbb{R}^d}\sup_{q\in\mathbb{R}}|S_m(\mathbf{x}+\boldsymbol{\xi}_m,q) - S_m(\mathbf{x},q)|^2\mathrm{d}\mathbf{x}\mathrm{d}t \lesssim |\boldsymbol{\xi}_m|. \quad (3.24)$$

On the other hand, by definition of $\mathcal{T}_{D_S}$ and the Lipschitz continuity of S_m,

$$\begin{aligned}&\int_0^T\int_{\mathbb{R}^d}|S_m(\mathbf{x}+\boldsymbol{\xi}_m, \Pi^m_{\mathcal{D}}p_{\mathcal{D}}(\mathbf{x}+\boldsymbol{\xi}_m,t)) - S_m(\mathbf{x}+\boldsymbol{\xi}_m, \Pi^m_{\mathcal{D}}p_{\mathcal{D}}(\mathbf{x},t))|^2\mathrm{d}\mathbf{x}\mathrm{d}t\\ &\qquad\lesssim \int_0^T\int_{\mathbb{R}^d}|\Pi^m_{\mathcal{D}}p_{\mathcal{D}}(\mathbf{x}+\boldsymbol{\xi}_m,t) - \Pi^m_{\mathcal{D}}p_{\mathcal{D}}(\mathbf{x},t)|^2\mathrm{d}\mathbf{x}\mathrm{d}t \lesssim \|p_{\mathcal{D}}\|^2_{\mathcal{D}}\mathcal{T}_{D_S}(\boldsymbol{\xi}). \quad (3.25)\end{aligned}$$

Plugging (3.24) and (3.25) into (3.23) and reasoning similarly for S_f and $S_{\mathfrak{a}}$ concludes the proof. □

Remark 3.4.2 *This proof is the only place where the assumption that each* M^j_μ *is polytopal is used; this is to ensure that* $|\Omega_{\boldsymbol{\xi}_m}| \lesssim |\boldsymbol{\xi}_m|$ *(and likewise for fracture and interfacial terms). Obviously, this asssumption on the sets* M^j_μ *could be relaxed (e.g., into "each* M^j_μ *has a Lipschitz-continuous boundary"), but assuming that these sets are polytopal is not restrictive for practical applications.*

3.4.2 Initial convergences

We can now state our initial convergence theorem for sequences of solutions to gradient schemes. This theorem does not yet identify the weak limits of such sequences.

Theorem 3.4.2 (Averaged-in-time convergence of approximate solutions) *Let $(\mathcal{D}_l)_{l\in\mathbb{N}}$ be a coercive, consistent, limit-conforming and compact sequence of space-time gradient discretisations, with piecewise constant reconstructions. Let $(u^\alpha_{\mathcal{D}_l})_{\alpha=1,2,l\in\mathbb{N}}$ be such that $(u^\alpha_{\mathcal{D}_l})_{\alpha=1,2} \in [(X^0_{\mathcal{D}_S^l})^{N_l+1}]^2$ is a solution of (3.4) with $\mathcal{D} = \mathcal{D}_l$. Then, there exists $(\overline{u}^\alpha)_{\alpha=1,2} = (\overline{u}^\alpha_m, \overline{u}^\alpha_f)_{\alpha=1,2} \in [L^2(0,T;V^0_m) \times L^2(0,T;V^0_f)]^2$ such that, up to a subsequence as $l \to \infty$, the convergences (3.6) and (3.7) hold.*

Proof Combining Lemmata 3.4.1 and 3.A.1 immediately gives (3.6). By assumption, $0 \le S_\mu, S_\mathfrak{a} \le 1$ and therefore, by Lemmata 3.4.3 and 3.4.4 and the Kolmogorov compactness theorem, there exists a subsequence of $(\Pi^\mu_{\mathcal{D}_l} S_\mu(p_{\mathcal{D}_l}))_l$ that strongly converges in $L^2((0,T)\times M_\mu)$ and a subsequence of $(\mathbb{T}^\mathfrak{a}_{\mathcal{D}_l} S_\mathfrak{a}(p_{\mathcal{D}_l}))_l$ that strongly converges in $L^2((0,T)\times\Gamma_\mathfrak{a})$. Also, by assumption, $S_\mu, S_\mathfrak{a}$ are non-decreasing functions, which allows us to identify the limits in (3.7) by applying Corollary 3.A.1. □

Let C^∞_Ω be the subspace of functions in $C^\infty_b(\Omega\setminus\overline{\Gamma})$ vanishing on a neighbourhood of the boundary $\partial\Omega$. Define also $C^\infty_\Gamma = \gamma_\Gamma(C^\infty_0(\Omega))$ as the image of $C^\infty_0(\Omega)$ of the trace operator $\gamma_\Gamma\colon H^1_0(\Omega) \to L^2(\Gamma)$.

The following lemma and theorem add a uniform-in-time weak L^2 convergence property to the properties already established in Theorem 3.4.2.

Lemma 3.4.5 (Uniform-in-time, weak-in-space translate estimates) *Under the assumptions of Section 3.2, let $\mathcal{D}$ be a gradient discretisation with piecewise constant reconstructions $\Pi^\mu_\mathcal{D}$, $\mathbb{T}^\mathfrak{a}_\mathcal{D}$. Let $(u^\alpha_\mathcal{D})_{\alpha=1,2} \in [(X^0_{\mathcal{D}_S})^{N+1}]^2$ be a solution of the gradient scheme of (3.4), and $p = u^1_\mathcal{D} - u^2_\mathcal{D}$. Then, for all $\varphi = (\varphi_m, \varphi_f) \in C^\infty_\Omega \times C^\infty_\Gamma$ and all $s,t \in [0,T]$,*

$$\begin{aligned}
&\Bigg| \sum_{\mu\in\{m,f\}} \left\langle d_\mu\phi_\mu \Pi^\mu_\mathcal{D} S_\mu(p_\mathcal{D})(s) - d_\mu\phi_\mu\Pi^\mu_\mathcal{D} S_\mu(p_\mathcal{D})(t), \varphi_\mu\right\rangle_{L^2(M_\mu)} \\
&\qquad + \sum_{\mathfrak{a}\in\chi} \left\langle \eta \mathbb{T}^\mathfrak{a}_\mathcal{D} S_\mathfrak{a}(p_\mathcal{D})(s) - \eta\mathbb{T}^\mathfrak{a}_\mathcal{D} S_\mathfrak{a}(p_\mathcal{D})(t), \gamma_\mathfrak{a}\varphi_m\right\rangle_{L^2(\Gamma_\mathfrak{a})} \Bigg| \\
&\qquad \lesssim \mathcal{S}_{\mathcal{D}_S}(\varphi) + (\mathcal{S}_{\mathcal{D}_S}(\varphi) + C_\varphi)\left(1 + \sum_{\alpha=1}^2 \|u^\alpha_\mathcal{D}\|^2_\mathcal{D}\right)^{\frac12} \left[|s-t|^{\frac12} + (\Delta t)^{\frac12}\right]. \qquad (3.26)
\end{aligned}$$

where C_φ only depends on φ, d_f is the width of the fractures, and $d_m = 1$.

Proof Let us introduce an interpolant $\mathrm{P}_{\mathcal{D}_S} : C^\infty_\Omega \times C^\infty_\Gamma \to X^0_{\mathcal{D}_S}$ such that, for all $\varphi \in C^\infty_\Omega \times C^\infty_\Gamma$,

$$s_{\mathcal{D}_S}(\mathrm{P}_{\mathcal{D}_S}\varphi, \varphi) = \mathcal{S}_{\mathcal{D}_S}(\varphi).$$

As in the proof of Lemma 3.4.3, let $n(r) = \min\{k = 1, \dots, N \mid t^k \geq r\}$ for all $r \in [0, T]$. Denote by L the left-hand side of (3.26) and introduce $\Pi^\mu_{\mathcal{D}_S} \mathrm{P}_{\mathcal{D}_S}\varphi$ in the first sum and $\mathbb{T}^{\mathfrak{a}}_{\mathcal{D}_S} \mathrm{P}_{\mathcal{D}_S}\varphi$ in the second sum to write

$$
\begin{aligned}
L \leq & \sum_{\mu\in\{m,f\}} \Big(\Big| \big\langle d_\mu \phi_\mu \Pi^\mu_{\mathcal{D}} S_\mu(p_{\mathcal{D}})(s) - d_\mu \phi_\mu \Pi^\mu_{\mathcal{D}} S_\mu(p_{\mathcal{D}})(t), \varphi_\mu - \Pi^\mu_{\mathcal{D}_S} \mathrm{P}_{\mathcal{D}_S}\varphi \big\rangle_{L^2(M_\mu)} \Big| \Big) \qquad (3.27) \\
& + \sum_{\mathfrak{a}\in\chi} \Big(\Big| \big\langle \eta \mathbb{T}^{\mathfrak{a}}_{\mathcal{D}} S_{\mathfrak{a}}(p_{\mathcal{D}})(s) - \eta \mathbb{T}^{\mathfrak{a}}_{\mathcal{D}} S_{\mathfrak{a}}(p_{\mathcal{D}})(t), \gamma_{\mathfrak{a}}\varphi_m - \mathbb{T}^{\mathfrak{a}}_{\mathcal{D}_S} \mathrm{P}_{\mathcal{D}_S}\varphi \big\rangle_{L^2(\Gamma_{\mathfrak{a}})} \Big| \Big) \qquad (3.28) \\
& + \Bigg| \sum_{\mu\in\{m,f\}} \Big\langle d_\mu \phi_\mu \Big[\Pi^\mu_{\mathcal{D}} S_\mu(p_{\mathcal{D}})(s) - \Pi^\mu_{\mathcal{D}} S_\mu(p_{\mathcal{D}})(t) \Big], \Pi^\mu_{\mathcal{D}_S} \mathrm{P}_{\mathcal{D}_S}\varphi \Big\rangle_{L^2(M_\mu)} \\
& \qquad + \sum_{\mathfrak{a}\in\chi} \Big\langle \eta \Big[\mathbb{T}^{\mathfrak{a}}_{\mathcal{D}} S_{\mathfrak{a}}(p_{\mathcal{D}})(s) - \mathbb{T}^{\mathfrak{a}}_{\mathcal{D}} S_{\mathfrak{a}}(p_{\mathcal{D}})(t) \Big], \mathbb{T}^{\mathfrak{a}}_{\mathcal{D}_S} \mathrm{P}_{\mathcal{D}_S}\varphi \Big\rangle_{L^2(\Gamma_{\mathfrak{a}})} \Bigg| \\
\lesssim & \, \mathcal{S}_{\mathcal{D}_S}(\varphi) + \Bigg| \sum_{\mu\in\{m,f\}} \Big\langle d_\mu \phi_\mu \Big[\Pi^\mu_{\mathcal{D}} S_\mu(p_{\mathcal{D}})(s) - \Pi^\mu_{\mathcal{D}} S_\mu(p_{\mathcal{D}})(t) \Big], \Pi^\mu_{\mathcal{D}_S} \mathrm{P}_{\mathcal{D}_S}\varphi \Big\rangle_{L^2(M_\mu)} \\
& \qquad + \sum_{\mathfrak{a}\in\chi} \Big\langle \eta \Big[\mathbb{T}^{\mathfrak{a}}_{\mathcal{D}} S_{\mathfrak{a}}(p_{\mathcal{D}})(s) - \mathbb{T}^{\mathfrak{a}}_{\mathcal{D}} S_{\mathfrak{a}}(p_{\mathcal{D}})(t) \Big], \mathbb{T}^{\mathfrak{a}}_{\mathcal{D}_S} \mathrm{P}_{\mathcal{D}_S}\varphi \Big\rangle_{L^2(\Gamma_{\mathfrak{a}})} \Bigg| . \qquad (3.29)
\end{aligned}
$$

Here, the terms (3.27) and (3.28) have been estimated by using $0 \leq S_\mu, S_{\mathfrak{a}} \leq 1$ and the definition of $\mathrm{P}_{\mathcal{D}_S}\varphi$. Let L_1 be the second addend in (3.29). Assuming that $t < s$, and hence $n(t) \leq n(s)$, write $\Pi^\mu_{\mathcal{D}} S_\mu(p_{\mathcal{D}})(s) - \Pi^\mu_{\mathcal{D}} S_\mu(p_{\mathcal{D}})(t)$ and $\mathbb{T}^{\mathfrak{a}}_{\mathcal{D}} S_{\mathfrak{a}}(p_{\mathcal{D}})(s) - \mathbb{T}^{\mathfrak{a}}_{\mathcal{D}} S_{\mathfrak{a}}(p_{\mathcal{D}})(t)$ as the sum of their jumps, and recall the definition (3.17) of $|\cdot|_{\mathcal{D}_S,*}$ to obtain

$$
\begin{aligned}
L_1 \leq & \Bigg| \sum_{k=n(t)}^{n(s)-1} \Delta t^{k+\frac{1}{2}} \Big(\sum_{\mu\in\{m,f\}} \big\langle d_\mu \phi_\mu \Pi^\mu_{\mathcal{D}} \delta_t S_\mu(p_{\mathcal{D}})(t^k), \Pi^\mu_{\mathcal{D}_S} \mathrm{P}_{\mathcal{D}_S}\varphi \big\rangle_{L^2(M_\mu)} \\
& \qquad + \sum_{\mathfrak{a}\in\chi} \big\langle \eta \mathbb{T}^{\mathfrak{a}}_{\mathcal{D}} \delta_t S_{\mathfrak{a}}(p_{\mathcal{D}})(t^k), \mathbb{T}^{\mathfrak{a}}_{\mathcal{D}_S} \mathrm{P}_{\mathcal{D}_S}\varphi \big\rangle_{L^2(M_\mu)} \Big) \Bigg| \\
\leq & \sum_{k=n(t)}^{n(s)-1} \Delta t^{k+\frac{1}{2}} \Big| \Big[\delta_t S_m(p_{\mathcal{D}})(t^k), \delta_t S_f(p_{\mathcal{D}})(t^k), (\delta_t S_{\mathfrak{a}}(p_{\mathcal{D}})(t^k))_{\mathfrak{a}\in\chi} \Big] \Big|_{\mathcal{D}_S,*} \|\mathrm{P}_{\mathcal{D}_S}\varphi\|_{\mathcal{D}_S} \\
\leq & \, \|\mathrm{P}_{\mathcal{D}_S}\varphi\|_{\mathcal{D}_S} \int_0^T \mathbb{1}_{[t^{n(t)}, t^{n(s)}]}(r) \Big| \Big[\delta_t S_m(p_{\mathcal{D}})(r), \delta_t S_f(p_{\mathcal{D}})(r), (\delta_t S_{\mathfrak{a}}(p_{\mathcal{D}})(r))_{\mathfrak{a}\in\chi} \Big] \Big|_{\mathcal{D}_S,*} \mathrm{d}r.
\end{aligned}
$$

Use now Lemmata 3.4.2 and the Cauchy–Schwarz inequality to infer

$$
L_1 \lesssim \|\mathrm{P}_{\mathcal{D}_S}\varphi\|_{\mathcal{D}_S} \left(1 + \sum_{\alpha=1}^{2} \|u^\alpha_{\mathcal{D}}\|^2_{\mathcal{D}} \right)^{\frac{1}{2}} \Big[(s-t)^{\frac{1}{2}} + (\Delta t)^{\frac{1}{2}} \Big]. \qquad (3.30)
$$

By the triangle inequality,

$$\|\mathrm{P}_{\mathcal{D}_S}\varphi\|_{\mathcal{D}_S} \leq \mathcal{S}_{\mathcal{D}_S}(\varphi) + \|\nabla\varphi_m\|_{L^2(\Omega)^d} + \|\nabla_\tau\varphi_f\|_{L^2(\Gamma)^{d-1}} + \sum_{\mathfrak{a}\in\chi}\|[\![\varphi]\!]_\mathfrak{a}\|_{L^2(\Gamma_\mathfrak{a})} = \mathcal{S}_{\mathcal{D}_S}(\varphi) + C_\varphi.$$

Plugging this into (3.30) and the resulting inequality into (3.29) concludes the proof. □

Theorem 3.4.3 (Uniform-in-time, weak-in-space convergence) *Under the assumptions of Theorem 3.4.2, for all $\mu \in \{m, f\}$ and $\mathfrak{a} \in \chi$, $S_\mu(\overline{p}_\mu) : [0,T] \to L^2(M_\mu)$ and $S_\mathfrak{a}(\gamma_\mathfrak{a}\overline{p}_m) : [0,T] \to L^2(\Gamma_\mathfrak{a})$ are continuous for the weak topologies of $L^2(M_\mu)$ and $L^2(\Gamma_\mathfrak{a})$, respectively, and*

$$\begin{aligned}&\Pi^\mu_{\mathcal{D}_l} S_\mu(p_{\mathcal{D}_l}) \longrightarrow S_\mu(\overline{p}_\mu) \text{ uniformly in } [0,T], \text{ weakly in } L^2(M_\mu),\\ &\mathbb{T}^\mathfrak{a}_{\mathcal{D}_l} S_\mathfrak{a}(p_{\mathcal{D}_l}) \longrightarrow S_\mathfrak{a}(\gamma_\mathfrak{a}\overline{p}_m) \text{ uniformly in } [0,T], \text{ weakly in } L^2(\Gamma_\mathfrak{a}),\end{aligned} \tag{3.31}$$

where the definition of the uniform-in-time weak L^2 convergence is recalled in the appendix.

Proof The proof hinges on the discontinuous Arzelà-Ascoli theorem (Theorem 3.A.1 in the appendix). Consider first the matrix saturation. The space $\mathcal{R}_m = \left\{d_m\phi_m\varphi_m \mid \varphi_m \in C_0^\infty(\Omega\setminus\overline{\Gamma})\right\}$ is dense in $L^2(\Omega)$. Apply (3.26) to $\varphi = (\varphi_m, 0)$. Since $\varphi_f = \gamma_\mathfrak{a}\varphi_m = 0$ only the term involving S_m remains in the left-hand side. The resulting estimate and the property $0 \leq S_m \leq 1$ show that the sequence of functions $(t \mapsto \Pi^m_{\mathcal{D}_l} S_m(p_{\mathcal{D}_l})(t))_{l\in\mathbb{N}}$ satisfies the assumptions of Theorem 3.A.1 with $\mathcal{R} = \mathcal{R}_m$. Hence, $(\Pi^m_{\mathcal{D}_l} S_m(p_{\mathcal{D}_l}))_{l\in\mathbb{N}}$ has a subsequence that converges uniformly on $[0,T]$ weakly in $L^2(\Omega)$. Given (3.7), the weak limit of this sequence must be $S_m(\overline{p}_m)$.

A similar reasoning, based on the space $\mathcal{R}_f = \left\{d_f\phi_f\varphi_f \mid \varphi_f \in C_\Gamma^\infty\right\}$ – which is dense in $L^2(\Gamma)$ – and using $\varphi = (0, \varphi_f)$ in (3.26), gives the uniform-in-time weak $L^2(\Gamma)$ convergence of $\Pi^f_{\mathcal{D}_l} S_f(p_{\mathcal{D}_l})$ towards $S_f(\overline{p}_f)$.

Let us now turn to the convergence of the trace saturations. Take $\varphi_m \in C_\Omega^\infty$ such that the support of $\gamma_\mathfrak{a}\varphi_m$ is non empty for exactly one $\mathfrak{a} \in \chi$. Considering $\varphi = (\varphi_m, 0)$ in (3.26) leads to

$$\begin{aligned}&\left|\left\langle \eta\mathbb{T}^\mathfrak{a}_{\mathcal{D}_l} S_\mathfrak{a}(p_{\mathcal{D}_l})(s) - \eta\mathbb{T}^\mathfrak{a}_{\mathcal{D}_l} S_\mathfrak{a}(p_{\mathcal{D}_l})(t), \gamma_\mathfrak{a}\varphi_m\right\rangle_{L^2(\Gamma_\mathfrak{a})}\right|\\ &\qquad\lesssim \mathcal{S}_{\mathcal{D}_S}(\varphi) + (\mathcal{S}_{\mathcal{D}_S}(\varphi) + C_\varphi)\left(1 + \sum_{\alpha=1}^2 \|u^\alpha_\mathcal{D}\|^2_\mathcal{D}\right)^{\frac{1}{2}}\left[|s-t|^{\frac{1}{2}} + (\Delta t)^{\frac{1}{2}}\right]\\ &\qquad + \left|\left\langle d_m\phi_m\Pi^m_{\mathcal{D}_l} S_m(p_{\mathcal{D}_l})(s) - d_m\phi_m\Pi^m_{\mathcal{D}_l} S_m(p_{\mathcal{D}_l})(t), \varphi_m\right\rangle_{L^2(\Omega)}\right|.\end{aligned} \tag{3.32}$$

Since it was established that $(d_m\phi_m\Pi^m_{\mathcal{D}_l} S_m(p_{\mathcal{D}_l}))_{l\in\mathbb{N}}$ converges uniformly-in-time weakly in $L^2(\Omega)$, the sequence $(\langle d_m\phi_m\Pi^m_{\mathcal{D}_l} S_m(p_{\mathcal{D}_l}), \varphi_m\rangle_{L^2(\Omega)})_{l\in\mathbb{N}}$ is equi-continuous and the last term in (3.32) therefore tends to 0 uniformly in l as $s - t \to 0$. Hence, (3.32) enables the usage of Theorem 3.A.1, by noticing that $\{\eta\gamma_\mathfrak{a}\varphi_m \mid \varphi_m \in C_\Omega^\infty,\ \mathrm{supp}(\gamma_\mathfrak{b}\varphi_m) = \emptyset \text{ for all } \mathfrak{b} \in \chi \text{ with } \mathfrak{b} \neq \mathfrak{a}\}$ is dense in $L^2(\Gamma_\mathfrak{a})$, and gives the uniform-in-time weak $L^2(\Gamma_\mathfrak{a})$ convergence of $\mathbb{T}^\mathfrak{a}_{\mathcal{D}_l} S_\mathfrak{a}(p_{\mathcal{D}_l})$. □

3.4.3 Proof of Theorem 3.4.1

The proof of the main convergence theorem can now be given.

First step: passing to the limit in the gradient scheme.

Let us introduce the family of functions $(\mathrm{F}^{\mathfrak{a},\alpha}_{\mathcal{D}_l})^{\alpha=1,2}_{\mathfrak{a}\in\chi}$:

$$\mathrm{F}^{\mathfrak{a},\alpha}_{\mathcal{D}_l}(t,\mathbf{x},\beta)=\Big[T_f[kS]^\alpha_{\mathfrak{a}}(\mathbb{T}^{\mathfrak{a}}_{\mathcal{D}_l}p_{\mathcal{D}_l})\beta^+-T_f[kS]^\alpha_f(\Pi^f_{\mathcal{D}_l}p_{\mathcal{D}_l})\beta^-\Big](t,\mathbf{x}),\quad \text{for all } \beta\in L^2(\Gamma_{\mathfrak{a}}),$$

and their continuous counterparts $(\mathrm{F}^{\mathfrak{a},\alpha})^{\alpha=1,2}_{\mathfrak{a}\in\chi}$:

$$\mathrm{F}^{\mathfrak{a},\alpha}(t,\mathbf{x},\beta)=\Big[T_f[kS]^\alpha_{\mathfrak{a}}(\gamma_{\mathfrak{a}}\overline{p}_m)\beta^+-T_f[kS]^\alpha_f(\overline{p}_f)\beta^-\Big](t,\mathbf{x}),\quad \text{for all } \beta\in L^2(\Gamma_{\mathfrak{a}}).$$

The following properties are easy to check. Firstly, since T_f, $[kS]^\alpha_{\mathfrak{a}}$ and $[kS]_f$ are positive and $s\mapsto s^+$ and $s\mapsto -s^-$ are non-decreasing,

$$\Big[\mathrm{F}^{\mathfrak{a},\alpha}_{\mathcal{D}_l}(t,\mathbf{x},\beta)-\mathrm{F}^{\mathfrak{a},\alpha}_{\mathcal{D}_l}(t,\mathbf{x},\gamma)\Big]\Big[\beta(t,\mathbf{x})-\gamma(t,\mathbf{x})\Big]\geq 0,\quad \text{for all } \beta,\gamma\in L^2(\Gamma_{\mathfrak{a}}). \tag{3.33}$$

Secondly, by the convergences (3.7), for $(\beta_l)_{l\in\mathbb{N}}\subset L^2(\Gamma_{\mathfrak{a}})$ and $\beta\in L^2(\Gamma_{\mathfrak{a}})$,

$$\beta_l\longrightarrow\beta \text{ in } L^2((0,T)\times\Gamma_{\mathfrak{a}})\quad\Longrightarrow\quad \mathrm{F}^{\mathfrak{a},\alpha}_{\mathcal{D}_l}(\beta_l)\longrightarrow\mathrm{F}^{\mathfrak{a},\alpha}(\beta) \text{ in } L^2((0,T)\times\Gamma_{\mathfrak{a}}). \tag{3.34}$$

Thirdly, by Lemma 3.4.1, the sequences $(\mathrm{F}^{\mathfrak{a},\alpha}_{\mathcal{D}_l}([\![u_{\mathcal{D}_l}]\!]^{\mathfrak{a}}_{\mathcal{D}_l}))_{l\in\mathbb{N}}$ ($\mathfrak{a}\in\chi$, $\alpha=1,2$) are bounded in $L^2((0,T)\times\Gamma_{\mathfrak{a}})$ and there exists thus $\rho^\alpha_{\mathfrak{a}}\in L^2((0,T)\times\Gamma_{\mathfrak{a}})$ such that, up to a subsequence,

$$\mathrm{F}^{\mathfrak{a},\alpha}_{\mathcal{D}_l}([\![u^\alpha_{\mathcal{D}_l}]\!]^{\mathfrak{a}}_{\mathcal{D}_l})\rightharpoonup\rho^\alpha_{\mathfrak{a}}\quad \text{in } L^2((0,T)\times\Gamma_{\mathfrak{a}}). \tag{3.35}$$

Consider $\varphi^\alpha=(\varphi^\alpha_m,\varphi^\alpha_f)=\sum_{k=1}^b\theta^{\alpha,k}\otimes\psi^{\alpha,k}$, where $(\psi^{\alpha,k})_{k\in\mathbb{N}}=(\psi^{\alpha,k}_m,\psi^{\alpha,k}_f)_{k=1,\dots,b}\in C^\infty_\Omega\times C^\infty_\Gamma$ and $(\theta^{\alpha,k})_{k=1,\dots,b}\in C^\infty_0([0,T))$. Take $(v^{\alpha,n}_{\mathcal{D}_l})_{n=0,\dots,N_l}=(\mathrm{P}_{\mathcal{D}^l_S}\varphi^\alpha(t^n_l))_{n=0,\dots,N_l}\in(X^0_{\mathcal{D}^l_S})^{N_l+1}$ as "test function" in (3.4). Here, $\mathrm{P}_{\mathcal{D}^l_S}$ is defined as in the proof of Lemma 3.4.5. Apply the discrete integration-by-parts of [29, Section C.1.6] on the accumulation terms in (3.4), let $l\to\infty$ and use standard convergence arguments [27, 29] based on Theorem 3.4.2 to see that

$$\begin{aligned}
&\sum_{\alpha=1}^2\Bigg\{\sum_{\mu\in\{m,f\}}\Big(-\int_0^T\int_{M_\mu}\phi_\mu S^\alpha_\mu(\overline{p}_\mu)\partial_t\varphi^\alpha_\mu\mathrm{d}\tau_\mu\mathrm{d}t+\int_0^T\int_{M_\mu}[kS]^\alpha_\mu(\overline{p}_\mu)\,\Lambda_\mu\nabla\overline{u}^\alpha_\mu\cdot\nabla\varphi^\alpha_\mu\mathrm{d}\tau_\mu\mathrm{d}t\\
&\qquad-\int_{M_\mu}\phi_\mu S^\alpha_\mu(\overline{p}_{\mu,0})\varphi^\alpha_\mu(0,\cdot)\mathrm{d}\tau_\mu\Big)+\sum_{\mathfrak{a}\in\chi}\Big(\int_0^T\int_{\Gamma_{\mathfrak{a}}}\rho^\alpha_{\mathfrak{a}}[\![\varphi^\alpha]\!]_{\mathfrak{a}}\mathrm{d}\tau\mathrm{d}t\\
&\qquad-\int_0^T\int_{\Gamma_{\mathfrak{a}}}\eta S^\alpha_{\mathfrak{a}}(\gamma_{\mathfrak{a}}\overline{p}_m)\partial_t\gamma_{\mathfrak{a}}\varphi^\alpha_m\mathrm{d}\tau\mathrm{d}t-\int_{\Gamma_{\mathfrak{a}}}\eta S^\alpha_{\mathfrak{a}}(\gamma_{\mathfrak{a}}\overline{p}_{m,0})\gamma_{\mathfrak{a}}\varphi^\alpha_m(0,\cdot)\mathrm{d}\tau\Big)\Bigg\}\\
&=\sum_{\alpha=1}^2\sum_{\mu\in\{m,f\}}\int_0^T\int_{M_\mu}h^\alpha_\mu\varphi^\alpha_\mu\mathrm{d}\tau_\mu\mathrm{d}t.
\end{aligned}\tag{3.36}$$

Note that Equation (3.36) also holds for any smooth φ^α, by density of tensorial functions in smooth functions [26, Appendix D]. Recalling the weak formulation (3.2), proving Theorem 3.4.1 is now all about showing that

$$\sum_{\mathfrak{a},\alpha}\int_0^T\int_{\Gamma_\mathfrak{a}}\rho_\mathfrak{a}^\alpha[\![\varphi^\alpha]\!]_\mathfrak{a}\mathrm{d}\tau\mathrm{d}t=\sum_{\mathfrak{a},\alpha}\int_0^T\int_{\Gamma_\mathfrak{a}}\mathrm{F}^{\mathfrak{a},\alpha}([\![\overline{u}^\alpha]\!]_\mathfrak{a})[\![\varphi^\alpha]\!]_\mathfrak{a}\mathrm{d}\tau\mathrm{d}t. \tag{3.37}$$

This is achieved by using Minty's trick.

Second step: proof that

$$\limsup_{l\to\infty}\sum_{\mathfrak{a},\alpha}\int_0^T\int_{\Gamma_\mathfrak{a}}\mathrm{F}^{\mathfrak{a},\alpha}_{\mathcal{D}_l}([\![u^\alpha_{\mathcal{D}_l}]\!]^\mathfrak{a}_{\mathcal{D}_l})[\![u^\alpha_{\mathcal{D}_l}]\!]^\mathfrak{a}_{\mathcal{D}_l}\mathrm{d}\tau\mathrm{d}t\le\sum_{\mathfrak{a},\alpha}\int_0^T\int_{\Gamma_\mathfrak{a}}\rho_\mathfrak{a}^\alpha[\![\overline{u}^\alpha]\!]_\mathfrak{a}\mathrm{d}\tau\mathrm{d}t. \tag{3.38}$$

Having in mind to employ the energy inequality (3.11) with $T_0=T$, we first establish, for $\mu\in\{m,f\}$ and $\mathfrak{a}\in\chi$, the following convergences as $l\to\infty$:

$$\int_0^T\int_{M_\mu}h_\mu^\alpha\Pi^\mu_{\mathcal{D}_l}u^\alpha_{\mathcal{D}_l}\mathrm{d}\tau_\mu\mathrm{d}t\longrightarrow\int_0^T\int_{M_\mu}h_\mu^\alpha\overline{u}^\alpha_\mu\mathrm{d}\tau_\mu\mathrm{d}t\,, \tag{3.39}$$

$$\int_{M_\mu}B_\mu(S_\mu(\Pi^\mu_{\mathcal{D}^l_S}p^0_{\mathcal{D}_l}))\mathrm{d}\tau_\mu\longrightarrow\int_{M_\mu}B_\mu(S_\mu(\overline{p}_{\mu,0}))\mathrm{d}\tau_\mu\,, \tag{3.40}$$

$$\int_{\Gamma_\mathfrak{a}}B_\mathfrak{a}(S_\mathfrak{a}(\mathbb{T}^\mathfrak{a}_{\mathcal{D}^l_S}p^0_{\mathcal{D}_l}))\mathrm{d}\tau\longrightarrow\int_{\Gamma_\mathfrak{a}}B_\mathfrak{a}(S_\mathfrak{a}(\gamma_\mathfrak{a}\overline{p}_{m,0}))\mathrm{d}\tau. \tag{3.41}$$

The convergence (3.39) is obvious by Theorem 3.4.2. From the choice (3.3) of the scheme's initial conditions, together with the consistency of the interpolation operators $\mathrm{I}^m_\mathcal{D}$ and $\mathrm{I}^f_\mathcal{D}$, $S_\mu(\Pi^\mu_{\mathcal{D}^l_S}p^0_{\mathcal{D}_l})\to S_\mu(\overline{p}_{\mu,0})$ in $L^2(M_\mu)$ and $S_\mathfrak{a}(\mathbb{T}^\mathfrak{a}_{\mathcal{D}^l_S}p^0_{\mathcal{D}_l})\to S_\mathfrak{a}(\gamma_\mathfrak{a}\overline{p}_{m,0})$ in $L^2(\Gamma_\mathfrak{a})$, as $l\to\infty$. Then, (3.10) and [35, Lemma A.1] yield (3.40) and (3.41).

We further show that

$$\liminf_{l\to\infty}\int_{M_\mu}B_\mu(S_\mu(\Pi^\mu_{\mathcal{D}^l_S}p^{N_l}_{\mathcal{D}_l}))\mathrm{d}\tau_\mu\ge\int_{M_\mu}B_\mu(S_\mu(\overline{p}_\mu)(T))\mathrm{d}\tau_\mu\,, \tag{3.42}$$

$$\liminf_{l\to\infty}\int_{\Gamma_\mathfrak{a}}B_\mathfrak{a}(S_\mathfrak{a}(\mathbb{T}^\mathfrak{a}_{\mathcal{D}^l_S}p^{N_l}_{\mathcal{D}_l}))\mathrm{d}\tau\ge\int_{\Gamma_\mathfrak{a}}B_\mathfrak{a}(S_\mathfrak{a}(\gamma_\mathfrak{a}\overline{p}_m)(T))\mathrm{d}\tau\,, \tag{3.43}$$

$$\begin{aligned}\liminf_{l\to\infty}\int_0^T\int_{M_\mu}&[kS]^\alpha_\mu(\Pi^\mu_{\mathcal{D}_l}p_{\mathcal{D}_l})\Lambda_\mu\nabla^\mu_{\mathcal{D}_l}u^\alpha_{\mathcal{D}_l}\cdot\nabla^\mu_{\mathcal{D}_l}u^\alpha_{\mathcal{D}_l}\mathrm{d}\tau_\mu\mathrm{d}t\\&\ge\int_0^T\int_{M_\mu}[kS]^\alpha_\mu(\overline{p}_\mu)\Lambda_\mu\nabla\overline{u}^\alpha_\mu\cdot\nabla\overline{u}^\alpha_\mu\mathrm{d}\tau_\mu\mathrm{d}t.\end{aligned} \tag{3.44}$$

By the uniform-in-time weak L^2 convergences of Theorem 3.4.3, $S_\mu(\Pi^\mu_{\mathcal{D}^l_S}p^{N_l}_{\mathcal{D}_l})\rightharpoonup S_\mu(\overline{p}_\mu)(T)$ in $L^2(M_\mu)$ and $S_\mathfrak{a}(\mathbb{T}^\mathfrak{a}_{\mathcal{D}^l_S}p^{N_l}_{\mathcal{D}_l})\rightharpoonup S_\mathfrak{a}(\gamma_\mathfrak{a}\overline{p}_m)(T)$ in $L^2(\Gamma_\mathfrak{a})$, as $l\to\infty$. Note also that, since (by assumption) S_μ and $S_\mathfrak{a}$ are not explicitly space-dependent on each open set of the

formerly introduced partitions of M_μ and $\Gamma_\mathfrak{a}$, respectively, then $B_\mu, B_\mathfrak{a}$ are neither. On these partitions, the conditions of [33, Lemma 4.6] are fulfilled, namely $B_\mu, B_\mathfrak{a}$ are convex and l.s.c. This lemma, which essentially states the L^2-weak l.s.c. of strongly l.s.c. convex functions on L^2, establishes (3.42) and (3.43). To show (3.44), apply the Cauchy-Schwarz inequality to write

$$\begin{aligned}
&\int_0^T \int_{M_\mu} [kS]_\mu^\alpha(\Pi_{\mathcal{D}_l}^\mu p_{\mathcal{D}_l})\Lambda_\mu \nabla \overline{u}_\mu^\alpha \cdot \nabla_{\mathcal{D}_l}^\mu u_{\mathcal{D}_l}^\alpha \mathrm{d}\tau_\mu \mathrm{d}t \\
&\qquad \le \Big(\int_0^T \int_{M_\mu} [kS]_\mu^\alpha(\Pi_{\mathcal{D}_l}^\mu p_{\mathcal{D}_l})\Lambda_\mu \nabla \overline{u}_\mu^\alpha \cdot \nabla \overline{u}_\mu^\alpha \mathrm{d}\tau_\mu \mathrm{d}t\Big)^{\frac{1}{2}} \\
&\qquad\qquad \times \Big(\int_0^T \int_{M_\mu} [kS]_\mu^\alpha(\Pi_{\mathcal{D}_l}^\mu p_{\mathcal{D}_l})\Lambda_\mu \nabla_{\mathcal{D}_l}^\mu u_{\mathcal{D}_l}^\alpha \cdot \nabla_{\mathcal{D}_l}^\mu u_{\mathcal{D}_l}^\alpha \mathrm{d}\tau_\mu \mathrm{d}t\Big)^{\frac{1}{2}}
\end{aligned}$$

and take the inferior limit as $l \to \infty$, using the strong convergence of $[kS]_\mu^\alpha(\Pi_{\mathcal{D}_l}^\mu p_{\mathcal{D}_l})$ and weak convergence of $\nabla_{\mathcal{D}_l}^\mu u_{\mathcal{D}_l}^\alpha$ to pass to the limit in the left-hand side and the first term in the right-hand side.

Let us now come back to the proof of (3.38). Plugging the convergences (3.39)–(3.44) into (3.11) with $T_0 = T$ yields

$$\begin{aligned}
&\limsup_{l\to\infty} \sum_{\mathfrak{a},\alpha} \int_0^T \int_{\Gamma_\mathfrak{a}} \mathrm{F}_{\mathcal{D}_l}^{\mathfrak{a},\alpha}(\llbracket u_{\mathcal{D}_l}^\alpha \rrbracket_{\mathcal{D}_l}^\mathfrak{a}) \llbracket u_{\mathcal{D}_l}^\alpha \rrbracket_{\mathcal{D}_l}^\mathfrak{a} \mathrm{d}\tau \mathrm{d}t \\
&\qquad \le \sum_{\mu,\alpha} \Big(\int_0^T \int_{M_\mu} h_\mu^\alpha \overline{u}_\mu^\alpha \mathrm{d}\tau_\mu \mathrm{d}t - \int_0^T \int_{M_\mu} [kS]_\mu^\alpha(\overline{p}_\mu)\ \Lambda_\mu \nabla \overline{u}_\mu^\alpha \cdot \nabla \overline{u}_\mu^\alpha \mathrm{d}\tau_\mu \mathrm{d}t \Big) \\
&\qquad + \sum_{\mu} \Big(\int_{M_\mu} \phi_\mu B_\mu(S_\mu(\overline{p}_{\mu,0}))\mathrm{d}\tau_\mu - \int_{M_\mu} \phi_\mu B_\mu(S_\mu(\overline{p}_\mu)(T))\mathrm{d}\tau_\mu \Big) \\
&\qquad + \sum_{\mathfrak{a}} \Big(\int_{\Gamma_\mathfrak{a}} \eta B_\mathfrak{a}(S_\mathfrak{a}(\gamma_\mathfrak{a}\overline{p}_{m,0}))\mathrm{d}\tau - \int_{\Gamma_\mathfrak{a}} \eta B_\mathfrak{a}(S_\mathfrak{a}(\gamma_\mathfrak{a}\overline{p}_m)(T))\mathrm{d}\tau \Big).
\end{aligned} \tag{3.45}$$

Recall that $C_0^\infty([0,T)) \otimes [C_\Omega^\infty \times C_\Gamma^\infty]$ is dense in $(L^2((0,T)\times M_\mu))_{\mu\in\{m,f\}}$. Owing to Appendix 3.A.3, we infer from (3.36) that $\phi_f \partial_t S_f^\alpha(\overline{p}_f) \in L^2(0,T;V_f^{0\prime})$, that $\phi_m \partial_t S_m^\alpha(\overline{p}_m) + \sum_\mathfrak{a} \gamma_\mathfrak{a}^*(\eta \partial_t S_\mathfrak{a}^\alpha(\gamma_\mathfrak{a}\overline{p}_m)) \in L^2(0,T;V_m^{0\prime})$ (where $\gamma_\mathfrak{a}^*$ is the adjoint of $\gamma_\mathfrak{a}$), and that, for any $\varphi^\alpha \in V$,

$$\begin{aligned}
&\sum_{\alpha=1}^2 \Bigg\{ \sum_{\mu\in\{m,f\}} \Big(\int_0^T \langle \phi_\mu \partial_t S_\mu^\alpha(\overline{p}_\mu), \varphi_\mu^\alpha \rangle \mathrm{d}t + \int_0^T \int_{M_\mu} [kS]_\mu^\alpha(\overline{p}_\mu)\ \Lambda_\mu \nabla \overline{u}_\mu^\alpha \cdot \nabla \varphi_\mu^\alpha \mathrm{d}\tau_\mu \mathrm{d}t \Big) \\
&\qquad + \sum_{\mathfrak{a}\in\chi} \Big(\int_0^T \int_{\Gamma_\mathfrak{a}} \rho_\mathfrak{a}^\alpha \llbracket \varphi^\alpha \rrbracket_\mathfrak{a} \mathrm{d}\tau \mathrm{d}t + \int_0^T \langle \eta \partial_t S_\mathfrak{a}^\alpha(\gamma_\mathfrak{a}\overline{p}_m), \gamma_\mathfrak{a}\varphi_m^\alpha \rangle \mathrm{d}t \Big) \Bigg\} \\
&\qquad = \sum_{\alpha=1}^2 \sum_{\mu\in\{m,f\}} \int_0^T \int_{M_\mu} h_\mu^\alpha \varphi_\mu^\alpha \mathrm{d}\tau_\mu.
\end{aligned}$$

Note that the duality product between $(V_f^0)'$ and V_f^0 is taken respective to the measure $\mathrm{d}\tau_f(\mathbf{x}) = d_f(\mathbf{x})\mathrm{d}\tau(\mathbf{x})$, and remember the abuse of notation (3.53). Apply this to $\varphi^\alpha = (\overline{u}_m^\alpha, \overline{u}_f^\alpha)$. Recalling that $S_\mu^2 = 1 - S_\mu^1$, we have $\partial_t S_\mu^2(\overline{p}_\mu) = -\partial_t S_\mu^1(\overline{p}_\mu)$ and thus

$$\begin{aligned}
&\sum_{\mu\in\{m,f\}} \int_0^T \langle \phi_\mu \partial_t S_\mu^\alpha(\overline{p}_\mu), \overline{p}_\mu\rangle \mathrm{d}t + \sum_{\mathfrak{a}\in\chi} \int_0^T \langle \eta \partial_t S_\mathfrak{a}^\alpha(\gamma_\mathfrak{a}\overline{p}_m), \gamma_\mathfrak{a}\overline{p}_m\rangle \mathrm{d}t \\
&+ \sum_{\alpha=1}^2 \left\{ \sum_{\mu\in\{m,f\}} \int_0^T \int_{M_\mu} [kS]_\mu^\alpha(\overline{p}_\mu)\ \Lambda_\mu \nabla \overline{u}_\mu^\alpha \cdot \nabla \overline{u}_\mu^\alpha \mathrm{d}\tau_\mu \mathrm{d}t + \sum_{\mathfrak{a}\in\chi} \int_0^T \int_{\Gamma_\mathfrak{a}} \rho_\mathfrak{a}^\alpha [\![\overline{u}^\alpha]\!]_\mathfrak{a} \mathrm{d}\tau \mathrm{d}t \right\} \\
&\qquad = \sum_{\alpha=1}^2 \sum_{\mu\in\{m,f\}} \int_0^T \int_{M_\mu} h_\mu^\alpha \overline{u}_\mu^\alpha \mathrm{d}\tau_\mu \mathrm{d}t. \qquad (3.46)
\end{aligned}$$

[27, Lemma 3.6] establishes a temporal integration-by-parts property by using arguments purely based on the time variable, and that can easily be adapted to our context, even considering the "combined" time derivatives $\phi_m \partial_t S_m^\alpha(\overline{p}_m) + \sum_\mathfrak{a} \gamma_\mathfrak{a}^*(\eta \partial_t S_\mathfrak{a}^\alpha(\gamma_\mathfrak{a}\overline{p}_m))$ and the heterogeneities of the media treated here – i.e. the presence of ϕ_μ, see assumptions in Section 3.2. This adaptation yields

$$\int_0^T \langle \phi_f \partial_t S_f^\alpha(\overline{p}_\mu), \overline{p}_f\rangle_{V_f^{0\prime}, V_f^0} \mathrm{d}t = \int_{M_f} \phi_f B_f(S_f(\overline{p}_f)(T)) \mathrm{d}\tau_f - \int_{M_f} \phi_f B_f(S_\mu(\overline{p}_f)(0)) \mathrm{d}\tau_f$$

and

$$\begin{aligned}
&\int_0^T \langle \phi_m \partial_t S_m^\alpha(\overline{p}_m), \overline{p}_m\rangle \mathrm{d}t + \sum_{\mathfrak{a}\in\chi} \int_0^T \langle \eta \partial_t S_\mathfrak{a}^\alpha(\gamma_\mathfrak{a}\overline{p}_m), \gamma_\mathfrak{a}\overline{p}_m\rangle \mathrm{d}t \\
&\qquad = \int_{M_m} \phi_m B_m(S_m(\overline{p}_m)(T)) \mathrm{d}\mathbf{x} - \int_{M_m} \phi_m B_m(S_m(\overline{p}_m)(0)) \mathrm{d}\mathbf{x} \\
&\qquad\quad + \sum_{\mathfrak{a}\in\chi} \Big(\int_{\Gamma_\mathfrak{a}} \eta B_\mathfrak{a}(S_\mathfrak{a}(\gamma_\mathfrak{a}\overline{p}_m)(T)) \mathrm{d}\tau - \int_{\Gamma_\mathfrak{a}} \eta B_\mathfrak{a}(S_\mathfrak{a}(\gamma_\mathfrak{a}\overline{p}_m)(0)) \mathrm{d}\tau \Big).
\end{aligned}$$

Plugging these relations into (3.46) and using the result in (3.45) concludes the proof of (3.38).

Third step: conclusion.

As in the first step, take $\varphi^\alpha = (\varphi_m^\alpha, \varphi_f^\alpha) = \sum_{k=1}^b \theta^{\alpha,k} \otimes \psi^{\alpha,k}$ and set $(v_{\mathcal{D}_l}^{\alpha,n})_{n=0,\dots,N_l} = (\mathrm{P}_{\mathcal{D}_S^l} \varphi^\alpha(t_l^n))_{n=0,\dots,N_l} \in (X_{\mathcal{D}_S^l}^0)^{N_l+1}$. Developing the monotonicity property (3.33) of $\mathrm{F}_{\mathcal{D}_l}^{\mathfrak{a},\alpha}$ yields

$$\begin{aligned}
&\sum_{\mathfrak{a},\alpha} \int_0^T \int_{\Gamma_\mathfrak{a}} \mathrm{F}_{\mathcal{D}_l}^{\mathfrak{a},\alpha}([\![u_{\mathcal{D}_l}^\alpha]\!]_{\mathcal{D}_l}^\mathfrak{a})[\![u_{\mathcal{D}_l}^\alpha]\!]_{\mathcal{D}_l}^\mathfrak{a} \mathrm{d}\tau \mathrm{d}t - \sum_{\mathfrak{a},\alpha} \int_0^T \int_{\Gamma_\mathfrak{a}} \mathrm{F}_{\mathcal{D}_l}^{\mathfrak{a},\alpha}([\![v_{\mathcal{D}_l}^\alpha]\!]_{\mathcal{D}_l}^\mathfrak{a})([\![u_{\mathcal{D}_l}^\alpha]\!]_{\mathcal{D}_l}^\mathfrak{a} - [\![v_{\mathcal{D}_l}^\alpha]\!]_{\mathcal{D}_l}^\mathfrak{a}) \mathrm{d}\tau \mathrm{d}t \\
&\qquad - \sum_{\mathfrak{a},\alpha} \int_0^T \int_{\Gamma_\mathfrak{a}} \mathrm{F}_{\mathcal{D}_l}^{\mathfrak{a},\alpha}([\![u_{\mathcal{D}_l}^\alpha]\!]_{\mathcal{D}_l}^\mathfrak{a})[\![v_{\mathcal{D}_l}^\alpha]\!]_{\mathcal{D}_l}^\mathfrak{a} \mathrm{d}\tau \mathrm{d}t \geq 0.
\end{aligned}$$

Use (3.34) and (3.35) to pass to the limit in the second and third integral terms:

$$\limsup_{l\to\infty} \sum_{\mathfrak{a},\alpha} \int_0^T \int_{\Gamma_\mathfrak{a}} \mathrm{F}^{\mathfrak{a},\alpha}_{\mathcal{D}_l}([\![u^\alpha_{\mathcal{D}_l}]\!]^\mathfrak{a}_{\mathcal{D}_l})[\![u^\alpha_{\mathcal{D}_l}]\!]^\mathfrak{a}_{\mathcal{D}_l} \mathrm{d}\tau\mathrm{d}t$$
$$\geq \sum_{\mathfrak{a},\alpha} \int_0^T \int_{\Gamma_\mathfrak{a}} \mathrm{F}^{\mathfrak{a},\alpha}([\![\varphi^\alpha]\!]_\mathfrak{a})([\![\overline{u}^\alpha]\!]_\mathfrak{a} - [\![\varphi^\alpha]\!]_\mathfrak{a})\mathrm{d}\tau\mathrm{d}t + \sum_{\mathfrak{a},\alpha} \int_0^T \int_{\Gamma_\mathfrak{a}} \rho^\alpha_\mathfrak{a}[\![\varphi^\alpha]\!]_\mathfrak{a}\mathrm{d}\tau\mathrm{d}t.$$

Use (3.38) and the density of the tensorial function spaces $C_0^\infty([0,T)) \otimes [C_\Omega^\infty \times C_\Gamma^\infty]$ in $L^2(0,T;V)$ (cf. 1.2.2)to obtain

$$\sum_{\mathfrak{a},\alpha} \int_0^T \int_{\Gamma_\mathfrak{a}} \rho^\alpha_\mathfrak{a}([\![\overline{u}^\alpha]\!]_\mathfrak{a} - [\![\overline{v}^\alpha]\!]_\mathfrak{a})\mathrm{d}\tau\mathrm{d}t \geq \sum_{\mathfrak{a},\alpha} \int_0^T \int_{\Gamma_\mathfrak{a}} \mathrm{F}^{\mathfrak{a},\alpha}([\![\overline{v}^\alpha]\!]_\mathfrak{a})([\![\overline{u}^\alpha]\!]_\mathfrak{a} - [\![\overline{v}^\alpha]\!]_\mathfrak{a})\mathrm{d}\tau\mathrm{d}t$$

for all $(\overline{v}^\alpha)_{\alpha=1,2} \in L^2(0,T;V)^2$. The conclusion is now standard in the Minty trick, see e.g. [29, Proof of Theorem 3.34]. For any smooth $(\varphi^\alpha)_{\alpha=1,2}$, choose $\overline{v}^\alpha = \overline{u}^\alpha \pm \epsilon\varphi^\alpha$ and let $\epsilon \to 0$ to derive (3.37) and conclude the proof.

3.5 Two-phase flow test cases

We present in this section a series of test cases for two-phase flow through a fractured 2 dimensional reservoir of geometry as shown in figure 3.2. The domain Ω is of extension $(0,10)\mathrm{m} \times (0,20)\mathrm{m}$ and the fracture width d_f is assumed constant equal to 1 cm. We consider isotropic permeability in the matrix and in the fracture. The following geological configuration is considered: Matrix and fracture permeabilities are $\lambda_m = 0.1$ Darcy and $\lambda_f = 100$ Darcy, respectively, matrix and fracture porosities are $\phi_m = 0.2$ and $\phi_f = 0.4$, respectively.

Initially, the reservoir is saturated with water (density $\rho^2 = 1000$ kg/m^3, viscosity $\kappa^2 = 0.001$ Pa.s) and oil (density $\rho^1 = 700$ kg/m^3, viscosity $\kappa^1 = 0.005$ Pa.s) is injected from below. Also, hydrostatic distribution of pressure is assumed. The oil then rises by gravity, thanks to its lower density compared to water. At the lower boundary of the domain, we impose constant capillary pressure of 0.1 bar and water pressure of 3 bar; at the upper boundary, the capillary pressure is constant equal to 0 bar and the water pressure is 1 bar. Elsewhere, homogeneous Neumann conditions are imposed.

We use the VAG scheme to obtain solutions for the DFM. We refer to chapter 1 for a presentation of the scheme as a gradient scheme, and for proofs that, under standard regularity assumptions on the meshes, the corresponding sequences of gradient discretisations are coercive, GD-consistent, limit-conforming and compact. The tests are driven on a triangular mesh extended to a 3D mesh with one layer of prisms (we use a 3D implementation of the VAG scheme). The resulting numbers of cells and degrees of freedom are exhibited in Table 3.1. The mesh size is of order $10d_f$.

The non-linear system of equations occurring at each time step is solved via a Newton algorithm with relaxation. To solve the linear system obtained at each step of the Newton

Figure 3.2: Geometry of the reservoir under consideration. DFN in red and matrix domain in blue. $\Omega = (0,10)\text{m}\times(0,20)\text{m}$ and $d_f = 0.01\text{m}$.

iteration, we use the sequential version of the SuperLU direct sparse solver [24, 25]. The stopping criterion on the L^1 relative residual is $\text{crit}^{\text{rel}}_{\text{Newton}}$. To ensure well defined values for the capillary pressure, after each Newton iteration, we project the (oil) saturation on the interval $[0, 1 - 10^{-14}]$. The time stepping is progressive, i.e. after each iteration, the upcoming time step is deduced by multiplying the previous one by 2, while imposing a maximal time step Δt_{max}. If at a given time iteration the Newton algorithm does not converge after 35 iterations, then the actual time step is divided by 4 and the time iteration is repeated. The number of time step failures at the end of a simulation is indicated by $\mathbf{N}_{\text{Chop}}$.

Nb Cells	**Nb DOF**	**Nb DOF el.**	$\text{crit}^{\text{rel}}_{\text{Newton}}$	Δt_{max} for $0 \leq t \leq 1/2$ d	Δt_{max} for $1/2$ d $< t \leq 10$ d
5082	10610	5528	$1.E{-}6$	0.01 d	0.19 d

Table 3.1: **Nb Cells** is the number of cells of the mesh; **Nb DOF** is the number of discrete unknowns; **Nb DOF el.** is the number of discrete unknowns after elimination of cell unknowns without fill-in. Time steps used in the simulations in days (d)

Inside the matrix domain the capillary pressure function is given by Corey's law $p_m = -a_m \log(1 - S_m^1)$ with $a_m = 1$ bar. Inside the fracture network, we suppose $p_f = -a_f \log(1 - S_f^1)$ with $a_f = 0.02$ bar. The matrix and fracture relative permeabilities of each phase α are given by Corey's laws $k^\alpha_{r,m}(S^\alpha_m) = (S^\alpha_m)^2$ and $k^\alpha_{r,f}(S^\alpha_f) = S^\alpha_f$, and the phase mobilities are defined by $k^\alpha_\mu(S^\alpha_\mu) = \frac{1}{\kappa^\alpha} k^\alpha_{r,m}(S^\alpha_\mu)$, $\mu \in \{m, f\}$ (see Figure 3.3). The phase saturations at the interfacial layers are defined by the interpolation

$$S^\alpha_{\mathfrak{a}} = \theta S^\alpha_m + (1 - \theta) S^\alpha_f, \tag{3.47}$$

with parameter $\theta \in [0, 1]$. The mapping $S^\alpha_{\mathfrak{a}} : [0, +\infty) \to [0, 1)$ is a diffeomorphism so the choice

$$[kS]^\alpha_{\mathfrak{a}} = \theta k^\alpha_m(S^\alpha_m) + (1 - \theta) k^\alpha_f(S^\alpha_f).$$

is valid, since this function can be written as $k^\alpha_{\mathfrak{a}}(S^\alpha_{\mathfrak{a}})$ with $k^\alpha_{\mathfrak{a}}(\xi) = \theta k^\alpha_m(S^\alpha_m \circ (S^\alpha_{\mathfrak{a}})^{-1}(\xi)) +$

$(1-\theta)k_f^\alpha(S_f^\alpha \circ (S_\mathfrak{a}^\alpha)^{-1}(\xi))$. Finally, the interfacial porosity $\phi_\mathfrak{a}$ is set to 0.2 and

$$d_\mathfrak{a} = \frac{d_f}{2}\varepsilon,$$

with parameter $\varepsilon > 0$. The parameter η is then defined by $\eta = \phi_\mathfrak{a} d_\mathfrak{a}$.

Let us start with some remarks. From the capillary pressure functions (cf. figure 3.3), it is obvious that for given p, the one-sided jump of the oil saturation is negative, i.e.

$$S_m^1(p) - S_f^1(p) < 0. \tag{3.48}$$

To account for the interfacial zone properly, the mobilities have to be adjusted by choosing the model parameter θ depending on the rock type characteristics of the layer. Obviously, $\theta = 0$ refers to a fracture rock type and $\theta = 1$ to a matrix rock type.

On the other hand, with larger η, the volume of the interfacial layers gets augmented and the interfacial accumulation terms play a more important role. The availability of the supplementary volume has a direct impact on the phase front speed inside the fracture during its filling: (3.47)–(3.48) show that the volume of oil in the interfacial layers is strictly decreasing as a function of θ, given a distribution of capillary pressures. This indicates that, from the accumulation point of view, the fracture front speed should grow with growing θ, and this effect should be enhanced by a larger η.

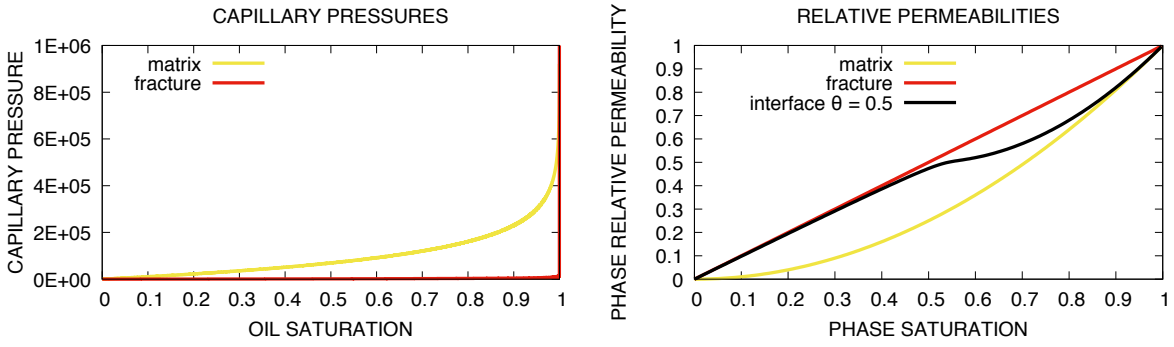

Figure 3.3: Curves for capillary pressures and relative permeabilities.

Figure 3.4 (a) indicates that, for a fixed $\theta = 0, 0.5, 1$, the solutions are not sensitive to small variations of ε. Quantitatively, we see that the solution for $\varepsilon = 0.1$ is close to the solution for $\varepsilon = 10^{-6}$. With respect to the computational performance exposed in Table 3.2, we thus see that choosing $\varepsilon = 0.1$ is a good compromise between accuracy and cost. This point is presented in more detail for the intermediate rock type, i.e. $\theta = 0.5$, in Figure 3.5. Figure 3.4 (b) confirms the aforementioned feature of extended (large ε) interfacial layers to delay the propagation of the oil in the drain. As suggested, this effect is even more important, with decreasing θ. In Figure 3.4 (c), we study the impact of the choice of the interfacial mobility for parameters $\theta = 0, 0.5, 1$ on the solution. Here, the

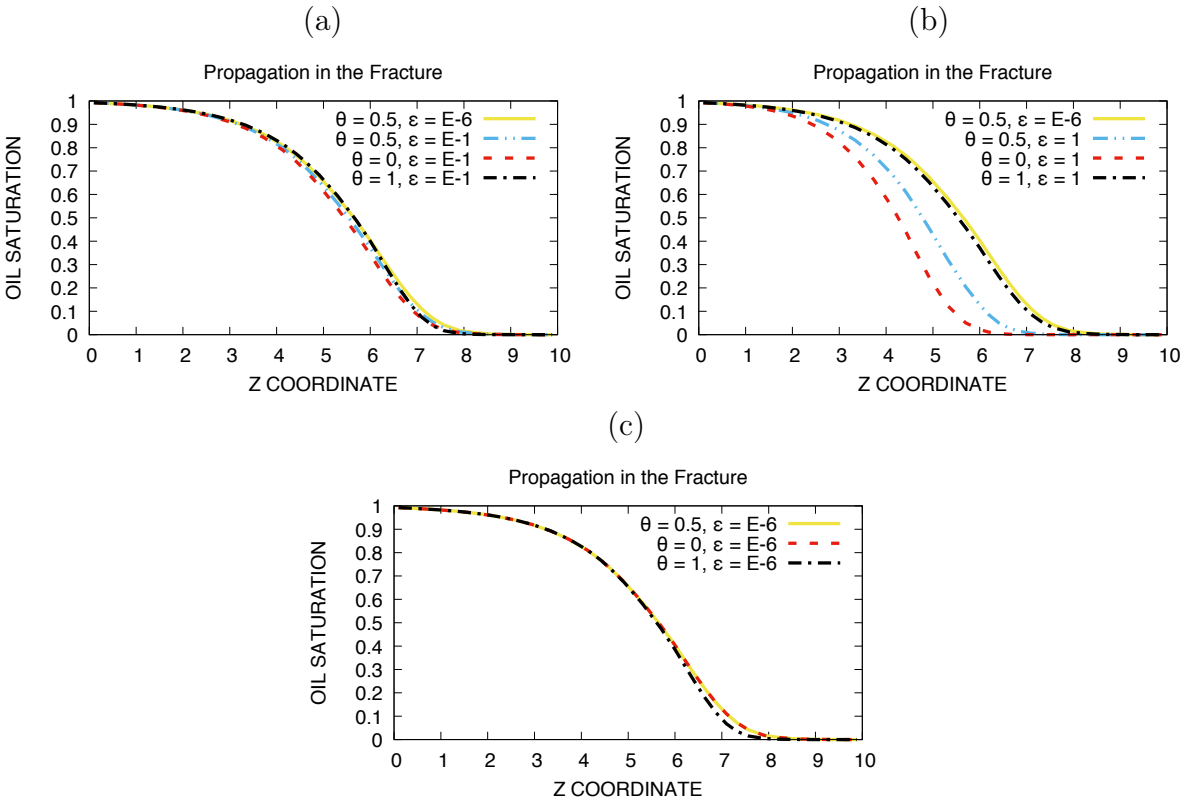

Figure 3.4: Fracture oil saturation for time $t = 6$h.

interfacial accumulation is negligible due to an ε close to zero. Let us shortly remark that in the limit of a vanishing interfacial layer, i.e. $\eta = 0$, we want to recover the fracture mobilities for the mass exchange fluxes between the matrix-fracture interface and the fracture. Hence, in this case, the right choice of θ would be 0. We observe that changing the mobilities does not much influence the solution, due to the fact that fluxes are mostly oriented from the fracture towards the interfacial layers. The regions where a difference is observed in the fracture oil front for the different models are those with a small positive oil saturations. There, the relative permeabilities for $\theta = 0$ and $\theta = 0.5$ are very close and the difference to $\theta = 1$ is at its peak; this explains the behaviour of the fracture front for the three models.

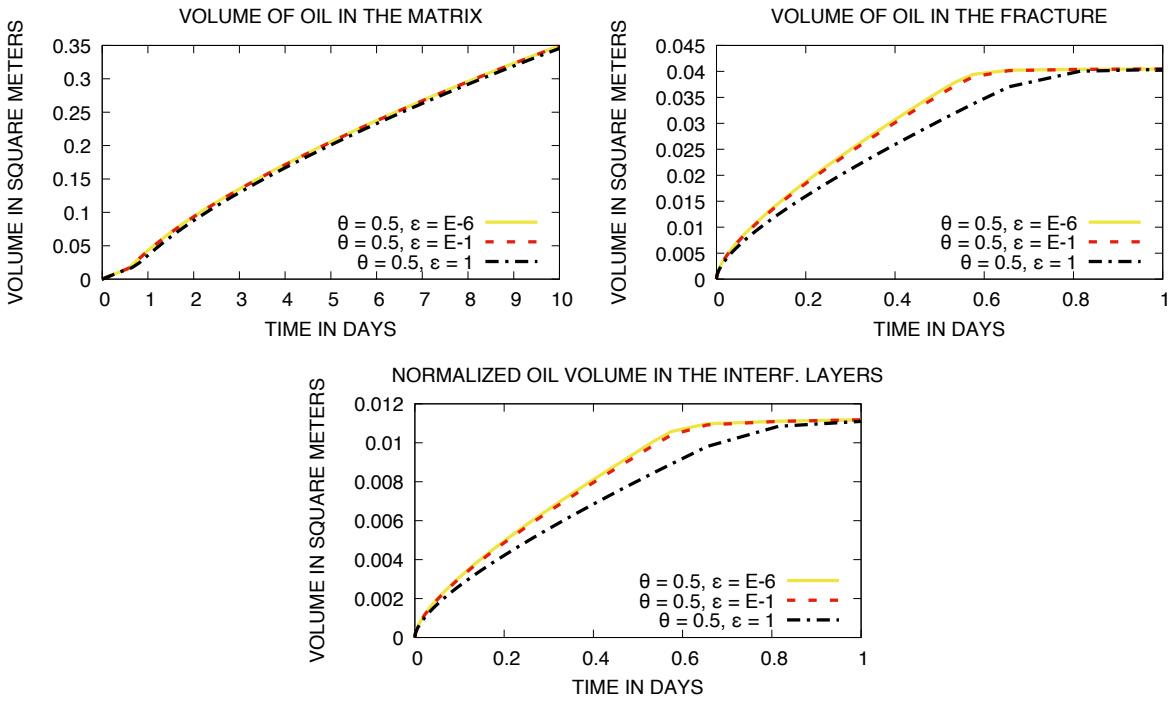

Figure 3.5: Volume occupied by oil in the matrix, fracture and oil volume normalised by ε in the interfacial layers, for $\theta = 0.5$, as a function of time.

θ	0				0.5				1			
ε	1	1.E-1	1.E-6	0	1	1.E-1	1.E-6	0	1	1.E-1	1.E-6	0
$\mathbf{N}_{\Delta t}$	125	125	125	-	125	125	125	-	183	284	377	-
$\mathbf{N}_{Newton}$	506	521	547		513	521	546		674	892	1410	
$\mathbf{N}_{\text{Chop}}$	0	0	0		0	0	0		22	61	94	
CPU	147	160	159		151	152	170		402	860	1402	

Table 3.2: Computational cost

Table 3.2 shows that the computational cost increases with decreasing ε and that, in the case of $\varepsilon = 0$, the Jacobian becomes singular. Furthermore, the efficiency severely deteriorates for $\theta = 1$. In this case, $S_{\mathfrak{a}}^{1\prime}(p)$ is (significantly) smaller during the filling of the fracture (for capillary pressures p below a characteristic $p_1 \in \mathbb{R}^+$), since $S_m^{1\prime}(p) \ll S_f^{1\prime}(p)$. When oil fluxes oriented from the fracture to the interface are present, the Jacobian is thus ill-conditioned.

3.6 Conclusion

We introduced a new discrete fracture model for two phase Darcy flow, permitting pressure discontinuity at the matrix-fracture interfaces. It respects the heterogeneities of the media and between the matrix and the fractures, since it takes into account saturation jumps due to different capillary pressure curves in the respective domains. It also considers damaged layers located at the matrix-fracture interfaces. Another feature of the model are upwind fluxes between these interfacial layers and the fractures. The upwinding is needed for transport dominated flow in normal direction to the fractures. The extension to gravity is straightforward (cf. chapter 2).

We developed the numerical analysis of the model in the framework of the gradient discretisation method, which contains for example the VAG and HMM schemes. Based on compactness arguments, we showed in Theorem 3.4.1 the strong L^2 convergence of the saturations and the weak L^2 convergence for the pressures to a solution of Model (3.1). In Theorem 3.4.3, we established uniform-in-time, weak L^2 in space convergence for the saturations, a result that is extended to uniform-in-time, strong L^2 in space convergence in [34].

Finally, we presented a series of test cases, with the objective to study the impact of the interfacial layer on the solution. The observed behaviour of the solutions for the different situations corresponds to the expectations. It exhibits significant differences, during the filling of the fracture, for large interfacial layers and small differences for small layers. In terms of computational cost, we saw that the presence of a damaged zone at the matrix-fracture interface is needed in order to solve the linear system of the discrete problem, occurring at each time step. We also observed that for a large contrast between the drain's and the interfacial layer's capillary pressures, the simulation becomes expensive. Therefore, we see that, in order to cope with both, fractures acting as drains or as barriers, the possibility to deal with mixed rock types for the damaged zone is essential.

3.A Appendix

3.A.1 Uniform-in-time weak L^2 convergence

Let A be a subset of $\mathbb{R}^n$, endowed with the standard Lebesgue measure, and $\{\varphi_\ell : \ell \in \mathbb{N}\}$ be a dense countable set in $L^2(A)$. On any bounded ball of $L^2(A)$, the weak topology can be defined by the following metric:

$$\mathrm{dist}(v, w) = \sum_{\ell \in \mathbb{N}} \frac{\min\left(1, |\left\langle v - w, \varphi_\ell \right\rangle_{L^2(A)}|\right)}{2^\ell}.$$

A sequence $(v_m)_{m\in\mathbb{N}}$ of bounded functions $[0,T] \to L^2(A)$ converges uniformly on $[0,T]$ weakly in $L^2(A)$ to some v if it converges uniformly for the weak topology of $L^2(A)$, meaning that, for all $\phi \in L^2(A)$, $\langle v_m(\cdot), \phi\rangle_{L^2(A)} \to \langle v(\cdot), \phi\rangle_{L^2(A)}$ uniformly on $[0,T]$ as $m \to \infty$.

With this introductory material, the following result is a consequence of [29, Theorem 4.26] or [27, Theorem 6.2] (see also the reasoning at the end of [27, Proof of Theorem 3.1]).

Theorem 3.A.1 (Discontinuous weak L^2 Ascoli–Arzela theorem) *Let $\mathcal{R}$ be a dense subset of $L^2(A)$ and $(v_m)_{m\in\mathbb{N}}$ be a sequence of functions $[0,T] \to L^2(A)$ such that*

- $\sup_{m\in\mathbb{N}} \sup_{t\in[0,T]} \|v_m(t)\|_{L^2(A)} < +\infty$,
- *for all $\varphi \in \mathcal{R}$, there exist $\omega_\varphi : [0,T]^2 \to [0,\infty)$ and $(\delta_m(\varphi))_{m\in\mathbb{N}} \subset [0,\infty)$ satisfying*

$$\begin{aligned}&\omega_\varphi(s,t) \to 0 \text{ as } s - t \to 0\,,\ \delta_m(\varphi) \to 0 \text{ as } m \to \infty\,, \text{ and}\\ &\forall (s,t) \in [0,T]^2\,,\ \forall m \in \mathbb{N}\,,\ |\langle v_m(s) - v_m(t), \varphi\rangle_{L^2(A)}| \le \delta_m(\varphi) + \omega_\varphi(s,t).\end{aligned}$$

Then, there exists a function $v : [0,T] \to L^2(A)$ such that, up to a subsequence as $m \to \infty$, $v_m \to v$ uniformly on $[0,T]$ weakly in $L^2(A)$. Moreover, v is continuous on $[0,T]$ for the weak topology of $L^2(A)$.

3.A.2 Generic results on gradient discretisations

The following lemma is a classical result in the context of the standard gradient discretisation method, see e.g. [29, Lemma 4.7]. We give a sketch of its proof for gradient discretisations adapted to discrete fracture model.

Lemma 3.A.1 (Regularity of the Limit) *Let $(\mathcal{D}_l)_{l\in\mathbb{N}}$ be a coercive and limit-conforming sequence of gradient discretisations, and let $(v_{\mathcal{D}_l})_{l\in\mathbb{N}}$ be such that $v_{\mathcal{D}_l} \in (X^0_{\mathcal{D}_S^l})^{N_l+1}$, where N_l is the number of time steps of $\mathcal{D}_l$. We assume that $(\|v_{\mathcal{D}_l}\|_{\mathcal{D}_l})_{l\in\mathbb{N}}$ is bounded. Then,*

there exists $\overline{v} = (\overline{v}_m, \overline{v}_f) \in L^2(0,T;V_m^0) \times L^2(0,T;V_f^0)$ *such that, up to a subsequence, the following weak convergences hold:*

$$\left\{\begin{array}{ll} \Pi^\mu_{\mathcal{D}_l} v_{\mathcal{D}_l} \rightharpoonup \overline{v}_\mu & \text{in } L^2((0,T)\times M_\mu)\,, \text{ for } \mu \in \{m,f\}, \\ \nabla^\mu_{\mathcal{D}_l} v_{\mathcal{D}_l} \rightharpoonup \nabla \overline{v}_\mu & \text{in } L^2((0,T)\times M_\mu)^d\,, \text{ for } \mu \in \{m,f\}, \\ \mathbb{T}^{\mathfrak{a}}_{\mathcal{D}_l} v_{\mathcal{D}_l} \rightharpoonup \gamma_{\mathfrak{a}} \overline{v}_m & \text{in } L^2((0,T)\times \Gamma_{\mathfrak{a}}), \text{ for all } \mathfrak{a} \in \chi, \\ [\![v_{\mathcal{D}_l}]\!]^{\mathfrak{a}}_{\mathcal{D}_l} \rightharpoonup [\![\overline{v}]\!]_{\mathfrak{a}} & \text{in } L^2((0,T)\times \Gamma_{\mathfrak{a}}), \text{ for all } \mathfrak{a} \in \chi. \end{array}\right. \tag{3.49}$$

Proof By coercivity and since $(\|v_{\mathcal{D}_l}\|_{\mathcal{D}_l})_{l\in\mathbb{N}}$ is bounded, all the sequences in (3.49) are bounded in their respective spaces. Up to a subsequence, we can therefore assume that there exists $\overline{v}_\mu \in L^2((0,T)\times M_\mu)$, $\boldsymbol{\xi}_\mu \in L^2((0,T)\times M_\mu)^d$, $\beta_{\mathfrak{a}} \in L^2((0,T)\times\Gamma_{\mathfrak{a}})$ and $j_{\mathfrak{a}} \in L^2((0,T)\times\Gamma_{\mathfrak{a}})$ such that $\Pi^\mu_{\mathcal{D}_l} v_{\mathcal{D}_l} \rightharpoonup \overline{v}_\mu$, $\nabla^\mu_{\mathcal{D}_l} v_{\mathcal{D}_l} \rightharpoonup \boldsymbol{\xi}_\mu$, $\mathbb{T}^{\mathfrak{a}}_{\mathcal{D}_l} v_{\mathcal{D}_l} \rightharpoonup \beta_{\mathfrak{a}}$ and $[\![v_{\mathcal{D}_l}]\!]^{\mathfrak{a}}_{\mathcal{D}_l} \rightharpoonup j_{\mathfrak{a}}$ weakly in their respective L^2 spaces as $l \to \infty$.

Take $\mathbf{q} \in \mathbf{C}^\infty_\Omega \times \mathbf{C}^\infty_\Gamma$, $\varphi_{\mathfrak{a}} \in C^\infty_0(\Gamma_{\mathfrak{a}})$ and $\rho \in C^\infty_c(0,T)$. For F a function of $\mathbf{x}$, define $\rho \otimes F(t,\mathbf{x}) = \rho(t)F(\mathbf{x})$. The definition of $\mathcal{W}_{\mathcal{D}^l_S}$ yields

$$\begin{aligned} &\Bigg| \int_0^T \int_\Omega \Big(\nabla^m_{\mathcal{D}_l} v_{\mathcal{D}_l} \cdot (\rho \otimes \mathbf{q}_m) + (\Pi^m_{\mathcal{D}_l} v_{\mathcal{D}_l}) \mathrm{div}(\rho \otimes \mathbf{q}_m) \Big) \mathrm{d}\mathbf{x}\mathrm{d}t \\ &+ \int_0^T \int_\Gamma \Big(\nabla^f_{\mathcal{D}_l} v_{\mathcal{D}_l} \cdot (\rho \otimes \mathbf{q}_f) + (\Pi^f_{\mathcal{D}_l} v_{\mathcal{D}_l}) \mathrm{div}_\tau(\rho \otimes \mathbf{q}_f) \Big) \mathrm{d}\tau(\mathbf{x})\mathrm{d}t \\ &- \sum_{\mathfrak{a}\in\chi} \int_0^T \int_{\Gamma_{\mathfrak{a}}} (\rho \otimes (\gamma_{\mathbf{n}_{\mathfrak{a}}} \mathbf{q}_m)) \mathbb{T}^{\mathfrak{a}}_{\mathcal{D}_l} v_{\mathcal{D}_l} \mathrm{d}\tau(\mathbf{x})\mathrm{d}t \\ &+ \sum_{\mathfrak{a}\in\chi} \int_0^T \int_{\Gamma_{\mathfrak{a}}} (\rho \otimes \varphi_{\mathfrak{a}}) \Big(\mathbb{T}^{\mathfrak{a}}_{\mathcal{D}_l} v_{\mathcal{D}_l} - \Pi^f_{\mathcal{D}_l} v_{\mathcal{D}_l} - [\![v_{\mathcal{D}_l}]\!]^{\mathfrak{a}}_{\mathcal{D}_l} \Big) \mathrm{d}\tau(\mathbf{x})\ dt \Bigg| \\ &\qquad \le \|v_{\mathcal{D}_l}\|_{\mathcal{D}_l} \|\rho\|_{L^2(0,T)} \mathcal{W}_{\mathcal{D}^l_S}(\mathbf{q}, \varphi_{\mathfrak{a}}). \end{aligned}$$

The limit-conformity shows that the right-hand side of this inequality tends to 0. Hence,

$$\begin{aligned} &\int_0^T \int_\Omega \Big(\boldsymbol{\xi}_m \cdot (\rho \otimes \mathbf{q}_m) + \overline{v}_m \mathrm{div}(\rho \otimes \mathbf{q}_m) \Big) \mathrm{d}\mathbf{x}\mathrm{d}t \\ &+ \int_0^T \int_\Gamma \Big(\boldsymbol{\xi}_f \cdot (\rho \otimes \mathbf{q}_f) + \overline{v}_f \mathrm{div}_\tau(\rho \otimes \mathbf{q}_f) \Big) \mathrm{d}\tau(\mathbf{x})\mathrm{d}t \\ &- \sum_{\mathfrak{a}\in\chi} \int_0^T \int_{\Gamma_{\mathfrak{a}}} (\rho \otimes (\gamma_{\mathbf{n}_{\mathfrak{a}}} \mathbf{q}_m)) \beta_{\mathfrak{a}} \mathrm{d}\tau(\mathbf{x})\mathrm{d}t \\ &+ \sum_{\mathfrak{a}\in\chi} \int_0^T \int_{\Gamma_{\mathfrak{a}}} (\rho \otimes \varphi_{\mathfrak{a}}) \Big(\beta_{\mathfrak{a}} - \overline{v}_f - j_{\mathfrak{a}} \Big) \mathrm{d}\tau(\mathbf{x})\ dt = 0. \end{aligned}$$

Applying this to $(\mathbf{q}, \varphi_{\mathfrak{a}}) = ((\mathbf{q}_m, 0), 0)$ with $\mathbf{q}_m \in C^\infty_0(\Omega \setminus \overline{\Gamma})^d$, and using the density of tensorial functions $\{\sum_{r=1}^N \rho_r \otimes \mathbf{q}_m \,:\, N \in \mathbb{N},\ \rho_r \in C^\infty_c(0,T)\,,\ \mathbf{q}_m \in C^\infty_0(\Omega \setminus \overline{\Gamma})^d\}$ in $C^\infty_c((0,T)\times\Omega\setminus\overline{\Gamma})^d$ (see [26, Appendix D]) shows that $\boldsymbol{\xi}_m = \nabla \overline{v}_m$. With $(\mathbf{q}, \varphi_{\mathfrak{a}}) =$

$((0,\mathbf{q}_f),0)$ where $\mathbf{q}_f \in C^\infty(\overline{\Gamma}_i)^{d-1}$, we obtain $\boldsymbol{\xi}_f = \nabla\overline{v}_f$. Considering now $(\mathbf{q},\varphi_\mathfrak{a}) = ((\mathbf{q}_m,0),0)$ with $q_m \in C_b^\infty(\Omega\setminus\overline{\Gamma})^d$ and applying the divergence theorem gives $\beta_\mathfrak{a} = \gamma_\mathfrak{a}\overline{v}_m$. Finally, taking $(\mathbf{q},\varphi_\mathfrak{a}) = ((0,0),\varphi_\mathfrak{a})$ with a general $\varphi_\mathfrak{a} \in C_0^\infty(\Gamma_\mathfrak{a})$ yields $j_\mathfrak{a} = \beta_\mathfrak{a} - \overline{v}_f = \gamma_\mathfrak{a}\overline{v}_m - \overline{v}_f = [\![\overline{v}]\!]_\mathfrak{a}$. □

With [40, Lemma 3.6], we can state the following.

Corollary 3.A.1 *Under the assumptions of Lemma 3.A.1, if $g_\mu : \mathbb{R}\to\mathbb{R}$ ($\mu\in\{m,f\}$) and $g_\mathfrak{a} : \mathbb{R}\to\mathbb{R}$ ($\mathfrak{a}\in\chi$) are continuous, non-decreasing functions and if $(\Pi^\mu_{\mathcal{D}_l} g_\mu(v_{\mathcal{D}_l}))_l$ strongly converges in $L^2((0,T)\times M_\mu)$ and $(\mathbb{T}^\mathfrak{a}_{\mathcal{D}_l} g_\mathfrak{a}(v_{\mathcal{D}_l}))_l$ strongly converges in $L^2((0,T)\times\Gamma_\mathfrak{a})$, then*

$$\begin{cases} \Pi^\mu_{\mathcal{D}_l} g_\mu(v_{\mathcal{D}_l}) \to g_\mu(\overline{v}_\mu) & \text{in } L^2((0,T)\times M_\mu), \\ \mathbb{T}^\mathfrak{a}_{\mathcal{D}_l} g_\mathfrak{a}(v_{\mathcal{D}_l}) \to g_\mathfrak{a}(\gamma_\mathfrak{a}\overline{v}_m) & \text{in } L^2((0,T)\times\Gamma_\mathfrak{a}). \end{cases}$$

3.A.3 Identification of time derivatives

We discuss here how weak formulations, with derivatives on test functions, enable us to recover some regularity properties on time derivatives of quantities of interest.

Let us start with a classical situation, similar to [27, Remark 1.1]. Let (M,ν) be a measured space and E be a Banach space densely embedded in $L^2(M)$, so that $E\hookrightarrow L^2(M)\hookrightarrow E'$. Assume also that E' is separable. Let $\mathcal{L} : L^2(0,T;E)\to\mathbb{R}$ be a continuous linear form and let $\mathcal{E}\subset C_0^1([0,T);E)$ be such that $\mathcal{E}_0 = \{\Phi\in\mathcal{E} : \Phi(0,\cdot)=0\}$ is dense in $L^2(0,T;E)$. Suppose that $U\in L^2(0,T;E)$ and $U_0\in L^2(M)$ satisfy, for all $\Phi\in\mathcal{E}$,

$$-\int_0^T\int_M U(t,\mathbf{x})\partial_t\Phi(t,\mathbf{x})\mathrm{d}\nu(\mathbf{x})\mathrm{d}t + \int_M U_0(\mathbf{x})\Phi(0,\mathbf{x})\mathrm{d}\nu(\mathbf{x}) = \mathcal{L}(\Phi). \tag{3.50}$$

This relation shows that

$$\Xi : \Phi\mapsto -\int_0^T\int_M U(t,\mathbf{x})\partial_t\Phi(t,\mathbf{x})\mathrm{d}\nu(\mathbf{x})\mathrm{d}t$$

is linear (equal to $\mathcal{L}$) on $\mathcal{E}_0$, and continuous for the topology of $L^2(0,T;E)$. By density of $\mathcal{E}_0$ in this space, Ξ can be extended into an element of $(L^2(0,T;E))' = L^2(0,T;E')$ (see [26, Theorem 1.4.1]). We denote this element by $\partial_t U$, as it clearly corresponds to the distributional derivative of U [26, Section 2.1.2]. By [26, Section 2.5.2] this shows that $U\colon[0,T]\to L^2(M)$ is continuous and, using [26, Proposition 2.5.2] to integrate by parts in (3.50), that $U(0)=U_0$ and

$$\forall\Phi\in\mathcal{E}\,,\ \langle\partial_t U,\Phi\rangle_{L^2(0,T;E'),L^2(0,T;E)}\mathrm{d}t = \int_0^T\langle\partial_t U(t),\Phi(t)\rangle_{E',E}\mathrm{d}t = \mathcal{L}(\Phi). \tag{3.51}$$

By density of $\mathcal{E}$ in $L^2(0,T;E)$, this relation actually holds for any $\Phi\in L^2(0,T;E)$.

Fixing $M = M_f$, $\mathrm{d}\nu = \mathrm{d}\tau_f$, $E = V_f^0$, $\mathcal{E} = C^1([0,T]; C_\Gamma^\infty)$ and

$$\mathcal{L}(\Phi) = \int_0^T \int_{M_f} h_f^\alpha \Phi \mathrm{d}\tau_f \mathrm{d}t - \int_0^T \int_{M_f} [kS]_f^\alpha(\overline{p}_f)\ \Lambda_f \nabla \overline{u}_f^\alpha \cdot \nabla \Phi \mathrm{d}\tau_f \mathrm{d}t + \sum_{\mathfrak{a}\in\chi} \Big(\int_0^T \int_{\Gamma_\mathfrak{a}} \rho_\mathfrak{a}^\alpha(-\Phi) \mathrm{d}\tau \mathrm{d}t \Big),$$

and using (3.36) with $\varphi_m^\alpha = 0$ and $\varphi_f^\alpha = \Phi$, $\varphi_f^\beta = 0$, for $\alpha, \beta = 1, 2$ with $\alpha \neq \beta$, this identifies $\partial_t(\phi_f S_f^\alpha(\overline{p}_f)) = \phi_f \partial_t S_f^\alpha(\overline{p}_f)$ as an element of $L^2(0,T; V_f^{0\prime})$.

Let us now consider a slightly more complicated case, in which the time derivatives of two functions need to be combined to exhibit a certain regularity. With the same M and E as above, take (N, λ) a measured space and $\gamma : E \to L^2(N)$ a continuous linear mapping. Assume that $U \in L^2(0,T;E)$, $V \in L^2(0,T;L^2(N))$, $U_0 \in L^2(M)$ and $V_0 \in L^2(N)$, satisfy, for all $\phi \in \mathcal{E}$,

$$\begin{aligned} -\int_0^T \int_M U(t,\mathbf{x}) \partial_t \Phi(t,\mathbf{x}) \mathrm{d}\nu(\mathbf{x}) \mathrm{d}t - \int_0^T \int_N V(t,\mathbf{x}) \partial_t \gamma(\Phi(t))(\mathbf{x}) \mathrm{d}\lambda(\mathbf{x}) \mathrm{d}t \\ + \int_M U_0(\mathbf{x}) \Phi(0,\mathbf{x}) \mathrm{d}\nu(\mathbf{x}) + \int_N V_0(\mathbf{x}) \gamma(\Phi(0))(\mathbf{x}) \mathrm{d}\lambda(\mathbf{x}) = \mathcal{L}(\Phi). \end{aligned} \tag{3.52}$$

The same reasoning as above shows that

$$\widetilde{\Xi} : \Phi \mapsto -\int_0^T \int_M U(t,\mathbf{x}) \partial_t \Phi(t,\mathbf{x}) \mathrm{d}\nu(\mathbf{x}) \mathrm{d}t - \int_0^T \int_M V(t,\mathbf{x}) \partial_t \gamma(\Phi(t))(\mathbf{x}) \mathrm{d}\lambda(\mathbf{x}) \mathrm{d}t$$

can be extended into a linear continuous form on $L^2(0,T;E)$. Letting $\gamma^* : L^2(N) \to E'$ be the adjoint of γ (that is, $\langle g, \gamma(\Phi)\rangle_{L^2(N)} = \langle \gamma^* g, \Phi\rangle_{E',E}$ for all $g \in L^2(N)$ and $\Phi \in E$), the form $\widetilde{\Xi}$ is naturally denoted by $\partial_t U + \gamma^* \partial_t V$. Note that, in this sum, the two terms cannot be separated and it cannot, for example, be asserted that $\partial_t U \in L^2(0,T;E')$ and $\gamma^* \partial_t V \in L^2(0,T;E')$. Then, a reasoning similar to the one in [26] shows that $U + \gamma^* V : [0,T] \to L^2(M)$ is continuous with value $U_0 + \gamma^* V_0$ at $t = 0$, and that, for all $\Phi \in L^2(0,T;E)$,

$$\langle \partial_t U + \gamma^* \partial_t V, \Phi \rangle_{L^2(0,T;E'),L^2(0,T;E)} = \mathcal{L}(\Phi).$$

To write more natural equations, in the rest of the chapter we sometimes make an abuse of notation and separate the two derivatives. We then write

$$\begin{aligned} \langle \partial_t U + \gamma^* \partial_t V, \Phi \rangle_{L^2(0,T;E'),L^2(0,T;E)} &= \int_0^T \langle \partial_t U, \Phi \rangle \mathrm{d}t + \int_0^T \langle \gamma^* \partial_t V, \Phi \rangle \mathrm{d}t \\ &= \int_0^T \langle \partial_t U, \Phi \rangle \mathrm{d}t + \int_0^T \langle \partial_t V, \gamma\Phi \rangle \mathrm{d}t, \end{aligned} \tag{3.53}$$

where, in the right-hand side, the duality brackets do not have indices, to avoid claiming that $\partial_t U \in L^2(0,T;E')$ or $\gamma^* \partial_t V \in L^2(0,T;E')$, and to remember that these two terms must be understood together.

Used in (3.36) with $\gamma = \gamma_{\mathfrak{a}}$ for all $\mathfrak{a} \in \chi$, the above reasoning and notations enable us to identify the (combined) time derivatives of $\phi_m S_m^{\alpha}(\overline{p}_m)$ and $\sum_{\mathfrak{a}} \eta S_{\mathfrak{a}}^{\alpha}(\gamma_{\mathfrak{a}} \overline{p}_m)$ as elements of $L^2(0, T; V_m^{0\prime})$.

Conclusions et perspectives

Bilan des résultats obtenus

Dans cette thèse, nous avons établi des modèles monophasiques et diphasiques à dimensions hybrides pour des réseaux généraux de fractures discrètes. Les modèles intègrent les sauts de pression aux interfaces matrice fracture et permettent ainsi de traiter des fractures agitant comme des drains ainsi que comme des barrières. En outre, ils prennent en compte des perméabilités anisotropes et des hétérogénéités dans les différents millieux, notamment la dépendance (non continue) en espace de la perméabilité, la porosité et, en diphasique, des courbes de pression capillaire ainsi que des mobilités. Nous avons étendu la méthode de discrétisations gradient aux modèles à dimensions hybrides, et montré la convergence dans ce cadre général. Deux exemples de schémas gradient ont été d'abord développés, puis analysés : les schémas VAG et HFV. En diphasique, nous avons conduit une comparaison des modèles équi-dimensionnels et dimensionnels hybrides à pressions continues et discontinues pour l'écoulement dans les milieux poreux fracturés.

Dans le chapitre 1, nous avons étendu les modèles présentés dans [6, 45, 56] aux réseaux de fractures généraux, ce que nous a mené au problème (1.5) de l'écoulement Darcy stationaire. Ensuite, nous avons adapté la méthode de discrétisations gradient (cf. [38]) et obtenu la régularité à la limite, théorème 1.3.1, qui est un résultat important dans l'analyse de convergence pour le modèle diphasique, et l'estimation d'erreur, théorème 1.3.3, qui représente le résultat principal de l'analyse numérique de ce chapitre. Comme schémas numériques, nous avons proposé des adaptations des schémas VAG et HFV [37, 38] aux modèles à dimensions hybrides. Des inconnues supplémentaires aux interfaces matrice fracture ont été introduites, pour capter les discontinuités de pression entre ces interfaces et l'intérieur de la fracture. C'est une différence cruciale par rapport aux modèles dimensionnels hybrides à pression continue [5, 15], qui permet de traiter les fractures avec une perméabilité normale quelconque. De plus, dans le cas diphasique, on a vu dans le chapitre 2 que la reproduction des flux gravitaires et capillaires dans la direction normale dans la fracture - qui peuvent influencer significativement l'écoulement global - nécessite l'intégration de ces inconnues supplémentaires. Deux versions de VAG ont été présentées, la version éléments finis conformes et la version volumes de contrôle non conformes, la dernière particulièrement adaptée quand des hétérogénéités sont présentes (cf. [39]). On a montré que les schémas VAG et HFV appartiennent à la classe des schémas gradients. En

appliquant les résultats pour les schémas gradients, nous avons obtenu ainsi la convergence pour VAG et HFV, et en particulier la convergence d'ordre 1 pour des solutions «régulières par morceaux». Des cas tests ont été conduits sur des maillages tetra- et hexaédrique avec une famille de solutions analytiques dans un domaine comportant la matrice et un réseau de quatre fractures avec intersections. Ces tests ont montré que les schémas VAG offrent un meilleur compromis entre taux d'erreur et temps de calcul que le schéma HFV, en particulier pour des problèmes anisotropes. Dans l'appendice, une formulation volumes finis équivalente à la formulation variationnelle discrète a été présentée pour VAG et HFV.

Le modèle à dimensions hybrides introduit dans le chapitre 2 enrichit la littérature d'une formulation en pressions de phases du problème diphasique. Il utilise un décentrage entre les conditions de transmission entre matrice et fracture et prend en compte les flux gravitaires et capillaires dans la direction normale dans la fracture. Pour les problèmes de traceur équi-dimensionnels et dimensionnels hybrides, des solutions analytiques sur un domaine matrice divisé par une fracture ont été calculées pour différents paramètres. Il se manifestait que les modèles à dimensions hybrides perdent en précision pour des ratios de conductivités $\frac{d_f \lambda_f}{L \lambda_m}$ décroissants, ce qui correspond à diminuer l'angle entre la vitesse équi-dimensionnelle dans la fracture et la direction normale à la fracture. Puis, il a été montré que la solution équi-dimensionnelle s'assimile à la solution dimensionnelle hybride, si on ajoute une petite diffusion normale dans la fracture. Ce résultat s'étend aux écoulements diphasiques, comme décrit ci-dessous. Des formulations volumes finis de la version volumes de contrôles du schéma VAG, introduit dans le chapitre 1 pour les problèmes monophasiques stationnaires, ont été présentées pour les modèles diphasiques. En sus de la discrétisation générique du modèle continu (dénommée : modèle 1), nous avons posé un problème discret avec flux matrice fracture linéarisés (dénommé : modèle 2), pour améliorer le temps de calcul pour la simulation, toute en captant les sauts des pressions aux interfaces matrice fracture. Le schéma VAG a été employé pour comparer numériquement quatres modèles différents pour des écoulements dans un réservoir bidimensionnel comportant un réseau de failles. Plus précisément, les solutions des modèles dimensionnels hybrides à pressions discontinues 1 et 2 ont été comparées aux solutions dimensionnelles hybrides à pressions continues (cf. [16]) vis-à-vis la solution référence obtenue par le modèle à dimensions équivalentes. Les tests numériques ont été menés avec une variation des configurations physiques et géologiques, en ce qui concerne les perméabilités et courbes de pression capillaire dans la matrice et dans les failles. La stratification dans la direction normale à l'intérieur des fractures peut jouer un rôle majeur, ce qui indique qu'on doit avoir plus qu'une couche de mailles fractures pour obtenir des solutions de référence valables. Nous avons constaté que le modèle 2 et le modèle dimensionnel hybride à pressions continues produisent des solutions quasiment équivalentes. Quant à la robustesse, les cas tests montrent un clair avantage à ces modèles. Toutefois, le modèle 1 est beaucoup plus robuste que le modèle équi-dimensionnel. En outre, le modèle équi-dimensionnel n'est pas praticable pour des ratios $\frac{\lambda_f}{\lambda_m}$ ou $\frac{L}{d_f}$ trop grands. En analogie au problème de transport de solvant idéal, nous avons observé une bonne concordance entre les solutions à dimensions équivalentes et hybrides pour des grands ratios de conductivité

fracture et matrice, et une augmentation de l'écart pour des ratios plus petits. D'autre part, en ajoutant de la capillarité dans les fractures, la solution équi-dimensionnelle tend vers les solutions dimensionnelles hybrides. Dans le premier test, nous avons vu l'influence de la ségrégation gravitaire sur le comportement global de l'écoulement. Cet effet n'a pas pu être reproduit par le modèle 2 ou le modèle à pressions continues, car ces modèles ne connaissent qu'une saturation constante au travers de la fracture. Cette remarque s'étend à tout schéma centré aux mailles. L'information supplémentaire sur les saturations aux interfaces permets au modèle 1 de capter la ségrégation gravitaire dans les fractures. Une autre différence entre ces modèles apparaît dans les tests avec capillarité dans le milieu matriciel : modèle 1 reconstruit les forces dûes à la différence de la pression capillaire entre les interfaces matrice fracture et l'intérieur de la fracture, où le modèle 2 et le modèle à pression continue négligent cette différence des pressions capillaires pour la construction des flux matrice fracture. Ces caractéristiques font que le modèle 1 est significativement plus précis sur le transport à travers des fractures. L'hypothèse de pressions continues aux interfaces matrice fracture dans le modèle hybride à pressions continues (et l'absence du paramètre $\lambda_{f,\mathbf{n}}$) n'est plus valable pour des barrières. Dans le cas test avec barrière, nous avons vu que les deux modèles dimensionnels hybrides à pressions discontinues donnent des bons résultats en termes de robustesse et de précision. Dans tout les cas, nous avons pu constater un gain significatif en précision pour la solution du modèle 1 relatif à la solution équi-dimensionnelle de référence, comparée aux solutions du modèle 2 et du modèle à pression continue.

Dans le chapitre 3, nous avons proposé une légère modification du modèle diphasique dimensionnel hybride à pressions discontinues, en attribuant un propre type de roche aux interfaces matrice fracture avec la capacité d'accumuler de fluide. Cette modification est motivée d'un part par l'ambition de modéliser des effets d'endommagement de ces interfaces, et d'autre part pour permettre une analyse numérique. Pour réaliser l'analyse de convergence, nous avons étendu la méthode de discrétisations gradient à ce problème. Fondé sur des arguments de compacité, nous avons montré dans théorème 3.4.1 la convergence forte L^2 des saturations et la convergence faible L^2 des pressions vers une solution faible du modèle continu. Nous avons établi dans théorème 3.4.3 la convergence uniforme en temps, faible L^2 en espace des saturation, un résultat qui a été étendu à la convergence uniforme en temps, forte L^2 en espace dans [34], en appliquant des idées initialement formulées dans [27]. Puis, nous avons présenté une série d'expériences numériques, avec l'objectif d'étudier l'impact de la couche de roche endommagée aux interfaces matrice fracture. Le comportement des solutions dans les différentes situations correspond aux attentes. On a observé des différences significatives des solutions pendant le remplissage de la fracture, par rapport au jeu de types de roches, quand l'épaisseur des couches étaient de l'ordre de celle de la fracture, et des différences négligables pour les épaisseurs petites (relativement à l'épaisseur de la fracture). En termes de robustesse et temps de calcul, nous avons vu que la présence d'une zone endommagée aux interfaces matrice fracture est indispensable pour résoudre le problème discret implicitement. Nous avons vu également que la simulation est coûteuse pour des grands contrastes entre les courbes de pressions

capillaires aux interfaces et dans le drain.

Perspectives

Elimination des inconnues aux interfaces matrice fracture. Suivant les études du chapitre 2, la connaissance des saturations aux interfaces matrice fracture et à l'intérieur de la fracture est essentielle pour une modélisation discrète adéquate de l'écoulement diphasique. Le point critique du modèle 1 est un manque de robustesse relatif au modèle 2. Pour les applications, il serait désirable d'augmenter la robustesse. Il serait par exemple envisagable d'implémenter une élimination non linéaire des inconnues aux interfaces matrice fracture au début de chaque itération de Newton, ce qui demanderait certes une adaptation du schéma pour découpler ces inconnues l'une de l'autre.

Estimation d'erreur entre les modèles à dimensions hybrides et équivalentes. Nous avons vu dans les expériences numériques que les solutions des modèles dimensionnels hybrides perdent en précision par rapport aux solutions équi-dimensionnelles avec un ratio de conductivités drain matrice décroissant. On avait également observé que cet effet disparait, si on ajoute un terme de diffusion normale dans la fracture. Ces observations motivent une analyse pour estimer l'erreur entre les modèles dimensionnels hybrides et le modèle équi-dimensionnel.

Généralisation du modèle. Pour traiter les intersections de fractures fortement hétérogènes ou d'épaisseurs fortement variables, le modèle doit être généralisé. Il serait nécéssaire de prendre en compte des sauts de pressions aux intersections, ce qui est exclu dans le cadre de ce présent travail, par la définition de l'espace fonctionnel V_f. Pour un traitement de domaines comportant des fractures de différents échelles, il serait aussi envisagable de coupler le modèle réduit avec des modèles multi milieux. D'autre part, il serait utile pour la plupart des applications, d'étendre le modèle aux écoulements compositionnels et thermiques. Un autre objectif pourrait être l'intégration de la mécanique dans le modèle.

Applications industrielles. Les résultats de cette thèse montrent que les modèles reduits avec simples inconnues aux fractures sont insuffisants en termes de précision de la simulation. Une perspective serait donc d'intégrer le modèle 1 dans les simulateurs de réservoirs industriels.

Bibliography

[1] R. A. Adams. Sobolev Spaces. *Academic Press New York San Francisco London*, 1975.

[2] M. Ahmed, E., J. Jaffré, and J. E. Roberts. A reduced fracture model for two-phase flow with different rock types. *Math. Comput. Simulation*, 2016.

[3] R. Ahmed, M. Edwards, S. Lamine, B. Huisman, and M. Pal. Control-volume distributed multi-point flux approximation coupled with a lower-dimensional fracture model. *Journal of Computational Physics*, 284:462–489, mar 2015.

[4] R. Ahmed, M. G. Edwards, S. Lamine, B. A. Huisman, and M. Pal. Three-dimensional control-volume distributed multi-point flux approximation coupled with a lower-dimensional surface fracture model. *Journal of Computational Physics*, 303:470–497, dec 2015.

[5] C. Alboin, J. Jaffré, J. Roberts, and C. Serres. Modeling fractures as interfaces for flow and transport in porous media. volume 295, pages 13–24, 2002.

[6] P. Angot, F. Boyer, and F. Hubert. Asymptotic and numerical modelling of flows in fractured porous media. *ESAIM: Mathematical Modelling and Numerical Analysis*, 43(2):239–275, mar 2009.

[7] P. F. Antonietti, L. Formaggia, A. Scotti, M. Verani, and N. Verzotti. Mimetic finite difference approximation of flows in fractured porous media. *ESAIM M2AN*, 50:809–832, 2016.

[8] S. N. Antontsev, A. V. Kazhikhov, and V. N. Monakhov. Boundary value problems in mechanics of nonhomogeneous fluids. *Studies in Mathematics and its Applications, North-Holland Publishing Co.*, 22, 1990. Translated from Russian.

[9] G. Barenblatt, I. Zheltov, and I. Kochina. Basic concepts in the theory of seepage of homogeneous liquids in fissured rocks. *Journal of Applied Mathematics and Mechanics*, 20:825–864, 1960. English translation.

[10] S. Berrone, S. Pieraccini, and S. Scialò. An optimization approach for large scale simulations of discrete fracture network flows. *Journal of Computational Physics*, 256:838–853, 2014.

[11] I. I. Bogdanov, V. V. Mourzenko, J.-F. Thovert, and P. M. Adler. Two-phase flow through fractured porous media. *Physical Review E*, 68(2), aug 2003.

[12] J. Bonelle and A. A. Ern. Analysis of compatible discrete operator schemes for elliptic problems on polyhedral meshes. *ESAIM Math. Mod. Numer. Anal.*, 48(2):553–581, 2014.

[13] K. Brenner. *Méthodes de volumes finis sur maillages quelconques pour des systèmes d'évolution non linéaires*. PhD thesis, Université d'Orsay, 2011.

[14] K. Brenner, C. Cancès, and D. Hilhorst. Finite volume approximation for an immiscible two-phase flow in porous media with discontinuous capillary pressure. *Computational Geosciences*, 2013.

[15] K. Brenner, M. Groza, C. Guichard, G. Lebeau, and R. Masson. Gradient discretization of hybrid-dimensional Darcy flows in fractured porous media. *Numerische Mathematik*, 134(3):569–609, nov 2016.

[16] K. Brenner, M. Groza, C. Guichard, and R. Masson. Vertex Approximate Gradient scheme for hybrid-dimensional two-phase Darcy flows in fractured porous media. *ESAIM: Mathematical Modelling and Numerical Analysis*, 2(49):303–330, 2015.

[17] K. Brenner, M. Groza, L. Jeannin, R. Masson, and J. Pellerin. Immiscible two-phase darcy flow model accouting for vanishing and discontinuous capillary pressures: application to the flow in fracture porous media. In *ECMOR XV- 15th European Conference on the Mathematics of Oil Recovery*, 2016.

[18] K. Brenner and R. Masson. Convergence of a Vertex centered Discretization of Two-Phase Darcy flows on General Meshes. *Int. Journal of Finite Volume Methods*, 15(10), 2013.

[19] F. Brezzi, K. Lipnikov, and V. Simoncini. A family of mimetic finite difference methods on polygonal and polyhedral meshes. *Mathematical Models and Methods in Applied Sciences*, 15(10):1533–1552, 2005.

[20] C. Cancès. Finite volume scheme for two-phase flows in heterogeneous porous media involving capillary pressure discontinuities. *M2AN, Mathematical Modelling and Numerical Analysis*, 43(5):973–1001, 2009.

[21] C. Cancès and M. Pierre. An existence result for multidimensional immiscible two-phase flows with discontinuous capillary pressure field. *SIAM J. Math. Anal.*, 44(2):966–992, 2012.

[22] G. Chavent and J. Jaffré. Mathematical models and finite elements for reservoir simulation. *Studies in Mathematics and its Applications, North-Holland*, 17, 1986.

[23] C. D'Angelo and A. Scotti. A mixed finite element method for Darcy flow in fractured porous media with non-matching grids. *ESAIM: Mathematical Modelling and Numerical Analysis*, 46(2):465–489, mar 2012.

[24] J. Demmel, S. Eisenstat, J. Gilbert, X. Li, and J. Liu. A supernodal approach to sparse partial pivoting. *SIAM J. Matrix Analysis and Applications*, 20(3):720–750, 1999.

[25] J. Demmel, J. Gilbert, L. Grigori, X. Li, M. Shao, and I. Yamazaki. Technical Report LBNL-44289, Lawrence Berkeley National Laboratory, SuperLU Users' Guide, September 1999. `http://crd.lbl.gov/~xiaoye/SuperLU`.

[26] J. Droniou. Intégration et espaces de sobolev à valeurs vectorielles. Polycopiés de l'Ecole Doctorale de Maths-Info de Marseille. `https://hal.archives-ouvertes.fr/hal-01382368`, 2001.

[27] J. Droniou and R. Eymard. Uniform-in-time convergence of numerical methods for non-linear degenerate parabolic equations. *Numer. Math.*, 132(4):721–766, 2016.

[28] J. Droniou, R. Eymard, and P. Feron. Gradient Schemes for Stokes problem. *IMA J. Numer. Anal.*, 36(4):1636–1669, 2016.

[29] J. Droniou, R. Eymard, T. Gallouët, C. Guichard, and R. Herbin. *The gradient discretisation method: A framework for the discretisation of linear and nonlinear elliptic and parabolic problems*. 2016. Submitted. `https://hal.archives-ouvertes.fr/hal-01382358`.

[30] J. Droniou, R. Eymard, T. Gallouët, and R. Herbin. A unified approach to mimetic finite difference, hybrid finite volume and mixed finite volume methods. *Math. Models Methods Appl. Sci.*, 20(2):265–295, 2010.

[31] J. Droniou, R. Eymard, T. Gallouët, and R. Herbin. Gradient schemes: a generic framework for the discretisation of linear, nonlinear and nonlocal elliptic and parabolic equations. *Math. Models Methods Appl. Sci.*, 13(23):2395–2432, 2013.

[32] J. Droniou, R. Eymard, and R. Herbin. Gradient schemes: generic tools for the numerical analysis of diffusion equations. *M2AN Math. Model. Numer. Anal.*, 50(3):749–781, 2016. Special issue – Polyhedral discretization for PDE.

[33] J. Droniou, R. Eymard, and K. S. Talbot. Convergence in $C([0;T];L^2(\Omega))$ of weak solutions to perturbed doubly degenerate parabolic equations. *J. Differential Equations*, 260(11):7821–7860, 2016.

[34] J. Droniou, J. Hennicker, and R. Masson. Uniform-in-time convergence of numerical schemes for a model of diphasic flow in a discrete fractured network media. 2016. Submitted to the FVCA8 proceedings.

[35] J. Droniou and K. S. Talbot. On a miscible displacement model in porous media flow with measure data. *SIAM J. Math. Anal.*, 46(5):3158–3175, 2014.

[36] C. J. Duijn, J. Molenaar, and M. J. Neef. The effect of capillary forces on immiscible two-phase flows in heterogeneous porous media. *Transp. Porous Media*, 21:71–93, 1995.

[37] R. Eymard, T. Gallouët, and R. Herbin. Discretization of heterogeneous and anisotropic diffusion problems on general nonconforming meshes : a scheme using stabilisation and hybrid interfaces. *IMA J Numer Anal*, 30(4):1009–1043, 2010.

[38] R. Eymard, C. Guichard, and R. Herbin. Small-stencil 3D schemes for diffusive flows in porous media. *ESAIM: Mathematical Modelling and Numerical Analysis*, 46(2):265–290, 2012.

[39] R. Eymard, C. Guichard, R. Herbin, and R. Masson. Vertex-centred discretization of multiphase compositional Darcy flows on general meshes. *Computational Geosciences*, 16(4):987–1005, 2012.

[40] R. Eymard, C. Guichard, R. Herbin, and R. Masson. Gradient schemes for two-phase flow in heterogeneous porous media and Richards equation. *ZAMM Z. Angew. Math. Mech.*, 94(7-8):560–585, 2014.

[41] R. Eymard, C. Guichard, R. Herbin, and R. Masson. Tp or not tp, that is the question. *Computational Geosciences*, 18:285–296, 2014.

[42] R. Eymard, R. Herbin, and A. Michel. Mathematical study of a petroleum-engineering scheme. *M2AN Math. Model. Numer. Anal.*, 37(6):937–972, 2003.

[43] I. Faille, A. Fumagalli, J. Jaffré, and J. Robert. Reduced models for flow in porous media containing faults with discretization using hybrid finite volume schemes. 2015.

[44] I. Faille, A. Fumagalli, J. Jaffré, and J. E. Roberts. Model reduction and discretization using hybrid finite volumes of flow in porous media containing faults. *Computational Geosciences*, 20:317–339, 2016.

[45] E. Flauraud, F. Nataf, I. Faille, and R. Masson. Domain decomposition for an asymptotic geological fault modeling. *Comptes Rendus Mécanique*, 331(12):849–855, dec 2003.

[46] L. Formaggia, A. Fumagalli, A. Scotti, and P. Ruffo. Vertex-centred discretization of multiphase compositional Darcy flows on general meshes. *ESAIM Mathematical Modelling and Numerical Analysis*, 48(4):1089–1116, 2014.

[47] A. Fumagalli, A. Scotti, A. Cangiani, R. L. Davidchack, E. Georgoulis, and A. N. Gorban. A reduced model for flow and transport in fractured porous media with non-matching grids. *Numerical Mathematics and Advanced Applications*, pages 499–507, 2013.

[48] M. Groza. *Modélisation et discrétisation des écoulements diphasiques en milieux poreux avec réseaux de fractures discrètes*. PhD thesis, Université Nice Sophia Antipolis, 2016.

[49] H. Haegland, A. Assteerawatt, H. Dahle, G. Eigestad, and R. Helmig. Comparison of cell- and vertex-centered discretization methods for flow in a two-dimensional discrete-fracture-matrix system. *Advances in Water resources*, 32:1740–1755, 2009.

[50] H. Hoteit and A. Firoozabadi. An efficient numerical model for incompressible two-phase flow in fractured media. *Advances in Water Resources*, 31(6):891–905, jun 2008.

[51] J. Jaffré, M. Mnejja, and J. Roberts. A discrete fracture model for two-phase flow with matrix-fracture interaction. *Procedia Computer Science*, 4:967–973, 2011.

[52] J. Jaffré, M. Mnejja, and J. E. Roberts. A discrete fracture model for two-phase flow with matrix-fracture interaction. *Procedia Computer Science*, 4:967–973, 2011.

[53] D. Jansen. Identifikation des mehrkontinuum–modells zur simulation des stofftransportes in multiporösen festgesteinsaquiferen. *Mitteilungen 118, Lehrstuhl und Institut für Wasserbau und Wasserwirtschaft, RWTH Aachen*, 1999.

[54] M. Karimi-Fard, L. Durlofsky, and K. Aziz. An efficient discrete-fracture model applicable for general-purpose reservoir simulators. *SPE Journal*, 9(02):227–236, jun 2004.

[55] H. Kazemi. Pressure transient analysis of naturally fractured reservoirs with uniform fracture distribution. *Trans. Soc. Pet. Engng AIME*, 246:451–462, 1969.

[56] V. Martin, J. Jaffré, and J. E. Roberts. Modeling fractures and barriers as interfaces for flow in porous media. *SIAM Journal on Scientific Computing*, 26(5):1667–1691, 2005.

[57] S. K. Matthai, A. A. Mezentsev, and M. Belayneh. Finite element - node-centered finite-volume two-phase-flow experiments with fractured rock represented by unstructured hybrid-element meshes. *SPE Reservoir Evaluation & Engineering*, 10(06):740–756, dec 2007.

[58] A. Michel. A finite volume scheme for two-phase immiscible flow in porous media. *SIAM J. Numer. Anal.*, 41(4):1301–1317, 2003.

[59] J. E. Monteagudo and A. Firoozabadi. Control-volume model for simulation of water injection in fractured media: incorporating matrix heterogeneity and reservoir wettability effects. *SPE Journal*, 12(03):355–366, sep 2007.

[60] K. Pruess and T. Narasimhan. A practical method for modeling fluid and head flow in fractured porous media. *Society of Petroleum Engineers Journal*, 25(1):14–26, 1985.

[61] P. Raviart. Résolution Des Modèles Aux Dérivées Partielles. *Ecole Polytechnique, Département de Mathématiques appliquées*, 1992.

[62] V. Reichenberger, H. Jakobs, P. Bastian, and R. Helmig. A mixed-dimensional finite volume method for two-phase flow in fractured porous media. *Advances in Water Resources*, 29(7):1020–1036, jul 2006.

[63] Y. Saad. Iterative Methods for Sparse Linear Systems. *2nd edition, SIAM, Philadelphia, PA*, 2003.

[64] Y. Saad. Technical report, ITSOL Library, 2010.

[65] M. Sahimi. *Flow and transport in porous media and fractured rock: from classical methods to modern approaches*. John Wiley & Sons, 2011.

[66] T. Sandve, I. Berre, and J. Nordbotten. An efficient multi-point flux approximation method for Discrete Fracture-Matrix simulations. *Journal of Computational Physics*, 231(9):3784–3800, may 2012.

[67] N. Schwenck, B. Flemisch, R. Helmig, and B. Wohlmuth. Dimensionally reduced flow models in fractured porous media: crossings and boundaries. *Computational Geosciences*, 19:1219–1230, 2015.

[68] B. Singhal and R. Gupta. *Applied Hydrogeology of Fractured Rocks*. Springer Netherlands, 2010.

[69] X. Tunc, I. Faille, T. Gallouët, M. C. Cacas, and P. Havé. A model for conductive faults with non-matching grids. *Computational Geosciences*, 16(2):277–296, mar 2012.

[70] J. Warren and P. Root. The behavior of naturally fractured reservoirs. *SPEJ*, pages 245–55, 1963.

[71] F. Xing, R. Masson, and S. Lopez. Parallel Vertex Approximate Gradient discretization of hybrid-dimensional Darcy flow and transport in discrete fracture networks. *Computational Geosciences*, 2016.